UNIVERSIDAD COMPLUTENSE DE MADRID

FACULTAD DE CIENCIAS FÍSICAS

Departamento de Arquitectura de Computadores y Automática

TESIS DOCTORAL

Modeling piezoresistive force sensors and usage of a dataglove interface towards the impedance control of robotic manipulators.

Modelado de sensores piezoresistivos y uso de una interfaz basada en guantes de datos para el control de impedancia de manipuladores robóticos

MEMORIA PARA OPTAR AL GRADO DE DOCTOR

PRESENTADA POR

Leonel Paredes Madrid

Director

Pablo González de Santos

Madrid, 2014

UNIVERSIDAD COMPLUTENSE DE MADRID
FACULTAD DE CIENCIAS FÍSICAS

DEPARTAMENTO DE ARQUITECTURA DE COMPUTADORES Y AUTOMÁTICA

MODELING PIEZORESISTIVE FORCE SENSORS AND USAGE OF A DATAGLOVE INTERFACE TOWARDS THE IMPEDANCE CONTROL OF ROBOTIC MANIPULATORS

Modelado de sensores piezoresistivos y uso de una interfaz basada en guantes de datos para el control de impedancia de manipuladores robóticos

Tesis Doctoral

Leonel Paredes Madrid

2014

UNIVERSIDAD COMPLUTENSE DE MADRID
FACULTAD DE CIENCIAS FÍSICAS
DEPARTAMENTO DE ARQUITECTURA DE COMPUTADORES Y AUTOMÁTICA

MODELING PIEZORESISTIVE FORCE SENSORS AND USAGE OF A DATAGLOVE INTERFACE TOWARDS THE IMPEDANCE CONTROL OF ROBOTIC MANIPULATORS

Modelado de sensores piezoresistivos y uso de una interfaz basada en guantes de datos para el control de impedancia de manipuladores robóticos

Tesis Doctoral

Autor: Leonel Paredes Madrid
Director: Pablo González de Santos

2014

To God, for being the source of my daily life inspirations
and unconditional support

In the memory of my father, Perfecto Paredes.

Index of Contents

Index of Figures

Index of Tables

Acknowledgements

This thesis has been the result of five years of intensive and collaborative research in which several people have directly and indirectly helped me to pursue my professional and personal goals. Recalling all those who helped me during my PhD trip is a task that would require a second PhD to be written! and thus, the next lines are only an attempt to thank those whom have more deeply and constantly helped me throughout my trip. For all those who helped me but not next listed, please, do not shame on me!

First of all, I would like to thank my mother and my sister who have been as father-mother for me, especially after my father decease. There are simply no words to express my affections for them.

There are two persons who made possible this experience, my thesis supervisor PhD Pablo González de Santos and PhD Gerardo Fernández. They played together as matchmakers in uncountable situations and allowed many of my close friends to pursue his dreams. My relationship with them along these five years has been of paramount importance to get inspiration, ideas and to overcome the technical and personal challenges which naturally emerge during research activities. I can not forget the multiple talks I had with my advisor, PhD Pablo González, while some of them were heated and mostly fraternal; they all helped me to learn the research way of thinking and to grow in humbleness.

Following with the line of my strong inspirers, the head of the Centre for Automation and Robotics, PhD Manuel Armada, is the next person I owed the most. He was the first who kindly welcomed me at the old IAI and often shared with me a coffee at the Centre's local bar. PhD Elena García has been also a cornerstone during these last five years due to her support and the provided facilities. Likewise, I appreciate the Spanish National Research Council, CSIC, and the grant program JAE Predoc, for supporting my personal expenses and providing me an adequate framework for my research activities.

The contribution of my advisor at UCM, PhD Segundo Esteban, was also remarkable in multiple aspects, but mainly during my DEA project writing and when dealing with paper works at the UCM. The contribution of the staff professors at UCM was highly valuable for my education in the early stages of my PhD. Therefore, I thank the Physics and Computer Science Faculties from UCM, and specifically the Department of Computer Architecture and Automation which host me several times during classes, seminars, tutoring activities and on daily talks.

I am also grateful to PhD James E. Colgate and PhD Michael Peshkin, my former advisors at Northwestern University; they were examples of hard and dedicated work in

projects with little background research, and thus, my inspiration for seeking novel ideas. Likewise I would like to thank MSc Nick Marchuk who was my loyal team fellow during my appointment at NU.

The team fellows at the CAR UPM-CSIC were of great help towards the prosecution of my professional goals, but specially on making more enjoyable the work time. Among many others, I am grateful to PhD Héctor Montes, PhD Emilia Fernández, Javier Sarria and Eng. Carlota Salinas, and of course, to my Venezuelan colleagues who currently keep doing his best to finish his projects. I definitely must recall the name of my last office partner, Eng. Jesus Reviejo, for his mute -but nicely- behavior and for his support in solving QNX technical problems. Special thanks to MSc Luis Emmi who helped me a lot to set-up my experiments and for sparking lively discussion one-on-one. I can not forget the help provided by the undergrad students who attended the CAR for making their final career project. However, I must specially thank Eng. Bruno Pierucci who entirely designed – with little supervision- the conditioning board of the dataglove interface herein presented.

I can not forget the support provided by the Community of Madrid which continuously granted me through the project TECHNOFUSION (S2009/ENE-1679).

Two special friends have shared with me unforgettable moments and have become part of my abroad family, they are PhD Sylvia Méndez, who started this trip by my side and has been always a cornerstone on my highs but specially on my lows, and Isabella Rossi who became my proxy sister and taught me the German way of living.

Last, but not least, I recall all my friends who showed me how marvelous living on Spain and Germany is by sharing multiple tapas and beers on local bars, but since the list would be too long, I prefer to keep it on my mind.

Madrid, 2014

Leonel Paredes Madrid.

Abstract

This thesis presents a dataglove-based interface for the impedance control of robotic manipulators. The interface comprises a commercial dataglove for measuring fingers' position, an Inertial Measurement Unit (IMU) for tracking hand motion and 11 piezoresistive sensors to measure the applied hand forces. The interface was thoroughly tested on a 6-DOF manipulator with a load cell installed near the robot's end effector. The accuracy of the dataglove interface was assessed through a static test in which the load cell measurements were used as reference on a time-basis. The final test comprised the implementation of an impedance control algorithm in the aforesaid manipulator, in which the interface force readings were used as input for controlling robot motion.

A second line of research is addressed on this thesis regarding the modeling of the piezoresistive sensor FlexiForce A201-100. The sensor, used in the assembling of the dataglove interface, was thoroughly characterized under DC and AC sourcing for multiple applied forces and different puck areas. Three new properties that enhance sensor's capabilities and sensor's response were found. First, it was studied the conductance nonlinearity for DC input voltages under **1 V** and a method to estimate sensor's sensitivity was presented. Second, a piezocapacitive response was found in the sensor which demonstrated its usefulness towards the reduction of the force estimation error, and third; a combined estimation of the applied force and the exertion area was presented through the combined conductance-capacitance estimation.

Chapter 1

1. Introduction: Understanding the basis of haptic perception and object manipulation

The identification and manipulation of objects through tactile exploration is a daily life activity for humans. Turning a door knob is a common, yet not simple, task that involves the combination of multiple sources of information from the visual, tactile and motion domains. This ability, almost exclusive of humans, relies mostly on the visual and somatosensory receptors that together with the central nervous system generate a suitable trajectory for the hand and fingers. Two separate tasks, hand approach to the knob and knob turning, are the subjects to be introduced in this chapter towards the understanding and further emulation of human skills in bioinspired robots.

1.1 The importance of force measurements in Hand-Centered Studies

The Human hand is a complex 27 degrees-of-freedom (DOF) member [108]. It provides humans with a huge variety of grasp types that may be classified in 4 major categories: power grip, intermediate grip, precision grip and grips with no thumb involvement [83]. Human-hand dexterity is especially remarkable, among the rest of species, due to the ability to fully oppose the thumb to rest of the fingers [21]. Analogously, primates such as chimpanzees and orangutans are able to partially oppose their thumbs which allow them to use a variety of sophisticated tools [114]; the restriction of partially opposition implies that pulp-to-pulp contact is not possible between the primates' thumb and the rest of fingers, even though, primates' dexterity is highly remarkable among animals. They are capable of constructing elaborate sleeping nests each night from branches and foliage. These handling abilities are far from being reached by robotic hands, thereby a great effort has been placed to track and understand the primates and humans prehension in an attempt to emulate their abilities.

There are two basic properties that a cybernetic hand must have: an adequate sensory and actuator system accordingly designed for the task to perform, and the ability to gather and analyze the sensory data in order to perform the proper finger and hand motion commands.

A bioinspired sensory system should be available in cybernetic hands if the required dexterity is similar to that of a real hand. This is a major challenge in nowadays research because sensors tend to be bulky, expensive and unable to measure certain properties of the grasped objects such as sharpness, rigidness and temperature. Likewise, the hand muscles exhibit power densities that the leading-edge servomotors are still unable to provide [16], this yields underactuated robotic hands (in an attempt to save space) or off-the-robot location of actuators. In any case, finger motion of cybernetic hands is awkward compared to those of a real hand; even for the *shadow hand* [161], the most realistic realization of a robotic hand ever made with a total of 24 DOF.

The development of adaptive and flexible algorithms for controlling cybernetic hands is also an active research in robotics. Hiden-Markov Models and neural network techniques are often used to obtain a human-like behavior in robotic hands [1]. The ability to deal with unstructured environments and with constantly changing objects is the key factor to overcome in the development of control algorithms. However, there is still a long road ahead to emulate human skills when manipulating objects of different sizes and weights in a time shared basis. The lack of dexterity not only lies in the existing algorithms intended to control hand motion; the sensory system also plays an important role in this task, because as previously stated, the sensory system of robotic hands is not yet capable of measuring certain properties of the grasped objects, and thus, the control algorithm generates grasp commands based on incomplete-object information.

1.2 Emulating haptic perception in robotic applications: A challenging task for the leading-edge technology of force sensors

The process of recognizing objects through tactile exploration is known as *haptic perception*, which is an ability that the proprioceptors and kinesthesic senses provide to the humans. Proprioceptors and kinesthesis senses are also responsible for a wide variety of human skills such as: sense of equilibrium, ability to determine where a particular body part is located in the space and the ability to determine if a body part has moved. People can rapidly and accurately identify three-dimensional objects by touch; this outstanding human ability combines two processes: *proprioceptive perception* (hand and finger position) and *somatosensory perception of patterns* (texture, edge and curvature of the grasped object). Human skin plays a key role in the latter process because mechanoreceptors and nociceptors lie in the skin; these receptors are responsible for pressure and pain measurement respectively.

A human-like robotic skin should be able to measure, at least, the same object properties than a real hand can actually do. Carrozza and Lamy have presented partial solutions for this task employing strain gages and piezoresistive sensors respectively [16, 100]. These solutions are addressed as partial because current technology is only capable of measuring force and contact. However, these solutions combined with an adequate control algorithm can improve the interaction between the cybernetic hands and the grasped objects in terms of new skills, such as: slippage detection, precision grasp and object liftoff [16].

Likewise, human-like robotic skins can help to ensure safety in a shared human-robot environment by detecting unwanted collision during comanipulation tasks [100]. Safety is of great importance in the domain of Collaborative Robots (Cobots) [98]. In such scenarios, an operator and a robot are working in the same space and physically interacting. Comanipulation is often used to mix the advantages of human workers, such as:

- Outstanding sensory system
- Ability to learn complex tasks and
- Adaptability to changing environments

with the benefits of robots, such as:

- Precision and strength in motion, without getting tired after hours of continuous work and
- Highly Repeatable trajectories, this is of great importance when performing repetitive tasks.

Above advantages must be combined in a framework that ensures comfort and safety for the operator. Then, it becomes natural that force and motion are the variables to monitor and control in a shared human-robot environment. This statement yields the *impedance control of robots*; which has been an active research trend for many years.

Joint encoders, force/torque sensors and accelerometers have been widely used in impedance control applications to provide force/position feedback. A thorough review of impedance control of manipulators shows that force sensors have been usually mounted on the robot end effector, whereas position/speed sensors are integrated in the robot joints. However, this sensory set-up does not warrant user safety, because as previously stated, unwanted collision during comanipulation tasks may still occur. It must be remarked that impedance control is only effective around the robot end effector, but not around the whole robot´s structure, and thus, an unwanted collision between the operator and the robot´s body may go unnoticed and robot motion unaffected.

Human-like robotic skins are a promising approach in the direction of ensuring safety in shared human-robot environments, since they can detect unwanted collision during comanipulation tasks. However, it has not been yet implemented a control layout where the only source of force feedback is provided by such a robotic skin, just as a mute volunteer guides a blind person to walk across the street by holding the blind-person's arm. Under this scenario, the person responds to the force commands from the volunteer in a compliant way, relying solely on her arm mechanoreceptors, just like a robot should respond to the operator intention in case of motion guidance.

Sudden Collisions between the mute volunteer and the blind person are likely to happen during the guidance process. Nevertheless, these collisions do not represent serious harm for any of them; due to the sophisticated proprioceptive system and the intelligence available in both subjects. Hence, it is a logical approach of current research to focus on providing robots with the aforementioned two capabilities (sophisticated proprioceptive system and intelligence); this fact is the main motive for the realization of this thesis.

1.3 Statement of Purpose

This thesis addresses two issues emerging from the interaction of human and robots in cooperative environments. Consequently, two goals are presented as alternatives for overcoming such restrictions.

The first issue is the lack of a detailed model for most of the available skin sensors. This condition is one of the key aspects for the underperformance of such devices and the consequent underused in robotic applications. Skin sensors are mostly of piezoresistive type, which means that incremental forces yield proportional changes in conductance.

The first goal of the current research is to improve the performance of the piezoresistive sensors by modeling sensors' response under DC and AC sourcing. Sensor characterization is merely empirical, and is presented in terms of conductance and capacitance. The force sensor chosen for the current research is the *A201-100 FlexiForce* manufactured by Tekscan Inc, with a nominal range of **440 N** and a sensing area of **71 mm^2** (similar to the size of a 1 cent Euro coin).

The second issue is the employment of piezoresistive sensors in an impedance control application involving a robotic manipulator and an operator. This is a major concern in a shared workspace application if the robot reaction is likely to emulate that of a human being.

The second goal is to implement an impedance control scheme on a manipulator using piezoresistive sensors as the only source of force feedback to the control loop. The developed application uses impedance control as the underlying basis for controlling robot motion. However, an important difference exists with the robotic-skin approach. Instead of placing the force sensors along the robot´s structure, the operator wears a handheld device with the sensors integrated into the palm-side fabric of a 15-DOF dataglove. An Inertial Measurement Unit (IMU) is integrated to the dorsal-side of the dataglove to measure hand orientation within the workspace.

The proposed dataglove-based interface is capable of measuring individual force contributions through a combination of finger position, force sensors and hand orientation. A resultant force vector is calculated and proper motion is achieved in the manipulator. This vector represents user intention, just as a human-like robotic skin measures the operator applied forces.

1.4 Abbreviations and Terminology

Here are presented the basic definitions and abbreviations which are addressed throughout this document.

AC: abbreviation of Alternate Current.

Conf.: Abbreviation of Conference.

DC: abbreviation of Direct Current.

IAD: abbreviation for Intelligent Assist Device. A new concept of robotic manipulators for industrial applications which are intended to work in direct cooperation with humans under shared-time and shared-workspace conditions

Int.: Abbreviation for International.

Mechanical Impedance: The ratio of the mechanical force acting in the direction of motion, to the velocity of the resulting vibration. Mechanical impedance is a frequency dependent magnitude, and thus, a phasor notation is used to represent it.

MEMs: Abbreviation for *Microelectromechanical* systems. It is the technology of very small devices within the range of 1 up to 100 micrometers. *MEMs* applications are multiple and range from inkjet printers, accelerometers, gyroscopes, pressure and fluid sensors.

OEM: Abbreviation of *Original Equipment Manufacturer*. It refers to the original manufacturer of a product, rather than the product reseller. When dealing with product manufacturing, the phrase OEM quantities is a synonym for large quantities.

OPAMP: Abbreviation of *OPerational AMPlifier*. It refers to an electronic circuit with a differential input and a single output, which is capable of producing an output potential thousand times greater than the applied between its terminals.

RS-232: is a communication standard working on a serial-basis which allows baud rates of up to 115Kbits/s; it works on voltage levels of ±12V. The RS-232 standard was widely used on Personal Computers till the introduction of the faster USB standard. Nonetheless, and due to its simplicity, the RS-232 standard is still widely used to communicate peripherals in industrial environments that require a low data throughput.

Strain: is the amount of deformation of a body due to an applied force. More specifically, strain is defined as the fractional change in length.

Strain gauge: Strain gauge: A strain gauge's electrical resistance varies in proportion to the amount of strain placed on it. The most widely used gauge is the bonded metallic strain gauge. The metallic strain gauge consists of a very fine wire or, more commonly, metallic foil arranged in a grid pattern. The grid pattern maximizes the amount of metallic wire or foil subject to strain in the parallel direction (shown as the "active grid length" in the Bonded Metallic Strain Gauge figure)

Stress: is defined as the measure of the internal forces acting within a deformable body. More general definitions of stress and strain are possible by taking a differential element; in such case, stress is defines as the force per unit area upon which it acts, and strain is the deformation produces by such force.

Symp.: Abbreviation of Symposium.

USB: Stands for *Universal Serial Bus*. It is an industry standard that defines the hardware connections and software protocol used in a bus for communications and sourcing between computers and peripheral devices. It provides data throughput of up to 4Gbits/s in its latest release, the USB 3.0. Unlike the RS-232, the USB standard has power handling capabilities of up to 1.5A which provides power enough for most PC peripherals.

1.5 Summary of the Remaining Chapters

Chapter 2 reviews the state of the art in force measurements. A comparison is presented for the different approaches of each technology, with special focus on the noninvasive force measuring techniques. A thorough revision of the A201-100 force sensor is presented with representative examples of industrial and research applications.

In Chapter 3 the capabilities of the A201-100 sensor are exploited by performing a set of empirical tests on the sensor. An electrical model for the A201-100 sensor is obtained by combining test results with curve fitting techniques. A series of benefits are derived from the proposed sensor model: the force estimation error is dwindled when

combined capacitance-conductance estimation is done. Also, a method to predict sensor's sensitivity under a specific driving voltage is derived.

The ability to determine the applied-force area is a novel property found in the sensor; it implies that the A201-100 device is not only capable of measuring the applied force, but also capable of estimating the area where the force is being applied.

In Chapter 4 a review of the most relevant implementation of IADs is presented. IAD Operation Modes and IAD Control Algorithms are addressed. Passive and Active implementations of assistive robots are explored and compared from the safety and the flexibility standpoints. The notion of non-colocation of actuators and sensors in IADs is introduced together with the complication arising from such condition. Some solutions for the instability problems resulting from the non-colocation are discussed.

A thorough description of the developed dataglove interface is presented in Chapter 5. Static and dynamic tests are presented in order to demonstrate the feasibility of the interface to operate in a shared human-robot environment. A 6-DOF manipulator and a 6-DOF force/torque sensor are arranged for performing validation and throughput tests. The 6-DOF force/torque sensor is installed on the manipulator`s wrist.

Additional tests comprising the 6-DOF manipulator and the dataglove interface are introduced on Chapter 6. Handling operations with a dummy load are therein presented. Some conclusions and future work are presented in Chapter 7, with emphasis on the possible applications for the new techniques herein proposed.

Chapter 2

2. State of the art in force measurements

This Chapter examines the state of the art on force measurements in industrial and research applications. A review on the basic concepts and procedures is presented first, followed by plenty of examples which are examined with special focus on the piezoresistive effect and its applications. Metal and single-crystal silicon and polymer sensors are explored together with the advantages and drawbacks of each technology.

2.1 A review on the basic concepts of force measurement

In physics, force is defined as any influence that causes an object to undergo a certain change in one or more of the following properties: movement, direction (orientation) or geometrical dimension. The concept of force and its implications to a mass particle can be derived from the Newton's laws of motion, first published in 1687 under the title *Mathematical Principles of Natural Philosophy*. Since then, remarkable physics have used the original Newton's proposal as the start point for further generalizations and extensions of the basic Newton's ideas. This is the case of Euler, who extended the concepts of force and acceleration to objects with continuously distributed mass.

The generalization of the Newton's ideas was of great importance towards the formulation of the classical and continuum mechanic concepts. Based on the Euler's contribution, the concepts of linear and angular momentum could be extended to study the motion and deformation of objects with continuously distributed mass; this also allowed the introduction of two new notions: stress and strain.

2.1.1 Definition of stress and strain

Stress is defined as the measure of the internal forces acting within a deformable body, whereas strain is defined as the amount of deformation of a body due to an applied force.

A simple yet illustrative formulation for a one-dimensional (1 D) strain is expressed as the ratio between the length variation **ΔL**, and the original length of the object **L**, see Figure 2.1. The final length is expressed as ℓ in the equation below:

$$\boldsymbol{e} = \frac{\ell - \boldsymbol{L}}{\boldsymbol{L}} = \frac{\Delta \boldsymbol{L}}{\boldsymbol{L}} \qquad \textbf{(2.1)}$$

Note that tensile strain **e** is a scalar, unit-less quantity that expresses the ratio of compression of an object along one of its axes.

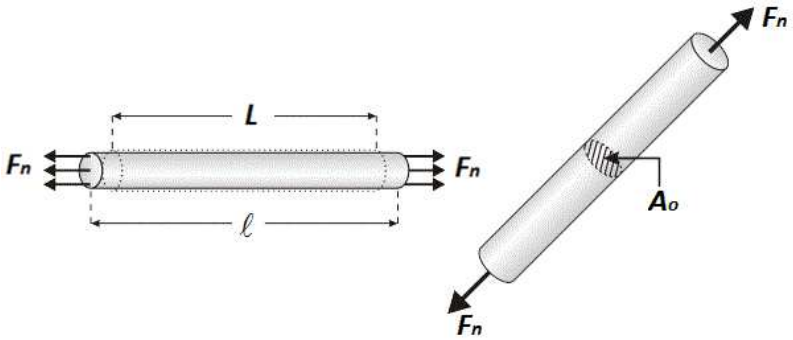

Figure 2.1: Representation of a strained bar (left) due to an evenly distributed stress (right).

A simple formulation for mechanical stress is expressed as the ratio between the total normal forces $\mathbf{F_n}$ applied over a region with cross-sectional area $\mathbf{A_o}$ see Figure 2.1:

$$\sigma = \frac{F_n}{A_o} \qquad \textbf{(2.2)}$$

Conversely to strain, stress $\boldsymbol{\sigma}$ has units of Pascal (symbol Pa), **1 Pa = 1 N/m²** in the *Système international d'unités* (SI). The ratio between the tensile stress and the tensile strain is an intrinsic property of a material; such a ratio is known in literature as the Young's modulus **E**, and can be computed for small displacements using the formula:

$$E = \frac{\sigma}{e} = \frac{F_n / A_o}{\Delta L / L} \qquad \textbf{(2.3)}$$

Recalling the concept of force given at the beginning of this section, force estimation is possible for an object if one or more of the following properties are tracked: motion, orientation and/or geometrical dimension. For the simple case of a 1D force causing a linear displacement in a given object, the usage of at least one encoder or resolver is sufficient to estimate the applied force via the Newton's laws of motion.

Another approach towards the measurement of force is focused on tracking the changes in the geometrical dimensions of the object, see Figure 2.1; this is possible by combining the concepts of continuum mechanics, summarized in the equations **(2.1)**, **(2.2)** and **(2.3)**, with an adequate set of sensors and conditioning electronics. This can be demonstrated as follows:

Given an object that is fully characterized in terms of its length **L**, cross sectional area $\mathbf{A_o}$, Young's modulus **E**, and assuming that is possible to gauge the length variation $\boldsymbol{\Delta L}$ of the object, then an estimation of the applied force can be obtained by solving the equation **(2.3)** for the unknown $\mathbf{F_n}$:

$$F_n = \frac{E\,\Delta L\,A_o}{L} \qquad \textbf{(2.4)}$$

The indirect procedure of equation **(2.4)** is not far from the methods used in commercial force sensors. The underlying basis of force measurements is simply and states that if the displacement produced by an external force can be gauged, then such a force can be estimated.

2.1.2 Gauging external forces in a Cantilever Beam

A well-studied case of force gauging with practical implications can be found in the cantilever beam and its variations. Some Applications of cantilevers can be found in fixed-wing aircrafts, balconies, and cantilever bridges. The simplest form of cantilever is the cantilever beam of Figure 2.2 that is basically a beam anchored at only one end. When loaded, the beam bends and thus it is possible to estimate such a force if the following two conditions are met:

- The length **L**, cross sectional area $\mathbf{A_o}$ and Young's modulus **E** of the cantilever are known.
- It is possible to measure the deflection **δ** of the cantilever from the unloaded position.

The following expression relates the displacement **δ** to the unknown force $\mathbf{F_n}$:

$$\delta = \frac{1}{3}\frac{F_n L^3}{EI} \tag{2.5}$$

Where **I** is the second moment of area, moment of inertia, of a prismatic beam with a rectangular section with depth **h** and width **w**:

$$I = \frac{wh^3}{12} \tag{2.6}$$

A derivation of equations **(2.5)** and **(2.6)** is out of the scope of this thesis, but is available at [11].

Nonetheless, above examples of Figure 2.1 and Figure 2.2 are not complete because an important aspect is left unanswered. In order to provide a thorough explanation regarding force gauging, it is first necessary to answer the following concerns:

- *How can be gauged the length variation* **ΔL** *of the object under study when a force is applied over its surface?* This question is applicable to the representation of Figure 2.1 and equation **(2.4)**.
- *How can be measured the displacement* **δ** *in a cantilever beam when loaded?* This equation is derived from the cantilever beam of Figure 2.2 and equations **(2.5)** and **(2.6)**.

To answer above concerns, it must be introduced the concept of *piezoresistivity*.

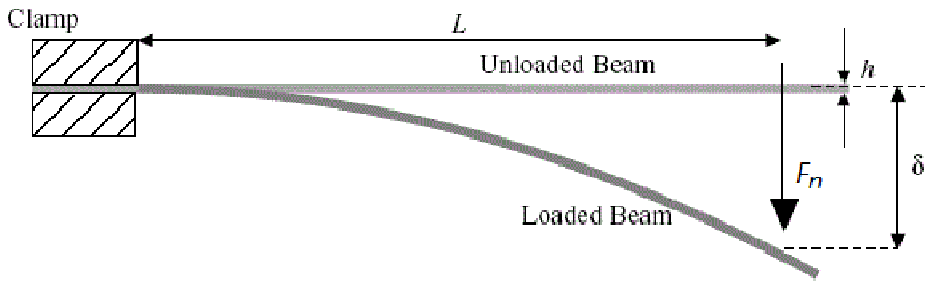

Figure 2.2: Sketch of cantilever beam subject to a force $\mathbf{F_n}$ with subsequent displacement **δ** at the tip

2.1.3 Definition of Piezoresistivity. Applying the Piezoresistive effect to force gauging

Piezoresistivity has been a widely used principle in force measurement systems throughout many years; it was discovered by Lord Kelvin in 1856 and is *defined as the change in resistance due to an applied force*. There are two possible sources for a change in the resistance value:

- A dimensional change in the material. Strain is produced in the material when subject to an external force; see examples on Figure 2.1 and Figure 2.2.
- Variations on the mobility charge carriers. A rearrangement occurs in the Electrons and Electron Holes when the material is subject to stress.

Both sources may occur simultaneously in a given piezoresistive material. However, the former case is the major source of change in metal resistors; while the latter source is mostly observed on single-crystal silicon and polymer materials.

Applying the concept of piezoresistivity to the examples of Figure 2.1 and Figure 2.2 is a valid approach towards force gauging. Assuming that metal resistors could be bonded to both, the strained bar and the cantilever beam, it would be possible to measure the length variation $\Delta\mathbf{L}$ and the displacement $\boldsymbol{\delta}$ respectively.

The concept of piezoresistivity answers the two concerns above presented, but in order to go further with the piezoresistivity theory, the practical implications of displacement gauging are not discussed in this section; they are fully addressed in Section 2.6. Likewise, a formal definition of *strain gauges* is presented on Section 2.3 and the *underlying basis of single-crystal silicon and polymer materials* is discussed on Section 2.7. Next Section presents a set of features and metrics to assess the performance of piezoresistors.

2.2 Features and metrics to assess the performance of sensing solutions

The three piezoresistive technologies, metal, single-crystal silicon and polymer have inherent advantages and drawbacks and are preferably chosen depending on the application needs, e.g. if the geometrical variations of the structure are considerable, a metal resistor is selected due to the high-strain tolerance of metals. Some other applications require the measurement of compression forces with negligible deformation over the structure, and consequently a silicon or polymer resistor is chosen.

Another factor that is usually taken into account is the gauge factor of the resistor. Given the resistance **R** and length **L** of the device under no stress applied; the gauge factor G can be obtained as follows:

$$G = \frac{\Delta R / R}{\Delta L / L} \qquad \textbf{(2.7)}$$

The greater the variations in resistance with little variations in the length, the higher gauge factors are obtained. Note from equation **(2.7)** that the Gauge factor can be also taken as the resistor sensitivity or gain, since it relates the output variable to variations in the measured variable. Typically, metal resistors exhibit gauge factors of up to 0.1, whereas for silicon and polymer resistors the gauge factor can easily go over 100. Note that the concept of gauge factor is of great importance when attempting to measure little displacements.

The temperature coefficient of the gauge factor is also an important factor to consider. Metal resistors are less affected by temperature compared to silicon and polymer resistors. However, it is possible to design a resistor framework to compensate for changes in ambient temperature and even for the self-heating in the resistor; such a framework will be discussed in Section 2.3.

The *rule of the thumb* when designing a force measuring system states that, in order to improve the accuracy and precision, an increasing number of resistors must be used; this often yields the usage of several resistors to measure a 1D force. So, it is common to find in literature designations such as *array of resistor* or *resistor arrangement*. Also, since each resistor is basically a transducer of strain, the piezoresistors are usually cited as *strain gauges*, *strain sensors* or as *force sensors* depending on the context.

Last but not least, the properties of linearity, hysteresis, repeatability and accuracy must be considered before choosing the most adequate framework of piezoresistors. An ideal piezoresistor or piezoresistor array should satisfy the two following properties in order to be considered as an ideal device:

- Additivity, also called superposition property, defined from:

$$f(x+y) = f(x) + f(y) \tag{2.8}$$

- Homogeneity of degree one, this is:

$$f(\alpha x) = \alpha f(x), \forall \alpha \tag{2.9}$$

In practice, none of the above properties are fully achieved and thus it is common to compare the piezoresistor performance based on some metrics, typically identified as sensor's specification, such as: nonlinearity error, hysteresis, non-repeatability error and rated accuracy, also known as measurement error.

Providing an adequate, consistent, and useful definition of each error is probably one of the hardest tasks in sensor literature. The reason for such inconsistency in error definition is based on the manufacturer interest of showing his products as the best-market solution, so often, error is estimated on different ways by each manufacturer; this implies the usage of different formulas, but also different methods and set-ups. This inconsistency is even accepted by some manufacturers; e.g. Beyer, an employee of WIKA (a company leader in the manufacturing of force measuring systems), declared that [10]:

> *The term "Accuracy" exists only in the user's language. It is not defined in any standard. Nevertheless, it can be found in many data sheets for sensors. Unfortunately, there is no common idea of what accuracy means.*

Beyer goes further into the multiple definitions available in sensor literature by declaring that:

> *There is not "one accuracy" but a large number of different specifications with regard to accuracy.*

A complete overview of the most accepted metrics to assess the performance of sensors is presented on the Appendix A. However, the concept of measurement error is next presented since it will be extensively used in Chapter 3.

2.2.1 Measurement error

The measurement error **ME** is the largest deviation between actual characteristic curve and ideal straight line [10], where the actual characteristic curve is the sensor output due to a random variation of the input signal within the nominal sensor range. Note that the imposition of identical condition is not present in the definition of measurement error, so the input signal can increase or decrease during the sensor's characterization; this is fairly more realistic since the conditions of a real application are emulated, and thus, a more representative estimation of the error is provided. The **ME** can be understood as a combination of hysteresis and non-repeatability error; this is so because the input signal does not follow a monotonic or predefined pattern during characterization and because different trials are collected to average the error.

Unfortunately, sensor manufacturers seldom specify the measurement error, mainly because it is bigger than the non-repeatability error and manufacturers do not want to show their products as inaccurate devices; this is an expected result considering that error sources from hysteresis and non-repeatability error are combined into the measurement error. There are two approaches towards the estimation of the measurement error.

1. Maximum deviation: It is the simplest approach of the Measurement Error; it is defined as *the largest deviation in the sensor output obtained under random variations in the measured variable.* The Maximum Deviation of the Measurement Error **MD-ME** is defined under the basis of equation (A.9), with the difference that the input signal varies in a random-basis during sensor characterization. So, the trendline **h(x)** is obtained from a regression analysis of the data acquired during the characterization, and the maximum deviation between the sensor output **f(x)** and the trendline **h(x)** is used to compute the **MD-ME**:

$$MD-ME=\frac{f(x_c)-h(x_c)}{h(x_M)}\cdot 100\% \qquad \textbf{(2.10)}$$

Where $\mathbf{x_c}$ is the point of maximum deviation between **f(x)** and **h(x)** occurring at $\mathbf{x_c}$,. The term $\mathbf{h(x_M)}$ is the nominal sensor's range. However, just as all the above definitions of maximum-deviation metrics, they fall to provide an exhaustive evaluation of the error over the entire region of operation. So, it is presented next a metric to embrace the hysteresis and non-repeatability error for all the datapoints involved.

2. Integral Formulation: Based on the concept of the Integral non-linearity error **I-NLE$_d$**, it is possible to calculate the measurement error by averaging the square of the errors of each individual measurement; this is, calculating the *Mean Squared Error* of the entire sample. A detailed formulation of the **I-NLE$_d$** is available on the Appendix A; likewise, equations **(A.6)** and **(A.7)** define the basis for its calculation.

$$MSE = \frac{1}{n}\sum_{i=1}^{n}[y_i - h(x_i)]^2 \qquad \textbf{(2.11)}$$

Where **h(x_i)** is the best fit trendline calculated on the basis of equation **(A.6)**. The function **h(x_i)** can be also understood as the predictor and **y_i** as the true value, where **y_i = f(x_i)** using the notation of equation **(A.7)**. The lower the MSE for a given sensor, the better the performance is over its entire region of operation.

2.2.2 Usage of the Mean Squared Error MSE to assess sensors' performance

The usage of the mean squared method provides a systematic and statistical technique towards the evaluation of sensor performance; this is in fact the method used to assess the accuracy of the piezoresistive sensors in the present thesis.

Recalling the concept of measurement error, the amount stem from equation **(2.11)** can be either taken as:

- A quantitative evaluation of the combined, hysteresis and non-repeatability error. This is probably the most straightforward application of the **MSE** concept, but not limited to it.
- If two or more predictors are compared for the same sensor, that predictor with the lowest **MSE** suits better for the sensor. In other words, the **MSE** can be used to gauge the accuracy of a predictor.

Once the metrics for assessing sensor performance have been examined, it is next discussed the two different technologies of force gauging that make use of the piezoresistive effect; these technologies are the metal resistors, single-crystal silicon and polymer materials. Metal resistors are addressed as strain gauges, whereas single-crystal silicon and polymer materials are simply known as piezoresistive sensors or as *Force Sensing Resistors, FSR*. A literature review is presented for each technology with plenty of examples.

2.3 Strain gauges in force measurements. A simple yet powerful device

The process of measuring and estimating force has always been a task of great importance in many research fields. Structural design of buildings, stress analysis of materials, blood pressure measurement and exoskeleton design are only some examples of applications that strongly depend on force readings. This dependency is not only present during the prototype design, but also exists during the full lifetime of the device.

When a bridge is to be designed, special attention is placed on identifying the loads which act upon the bridge's structure. There are multiple sources of loads such as the self-structure weight, moving loads (wheels), wind load, load from temperature changes, within many others. However, when the bridge is built and fully operational, forces and stresses keep registering in order to monitor structure's health over the time. Installing strain gauges along the bridge's structure is the preferred solution for this type of applications, since they are reliable and maintenance-free.

Strain gauges were chosen by the New Orleans Public Belt Railroad as the solution for measuring the stress over the Huey Long Bridge. The gauges were installed during the bridge widening project in 2009, see Figure 2.3.

Strain gauge technology has been one of the most widely used solutions for measuring forces over the time. Early applications of strain gages can be found back in the 50's, in the aircraft and health industry [167, 169]. As mentioned before, they are reliable and maintenance-free. But additional features may be added to the strain gauges by adding some extra circuitry to the sensor driver. Temperature compensation and full linearity are available if two gauges are installed on the strained surface; it is also common to find current sources, instead of voltage sources, as the power supply for driving the sensor [160, 113].

The Wheatstone bridge is the preferred circuit to drive the gauges; it consists of four resistors arranged in a bridge-like configuration, see Figure 2.4. The underlying principle of the Wheatstone bridge is the ability to balance the two legs of the circuit; this yield an offset-less output voltage (no strain implies **0 V**) which is ideal because positive strain produces a proportional positive voltage (depending on the gauge arrangement) and negative strain likewise. Hannah presents in [65] a thorough analysis of the strain gauges with the manifold variations of the Wheatstone bridge.

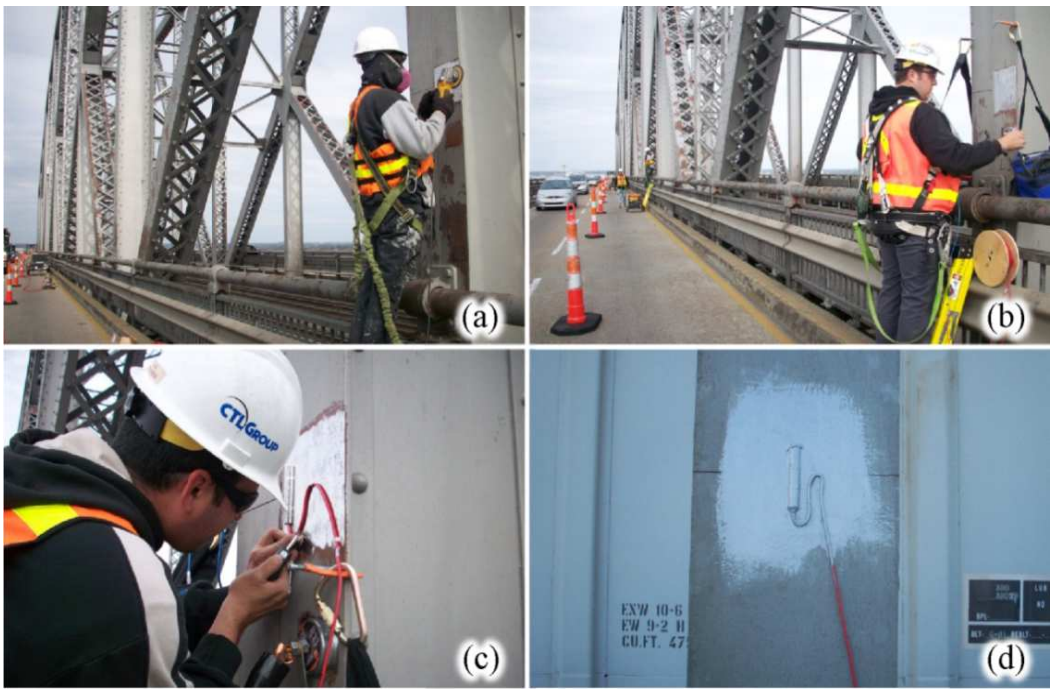

Figure 2.3: Installation of strain gauges on the Huey P Widening Project; LA, USA. (a) The worker prepares the bridge's surface. (b) The worker installs the strain gauges. (c) Close view of worker installing the strain gauge. (d) Installed strain gauge

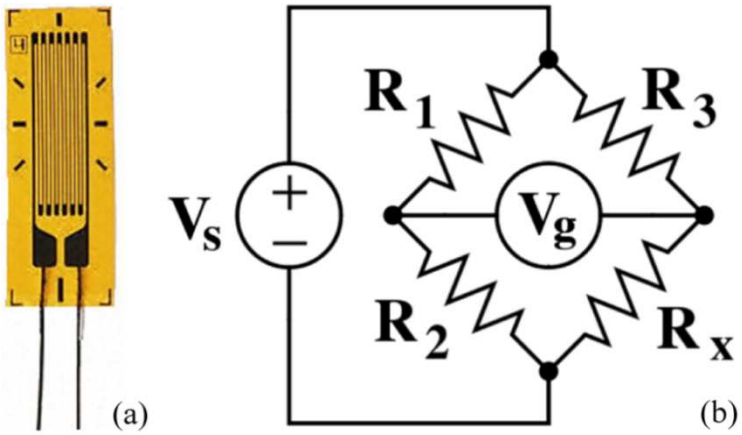

Figure 2.4: Overview of a strain gauge system and conditioning electronics. a) Photo of a metal strain gauge. (b) Circuit Diagram of the basic Wheatstone bridge. The strain gauge is the $\mathbf{R_x}$ Resistor, and $\mathbf{V_g}$ is the output voltage proportional to the mechanical strain

The key for strain gauge success lies on the simple gauge design and on the ease to measure conductance variations; these two facts yield low cost devices available in several off-the-shelf models to meet the specific requirements of each application. *Strain gauges take advantage of electrical conductance and its natural dependency on the conductor's geometry,* this phenomenon was earlier mentioned in Section 2.1.3, when the piezoresistivity effect was introduced.

Strain gauge conductance $\mathbf{1/R_x}$ can be related to its mechanical dimension as next:

$$\frac{1}{R_x} = \sigma \frac{A}{\ell} \qquad \textbf{(2.12)}$$

Where **σ** is the characteristic conductivity of the strain gauge material, **A** is the cross-sectional area of the conductor and ℓ is the length of the conductor. Note from equation **(2.12)** that strain gauge compression reduces ℓ while **A** is increased and consequently $\mathbf{1/R_x}$ becomes larger. Conversely, stretching the gauge increases ℓ while A is reduced and thus $\mathbf{1/R_x}$ is decreased. This scenario is depicted in Figure 2.5 for a membrane under uniform pressure and fixed boundaries.

It is also common to find equation **(2.12)** in its reciprocal form:

$$R_x = \rho \frac{\ell}{A} \qquad \textbf{(2.13)}$$

where $\mathbf{R_x}$ and **ρ** are the resistance and the characteristic resistivity of the device respectively. Equation **(2.13)** is more commonly used among semiconductors materials, whereas equation **(2.12)** is more likely on metal strain gauges.

Some other examples of material stretching/compression are available on Figure 2.1 and Figure 2.2. If a strain gauge is bonded to the cantilever beam of Figure 2.2, the deflection of the beam could be measured by reading the conductance variation of the metal resistor.

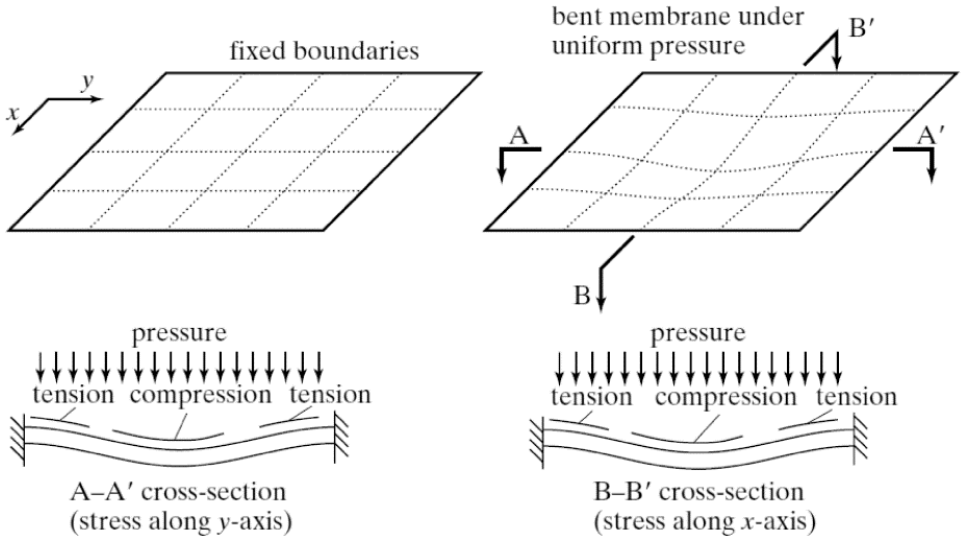

Figure 2.5: Image taken from [107] showing the dimension changes of a resistor under longitudinal stress

Nonetheless, equation **(2.12)** must be treated carefully if force is to be extracted from conductance measurements. Note that $\mathbf{1/R_x}$ is a measure of the strain gauge deformation, not of the applied force. If $\mathbf{1/R_x}$ is to be converted to a valid force, the full structure dynamics (the structure where the gauge is bounded to) must be considered as well as the strain gauge set-up, i.e. the number of gauges: one, two or four, and the strain gauge configuration: one-dimensional, Rossette-45° or Rossette-60° for shear strain measurements. A deduction of how conductance measurements can be converted to force is strongly dependent on the structure layout for each application and consequently is not addressed in this document. Some of the most common configuration and set-up for strain gauges are addressed by Hannah [65].

2.4 Strain gauge usage in robotic applications

Strain gauges and robotic developments have been paired since the early stages of robotic research. Some early relevant implementations of strain gauges in robots can be found back in the 70's and 80's by Craig [35] and Salisbury [146].

The combination of a Scheinman Stanford arm with strain gauges was probably one of the first relevant implementations of combined force/position control [35]. The arm was equipped with a force sensing wrist with 8 strain gauges. The gauges were arranged in a Maltese-cross configuration that produced 6 measurements of force and torque [151], see Figure 2.6. A position/force control scheme for a 6-DOF manipulator was successfully developed by Craig through the combination of force/torque sensors with joint encoders.

Following Craig ideas, an active stiffness control of a manipulator was introduced by Salisbury [146]. A Scheinman Stanford arm was programmed to assemble two parts of a garden sprinkler system; a compliant behavior of the manipulator was demanded by this application for proper assembly and thus, a combined position/force feedback was required. A feedback system similar to that employed by Craig was used in Salisbury application.

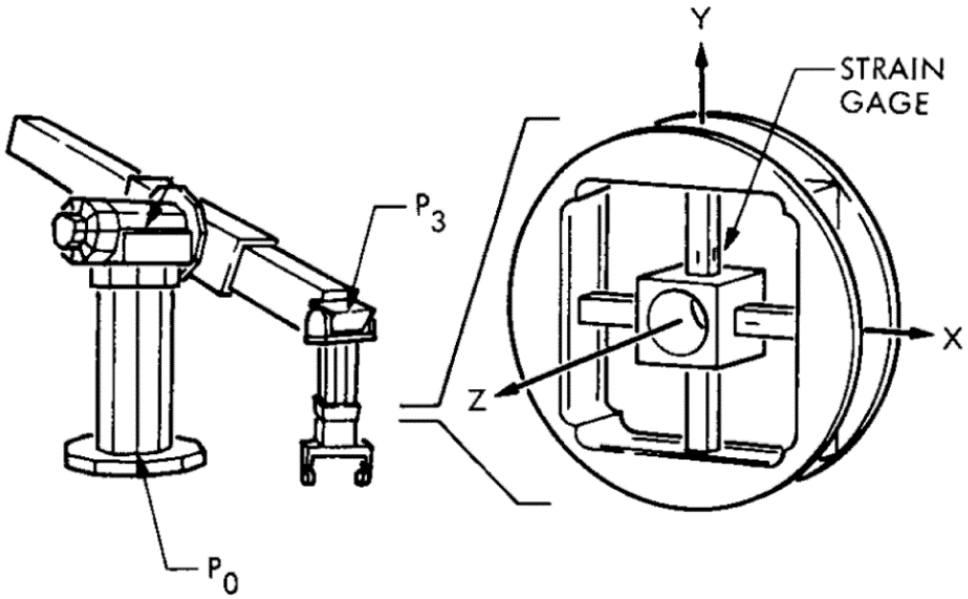

Figure 2.6: Image taken from [35] showing a modified Scheinman Stanford arm $\mathbf{P_0}$ equipped with a force sensing wrist $\mathbf{P_3}$. Close view on the right side depicts strain gauge location according to the Maltese-cross set-up

More recent usage of strain gauges can be found in flexible manipulators; this type of robots takes advantage on the structure's light weight to employ low power motors compared to those used in rigid manipulators that demand higher torques, and thus resulting in bulkier and heavier motors. However, this is a tradeoff advantage that demands a more challenging control algorithm capable of dealing with the oscillations on the light-weight structure.

An experimental study of a control policy for end-effector trajectory tracking of structurally flexible space-based manipulators was presented by Carusone [18]. The proposed control policy was tested on a *Radius two-link planar manipulator* with flexible links. The manipulator was modeled as an open chain of elastic bodies with a base body that may be free, partially or totally constrained; this modeling is an added challenge to the control of flexible manipulators, because the controller has to continuously measure and account for the link deformation on every cycle loop. The link deformation on Carusone application was monitored by four precision strain gauges in a full Wheatstone configuration. Similar approaches on flexible manipulators were adopted by Bolandi [12] and Payo [137].

Strain gauges also play an important role in the control of legged walking robots. Schneider addressed in [149] the improvements emerged from the implementation of force control in the overall control strategy of legged robots. Some approaches of force control addressed by Schneider comprise: local regulation and gait cycle correction of legs [156], large obstacles overcoming [86], motion control of legs in interaction with a support surface [99, 81] and locomotion problems when climbing [14]. These approaches rely on force measurements to enhance the mechanical properties of such robots. Typically, the force measurements are performed by strain gauges mounted along the robot legs or by custom strain gauge–based sensors, such as those employed on the *ALDURO* walking machine [121] or the *Katharina* walking robot [148].

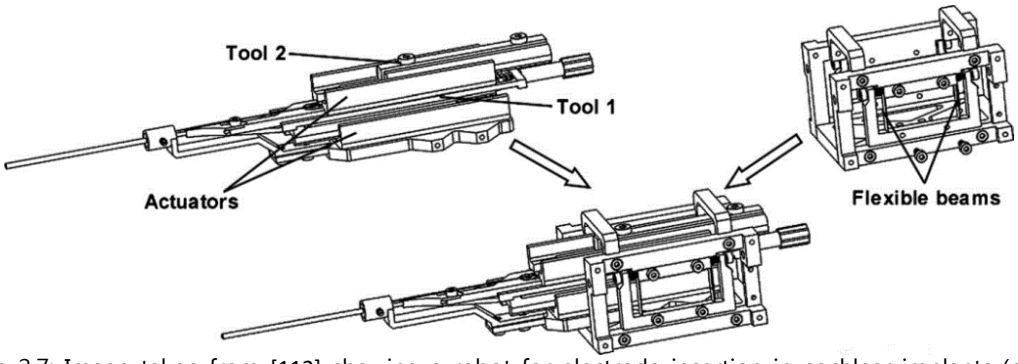

Figure 2.7: Image taken from [112] showing a robot for electrode insertion in cochlear implants (center low). The insertion robot is composed of a insertion mechanism described by Hussong [74, 75] (top left) and a unit equipped with strain gauges for measuring the insertion forces (top right)

Despite strain gauges may seem primitive devices, they are used in life support applications such as current biomedical developments. As earlier mentioned, the key for strain gauge success, among other force measuring techniques, lies in the simple gauge design that yield low cost devices available in several off-the-shelf models to the meet specific requirements of each instance.

This adaptability allows the usage of strain gauges in custom designs, such as the monitor of electrode insertion forces in cochlear implants with the help of an assistive robot [112]. Electrode insertion must be performed carefully and consistently on every trial. The outstanding ability of humans allows electrode insertion with relative ease and quickness compared to an awkward robot with a custom design tool for the same task. However the repeatability of the latter method is fairly better, because the insertion forces can be accurately tracked by force sensors installed on the robot tool. So the proposed challenge is to improve the maneuverability of the insertion robot while preserving repeatability.

Schurzig presented in [112] a robot for the aforementioned task, see Figure 2.7. The tool is based on the Hussong original design [74, 75]. It comprises two sets of actuator and tool assemblies, the first set is intended to grasp the electrode array via a modified surgical alligator forceps, whereas the second set is used to grip the stylet by a stainless steel hooked wire, see Figure 2.7 top left. The first set also includes a force-sensing carriage equipped with four flexible aluminum beams to transform the force along the axis of insertion into a deformation, which can be measured by the four semiconductor strain gauges, see Figure 2.7 top right.

Schurzig realization is a good example of how strain gauges can be taken up to limit by taking advantage of the flexibility and adaptability they provide. Schurzig modified the Hussong robot [74, 75], unable to measure forces, by adding the force-sensing carriage shown in Figure 2.7 top right. This adaptation yielded an improvement in the electrode implant process by adding support for the monitoring of forces during the electrode insertion, all these add-ons required minimal changes to the overall structure of the robot.

The Maltese-cross configuration employed by Craig is a typical set-up for strain gauge location; it is addressed by Sciavicco [150] and Siciliano [152] as the basic set-up for measuring forces on a manipulator's wrist. This simple, yet powerful, combination of

Maltese-cross set-up and strain gauges yields the introduction of a new concept; the concept of *load cell*.

Load cells are transducers that covert force to a measureable electrical signal or straight into a digital format, such as the RS-232 or USB communication protocols. Many of the commercially-available load cells employ the Maltese-cross configuration as the underlying principle to measure forces and torques; Voyles introduced some examples of commercially available sensors with the classic Maltese-cross set-up [166], such as the JR3 [82] products, whereas some other brands, like the ATI [77], reported the usage of a modified Maltese-cross with only 6 strain gauges. Unlike strain gauges, load cell's output can be directly fed back into a force control algorithm; this condition is ideal for robotic applications demanding off-the-shelf force sensors that can be easily attached to the robot wrist or to any robot limb.

2.5 The introduction of load cells into current interdisciplinary applications. Importance of load cells to robotic developments

Load cells are usually referred in robotic literature as force sensors or as force/torque sensors. It is also common to replace the term *sensor* by *transducer*; this is a logical designation because load cells convert strain to an electrical signal.

It is hard to imagine nowadays robotics without load cells. Apart from joint encoders for position sensing, load cells are probably the second most-used sensor in robotics. Teleoperation [3, 163] cybernetic hand control [16, 72], human-robot cooperation in shared environments [59, 60, 101], Minimally Invasive Surgery (MIS) [6, 159], and control of legged robots [56, 73] are only some examples of robotic applications that rely on load cells for providing force feedback to the control loop. Above examples comprise recurrent contact tasks between the robot and the environment, and thereby contact forces must be continuously monitored to ensure security within the workplace.

Bilateral control in teleoperation requires force estimation to provide force feedback to each control loop, the master control loop where the operator interacts with the master controller, and the slave control loop where the remote robot interacts with the environment. Some implementations of master-slave control, such as those of Ueda [163] and Akizono [2], solely rely on load cells to estimate human and environmental forces in the master-slave scenarios. However, a different solution has been adopted in more recent implementations of bilateral control, in an attempt to overcome the restrictions that arise from potentially-unstable contact tasks between the slave manipulator and the stiff environment [27, 28, 30, 89]. The solution comprises the substitution of the robots' load cell for force observers [53, 88].

A comparative analysis of the different approaches of bilateral control was presented by Aliaga [3]. He addressed the importance of force/torque transducers for the force-position (FP) and four-channel (4C) controllers. Despite the successful implementations of Katsura [88] and Forouzantabar [53] under the force-sensorless basis, a full modeling of the robot dynamics is required in order to replace the *physical* force sensors by force observers. However with such a replacement, the complexity of the resulting system could be considerably increased. This is so because, depending on the robot size and stiffness, the deduction of a dynamic model may result a challenging task. The addition

of elasticity terms is *mandatory* for large-workspace robots in order to increase the level of realism and validity of the robot model.

2.5.1 Teleoperation and Cybernetic Designs

Force/torque transducers are also employed in cybernetic hand control for monitoring forces during grasp-and-lift tasks. The CyberHand is a 16-DOF cybernetic anthropomorphic hand capable of power and low-load precision grasps developed by Carrozza [16]. The CyberHand is bioinspired and thus a set of sensors were included in an attempt to emulate the proprioceptive and somatosensory perception of humans. Also, custom-made triaxial force sensors were integrated to each fingertip of the CyberHand as a part of the device's exteroceptors. The triaxial sensors were designed to achieve mechatronic integration at the hand fingertip. A total of six strain gauges per sensor were mounted on an aluminum alloy 3-D flexible structure, see Figure 2.8b; this arrangement is similar to the aforementioned solution employed by Craig [35] reflecting that the underlying basis of force measurements has not changed much since the 70's. Additional exteroceptors sensors are listed below and shown in Figure 2.8:

- A flexible layer with contact sensors to cover the hand, see Figure 2.8a.
- Triaxial force sensors embedded in the fingertips, see Figure 2.8b.
- A compliant skin with embedded 3-D force microsensors to measure force distribution at the fingertips, see Figure 2.8c.

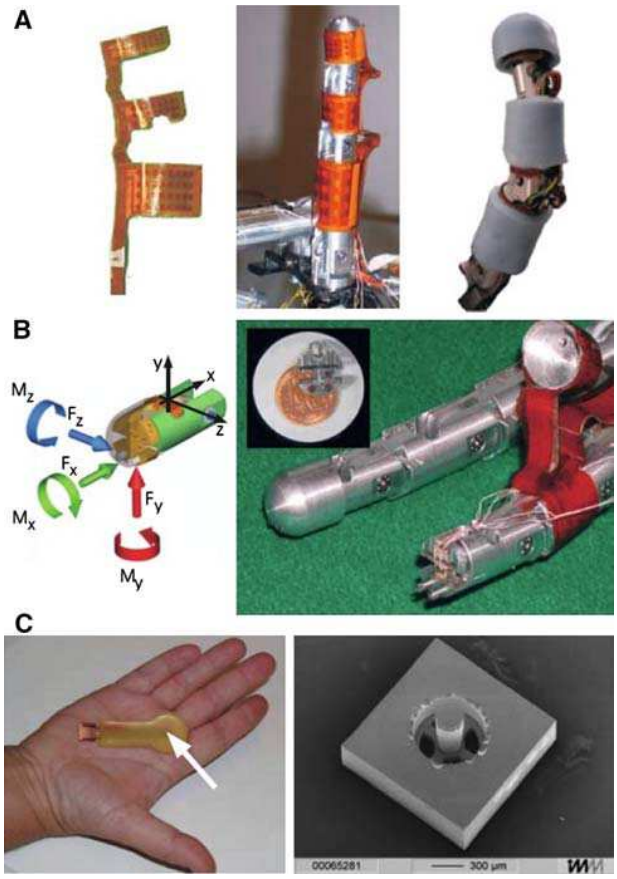

Figure 2.8: Image taken from [16] showing CyberHand exteroceptors. (a) Flexible contact sensors. (b) Triaxial force sensors embedded in each fingertip. (c) The soft and compliant triaxial microsensor (SCTM) sensor. Image reprinted from [9].

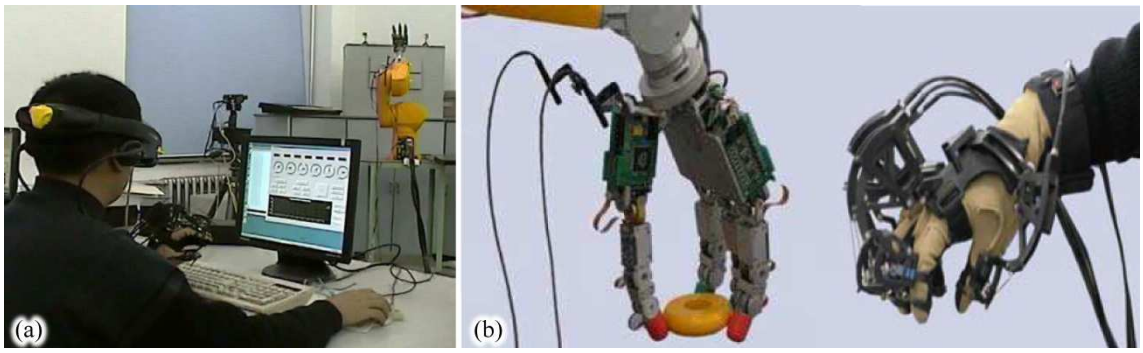

Figure 2.9: Pictures of the telepresence platform developed by Hu, images taken from [72]. (a) Picture of the Stäubli RX60 robot with the HIT/DLR hand on top (slave robot), and the CyberGrasp device worn by the operator (master robot). (b) Picture comparing the sizes of the HIT/DLR hand and the CyberGrasp device

Another realization of bilateral control that reflects the importance of load cells was presented by Hu [72]. His prototype comprised a teleoperated robotic arm/hand with telepresence and shared control. The definition of telepresence involves haptic feedback, vision feedback and audio feedback; consequently the system embraced cameras and a proper sensor system for the remote arm/hand robot. A HIT/DLR [13, 71] hand was mounted on the wrist of a *Stäubli RX60* robot arm as a part of the setup for the remote robot control. A *CyberGrasp* exoskeleton [39] was added together with a *Cyberglove* [38] on the master side to gather the operator's commands and to generate force feedback; see Figure 2.9 for a system overview.

The HIT/DLR hand is equipped with an adequate load-cell-based sensor system. A two dimensional torque sensor is installed on the based joint of each finger, whereas the middle joint and the fingertip are equipped with a one dimensional and six dimensional force/torque sensors respectively. The control of the teleoperated system is commuted between a PID position controller, for non-contact tasks, and a joint torque/position approach for contact tasks.

The responsible of commuting between each control law is given to a high level decision algorithm known as the *Parallel Observer*. The exerted torques by each motor are continuously monitored and fed back to the *Observer*. If the exerted torque goes beyond a predefined threshold, the joint torque/position controller is activated with the aim of controlling the mechanical impedance; this control scheme attempts to embody the human skills during a pick-and-place task. The system is capable of performing skills that demand a high level of dexterity such as building a tower with circle blocks and opening a drawer, see Figure 2.10.

2.5.2 Robots working in direct cooperation with humans

Load cells are also used in applications that involve human-robot cooperation in shared environments. In these applications, it is necessary to continuously monitor the contact forces that occur during the comanipulation tasks between the operator and the robot's structure. Apart from the skin-like sensors installed on the robot's limbs [100, 106], load cells are the preferred solution for monitoring the contact forces on the robot endpoint. Abovementioned examples of Garcia [59, 60] and Lamy [101] are only few examples of human-robot cooperation that rely on load cells for providing force feedback.

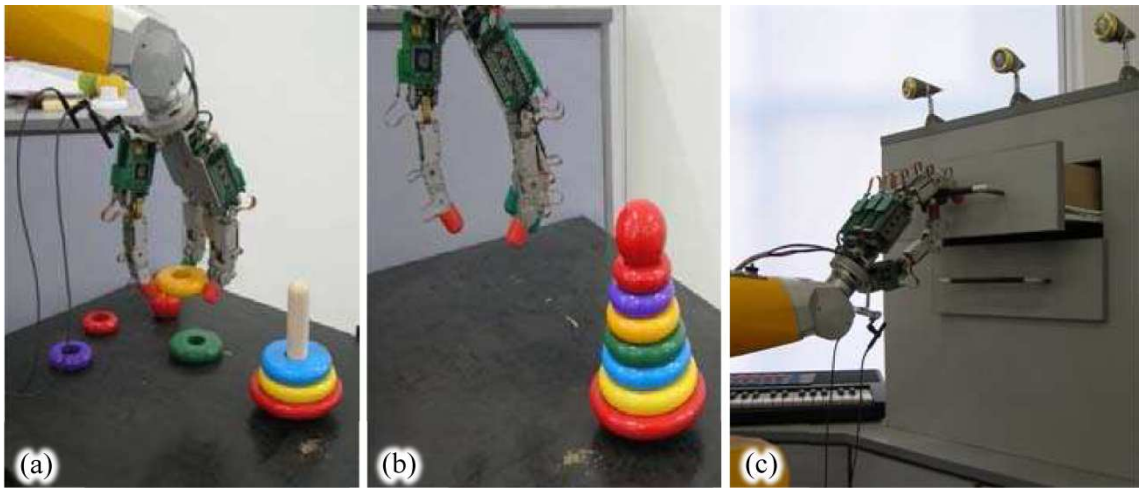

Figure 2.10: Images taken from [72] showing the skills of the HIT/DLR hand. (a) and (b) shows the HIT/DLR hand performing pick a place actions to build a pyramid with circle blocks. (c) A drawer is remotely opened

A sensor fusion implementation comprising a 6-DOF force/torque sensor and a 6-DOF inertial sensor was presented by Garcia in [59, 60]. A sketch of the system is depicted in Figure 2.11 remarking the location of the 6-DOF force/torque sensor and the 6-DOF inertial sensor. Garcia's realization was intended to cope with the difficulties arising from the control of robot motion under an unmodeled environment. Under such scenario, sudden collisions may occur between the robot endpoint and the environment, and thus high-frequency spectral content is added to the sensors' output (force, acceleration and position sensors), with the added difficulty that the measured signal is affected by the transmission dynamics and structural dynamics of each link; this condition is known as *non-colocation of actuators and sensors* [29, 30] and will be addressed in the Chapter 4 of this thesis. On the opposite side of the spectrum, low-frequency components appear on the sensors due to the inertia of a heavy tool or a heavy load. A proper control algorithm must discern between such inertial forces, the collision forces and the applied-human forces while maintaining safety and performance.

In order to overcome the aforementioned difficulties a sensor-fusion based, contact force-moment estimator was proposed by Garcia. The estimator combines position, force and acceleration data coming from rotational encoders, a 6-DOF force/torque sensor and a 6-DOF inertial sensor respectively. The underlying principle of the sensor fusion algorithm is the Kalman filter that allows the combination of data from multiple sources to accurately estimate a common, but noisy, parameter to all the data sources. For the study case of Garcia, the noisy parameter –that requires filtering from the Kalman filter– is the environmental force, whereas the sources of noise are multiple ranging from inertia, vibration and gravity, see Figure 2.11.

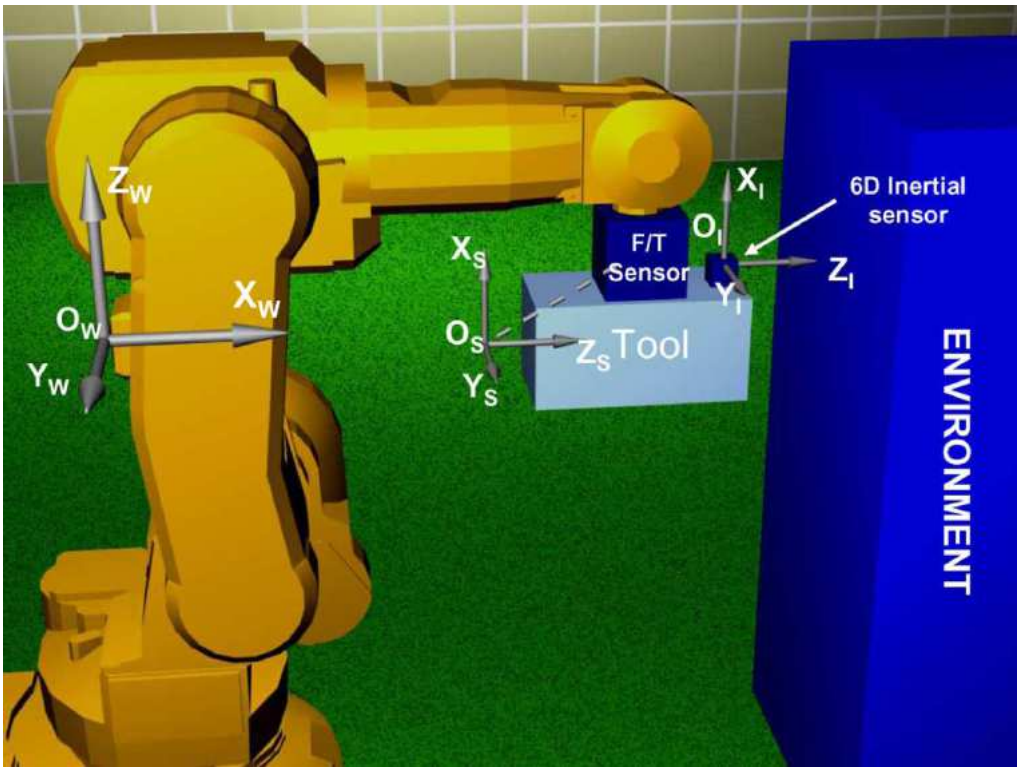

Figure 2.11: Image taken from [60] showing a sketch of a Staubli60 manipulator with a force/torque sensor and an inertial sensor. This set-up serves as a test bench for a sensor fusion algorithm working under an unmodeled environment

A similar approach to that of Garcia was presented by Lamy [101]. Lamy presented a study of the optimal sensor setup for a comanipulation task that involves human guidance in a force amplification scenario. Determining the optimal sensor set-up is a typical problem for the IADs; this complication arises from the non-colocation of actuators and sensors within the robot's structure [29, 30]. Instead of combining position, force and acceleration sensors just like Garcia did, Lamy proposed the usage of two load cells, one for measuring the human intention and another for measuring the contact force between the robot endpoint and the environment.

Three possible arrangements were analyzed by Lamy towards finding an optimal load-cell location, see Figure 2.12. Each set-up comes with advantages and drawbacks in terms of maximum allowed amplification, likelihood of instability (due to non-colocation) and range requirements of each sensor; the adopted solution was the (a), due to the following reasons:

- The first force/torque sensor could be independently chosen to deal with the required range of environmental forces whereas the second force/torque sensor, with a lower range, could accurately measure the forces stemming from the operator. This differentiation in sensor nominal range is not possible for option b) because both sensors directly interact with the load.
- If properly design, the distance between the handle and the tool can be minimized in option a), this is not possible in option c) because both sensors are radially opposed. Reducing such distance is mandatory for minimizing non-colocation effects.

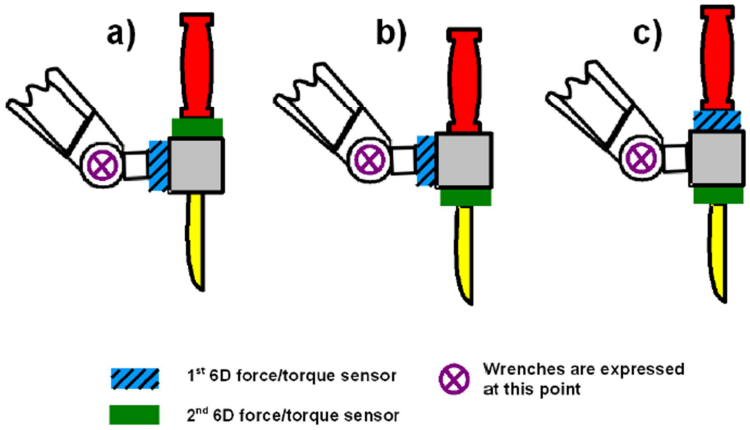

Figure 2.12: Image taken from [101] showing three possible arrangements for load-cell location

Lamy's approach of splitting force sensing in two counterparts is an effective way of minimizing the effects of non-colocation; the dictum *divide and conquer* is also valid in robotic research.

Some other representative applications of load cells in robotics are available from the cooperation between *Stanley Assembly* and *Northwestern University* during the late 90's. Colgate and Peshkin – from Northwestern University – developed together with Stanley Assembly an Intelligent Rail System [33, 155] that combines a single-axis load cell for measuring forces over the z-axis with a noncontact two-axis sensor, see Figure 2.13. The noncontact sensor is based on a cable angle sensor that detects user intention by measuring cable deviation from the vertical equilibrium position. The noncontact sensor provides information to control the IAD motion on the **(x-y)** plane. Both IADs are conveniently named as *iLift* for the z-axis IAD and *iTrolley* for the IAD moving on the **(x-y)** plane. A more detailed description of the *iLift* and the *iTrolley* systems is later addressed on Section 4.6.6.

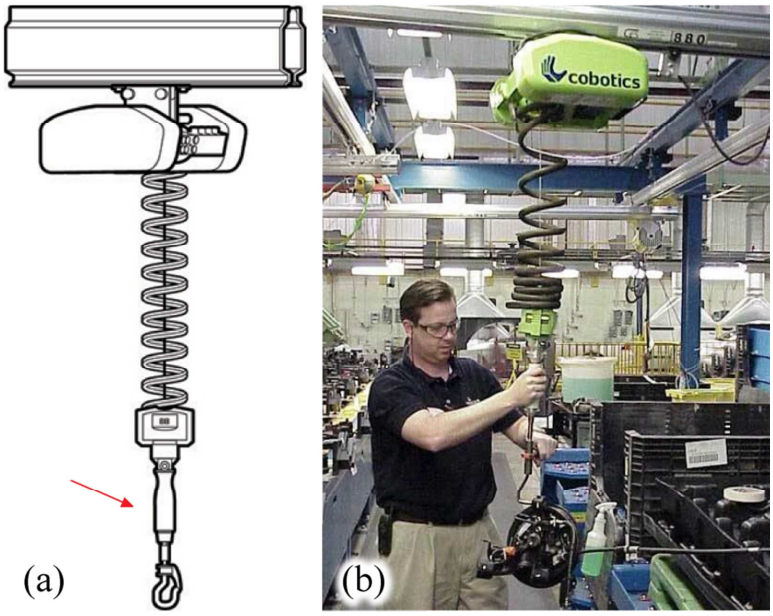

Figure 2.13: Image taken from [33] showing the iLift system. a) Sketch of the iLift with a red arrow pointing to the user handle equipped with the single-axis load cell for Z-axis force measurement. b) Operator lifting an object by pulling the handle

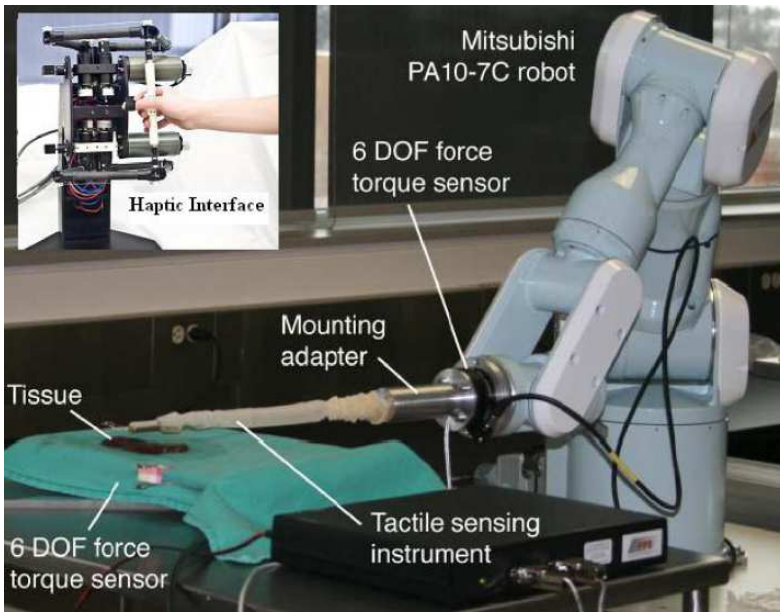

Figure 2.14: Image taken from [159] showing the Tactile Sensing Instrument (TSI) for tumor detection mounted on a Mitsubishi PA10 robot. The teleoperated system comprises a master 7-DOF Haptic Interface and the slave Mitsubishi manipulator

Note that analogously to Lamy's realization; Colgate halves the measurement of human intention. This solution is intended to move as close as possible the sensors to the contact point of the external force. Some other applications that report load cell usage in shared human-robot environments are addressed by Kruger in [98].

2.5.3 Robotic Surgery

Force/torque sensors have also been employed in Minimally Invasive Surgery (MIS) applications. Talasaz [159] developed a Tactile Sensing Instrument (TSI) for tissue exploration. The TSI allows tumor detection in soft tissue by measuring the distributed pressure profiles resulting from the interaction between the TSI and the tumor itself. The TSI is built from a combination of a surgical probe and a distributed pressure sensor. The detection is possible because the tumor exhibits a higher stiffness compared to a healthy tissue, and thus, it is possible to create a colored map of pressure distributions based on the TSI readings.

The TSI serves as endpoint for a slave Mitsubishi PA10 robot working under a master-slave set-up, see Figure 2.14. A bilateral control method with position control on the master is used, whereas an implementation of force control is used on the slave to control system motion during the tissue exploration. Note the resemblance between the control scheme of Talasaz [159] and the previous examples of Ueda [163] and Akizono [2]. The master controller is a 7-DOF haptic device enhanced at the CSTAR facilities.

Exerted forces to body parts must be accurately measured and kept within safety limits during the TSI insertion process; this task is better to be performed by a 6-DOF force/torque sensor rather than by the TSI itself. Within others, the following reason can be argued:

- The TSI pressure measurements are based on a *PPS TactArray* device [145] that surrounds the surgical probe. The *TactArray* is composed of hundreds of tiny pressure sensors evenly distributed along the surface emulating the mechanoreceptors of a human skin. These tiny sensors are only capable of measuring force in a single axis (compression) which straight limits the ability to estimate force and torques.
- Since the *TactArray* is mounted over the compliant surgical probe, it is impossible to accurately determine the direction of the pressure exerted by the tissue with respect to the manipulator frame. A bending or twisting on the TSI may occur at any time and go unnoticed by the TSI sensors. However, these forces and torques directly transmit from the TSI to the 6-DOF force/torque sensor installed on the manipulator wrist.

Special attention has been placed on Talasaz realization because he employed a basic set-up that could be found in almost any teleoperated testbench that is designed for robotic surgery. The basic set-up for a teleoperated system typically comprises a haptic wand for the master and a 6-DOF robot for the slave. However, robotic surgery applications require additional sensing elements, this is; a custom-made force sensor for the instrument tip and the *typical* 6-DOF load cell located between the robot tool and the manipulator. The custom-made force sensors may adopt multiple forms depending on the specific requirements of each application, just as the example of Houston [70] in which a strain gauge was embedded in the polymer housing of a microgripper for endoscopic surgery, see Figure 2.15.

2.5.4 Legged Robots

Gait control of legged robots is probably one of the most relevant applications that rely upon load cells to measure environmental forces. Given that surface profile is usually unknown or is constantly changing; it is mandatory to continuously monitor the interaction forces between each leg and the surface during the gait and static standing. This fact is always in mind of the legged robot designers and researches when attempting to propose adaptable, yet fast, control algorithms capable of coping with uneven terrain with little *a priori* knowledge of the surface properties. Since load cells have proven to be a reliable solution to measure forces, legged robots and load cells have been traditionally paired.

Mankind has always been interested in understanding and emulating the walking skills of humans and animals. It is not crazy to suggest that the humanoid robot ASIMO is part of the popular belief in many countries, see the evolution of ASIMO in Figure 2.16. If an average human is asked to think about a humanoid robot, there is a strong likelihood of thinking about ASIMO.

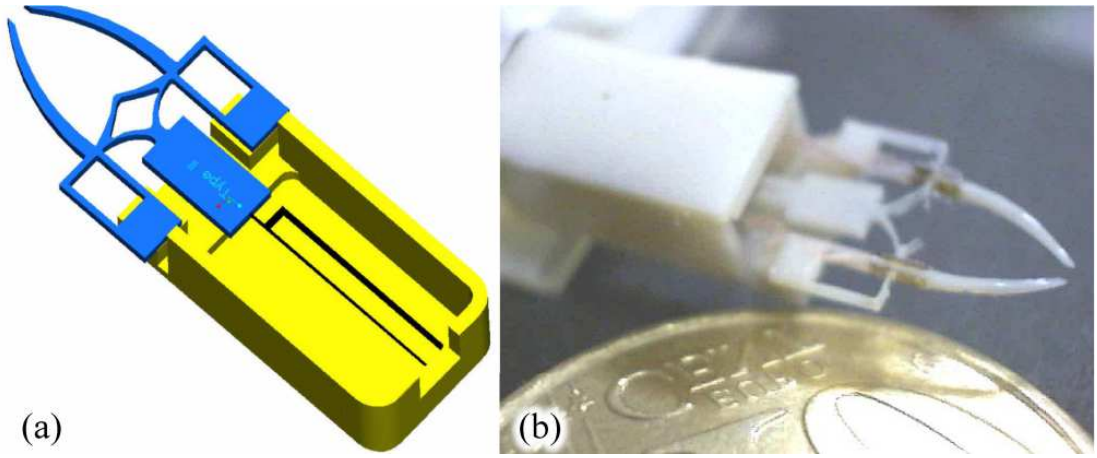

Figure 2.15: Image taken from [70] showing a microgripper for biomanipulation with embedded strain gauges. a) CAD design of the microgripper. b) Comparison of the microgripper to a 10 cent Euro coin

Figure 2.16: Evolution of the ASIMO, starting from the Experimental Model 0 (E0) on the left up to the latest version ASIMO 2000 on the right. ASIMO humanoid has been developed by HONDA

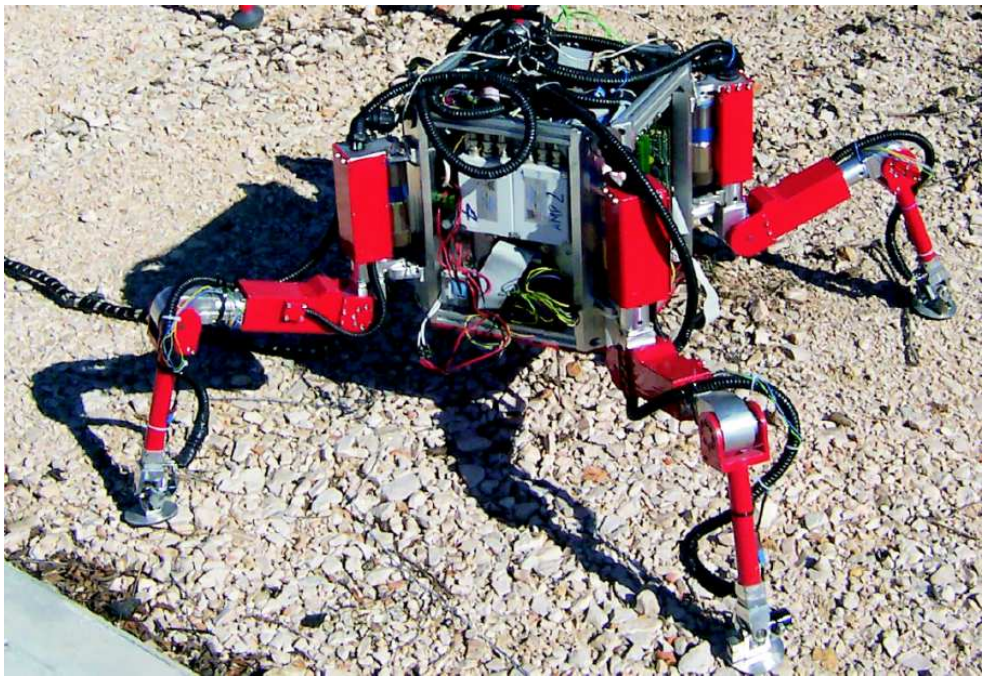

Figure 2.17: Picture of the SILO4 quadruped robot developed at CSIC, Spain

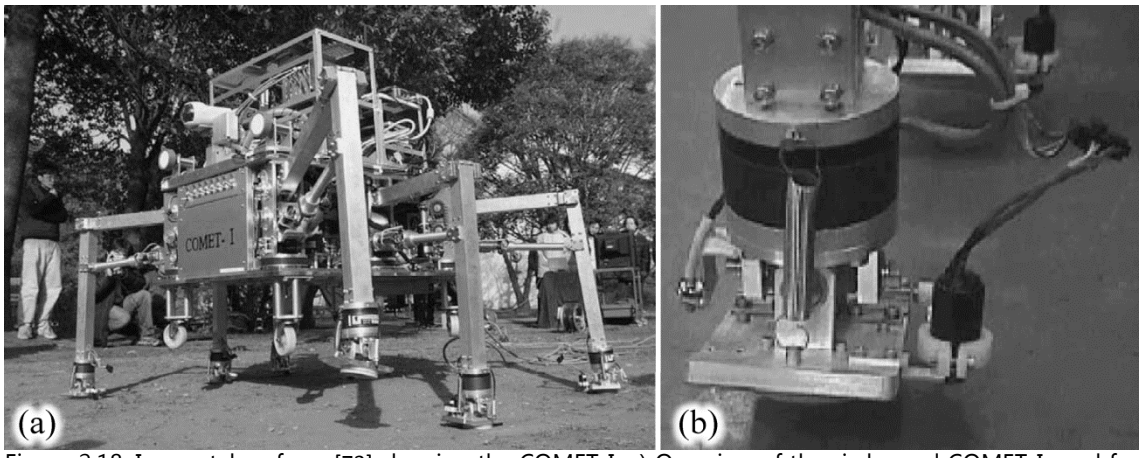

Figure 2.18: Image taken from [73] showing the COMET-I. a) Overview of the six legged COMET-I used for demining tasks on uneven terrain. b) Close up view of the foot equipped with a metal sensor, an optical proximity sensor and a force sensor

SILO4 is a quadruped walking robot developed at the Centre for Automation and robotics UPM-CSIC, Spain. It was designed for education and basic research purposes, featuring legs with insect configuration and a set of piezoelectric-based load cells located on each leg [56, 57]; the weight of SILO4 is **34 Kg**, see Figure 2.17. Force feedback from the sensors provide multiple benefits to the robot's performance, such as: ground detection on uneven terrain and obstacle detection in the transfer trajectories of the legs. Also, from a dynamic stand point, the sensed force on the legs is used as feedback on the ankle-level control loop and to compute the dynamic stability margin of the full robot [58]; this key feature allows legged robots to maintain stability despite uncertainties on the terrain.

It could be address almost any realization of legged robot to exemplify the usage of load cells. However the COMET-I, a six legged demining robot, is a special study case because each leg of the robot is equipped with a complex set of sensors comprising the following devices: a load cell, an optical proximity sensor and a metal sensor [73], see Figure 2.18.

During normal gait, a neuro-based nonlinear algorithm is used to control the locomotion of the COMET-I; this adaptive learning algorithm is an efficient way to cope with an unstructured ground surface. Load cell measurements are used by each leg's controller to achieve a compliant response of the full robot body. If mines are not detected in the surroundings of all of the robot legs, normal gait control is activated. Conversely if a mine is detected, a scanning motion over the surface is performed followed by an avoiding action that generates new walking gaits.

Normal gait occurs if the metallic detector installed on each leg of the manipulator fails to detect a considerable amount of metal on the step ahead. The threshold distance for metal detection is set by the proximity sensor at **3 cm**. The COMET-I walking mode produces a kind of awkward gait, because prior each leg contacts the surface a mine detection must be performed and consequently the strides seem to stop and go on each cycle. However, mine detection is maximized because a large area is scanned on each stride of the robot [126].

Figure 2.19: Image taken from [122] showing a sphere shaped load cell designed to quantify the compression and impact forces in fruits during the post-harvest and transportation process

2.5.5 Other applications

Some other examples of applications that report load cells usage were addressed by Muller [122]. Listing all of them is out of the scope of this thesis, but *it can be doubtlessly ascertained that load cells are among the most commonly used sensors in industrial and research applications* mainly because the magnitudes that a load cell measures, force and torque, describe the basic interaction between objects.

An interesting application regarding load cell usage in an unusual environment was reported by Muller [122]. A custom design load cell to quantify the compression and impact forces suffered by fruits during the post-harvest and transportation process was presented by Muller. The custom design load cell was fruit-like in terms of size and weight with a diameter of **80 mm**. similar to the size of an average apple. Three-ring load cells were employed in order to independently measure the compression and traction forces on each axis, see Figure 2.19. This unusual application shows the outstanding flexibility of this type of devices to measure forces.

2.6 Disadvantages of load cells and force measuring systems based on strain gauges

Despite all the advantages of load cells and strain gauge layouts to measure force, they exhibit some drawbacks when attempting to be installed in an existing application because bending elements are not always accessible along the structure, and thus, it results impossible to measure such deformations. This statement yields the discussion of strain gauge drawbacks to the strain definition itself:

Strain is the amount of *deformation* of a body due to an applied force.

So, if such a *deformation* is not possible to be *gauged*, *strain gauges* must be consequently discarded as the alternative to measure the applied force. From now on,

the designation of strain-gauge-based sensor is applied to any device that employs strain gauges as the underlying basis to measure deformation.

A proven solution is to modify the structure to embrace a deformable element in which strain gauges can be mounted on, e.g. the aforementioned Schurzig realization [112] in which a force-sensing unit was added to an electrode insertion robot, see Figure 2.7.

If strain can not be directly measured by a strain gauge, it may be suitable to install a load cell instead. Load cells already include a set of deformable beams with a proper layout of strain gauges to measure the applied forces and torques. However, this solution is not always possible for all the already existing applications because it implies the addition of a somehow bulky element to the overall structure. Load cell bulk and weight have been addressed as one of the main drawbacks that limit the extensive usage of such devices [173]. Load cell cost is also an important factor to take into account when designing products for mass production, but load cell bulk and weight are fairly more of this thesis' concern, because its scope is centered on the study of noninvasive force measurements, in particular to the force sensors with piezoresistive technology.

Take into account load cell bulk and weight from the early stages of design is a key part for a successful robot development and later robot operation. In fact; this consideration is a common issue for all the above cited instances that reported load cell usage. However, when designing anthropomorphic robots the dimensioning and selection of load cells is fairly more important because force transducers must naturally fit in the robot limbs, if not possible or not commercially available, a custom load cell must be designed to meet the application requirements, e.g. Carrozza developed a custom-made triaxial force sensor to fit in each fingertip of a cybernetic hand as a part of the device's exteroceptors [16].

Conversely, if the robot does not comprise a force sensing device from factory set-up and measuring deformation in one of the robot's limb is not possible; one solution is to add a deformable beam to gauge the applied forces, just as Schurzig did [112]. But sometimes adding a deformable beam is not possible; multiple reasons can be argued, each one tied to the specific characteristics of each application.

If force monitoring is mandatory for a given robotic application, but neither strain gauges nor load cells can be installed over the robot's structure, an effective solution towards force monitoring is to use a technology that does not require a strained surface as the sensing mechanism to gauge the applied forces. This was the case of Lamy research that yielded the introduction of a new concept; the concept of human-like robotic skins [100, 101].

Lamy presented a solution that comprised the usage of several piezoresistive sensors; these sensors were evenly distributed over the robot endpoint (or robot's structure) to emulate the proprioceptors available in a human skin. The robotic skin demonstrated to be a valid solution to detect collisions and to estimate contact forces during object manipulation. However, up to now, it has not been yet implemented a control layout where the only source of force feedback is provided by such a robotic skin.

The main reason that limits the extensive usage of piezoresistive sensors in force control applications is the relative low repeatability and low accuracy of such sensors

when compared to strain-gauge-based sensors [173]. So, if accuracy and repeatability are required and room requirements are not a limitation, a strain-gauge-based sensor is preferably used.

Conversely if room requirements are the main limitation, piezoresistive sensors are preferably chosen despite the subsequent performance degradation. Under this scenario, the capabilities of the sensor system are effectively lessen, just as the human-like robotic skin developed by Lamy which is only capable of collision detection and of providing a coarse estimation of force. If a force control or impedance control algorithm is to be implemented relying solely on the readings from a piezoresistive sensor, it is mandatory to improve first the performance of such devices. Chapters 3 and 5 address such a concern, but in order to situate the reader within the field, it is presented next a thorough description on the underlying basis of piezoresistive sensors, followed by a review on the most representative applications that involve the usage of such devices.

2.7 Underlying basis of piezoresistive sensors, also known in literature as Force Sensing Resistors *FSRs*

This section is focused on providing a physical explanation of the piezoresistive effect in single-crystal silicon and polymer materials. The introduction of polymers into the manufacturing of FSRs is a relatively recent fact, and thus the literature regarding polymer FSRs is rather scarce. So, most of the physical explanations herein presented are valid only for single-crystal silicon FSRs. Section 2.7.6 addresses some other difficulties that come up when attempting to obtain a theoretical model for polymer devices.

It is presented in this section a distinction between *silicon*, and the more generic *semiconductor materials*. When not specified, the statements made under the designation of semiconductor are valid for any material exhibiting a monocrystalline structure that falls within the semiconductor category. Conversely when characteristic constants are given, such as: Young's Modulus and piezocoefficients, it is specified the material they match for.

2.7.1 Crystallography of Silicon

Section 2.3 went through the basis of *metal strain gauges* by showing the relationship between sensor's resistance and its mechanical dimensions; such a relation was resumed in equation **(2.12)**. For the case of single-crystal silicon and polymer FSRs, finding a similar equation is rather complicated because such materials typically exhibit an *anisotropic behavior*. The *Anisotropy* is defined as the property of being directionally dependent.

Silicon atoms are regularly arranged in a crystal lattice structure. This causes that most of the material properties such as Young's modulus of elasticity and piezoresistivity exhibit an orientation dependency. Conversely, metals tend to be more isotropic and thus, the calculation of the Young's modulus of elasticity, **E**, and the material conductance, $\mathbf{1/R_x}$, become rather simple, see equations **(2.3)** and **(2.12)** for a detail formulation of **E** and $\mathbf{1/R_x}$.

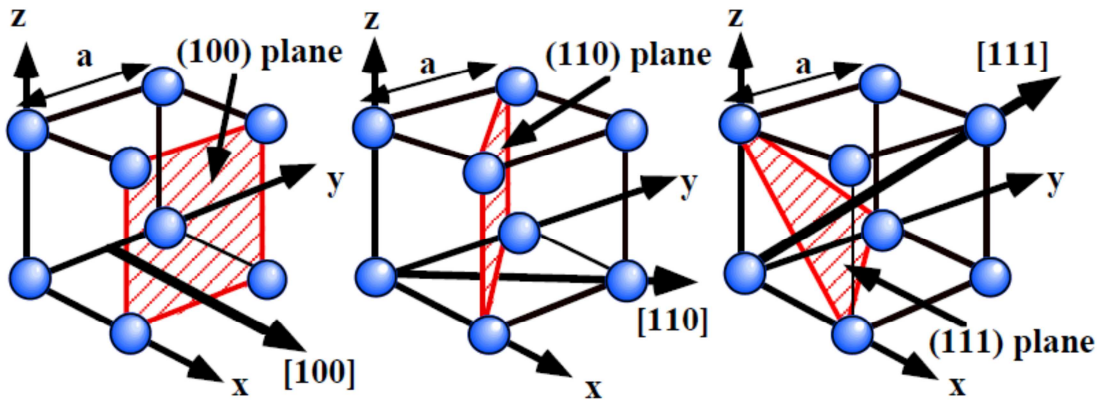

Figure 2.20: Crystallography of a silicon wafer taken from [142]. Three different cross-sections are shown for a silicon crystal lattice

Three cross-sectional views of the silicon crystal lattice are shown in Figure 2.20. A red-highlighted plane has been added to each cube in order to illustrate the different cutting angles which are usually performed on silicon crystals. Note that the 3D lattice has the form of a cube with side length a.

Each cross-sectional view produces a different 2D lattice when the cube is seen (or *cut*) from a determined standpoint. The designation of *cut* is added to the definition of cross-section because in the practice, silicon crystals are cut along different planes to obtain different properties in the resulting wafer. This procedure takes advantage of the anisotropic behavior of silicon crystals and also illustrates the complexity behind them.

A standard notation, called the *Miller Indices*, is used to describe the plane of visualization of the crystal lattice. Figure 2.20 shows the three most common planes under the Miller designations: **(100)**, **(110)** and **(111)**; this representation is usually referred as the *crystallography of a silicon waffle*. A derivation of the Miller Indices is available at [107].

2.7.2 Intrinsic and Extrinsic Semiconductors

A semiconductor crystal having no impurities is called an *intrinsic semiconductor*. The absence of impurities in the semiconductor lattice is impossible to obtain in the practice; however, a high degree of purity is achievable through a repeating refining process. For the case of silicon, the refining process can yield a "nine nines" purity (99.9999999%) for the case of *monocrystalline silicon*.

A semiconductor sample is called *monocrystalline* if the structure is absent of lattice defects and exhibits a regular pattern such as that of Figure 2.20, the pattern must be constantly and uniformly repeated over the entire semiconductor volume in order to be considered as a *monocrystalline* sample. The opposite case, a *polycrystalline* semiconductor is composed of a number of smaller crystals that follow a regular pattern but only for a short range. Both types of semiconductors are used in the manufacturing of FSRs and MEMs. The purity of a *polycrystalline* semiconductor may be also really high, reaching up to 99.9999% purity.

The intentional introduction of impurities, converts an *intrinsic* semiconductor into an *extrinsic* one. The impurities, usually called *dopant agents*, affect the mechanical and

the electrical properties of the semiconductor. There are two different types of dopant agents:

- n-type: A n-type dopant adds extra electrons to the semiconductor lattice. The Group V elements (from the periodic table) are n-type dopants because they have more electrons in their outermost shell than the host atoms have; these are the cases of phosphorous (P) and arsenic (As). This type of dopant is usually called a *donor.*
- p-type: A p-type dopants is capable of accepting electrons from the bulk. The Group III elements are p-type dopants because they have fewer electrons in their outermost shell than the host atoms have. Some examples of p-type dopants are the Boron (B) and Gallium (Ga). This type of dopant is usually called an *acceptor*.

A high level of purity in the semiconductor is often required when manufacturing semiconductors, because any impurity such as human sweat or dust may considerable affect the mechanical and the electrical properties of the resulting device. The controlled addition of dopant agents to a Silicon wafer is a standard procedure towards the manufacturing of semiconductor devices, such as diodes, transistors and MEMs.

The underlying basis on how dopant agents affect the properties (mechanical and electrical) of an intrinsic semiconductor is out of the scope of this document, due to its inherent complexity. This is in fact a procedure that is often done under an empirical basis [162, 172]. However, a formulation of the equations that relate doping with the mechanical and electrical properties is next presented.

2.7.3 An overview of Stress-Strain Relations in semiconductor materials

As earlier mentioned, the anisotropic behavior of semiconductor materials avoids a scalar formulation of the stress-strain relationship, so a *tensor* representation must be used instead. In order to visualize the vector components of stress and strain, a unit cube from the semiconductor material is isolated and then, the stress components are considered on each cube facet. The coordinate system is conveniently aligned with the cube sides, and the axes x, y and z are also labeled as 1, 2 and 3 respectively. A sketch of the cube and the axes is available on Figure 2.21.

A cube is a 3D solid object with six facets, and thereby, there are twelve possible shear force components (designated with the letter τ) and six normal force components (marked with the letter σ) acting on it. Nonetheless, these force components are not independent among them, i.e., each pair of shear stress components acting on parallel facets but along the same axis have equal magnitude and opposite direction, this is so because of the *force balance* stated by the Newton's First Law. This yields a reduction from twelve to six independent shear components as shown on Figure 2.21. There are two subscripts for each force, the first subscript indicates the normal direction on the facet on which the stress is applied, and the second denotes the direction of the stress component.

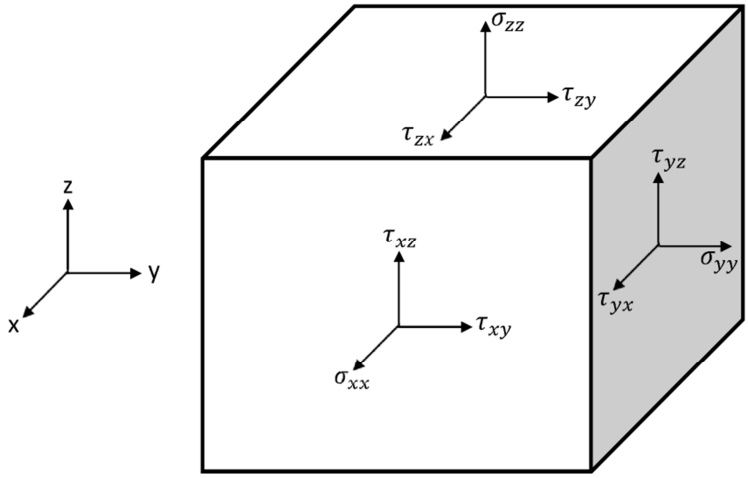

Figure 2.21: Principal stress components acting on a 3D solid object

Applying the torque balance principle to the shear force components of Figure 2.21 allows further simplification in the number of independent stresses. This can be seen from the following situation; two shear stresses acting on two contiguous facets but pointing towards a common edge have the same magnitude. This is the case of the components: $\tau_{xy}=\tau_{yx}$, $\tau_{xz}=\tau_{zx}$ and $\tau_{zy}=\tau_{yz}$. In other words, equal shear stresses always exist on mutually perpendicular planes. Finally, the number of independent shear stress components is reduced to three.

It is also possible to simplify the number of normal stress components by noting that under equilibrium conditions, the normal stress components acting on opposite facets have the same magnitude but point towards opposite directions. Normal stresses are represented with the Greek letter σ in Figure 2.21. This condition reduces from six to three the number of normal stress components. In brief, there are a total of three independent shear stresses and three normal stresses.

In order to represent the normal and shear stresses under a compact notation, the two indexes of each stress are substituted by a numeric convention as next:

- Normal stress components σ_{xx}, σ_{yy} and σ_{zz} are denoted as T_1, T_2 and T_3 respectively.
- Shear stress components τ_{yz}, τ_{xz} and τ_{xy} are simply denoted as T_4, T_5 and T_6 respectively.

Since each stress comes along with a strain, there are a total of six independent strains, these are: three normal strains (s_1 through s_3) and three shear strains (s_4 through s_6). The combination of both variables yields the formulation of the *generalized Hooke's law for anisotropic materials*:

$$\begin{pmatrix} T_1 \\ T_2 \\ T_3 \\ T_4 \\ T_5 \\ T_6 \end{pmatrix} = \begin{bmatrix} C_{11} & C_{12} & C_{13} & C_{14} & C_{15} & C_{16} \\ C_{21} & C_{22} & C_{23} & C_{24} & C_{25} & C_{26} \\ C_{31} & C_{32} & C_{33} & C_{34} & C_{35} & C_{36} \\ C_{41} & C_{42} & C_{43} & C_{44} & C_{45} & C_{46} \\ C_{51} & C_{52} & C_{53} & C_{54} & C_{55} & C_{56} \\ C_{61} & C_{62} & C_{63} & C_{64} & C_{65} & C_{66} \end{bmatrix} \cdot \begin{pmatrix} s_1 \\ s_2 \\ s_3 \\ s_4 \\ s_5 \\ s_6 \end{pmatrix} \qquad \textbf{(2.14)}$$

However, equation **(2.14)** is usually presented in compact form as below:

$$\bar{T} = C\bar{s} \tag{2.15}$$

The coefficient matrix **C** is known in literature as the *stiffness matrix*. Note that manipulating the equation **(2.14)** may result a challenging task due to its 36 elements. Fortunately, it is common to encounter several null and equal components in the stiffness matrix of semiconductors, this occurs because the crystallography of semiconductors is symmetrical around different axes. Specifically, the *silicon crystal belongs to the* $\mathbf{0_h}$ *group* [4]. This group of crystals has a symmetry that allows a range of different operations being performed for which the crystal structure is invariant, so for the $\mathbf{0_h}$ crystals the following components are equal:

- $\mathbf{C_{11} = C_{22} = C_{33}}$.
- $\mathbf{C_{12} = C_{21} = C_{13} = C_{31} = C_{23} = C_{32}}$.
- $\mathbf{C_{44} = C_{55} = C_{66}}$.

whereas the rest of components are null.

The stiffness matrix **C**, from equation **(2.14)**, allows the straight calculation of the Young's Modulus of a given anisotropic material along a specific axis. Given **C** for silicon:

$$C_{Si} = \begin{bmatrix} 1.66 & 0.64 & 0.64 & 0 & 0 & 0 \\ 0.64 & 1.66 & 0.64 & 0 & 0 & 0 \\ 0.64 & 0.64 & 1.66 & 0 & 0 & 0 \\ 0 & 0 & 0 & 0.8 & 0 & 0 \\ 0 & 0 & 0 & 0 & 0.8 & 0 \\ 0 & 0 & 0 & 0 & 0 & 0.8 \end{bmatrix} 10^{11} Pa \tag{2.16}$$

It is possible to calculate the Young's Modulus of Silicon along the [100] direction. For such a purpose, equations **(2.14)** and **(2.16)** are combined, and all the stress components are set to zero except for $\mathbf{T_1}$. This yields a three-unknown equation system that must be solved to find the quotient $\mathbf{T_1/s_1}$. The result, **130 GPa**, matches the Young's Modulus of Silicon around the **[100]** direction.

A similar procedure yields the Young's Modulus of Silicon along the **[110]** and **[111]** directions, they are equal to **168 GPa** and **187 GPa** respectively.

2.7.4 Calculation of Resistance in semiconductor materials

Given the dopant concentrations of a semiconductor material, it is possible to calculate its conductivity using the following set of formulas:

$$\sigma_n = n\mu_n q \tag{2.17}$$

$$\sigma_p = p\mu_p q \tag{2.18}$$

where $\boldsymbol{\sigma_n}$ and $\boldsymbol{\sigma_p}$ are the conductivity, in units of **1/(Ω cm)**, due to the n-type and p-type dopants respectively, **n** and **p** are the dopant concentrations in units of $\mathbf{cm^{-3}}$, **q** is

the charge of an electron, $\mathbf{q = 1.6 \cdot 10^{-19} C}$, and μ_n, μ_p are the mobility of charge carriers due to the electrons and the holes respectively.

The mobility of charge carries depends on multiple factors, the predominant influence lies on the type of the semiconductor used, e.g., the mobility of charge carriers for monocrystalline silicon is $\mu_n = 1400 cm^2/(Vs)$ and $\mu_p = 450 cm^2/(Vs)$, but quite larger values of mobility are exhibited by Gallium Arsenide (GaAs) with $\mu_n = 8500 cm^2/(Vs)$ and $\mu_p = 400 cm^2/(Vs)$. The GaAs is a semiconductor used in high speed switching circuits. It is later discussed in this section some other factors that usually affect the mobility of charge carriers.

Typically, only one type of dopant is added to a silicon material. However, if both types of dopants are present, the resistivity of the material can be calculated from:

$$\rho = \frac{1}{\sigma} = \frac{1}{\sigma_n + \sigma_p} = \frac{1}{q(\mu_n n + \mu_p p)} \qquad \textbf{(2.19)}$$

If the resistance of the semiconductor is required, it must be taken into account both: the doping concentration and the material dimension. In other words, the material conductivity must be first calculated on the basis of equation **(2.19)**, and then, the mechanical dimensions are evaluated **(2.13)** to obtain the sample resistance.

For any intrinsic semiconductor, the amount of electrons and holes which are available for recombination are the same, this is **n = p**. For intrinsic silicon at ambient temperature, the concentration of holes and electrons is: $\mathbf{n = p = 1.5 \cdot 10^{10}\ cm^{-3}}$. By substituting the concentration of holes and electrons into equation **(2.19)**, it is possible to estimate the resistivity of monocrystalline silicon: $\mathbf{2.25 \cdot 10^5\ \Omega \cdot cm}$. This is a quite large value for resistivity, but can be considerably lowered by adding dopant agents. It is also interesting to note that the concentration of holes and electrons is really low when compared to the atom density of silicon of $\mathbf{5 \cdot 10^{22}\ cm^{-3}}$.

2.7.4.1 Relationship between the effective mass of electrons and the mobility of charge carriers.

Under a wide range of conditions, the above given values of charge-carriers mobility can be taken as approximately constant for monocrystalline silicon and Gallium Arsenide. Nonetheless, such values are multivariable dependent and considerably vary from one device to another. The mobility of charge carriers can be calculated from the expressions below:

$$\mu_n = \frac{q\bar{t}}{m_n^*} \qquad \textbf{(2.20)}$$

$$\mu_p = \frac{q\bar{t}}{m_p^*} \qquad \textbf{(2.21)}$$

where $\bar{t}$ is the *mean free time* between two successive collision events, and $\mathbf{m^*_n}$, $\mathbf{m^*_p}$ are the *effective mass* for electrons and holes respectively. From now on, it is used the

letter **D** as the designator for electrical fields. It must be noted that the letter **E** was already reserved for the Young's Modulus, see equation **(2.3)**.

Given an extrinsic semiconductor with an evenly distribution of impurities along its structure, **n** or **p** type impurities, and under the effect of an electrical field **D**. It is possible to define $\bar{t}$ as the average time an electron can freely move along the semiconductor lattice with absence of collisions in response to **D**. This definition yields an important suggestion:

2.7.4.2 What happens when the impurity concentration is too high?

If the impurity concentration goes beyond a threshold, typically around $\mathbf{10^{17}\ cm^{-3}}$ for most semiconductors, the collision likelihood of electrons is increased and thus, the mean free time $\bar{t}$ is gradually reduced. The net effect over the material resistivity can be deducted by observing equations **(2.17)**, **(2.18)**, **(2.20)** and **(2.21)**. So, as the impurity concentration goes beyond $\mathbf{10^{17}\ cm^{-3}}$, the addition of further impurities does not proportionally increases the conductance of the semiconductor. This behavior is known as the saturation of the semiconductor's conductance. It is out of the scope of this thesis to present a thorough explanation of how such saturation occurs, but a detailed dissertation is available at [157].

A rather difficult task is found on describing the importance of effective mass in regard to the mobility of electrons and holes. For such a purpose, let's first define what the *effective mass* is.

2.7.4.3 Definition of Effective Mass ($\mathbf{m^*_n}$ and $\mathbf{m^*_p}$) in semiconductor materials.

Electron motion in free space is described by the *wave-particle principle* which embraces different concepts from the Classical Electromagnetic Theory and the Quantum Mechanics. Among other things, the wave particle principle attempts to describe, from a statistical standpoint, particle motion due to applied electrical fields $\mathbf{D_i}$ and magnetic fields $\mathbf{B_i}$.

The electrons of a semiconductor material are not completely free to interact with an electrical field $\mathbf{D_0}$. This is so because electron behavior is affected by the periodic potential of the semiconductor lattice. As a result, their *wave-particle motion* considerably differs from the wave-particle motion of electrons in free space. Therefore, if the equations of electrodynamics are used to describe electron motion in a semiconductor lattice, it is necessary to define a set of altered values for particle masses. In doing so, it is accounted for most of the influences on the lattice, so that electrons and holes can be treated as *almost free carriers* in most calculations.

Nonetheless given the orientation dependency of crystals from Figure 2.20, it is logical to suggest that the effective mass of particles is also an orientation-dependent quantity; this is in fact true and has the effect of inducing an anisotropic behavior in the resistivity of semiconductors, and thus, a tensor formulation for resistivity is also required for semiconductors, just as for the stress-strain relations from Section 2.7.3.

Fortunately, the effective mass of particles in semiconductors is a rather constant quantity that exhibits only a slight dependency on the crystal orientation. So for

simplification purposes, *the resistivity of semiconductors is considered as an isotropic property for further computations in this thesis, including silicon*. This is in fact a valid and widely accepted approach when dealing with piezoresistive materials, because as will be shown later, the piezoresistive effect studies the variation of the device resistance when stress is applied, and not, the accurate calculation of the device resistance under no-strain conditions.

The resistivity dependency on crystal orientation does not go unnoticed for the manufacturers of Bipolar Junction Transistor (BJTs). The **<111>** crystal oriented wafers are commonly used when manufacturing this type of transistors because they exhibit slightly higher values of μ_n and μ_p. Conversely, the **<100>** crystal oriented wafers are prevalently used in the manufacturing of Metal Oxide Semiconductors (MOS) due to their low density of interface states [107].

2.7.5 Piezoresistivity. Relating Stress to Resistance Variations

Previous sections went through the formal definition of stress/strain equations and resistivity calculation for semiconductor materials. This section studies the relationship between both properties; the mechanical and the electrical.

When subject to stress, a semiconductor exhibits an anisotropic form of the piezoresistive effect; this can be understood as an orientation dependency on the resistance variation regarding the direction of the applied stress. In order to study the piezoresistive effect in anisotropic materials, it is necessary to define a tensor version of the Ohm's law.

Given a rectangular coordinate system aligned with respect to the axes of a cubic semiconductor crystal, such as that of Figure 2.20, it is possible to define a tensor version of the Ohm's law in terms of the electrical field components $\mathbf{D_i}$ and the current density components $\mathbf{i_i}$. The matrix relating both vectors is the *resistivity matrix* as in:

$$\begin{pmatrix} D_x \\ D_y \\ D_z \end{pmatrix} = \begin{bmatrix} \rho_{xx} & \rho_{xy} & \rho_{xz} \\ \rho_{yx} & \rho_{yy} & \rho_{yz} \\ \rho_{zx} & \rho_{zy} & \rho_{zz} \end{bmatrix} \cdot \begin{pmatrix} i_x \\ i_y \\ i_z \end{pmatrix} \qquad \textbf{(2.22)}$$

Since semiconductors materials are arranged in crystal lattices, Equation **(2.22)** typically exhibits some repeated values because of the geometrical symmetries occurring in the crystal. For the case of *monocrystalline silicon*, the simplified version of the Ohm's Law is as follows:

$$\begin{pmatrix} D_x \\ D_y \\ D_z \end{pmatrix} = \begin{bmatrix} \rho_1 & \rho_6 & \rho_5 \\ \rho_6 & \rho_2 & \rho_4 \\ \rho_5 & \rho_4 & \rho_3 \end{bmatrix} \cdot \begin{pmatrix} i_x \\ i_y \\ i_z \end{pmatrix} \qquad \textbf{(2.23)}$$

The sub-indexes of equation **(2.23)** are arranged under the same convention used for the formulation of the stress/strain relationship in Section 2.7.3, that is, the normal contributions of resistivity are represented with the indexes 1~3 and the Greek letter **ρ**:

$$\rho_{xx} = \rho_1 \qquad \textbf{(2.24)}$$
$$\rho_{yy} = \rho_2$$
$$\rho_{zz} = \rho_3$$

and the shear contributions are represented with the indexes 4~6:

$$\rho_{yz} = \rho_{zy} = \rho_4 \qquad \textbf{(2.25)}$$
$$\rho_{xz} = \rho_{zx} = \rho_5$$
$$\rho_{xy} = \rho_{yx} = \rho_6$$

Note from the expressions **(2.24)** and **(2.25)** that there are only six different coefficients in the resistivity matrix **(2.23)**. This is consistent with the statement of Section 2.7.3 that declared the belonging of silicon to the $\mathbf{0_h}$ group. However, different crystal may exhibit different types of symmetries and thus, the simplified formulation of the Ohm's Law from equation **(2.23)** cannot be generalized to any semiconductor. *Henceforth in this section, it is only discussed the piezoresistive effect for monocrystalline silicon*.

Given a bulk sample of monocrystalline silicon with cubic geometry and *no applied stress*, the resistivity matrix can be further simplified as:

$$\rho^0 = \begin{bmatrix} \rho_0 & 0 & 0 \\ 0 & \rho_0 & 0 \\ 0 & 0 & \rho_0 \end{bmatrix} \qquad \textbf{(2.26)}$$

where $\boldsymbol{\rho_0}$ is the resistivity calculated according to the equations **(2.17)**, **(2.18)** and **(2.19)**. Only the diagonal coefficients are left in the resistivity matrix $\boldsymbol{\rho^0}$ because resistivity is taken as an isotropic property for silicon [4], see Section 2.7.4.3. Nonetheless, when silicon is subject to stress; the resistivity changes according to the spatial direction and magnitude of the applied force, and the isotropic approximation of equation **(2.26)** is no longer valid. It is necessary to use instead the tensor form of the resistivity matrix as in equation **(2.23)**.

In order to relate the applied stress to the resistivity variation, a quotient is defined for each of the six coefficients of the matrix **(2.23)**, as below:

$$\frac{\Delta\rho_\alpha}{\rho_0} = \pi_{\alpha\beta}\boldsymbol{T}_\beta \qquad \textbf{(2.27)}$$

where $\boldsymbol{\Delta\rho_\alpha}$ is the variation of the resistivity coefficients. The quotient is the product of the piezoresistivity coefficient $\boldsymbol{\pi_{\alpha\beta}}$ and the applied stress $\mathbf{T_\beta}$. The piezocoefficient reads as follows: given an applied stress $\mathbf{T_\beta}$ along the $\boldsymbol{\beta}$ direction, the variation of resistance along the α direction is proportional to $\boldsymbol{\pi_{\alpha\beta}}$. The sub-indexes for $\boldsymbol{\alpha}$ and $\boldsymbol{\beta}$ are the same presented earlier in equations **(2.24)** and **(2.25)**.

In order to obtain the resistivity value under stress condition, it must be combined the variation of resistivity **(2.27)** with the value under no-applied stress. Typically, the unstressed value is also known as initial value and thus designated with the **0** subscript:

$$\rho_\alpha = \rho_\alpha^0 + \Delta\rho_\alpha \quad \textbf{(2.28)}$$

The term $\boldsymbol{\rho^0_\alpha}$ is understood as the initial value of resistivity along each direction, but under the assumption of material isotropy, the only possible value for $\boldsymbol{\rho^0_\alpha}$ is either $\boldsymbol{\rho_0}$ or zero; this statement can be deducted from equation **(2.26)**. The final form of the piezoresistive tensor can be arranged by combining equations **(2.27)** and **(2.28)** under a matrix form with six stress components:

$$\begin{bmatrix}\rho_1\\ \rho_2\\ \rho_3\\ \rho_4\\ \rho_5\\ \rho_6\end{bmatrix} = \begin{bmatrix}\rho_0\\ \rho_0\\ \rho_0\\ 0\\ 0\\ 0\end{bmatrix} + \rho_0 \begin{bmatrix}\pi_{11} & \pi_{12} & \pi_{12} & 0 & 0 & 0\\ \pi_{12} & \pi_{11} & \pi_{12} & 0 & 0 & 0\\ \pi_{12} & \pi_{12} & \pi_{11} & 0 & 0 & 0\\ 0 & 0 & 0 & \pi_{44} & 0 & 0\\ 0 & 0 & 0 & 0 & \pi_{44} & 0\\ 0 & 0 & 0 & 0 & 0 & \pi_{44}\end{bmatrix} \begin{bmatrix}T_1\\ T_2\\ T_3\\ T_4\\ T_5\\ T_6\end{bmatrix} \quad \textbf{(2.29)}$$

For the case of silicon, there are only three piezocoefficients: $\boldsymbol{\pi_{11}}$, $\boldsymbol{\pi_{12}}$ and $\boldsymbol{\pi_{44}}$. This fact can be explained by recalling the belonging of silicon to the $\mathbf{0_h}$ group [4, 107]. However, each semiconductor may exhibit different patterns of piezoresistivity.

Smith was the first to experimentally characterize the piezoresistive response of monocrystalline silicon in 1954 [154]. However, a full characterization of silicon piezoresistivity had to expect until 1982 when Yamada carried out some experiments to explain some nonlinearities occurring under high stress loading in silicon devices [172].

Table 2.1 summarizes the experimental values of piezocoefficients found by Smith for n-type and p-type doped silicon. By replacing such piezocoefficients in the equation **(2.29)**, it is possible to estimate the applied stress over a silicon sample by measuring its resistivity variation. This is the working principle of the silicon FSRs.

Table 2.1: Piezocoefficients from monocrystalline silicon found by Smith [154]

Piezocoefficient	$\boldsymbol{\pi_{11}}$ **10^{-11} [Pa^{-1}]**	$\boldsymbol{\pi_{12}}$ **10^{-11} [Pa^{-1}]**	$\boldsymbol{\pi_{44}}$ **10^{-11} [Pa^{-1}]**
p-type, (ρ_0 = 7.8Ω·cm)	+6.6	-1.1	+138.1
n-type, (ρ_0 = 11.7Ω·cm)	-102.2	+53.4	-13.6

2.7.6 Difficulties arising from the modeling of silicon and polymer FSRs

Table 2.1 summarizes the piezocoefficients for monocrystalline silicon under a specific doping concentration. Several authors have characterized monocrystalline silicon under different doping concentrations, whereas other researches have kept constant the dopant level but varied the temperature; the results suggested that doping concentration influences each piezocoefficient in different proportions. Likewise, temperature also plays an important role and affects some piezocoefficients more than others.

Nonetheless, *it does not exist a theoretical model capable of predicting the piezocoefficient values under a specific dopant concentration at a given temperature*.

Finding such a model is a rather complicated task because it combines multiple variables from the mechanical and the electrical domain. This is a pending challenge in the current development of piezoresistors. However, it is possible to obtain from previous studies a set of discrete piezocoefficient values under many different levels of dopant concentrations and temperature conditions [162, 172].

2.7.6.1 Empirical approach on the characterization of polymer FSRs.

If the semiconductor used for manufacturing the FSR is different from silicon, finding such piezocoefficients becomes more difficult, and if the information is available, the piezocoefficients may be characterized only for a few dopant concentrations and over a restricted temperature range; this is so because silicon has notably dominated the manufacturing of FSRs over the years, due to its competitive cost and abundance on earth, and so, there has been little interest on characterizing additional piezoresistive materials. However, silicon lacks of certain properties to be discussed later in Section 2.7.6.2.

Given the recent introduction of polymers into the manufacturing of FSRs, the information regarding such technology is quite scarce. There are only a few manufacturers of polymer FSRs and the information provided by them is limited to the device's performance with little or null reference to the piezoresistive constants presented in this Section. Typically, the manufacturers of polymer FSRs only provide technical specifications under the metrics presented in Section 2.2, and *neither do exist a theoretical model for the piezocoefficient derivation in polymer FSRs*.

It is so scarce the information concerning polymer FSRs that, the manufacturers do not specify the typical sensitivity of his products, this is, the output response of the sensor in terms of V*olts per Kilogram-Force* is not given, and thus, the final user must characterize each device independently before using it.

Above statements are the main reasons that support the empirical characterization of polymer FSRs, including of course, the characterization of the FlexiForce sensor to be addressed in Chapter 3.

2.7.6.2 Comparison between silicon and polymer FSRs.

The obtaining of high purity silicon is an energy wasting procedure that must be repeated over and over up to reaching the target "nine nines" purity degree, see Section 2.7.2. Considering that the melting point of silicon is **1414 °C**, a large amount of energy is thus wasted during the refining process of raw silicon; this considerably increases the cost of manufacturing monocrystalline silicon. Conversely, polymers can be processed at lower temperatures. Also, the main components of polymers, carbon and hydrogen, are also abundant on earth (just as silicon is), so the raw material for polymer processing are also cheap. In brief, the synthetizing of polymers for the manufacturing of FSRs is cheaper than the use of monocrystalline silicon.

Another advantage of polymers lies on their remarkable mechanical properties. Polymers exhibit a high degree of ductility compared to monocrystalline silicon, which is rather a brittle material. The ductility of a senor is highly desirable during its installation and further operation. A brittle sensor has a greater likelihood of breaking

than a ductile one. Nonetheless, most polymers can withstand tensile stresses of only **100 MPa**, which is much lower than that of silicon and most semiconductors.

On the opposite side, silicon FSRs exhibit larger values on the mobility of charge carriers when compared to Polymer sensors, and thus, the gauge factor of silicon FSRs is greater than that of Polymer devices.

Last but not least, the non-repeatability and the measurement errors (see Section 2.2.4 and 2.2.5 for a definition of both errors) of silicon FSRs are quite lower than that of polymer FSRs; the underlying basis of this fact lies on an undesirable property of polymers known as the viscoelastic behavior. When a force is applied to a polymer, an instantaneous elastic deformation usually occurs, followed by a viscous and time-dependent strain change. As a result, most polymers are susceptible to time-dependent deformation under a constantly maintained stress. Such a deformation is called viscoelastic deformation.

The viscoelasticity have dramatic effects over the performance of polymer FSRs. Typically, these devices exhibit large amount of hysteresis and signal decay over time. Both properties are analogous to the mechanical definition of viscoelasticity. The net effect is a relative low repeatability in the force readings. *Currently, this is by far the main limitation in the extensive usage of polymer FSRs.*

2.7.6.3 Cutting-edge in the manufacturing of Polymer FSRs.

Polymers encounter plenty of applications at the macroscale, but only a few of them have been successfully tested and employed in the manufacturing of FSRs. Probably the most widely used polymer in the FSR manufacturing is the *Polyimide*, which is in fact the substrate chosen by Tekscan, Inc to manufacture the *FlexiForce* sensor.

Liu declared that despite the enormous progress in recent years, many polymer materials with potential applications in MEMs remain unexplored [107]. These candidates include conductive polymers, and the vast family of electroactive polymers such as polypyrrole, photopatternable gelatin, shape memory polymers and polyvinylidene fluoride (PVDF).

Moreover, there are seemingly endless ways to modify polymer properties. For instance, it has been discovered that the electrical and mechanical properties of polymer FSRs can be enhanced by adding conductive nanoparticles and nanowires.

In brief, the possible variations of piezoresistive polymers are enormous. They are only waiting to be discovered and implemented in the next generation of polymer FSRs. *This thesis is only a small contribution towards such direction.*

2.7.7 Comparison between the Tekscan and the Interlink FSRs

This section describes two of the most widely used piezoresistive sensors: The FlexiForce sensor and the Interlink FSR. Previous studies comparing both devices are also addressed in this section.

Typically, this type of sensors is built using two layers of flexible substrate. On each layer, a conductive material (silver or cooper) is applied, followed by a layer of piezoresistive material, a sketch of the device layers is depicted on Figure 2.22.

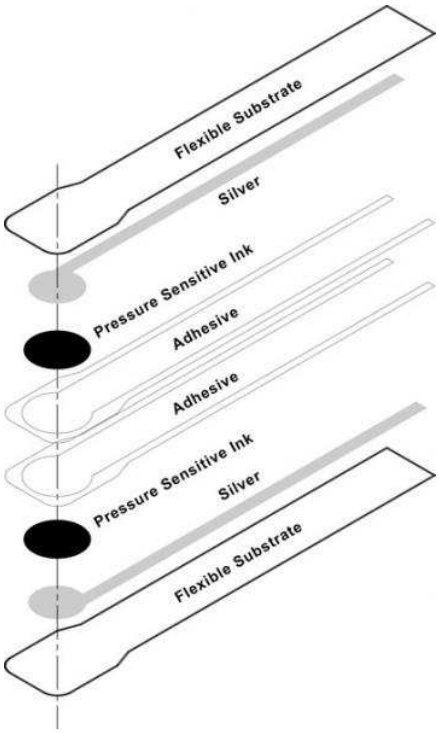

Figure 2.22: Layers of a FSR

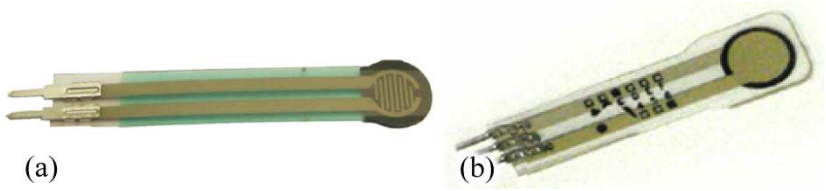

Figure 2.23: Pictures of two piezoresistive sensors: a) Interlink FSR 400 series and b) FlexiForce A201 series

The Tekscan A201 sensor and the Interlink FSR 400 device are shown on Figure 2.23. A thorough review of the existing literature shows that both sensors are the preferably chosen in current developments that require non-invasive force readings. Nonetheless, the information regarding both sensors is still scarce. For such a purpose, Lebosse [102, 103] and Hollinger [69] have presented comparative studies on such devices in an attempt to assess the benefits and drawbacks of each sensor. Likewise, a broader comparative study comprising three types of FSR was presented by Komi [92].

The experimental tests from Lebosse and Hollinger comprised several mechanical properties from the sensor. Sinusoidal force profiles and static forces (time invariant) were applied in order to gauge the hysteresis, the non-repeatability and the non-linearity errors of both devices. Furthermore, Lebosse developed a compensation model for the sensor drift when subject to sinusoidal forces.

The Lebosse's results can be summarized as follows. The non-repeatability error for both sensors is pretty similar, resulting slightly greater for the FlexiForce sensor, **3.6 %**, compared to a **2.1 %** in the Interlink device. It must be remarked that both values are ranged among the typical performance specifications for each device.

Hysteresis resulted greater for the FlexiForce sensor, **10 %**, when compared to the **8 %** exhibited by the Interlink device. This result is consistent with the magnitudes of the non-repeatability errors, because it is a logical consequence that increasing hysteresis

yields larger values of the non-repeatability error. Nonetheless, the found hysteresis errors are far from the typical performance specifications for each device. Lebosse argued that such a mismatch may be due to the low range of the exerted forces along his experiment. The typical hysteresis (according to the manufacturer datasheet) for both sensors is around **5 %** for a full scale force of **450 N**. On the opposite side, the maximum force applied by Lebosse was of only **7 N**.

The FlexiForce sensor exhibited a better linear response than the Interlink device, but Lebosse did not provide a numerical estimation of the non-linearity error for either device. Instead, a pair of plots was presented to show the typical response of each sensor.

2.7.7.1 Typical Performance of the FlexiForce sensor.

The FlexiForce sensor is manufactured by Tekscan Inc, a Los Angeles-based company. The preferably-chosen substrate in the sensor assembly is the Polyimide; however a polymeric binder with phenoxy polymers can be also used as the device substrate [95]. The typical performance of the FlexiForce sensor is summarized next:

- Full product name: FlexiForce A201-100.
- Nominal range: **100 lb**. (**450 N**).
- Linearity error: <**±3%**
- Repeatability: <**±2.5%** error of full scale.
- Hysteresis: <**4.5%** of full scale.

2.7.7.2 Typical Performance of the Interlink FSR.

The Interlink sensor is manufactured using a robust polymer thick film PTF [79] by Interlink Electronics. The typical performance of the device is listed below:

- Full Product name: Interlink FSR 400.
- Nominal Range: **0.2N** ~ **20N**.
- Hysteresis: <**10%**.
- Force Repeatability: <**2%** for a single device and <**6%** from one device to another.
- Linearity error: not specified in sensor's datasheet.

2.8 Review of representative applications involving piezoresistive sensors as force measuring devices

Previously, Lamy [100] and Carrozza [16] have been cited in Section 2.5 as representative examples that demonstrate the feasibility of piezoresistive sensors to measure contact forces in human-like robotic skins. However, there are several other applications that use this kind of sensors to perform, either force tracking tests, or primitive force-control algorithms. It is presented below a brief description of the most representative applications that report the usage of this type of sensors.

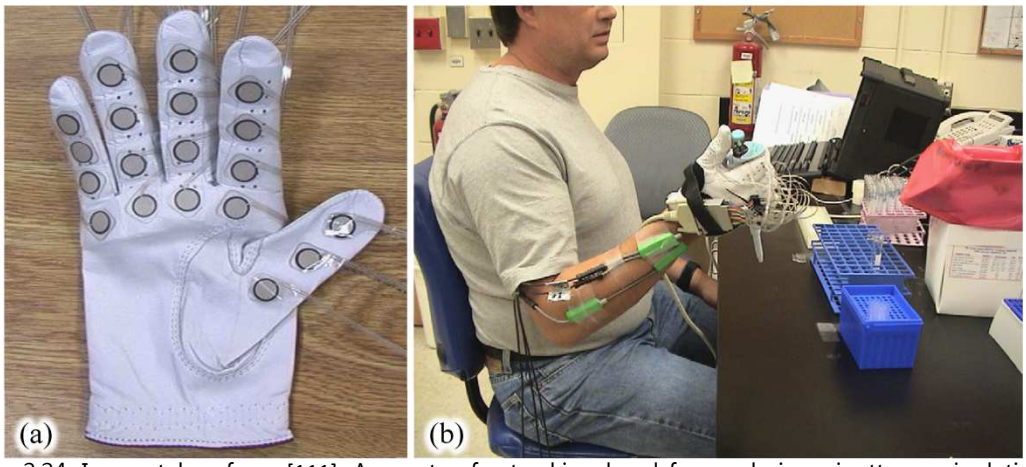

Figure 2.24: Image taken from [111]. Apparatus for tracking hand forces during pipette manipulation. a) Sensor glove equipped with 19 FlexiForce sensors. b) Picture of a subject grasping a pipette with the final sensor arrangement. Note the goniometer and torsiometer for tracking the wrist and forearm motion

2.8.1 Ergonomics

In ergonomics, it is of great interest to track the interaction forces between humans and the tools under design; this is done with the aim of providing comfort and safety to the user while maximizing the tools' effectiveness and performance.

Lu carried out an investigation of hand forces and postures while manipulating mechanical pipettes in a laboratory [111]. The aim of Lu's research was to provide useful information regarding the optimum pipette design that could minimize the physical risk factors associated with pipette handling. Lu's setup comprised a sensor glove with 19 piezoresistive sensors, an electrogoniometer for assessing wrist rotation and a torsiometer for measuring forearm torsion. The glove assembly is shown on Figure 2.24a, and the final setup for tracking forces is shown on Figure 2.24b.

The FlexiForce sensor was the device chosen by Lu to track the hand applied forces during pipette manipulation [76]. A brief description of this device was previously presented in section 2.7.7 and a picture of the sensor was shown in Figure 2.23b. A detailed study of the FlexiForce sensor is one of the key focuses of this research to be addressed in Chapter 3, and consequently, it is not presented in this section a thorough description of it.

The results of Lu's investigation suggested that altering body position between sitting and standing while pipetting may help to reduce the cumulative strain in the wrist and forearm. However, the force data collected from the sensor glove during sit and stand positions remained unchanged, but a significant dependency between the pipette design and the applied forces was found. Above facts yielded Lu to suggest that in order to reduce strain during continuous pipette manipulation, it is recommended to switch between sit and stand positions, but a reduction in hand strain is only possible by pipette redesigning.

A study towards comfort maximization of cylindrical grippers was presented by Kong [93]. The main contribution of his research was to find a relation between the subject's hand size and the gripper diameter that maximizes user's comfort. The setup employed by Kong was similar to that used by Lu [111]. A force glove containing 16 FlexiForce sensors was used to measure the applied hand forces during the gripper manipulation.

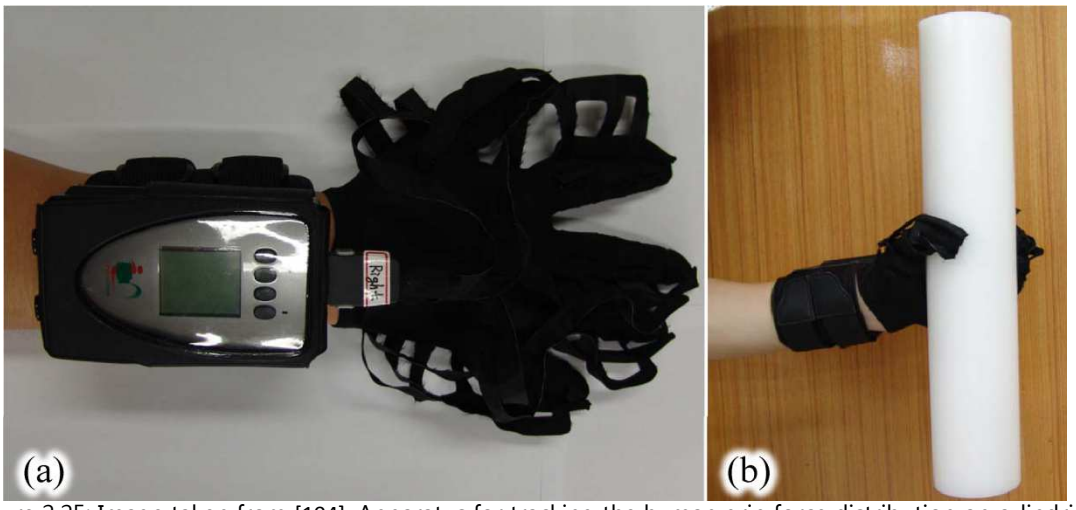

Figure 2.25: Image taken from [104]. Apparatus for tracking the human grip force distribution on cylindrical handles. a) Picture of the Intelligent Force Glove (I-Force Glove). b) A subject wears the I-Force glove while grasping a cylindrical handle

The research involved a total of 24 subjects with different hand sizes. It was found that the optimal handle diameter was **19.7 %** of the user's hand length.

Following Kong ideas, a similar research was carried out by Lee [104] towards the study of the human grip force distribution, with the difference that the sensor framework used by Lee was more realistic by incorporating a total of 46 piezoresistive sensors distributed across the palm side of two sensor gloves, 23 sensors for each hand compared to the 16 sensors used by Kong [93].

Another difference between Lee's and Kong's studies can be found on the sensors used for collecting the force data. While Kong used FlexiForce sensors, Lee used Force Sensing Resistors, FSRs, to assemble a sensor glove similar to that of Figure 2.24. Note that the designator of FSRs was used by Lee to describe the sensors, whereas Kong labeled the force sensors as piezoresistive devices; this name inconsistency is a mere formalism because the underlying basis of both devices is the same. However, it must be remarked that Lee and Kong employed different brands of force sensors in their respective studies. A picture of the Lee's sensor glove is available on Figure 2.25.

2.8.2 Haptic Interfaces

Within the field of haptics, a Sensorized Thimble for Haptics Applications was presented by Monroy [116] and Ferre [49]. The so-called *MasterFinger-2* comprised two modules, each one with a sensorized thimble to interface with the index and thumb fingers, see Figure 2.26a. Given that the FlexiForce sensors provide force tracking along a single axis, Monroy proposed a sensor setup with four of such sensors to enable force tracking in all directions. The final arrangement shown in Figure 2.26b, was capable of reading the normal forces from the sensors placed on the bottom of the thimble, whereas the tangential forces were measured from the sensors installed on the thimble's lateral sides.

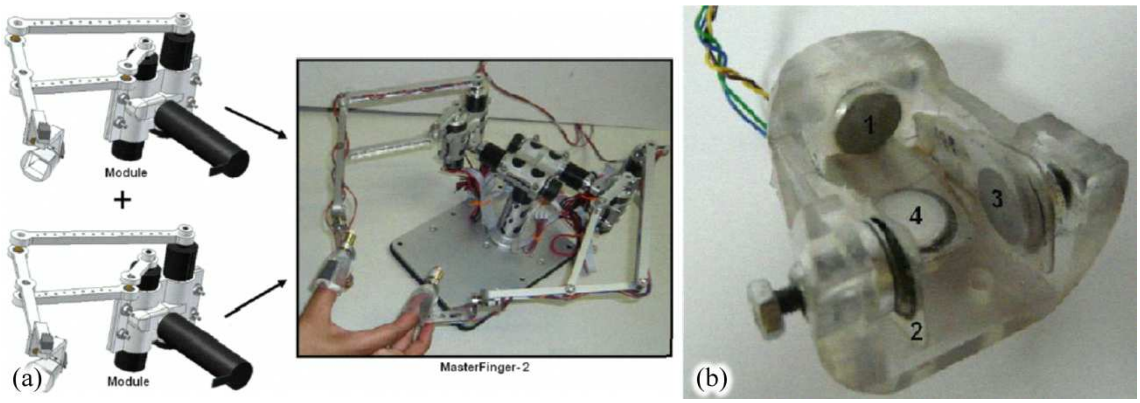

Figure 2.26: Images taken from [116] showing the components of the *MasterFinger-2*. a) Overview of the paired modules to enable object pick-up in a virtual environment. b) Sensorized thimble with four FlexiForce sensors to track the applied finger forces

The manipulation of a virtual object in an augmented reality scenario has been implemented to evaluate the performance of the MasterFinger-2 interface. Using the index and thumb fingers, the subject attempted to grasp and pull a solid red cube displayed on a screen, while the cube's weight and bulkiness were rendered by an impedance control algorithm. The concepts of virtual walls and virtual surfaces have been implemented together with the impedance controller in order to provide a realistic simulation environment. The resulting testbench is suitable for teleoperated applications and rehabilitation therapies. A more detailed description of the potential capabilities of the MasterFinger-2 interface was pointed out by Ferre [49, 50].

2.8.3 Orthopedics

In orthopedic treatments, it is necessary to ensure equalization of plantar foot pressures as a part of the recovery process from a Wagner Stage 1 and 2 neuropathic plantar ulcers. Baumhauer developed a wearable interface [8] to track the applied foot forces during a walk of **280 m**. The interface comprised 5 plantar foot sensors located at the first, third, and fifth metatarsal heads, together with the fifth metatarsal base and midplantar heel. Due to the space limitations imposed by the shoes' dimensions, Baumhauer chose FSRs as the force measuring technology. In this case, the Interlink sensors [79] manufactured by Interlink Electronics were chosen to assemble the pair of sensorized shoes.

A similar research towards the tracking of foot force profiles was presented by Nihal [125]. The research entitled: *Toe flexor forces in dancers and non-dancers*, made use of a pair of FlexiForce sensors to monitor the hallux and second toe forces during sitting and standing positions in 24 dancers and 29 non-dancers subjects. The results from Nihal's research suggested that the dancers exhibited a larger force profile on the toes than the non-dancers group.

2.8.4 Piezoresistive sensor arrays. A step towards the development of a human-like robotic skin

A review on the applications involving piezoresistive sensors is not complete without a reference to the sensor arrays. By combining multiple FSRs into a single-laminated

device, it is obtained an array of sensors capable of monitoring forces over a large surface. Moreover, if the individual FSRs are sufficiently small, it is possible to reconstruct the shape of the object which is located on top of the sensor array. Castellanos-Ramos has demonstrated such a reconstruction to be possible [19] as can be seen in Figure 2.27, similar results were also reported by Kane [85]. Sensor arrays are usually known as *pressure mapping systems*, whereas each individual FSR is designated as a tactel [165].

There is an increasing interest in the development of this type of FSR arrays, mainly because the FSR arrays can render some properties of the mechanoreceptors existing in human skins. As earlier mentioned in Chapter 1, a human-like robotic skin should be able to measure, at least, the same object properties than a real hand can actually do. Sensor arrays can effectively measure force and contact, but the capabilities of human skins go way beyond by providing readings of force, temperature and texture. Hence, there is currently a great effort towards the expansion of the robotic skin capabilities.

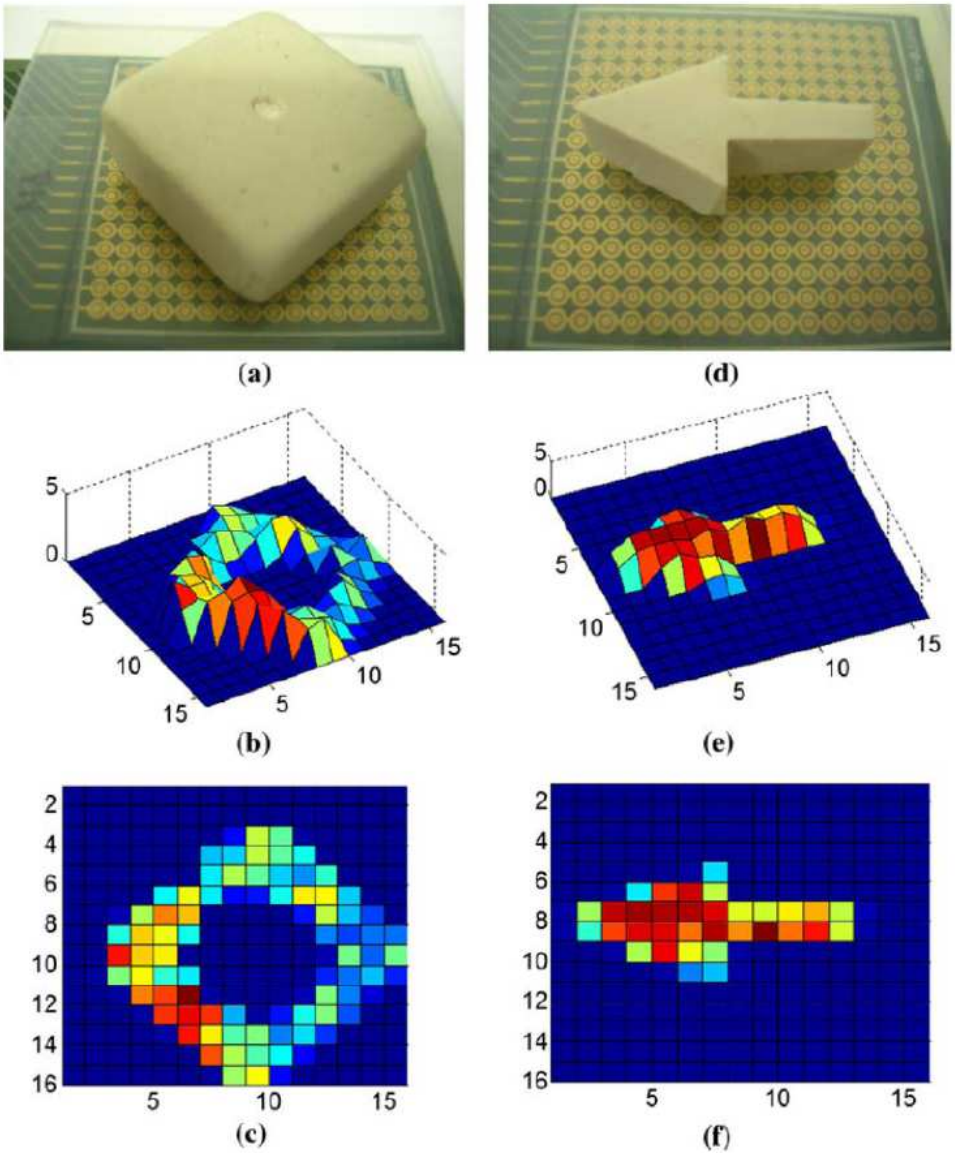

Figure 2.27: Image taken from [19] showing 3-D and 2-D force profiles generated from the analog data produced by the sensor arrays. a, b, c) A cube with a hole in the middle generates 3-D and 2-D force profiles. d, e, f) A rubber arrow and its corresponding 3-D and 2-D force profiles

Special attention must be placed on designing an appropriate multiplexer circuit (MUX) for the FSR array. Typically, the sensor driver is designed together with the MUX circuit to reduce the most the transistor count of the system; this yields low power requirements and an overall reduction in the system cost. However, the main reason for multiplexing the sensor array is to minimize the wire count of the array. So, for a non-multiplexed sensor array, wire count increases as a function of **2 x n**, with **n** as the number of tactels; whereas for a multiplexed array with the same number of rows and columns **n x n**, a total of only **2 x n** wires are required. In other words, if **n = 10**, it is possible to address **20** non-multiplexed tactels, but up to **100** tactels under a multiplexed addressing scheme. The plus and contras of each approach are next discussed.

For a non-multiplexed sensor array, the PCB sensing area typically exhibits a complex and multilayered routing, and consequently, it is common to find crosstalk effects when digitalizing tactel outputs in a timeshared basis; this fact is illustrated from the example below:

An average sensor array may have between **1000** and **8000** tactels, but only **10** Analog to Digital Converters (ADC), a typical update rate of **100Hz** is chosen for the hypothetical sensor array. Assuming that is possible to fit **2** wires for each tactel on the PCB, it would be necessary to switch from one tactel to another every **100 us** or **12.5 us** respectively; this high frequency switching may produce undesirable coupling signals between adjacent lines depending on the wire length.

The hypothetical sensor array also exhibits high density lines, with **2000** wires for the **1000**-tactel version and **16000** wires for the **8000**-tactel array. The requirement for high density lines increases the overall system cost, adds bulkiness and makes the system fault-likely due to the large amount of routing. Nonetheless, if high update rates are required, the only solution left is to add more ADCs to the system. This solution must be paired with the tactel count.

A solution towards the reduction of wire density is to use shared-addressing tracks, i.e. multiplexing the sensor array, this simplifies wiring but a new problem emerges if nearby tactels are pressed simultaneously. This is in fact a very likely problem considering that the tactel's size is usually smaller than the size of the object being sensed. When two or more nearby tactels are pressed at a time, a parasitic path is set among them affecting the resistance readout. A detailed analysis of such scenario was presented by Vidal-Verdu [164] and summarized in Figure 2.28.

Note from the sensor output in Figure 2.28b that the orange-colored areas are surrounded by yellow and green areas; this gradient is produced by the parasitic resistive path that exists between adjacent tactels that share the same MUX lines. Figure 2.28a illustrates this case in which the tactel $\mathbf{R_{wj}}$ is selected. However, the current finds alternative paths to flow through; these are the tactels marked with the dashed red line: $\mathbf{R_{w0}}$, $\mathbf{R_{x0}}$ and $\mathbf{R_{xj}}$. The net effect to the force map of Figure 2.28b is to exhibit a smooth force profile instead of an abrupt transition between the zero and nonzero force areas.

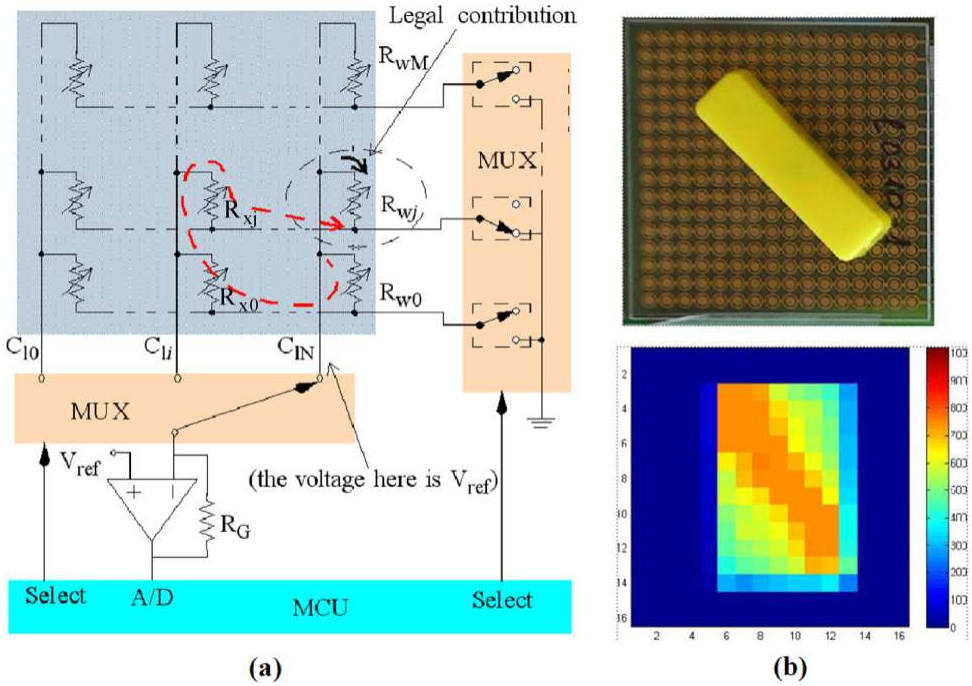

Figure 2.28: Image taken from [165] illustrating the effects of parasitic resistors in a MUX-ADC driving circuit. a) Electronic circuit for digitalizing 9 tactels of a sensor array, the parasitic path is marked with a dashed red line. b) Force profile produced by a slash bar placed on top of the sensor array

An extensive analysis of the driving circuits for sensor arrays was presented by Vidal-Verdu [164, 165]. He proposed that in order to avoid the occurrence of parasitic paths, it is necessary to virtually short-circuit the parasitic resistors across the tactel to be measured, i.e. short-circuit the resistors $\mathbf{R_{w0}}$, $\mathbf{R_{x0}}$ and $\mathbf{R_{xj}}$ when $\mathbf{R_{wj}}$ is being measured, see Figure 2.28a. Three possible implementations for short-circuiting of the parasitic resistors were examined by Vidal-Verdu; each solution combines MUXes, amplifiers, and ADCs to provide a scalable framework for different sizes of sensor arrays. The solutions range from: Microcontroller-based electronics, solutions based on Programmable System on Chip (PSoC) and FPGA-based electronics.

The cube and arrow identifications of Figure 2.27 were implemented using PSoC electronics. A PSoC circuit includes a set of programmable analog blocks that can be arranged to short-circuit parasitic resistors when performing an AD conversion. Specifically, Castellanos arranged the PSoC chip model CY8C29466 under the configuration depicted on Figure 2.29. Three programmable buffers commute between two possible states: High Impedance (HZ) and Low Voltage (LOW); these buffers serve as the row decoder for the multiplexed sensor array.

When a buffer is set to LOW, current flows through it and all the resistors in the row are enabled. Hence, a conversion occurs in the ADC for the selected row. Meanwhile, the remainder buffers are set to HZ, and thus the current is unable to flow through them. Note from Figure 2.29, that one terminal of the resistors is tied to $\mathbf{V_{ref}}$ through the bias resistor $\mathbf{R_{bias}}$; this virtually short circuits all the resistors in the row and avoids the occurrence of parasitic paths.

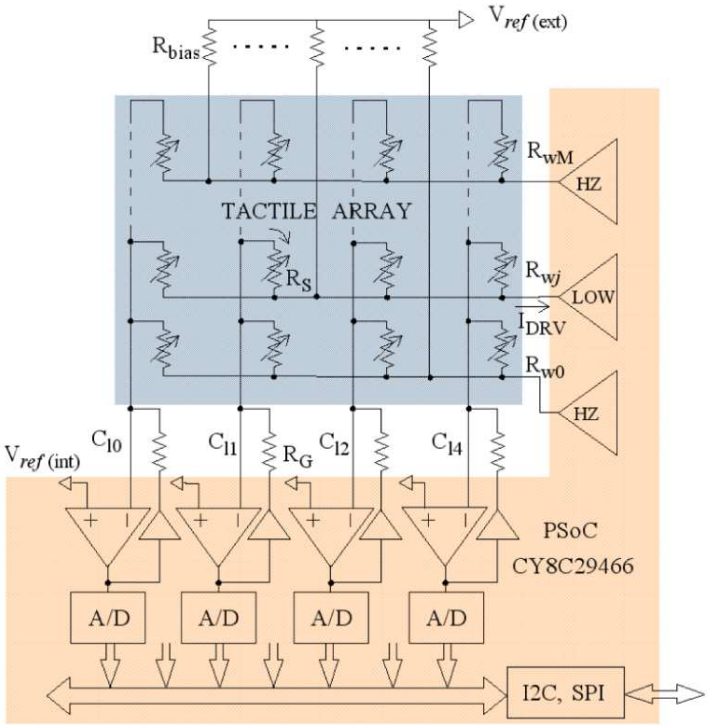

Figure 2.29: Image taken from [19] showing the schematics of a MUX-ADC circuit

The only way to enable a given row of resistors is to set a low voltage, LOW, on the buffer. This ties to ground all the resistors in the row, including the bias resistor $\mathbf{R_{bias}}$. The net result is a considerably great current I_{DRV} flowing through the buffer, so, it is required a careful dimensioning of the current driving capabilities of the buffer.

The advantages of the driver of Figure 2.29 are evident when looking at the abrupt transitions between zero and non-zero force zones in the force profiles of Figure 2.27b, Figure 2.27c, Figure 2.27e and Figure 2.27f. On the opposite side, the force profile of Figure 2.28b is rather smooth due to the parasitic paths.

Nonetheless, the improvements on the force profile generation are paid with an increase in the part count, the simple driver of Figure 2.28a has a part count of only 3 devices for reading 12 tactels, whereas the driver of Figure 2.29 requires 11 devices for reading the same amount of tactels. The increase in the part count is a rule of thumb when attempting to improve the performance of piezoresistive sensors; this is true not only for FSRs, but also for strain gauges [160, 113] and many other sensors. Chapter 3 examines some proposals of driving circuits for improving the performance of FSRs.

2.8.5 Piezocapacitive Sensor Arrays. A different technology with the same goal

Piezocapacitive technology has been used as an alternative approach towards the acquisition of force profiles. *Pressure Profile Systems, Inc (PPS)*, a Los Angeles-based company, has developed several custom design products to meet the specific requirements of multiple applications. Sensing solutions for: ergonomics, tire design and spray nozzle optimization are only few examples of applications that report the usage of the PPS piezocapacitive technology.

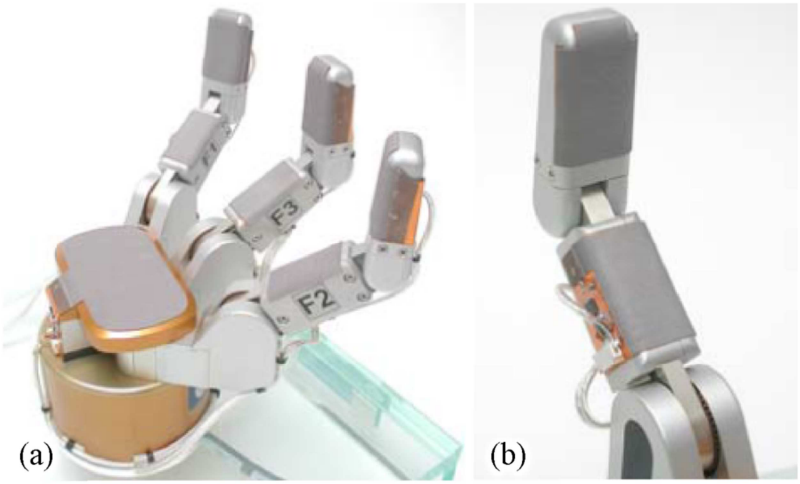

Figure 2.30: Pictures of the BarretHand with the PPS' tactile sensors. a) Picture of the 7 sensor arrays installed on the BarretHand palm side, 2 sensors are installed on each finger phalange plus 1 sensor on the palm. b) Zoom of the BarretHand and the PPS sensor around one finger

A PPS piezocapacitive sensor array was installed at the tip of a surgical probe to detect tumors during tissue exploration [159]. This realization was previously discussed in Section 2.5 and is only one of the several successful applications that have reported the usage of PPS sensing sheets.

One of the most fascinating frontiers in the piezocapacitive force sensing is the field of Robotics. PPS' RoboTouch Solutions have given some of the most advanced robots the human sense of touch. The BarrettHand, an anthropomorphic multi-fingered hand manufactured by Barrett Technology [7], has shown to be capable of stable object grasping and manipulation skills in structured environments. These abilities can be obtained by combining hand kinematic data with tactile feedback. For such a purpose, PPS has developed a tailored sensor array to fit on the palm side of the BarrettHand [144], see Figure 2.30.

Hao Dang developed a simulation software to assess the performance of the PPS RoboTouch under a huge variety of grasp postures and objects [40]. The results from Hao Dang simulation produced a valid strategy towards the classification of stable grasps from non-stables ones. The simulation results are of paramount importance during the approach stage of the BarretHand to the object.

A similar research was carried out by Khalil with the difference that real objects and devices were used [91]. The touch information from the PPS sensors was combined with joint encoders to produce a stable grasp in deformable objects. A neural network algorithm was chosen to combine the multisensory information under an off-line basis for training purposes, and then, during the real-time prediction when manipulating objects.

The Waseda University's Twendy-One [80, 158] and the Willow Garage's PR2 [153] are both robots designed to assist people in home and office tasks. PPS embedded tactile sensors in their hands/grippers so the robot could feel when an object is tightly held and also to allow the interfacing with brittle objects that require a careful handling. Figure 2.31 depicts the location of the PPS sensors on the Willow Garage's PR2.

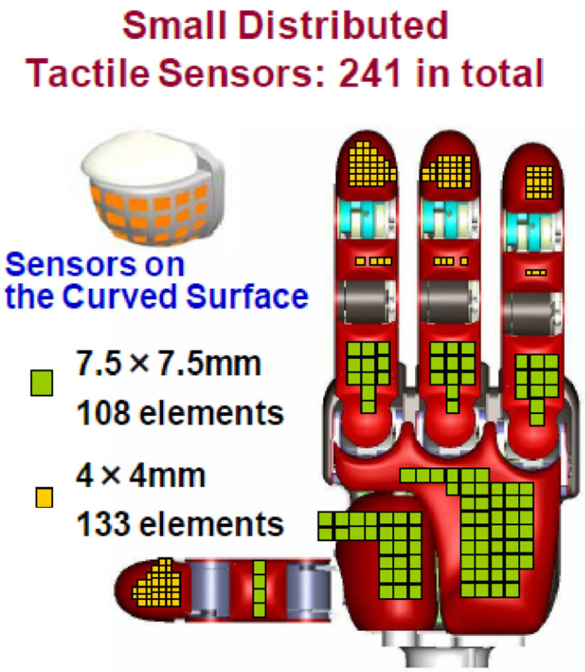

Figure 2.31: Sketch of the Willow Garage's PR2 hand showing the distribution of PPS tactile sensors

Despite piezocapacitive sensing technology is not the main focus of this thesis, it is important to remark that such technology is a valid approach towards the measurement of forces and towards the mapping of force profiles. It must be kept in mind that sensing solutions based on either piezocapacitive or piezoresistive principles are valid when attempting to gauge forces. The criteria for choosing between one of them may depend on multiple factors ranging from:

- Temperature: Certain applications may require high temperature tolerances. Tekscan developed a high temperature piezoresistive sensor and likewise did PPS. However, device performance may degrade as temperature rises and thereby, the designer must take into account the degradation of sensor performance. There is not information regarding which technology can better withstand temperature rises.
- Price: Both technologies offer a wide range of manufacturers and prices. Custom design solutions often yield higher costs, but OEM quantities often reduce production costs.
- Degree of customization: Some applications may require force sensing solutions that may not be manufactured. If the shape of the required sensing sheet is too irregular or too large, it may be impossible to manufacture such a device. Each technology offers different degrees of customization.
- Repeatability and performance: The repeatability and the overall performance of each technology may vary. There is not yet available a study that provides an in-depth comparison of both technologies.

2.9 Conclusion and resume

This Chapter presented an overview on the state of the art in force measuring techniques ranging from the metal strain gauges, load cells and the more recent introduction of piezoresistive and polymer-based technologies. Relevant concepts and basic definitions of each approach were introduced, as well as a review on representative implementations for each force sensing solution.

It was also discussed the different metrics to assess the performance of sensing solution. Such metrics can be applied in multiple circumstances, e.g., to compare the relative performance of load cells to the piezoresistive sensing techniques, but also, can be employed to compare the relative performance of one sensor to another. The metrics presented in this Chapter were: non-linearity error, hysteresis and measurement error. The measurement error is later used on Chapter 3 to assess the improvements generated by capacitance readings over piezoresistive sensors.

It was demonstrated that strain gauge systems, such as load cells, are remarkable force sensing solution in terms of reliability and accuracy, but this outstanding performance is paid by a rather bulky device.

On the opposite side, piezoresistive sensing technology can offer easier integration to already existing systems due to its relative low profile and customizability that avoids system redesigning. Promising applications have been also identified for the piezoresistive sensing technology within the fields of robotic skins, orthopedics and haptics. Besides, piezoresistive sensing solutions are cheaper than load cells and to silicon strain gauges. However, these advantages are paid by a relative poor performance that avoids the extensive usage of such devices in industrial and research applications limiting its use to applications that strictly require non-invasive force measuring.

In order to allow a massive usage of piezoresistive sensors, it was set as one of the objectives of this thesis, the performance improvement of the piezoresistive sensors in terms of the metrics described in this Chapter.

Chapter 3

3. Derivation of an empirical model for Piezoresistors. A step towards the improvement of sensors performance

Previous Chapter went through the basis of piezoresistors with special focus on two topics: examine the physics foundations of piezoresistivity, and, describe some representative applications involving piezoresistors. However, two questions were left hanging in the air: *is it possible to improve the performance of such devices? And if possible, what strategy should be taken?* This Chapter addresses both issues by presenting a detailed sensor model based on empirical data. The derived model is then used to improve the sensor's performance through a multivariable estimation of the applied force.

The available improvements on the FSR's performance are not limited to enhance the sensor metrics from Section 2.2, e.g. non-linearity, hysteresis and non-repeatability error. Additionally, a new property was found in the sensor. This property comprised that sensor's capacitance and resistance are both functions of the area where the force is being applied and the force itself. So, if the relationship among all the aforesaid parameters is obtained, then it is possible from capacitance and conductance readings to estimate the applied force, and the exertion area of such a force.

It must be recalled from Section 2.7.6.1 that the manufacturers of FSR do not specify the typical sensitivity of his products, this is, the output response of the sensor in terms of V*olts per Kilogram-Force* is not given, and consequently, the final user must perform a sensor characterization before using it. One of the focuses of this Chapter is to provide a method capable of predicting sensor sensitivity under any driving condition; such a method is addressed in Section 3.2.3.

In this chapter, it is also presented the testbench employed during the experimental data gathering, followed by the derivation of the sensor model. Further sections in this chapter examine how such a model can be used to improve sensor's performance in terms of the sensor metrics.

All of the tests and models derived in this chapter were done over the FlexiForce A201-100 sensor and reported previously in [128, 129, 132, 134].

3.1 Testbench and Procedure to collect the experimental data on the FlexiForce A201-100 sensor.

The testbench used in the characterization of the FlexiForce A201-100 sensor was custom designed to handle up to 8 sensors simultaneously. This was possible by means of an interleaved configuration with pucks between adjacent sensors, see Figure 3.1. The puck's weight was negligible due to the low density of the material used. This was important because it is mandatory to load every sensor with the same force.

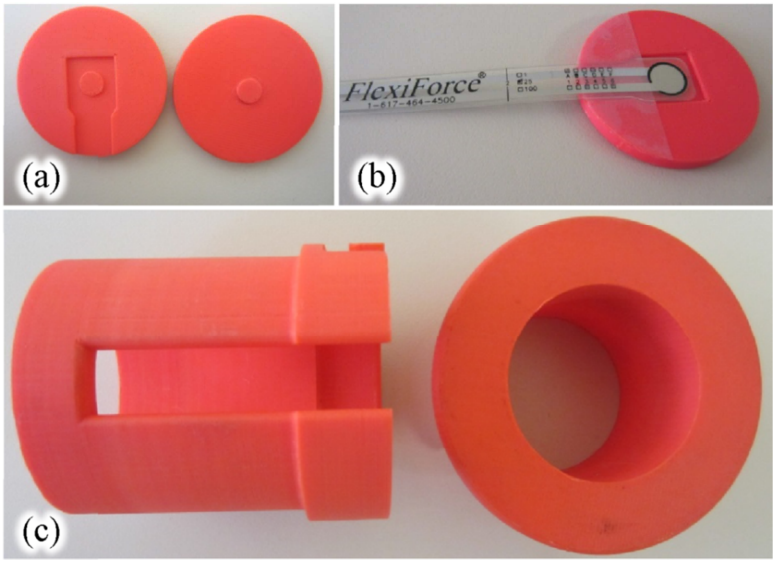

Figure 3.1: Pucks and puck holder for sensor arrangement. (a) Top and low views of sensors' pucks with tailored notch to allow sensor placement. (b) Puck with a bonded force sensor ready to be mounted on puck holder. (c) Unassembled puck holder to be mounted on the frame support

Recalling the concepts of piezoresistors introduced in Sections 2.7.1 through 2.7.5 and the limitations discussed in Section 2.7.6, the design of a testbench must be carried out with special attention, because the experimental data are the only source for sensor modeling and further model validation. Current progress in the development of FSRs is limited to the manufacturing and testing of new materials with little or null information regarding the sensor's theoretical model. This fact adds more importance to the appropriate designing of sensor testbenches, because the experimental tests are the only method to assess the capabilities and limitations of a given FSR.

The procedure for collecting the data was simple and repetitive. Each puck was loaded with a sensor, as in Figure 3.1b and Figure 3.2b. The puck's holder (see Figure 3.1c) was then assembled with all the pucks therein, see Figure 3.2a. Finally, the puck's holder was mounted on the metal frame and loaded with the weights, as in Figure 3.2e.

The forces were generated by placing calibrated weights on top of the pack of sensors, see Figure 3.2e. A metal bar, conveniently located in the middle of the testbench, was used to hold the weights during the tests, see Figure 3.2c and Figure 3.2d. The testbench could apply a maximum force of **250 N**. This force is located within the nominal range of the FlexiForce A201-100 sensor of **450 N**. The force step along the experiments was of **5 N** and the puck area (**51.1 mm^2**) was the same for all pucks.

Every time a different force was applied, the output voltage of each sensor was independently measured; this was true for the tests of Section 3.2.1 through Section 3.2.4 that employed DC sourcing.

Given the output voltage of each sensor for all the applied forces, the sensor characterization was resumed with a least-squares-root fit of the experimental data. The result was the sensor sensitivity, m, and the y-intercept, b. This type of characterization is the typical recommended by the manufacturer, but in the upcoming sections, additional data were taken from the sensor with the aim of improving its performance.

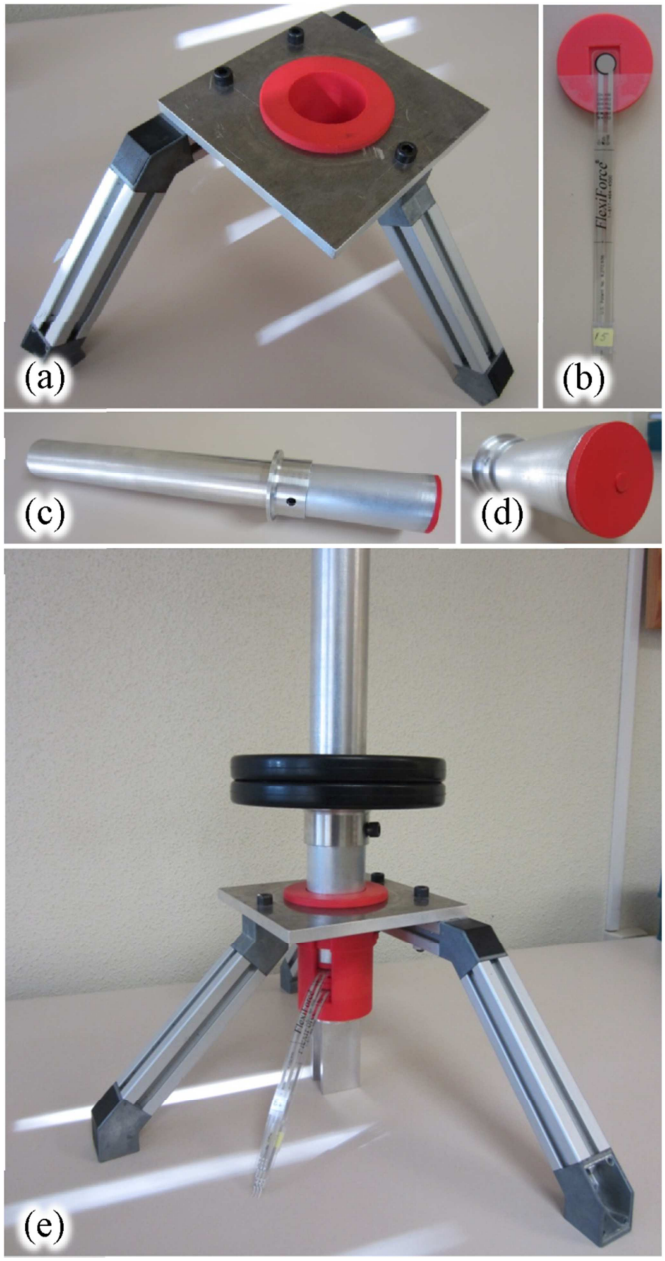

Figure 3.2: Assembly of test bench parts. (a) Metal frame with puck holder. (b) Puck with a bonded force sensor, ready to be installed on the puck holder. (c) Metal bar to allow weight holding. (d) Zoom of metal bar around front end puck. (e) Final assembly of test bench with a couple of **1.25 Kg** weights on top

For the tests involving AC sourcing a more complex measuring scheme was used, because different algorithms for relating conductance and capacitance were tested. The results of such tests are later addressed in Sections 3.2.5, 3.2.6 and 3.3. However, the process for gathering data under AC sourcing remained basically unchanged and can be resumed as follows:

Gradually increase the applied force in steps of 5N and simultaneously collect sensor data. Then, a fit must take place to relate the experimental data to the proposed model. This error-trial method is usually followed by a validation stage in which the proposed model is tested with a new set of applied forces.

The testbench depicted in Figure 3.1 and Figure 3.2 was used in the tests of Section 3.2 and Section 3.3, whereas a different puck configuration was used for the experiments of

Section 3.4. In order to study the effects of variable puck areas over sensor's conductance and resistance, it was built a set of increasing-size pucks which are carefully described on Section 3.4.

3.2 Derivation of an empirical model for the FlexiForce A201-100 under DC and AC sourcing

The derivation of a valid model for the sensor FlexiForce A201-100 was carried out following two criteria. The type of sourcing, DC or AC, and the magnitude of the driving voltage. Sections 3.2.1 through 3.2.4 deal with sensor modeling under DC sourcing, whereas Sections 3.2.5 and 3.2.6 present a derivation of sensor model under AC sourcing.

Different sensor responses have been found depending on the magnitude of the applied voltage, and thus, the derivation of a detailed sensor model must comprise the identification of sensor nonlinearities in two voltage ranges: input voltages under **1 V**, and input voltages over **1 V**. This voltage-dependent behavior is typically found on semiconductor devices just as Bipolar Junction Transistors (BJTs) and diodes.

It is next presented an in-depth derivation of the sensor model for input voltages below **1 V**, and then, it is briefly described in Section 3.2.4 the more complex nonlinearity occurring when the input voltage exceeds **1 V**.

3.2.1 Identification of amplitude non-linearity in the piezoresistor model FlexiForce A201-100 under DC sourcing below 1 V

Typically, the set-up used to drive a piezoresistor comprises an inverting operational amplifier with a DC source (switch at the $\mathbf{V_{s1}}$ position in Figure 3.3). When an external force is applied over the device, the resistance varies under a hyperbolical basis and the inverting function in the OPAMP produces a linear response in the output voltage, see Figure 3.4.

This response corresponds to the piezoresistive property of the sensor and it has been thoroughly described by the sensor manufacturer [76] and by many research articles [5, 48, 90, 102, 110, 134]. However, based on a state-of-the-art review, there is no information available about how the output voltage changes for a fixed force when the DC voltage is varied.

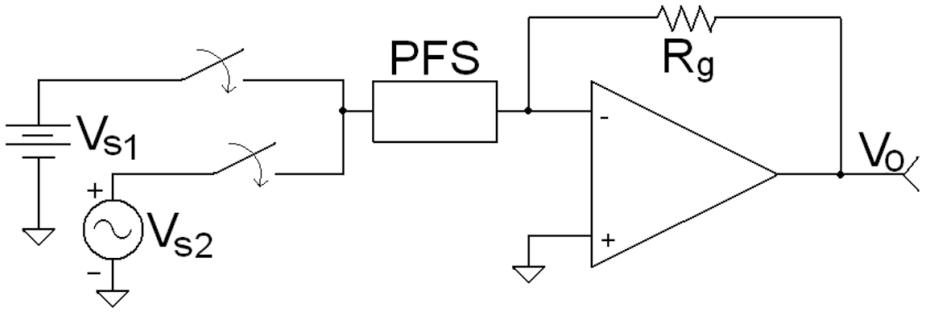

Figure 3.3: Typical sensor driver for a piezoresistor

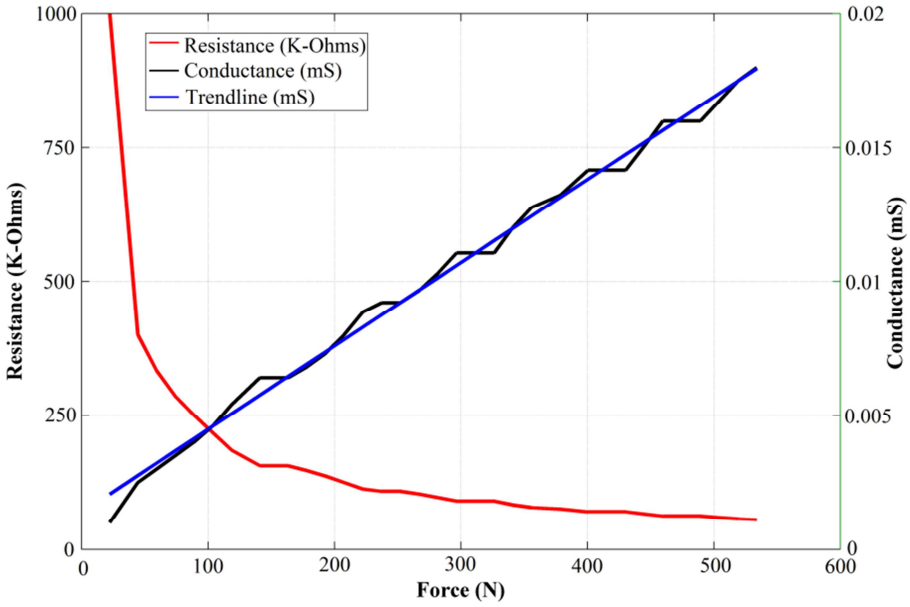

Figure 3.4: Typical variation of resistance and conductance for an A201-100 FlexiForce Sensor, image taken from [76]. The image axis and legend were modified for better comprehension

In order to study such a behavior, the input voltage, $\mathbf{V_{s1}}$, is swept from **-1 V** up to **1 V**, and the output voltage, $\mathbf{V_o}$, is plotted while the applied force remains constant. Figure 3.5 shows the output voltage for randomly chosen forces of **12 N**, **45 N**, **82 N** and **160 N**. The best function for relating the input voltage, $\mathbf{V_{s1}}$, to the corresponding sensor response, $\mathbf{V_o}$, is found to be:

$$Vo = -\frac{1}{q}\operatorname{atanh}\left(\frac{V_{s1}}{k}\right) \qquad \textbf{(3.1)}$$

where **k** and **q** are constants. However, it is inadvisable to fit **k** and **q** in the form presented in equation **(3.1)**, because complex values are yielded in $\mathbf{V_o}$, since the atanh domain is restricted to **(-1, 1)**. Thus, it is better for fitting purposes to rewrite equation **(3.1)** in terms of the tanh function as follows:

$$V_{s1} = k\tanh(-qV_o) \qquad \textbf{(3.2)}$$

The minus sign in equations **(3.1)** and **(3.2)** comes from the negative gain in the inverting amplifier used to drive the sensor, see Figure 3.3. The axes in Figure 3.5 are intentionally switched to represent $\mathbf{V_o}$ on the x-axis and $\mathbf{V_{s1}}$ on the y-axis with the aim of fitting the data points with equation **(3.2)** instead of equation **(3.1)**. The fitting process is highly confident, with a coefficient of determination, $\mathbf{R^2}$, of at least $\mathbf{R^2}$**=0.9992** for every applied force and an average value of $\mathbf{R^2}$**=0.9995**.

Parameters **k** and **q** were set to adjust independently for every applied force; however, the independent fitting processes returned values of **k** that remained almost constant regardless of the exerted force, **F**, whereas q was shown to be hyperbolically dependent on the exerted force. In other words, **1/q** is a linear function of **F**. Figure 3.6 shows the variation of **k** and **1/q** for different applied forces within the **0 N-250 N** range resulting from independent fitting processes.

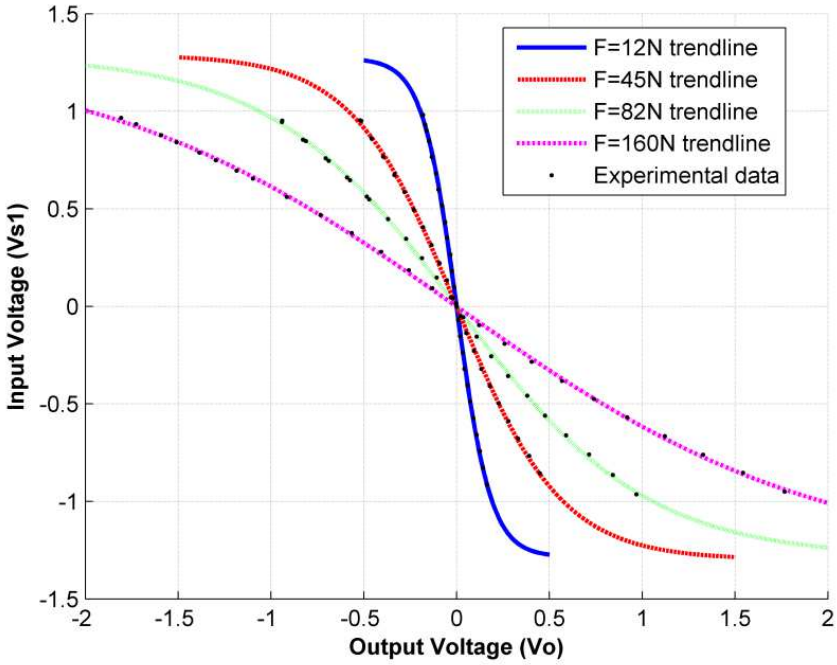

Figure 3.5: $\mathbf{V_{s1}}$ vs. $\mathbf{V_o}$ for the PFS for driving voltages below **1 V** and four different exerted forces of **12 N**, **45 N**, **82 N** and **160 N**. The trendline used for each individual fit was a hyperbolic tangent function equation **(3.2)**

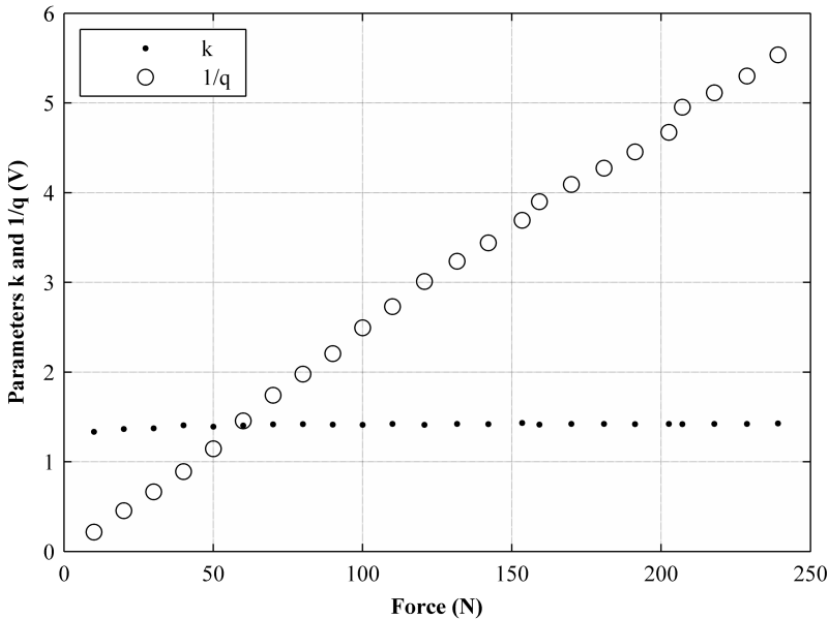

Figure 3.6: Graph representing the variation of sensor parameters k and q for different exerted forces within the range from **0 N** to **250 N**

In order to get a comprehensive view of sensor behavior, a relationship must be found between equation **(3.2)** and **F**. For that purpose, the fact that the sensor exhibits piezoresistive behavior is useful, as thus its conductance, $\mathbf{1/R_s}$, may be modeled in terms of the applied force, **F**, as:

$$1/R_s = mF + b \qquad \textbf{(3.3)}$$

Equation **(3.3)** is not explicitly stated in the PFS user manual [76]; however, the sensor manufacturer does declare that a linear interpolation between the conductance values and the applied forces can be done. Also, it can be easily deduced from a look at the conductance curve in Figure 3.4 that equation **(3.3)** is a valid fit for $\mathbf{1/R_s}$. Considering the inverting amplifier with feedback resistor $\mathbf{R_g}$, which is used to drive the PFS, it is possible to link equation **(3.3)** with the amplifier characteristic equation:

$$\frac{V_o}{V_{s1}} = -\frac{R_g}{R_s} \tag{3.4}$$

to obtain:

$$\frac{V_o}{V_{s1}} = -R_g(mF + b) \tag{3.5}$$

It is best to clarify that equation **(3.5)** is not explicitly stated in the PFS user manual [24]. Only equation **(3.4)** is stated in [24], but the manufacturer suggests that sensor sensitivity, **m**, can be changed by either replacing the feedback resistor, $\mathbf{R_g}$, or by changing the driving voltage, $\mathbf{V_{s1}}$.

With the aim of demonstrating that equation **(3.5)** is an approximate expression for fitting the data points of Figure 3.5, the **1/q** curve from Figure 3.6 is taken and represented as linearly dependent on the applied force.

$$1/q = m'F + b' \tag{3.6}$$

Note that the **1/q** curve in Figure 3.6 is analogous to the conductance curve of Figure 3.4. Equation **(3.6)** can be substituted into equation **(3.1)**, yielding:

$$V_o = -(m'F + b')\text{atanh}\left(\frac{V_{s1}}{k}\right) \tag{3.7}$$

Nevertheless, equation **(3.7)** cannot be stated the same way as equation **(3.5)**, because the input voltage, $\mathbf{V_{s1}}$, is part of the atanh argument. But if only the first term of the atanh-Taylor series is taken, the following approximate expression is yielded:

$$\frac{V_o}{V_{s1}} = -\frac{1}{k}(m'F + b') \tag{3.8}$$

Equation **(3.8)** *is an approximate expression for modeling sensor response, and so is equation* **(3.5)**. The **1/k** factor in equation **(3.8)** is analogous to $\mathbf{R_g}$ in equation **(3.5)**, in the same way that **m** is analogous to **m'**, **b** to **b'** and $\mathbf{1/R_s}$ to **1/q**. Equations **(3.5)** and **(3.8)** are valid if and only if the input voltage remains constant during the measurement process; this condition matches for the driving conditions recommended by the manufacturer [24].

3.2.2 Effect of Feedback Resistor in Sensor Response

The effect of the feedback resistor can be deduced from the fact that $\mathbf{R_g}$ changes only the feedback gain of the amplifier, without affecting sensor current. Thus, changing $\mathbf{R_g}$

will produce directly proportional changes in the output voltage, and thus, equation **(3.7)** can be rewritten as:

$$V_o = -\left(\frac{R_g}{R_{ref}}\right)(m'F + b')\text{atanh}\left(\frac{V_{s1}}{k}\right) \quad \textbf{(3.9)}$$

Henceforth equation **(3.9)** is referred to as *the general-sensor model*, with the restriction $\mathbf{|V_{s1}| < 1\ V}$, where $\mathbf{R_{ref}}$ is the feedback resistor used during the characterization to obtain the values of **m'**, **b'** and **k**. In case the feedback resistor is changed after the characterization process, the output voltage is multiplied by the ratio $\mathbf{R_g/R_{ref}}$ where $\mathbf{R_g}$ is the new feedback resistor. *Replacing the feedback resistor produces a directly proportional change in the output voltage, because the amplifier is inherently linear, whereas sensor resistance is not*. In fact, linking equations **(3.1)**, **(3.4)** and **(3.6)** produces an expression that *shows the nonlinear behavior of sensor conductance* in response to changes in the input voltage.

$$\frac{1}{R_s} = (m'F + b')\frac{\text{atanh}(V_{s1}/k)}{V_{s1}R_g} \quad \textbf{(3.10)}$$

However, note from equation **(3.10)** that sensor conductance is always linear to force changes.

3.2.3 Generalized Method for Obtaining a Specific Sensitivity in Sensor Response for DC sourcing below 1 V

Since a general-sensor model was deduced in equation **(3.9)**, a generalized method can be presented for obtaining a specific sensitivity in the sensor. The tests discussed in this section were done using four A201-100 sensors to provide more-representative results.

3.2.3.1 Derivation of the Method for obtaining specific sensor sensitivity.

Each PFS exhibits a considerably different sensitivity. This condition prevents the sensor from having plug-and-play capability, because a characterization must be run before sensor use. Moreover, for characterizations run at a given input voltage, it has been impossible until now to determine the new values of m and b under a new input voltage condition, because the amplitude nonlinearity was not accounted for. Nevertheless, equation **(3.9)** accounts for changes in both the input voltage, $\mathbf{V_{s1}}$, and the feedback resistor, $\mathbf{R_g}$. This implies that if **m'**, **b'**, **k**, and $\mathbf{R_{ref}}$ are given, it is possible to either determine sensor sensitivity for any input voltage and feedback resistor or design a specific driving circuit ,$\mathbf{V_{s1}}$ and $\mathbf{R_g}$, with the aim of matching a target sensitivity.

Note that the **k** *factor in equation* **(3.9)** *contains information about sensor sensitivity for any input voltage.* Unfortunately, the **k** factor is different for each sensor, just as sensitivity is too. The range of variation of the **k** factor for the four sensors under study was from **1.2 V** to **1.5 V**, with an average value of **1.41 V**. If **k** is not given, the only way to change sensor sensitivity is to replace the feedback resistor, $\mathbf{R_g}$; but, in certain applications where several sensors are being used [20, 37, 129, 147], it is more convenient to change the driving voltage instead of changing individual feedback

resistors. In addition, the feedback resistor is increased despite an increase in the noise level, so it is better to match a desired sensitivity by making a trade-off between $\mathbf{V_{s1}}$ and $\mathbf{R_g}$.

With the aim of proposing a method for obtaining a specific PFS sensitivity, it is necessary to fit the general-sensor model in equation **(3.9)** to the experimental data. However, the feedback resistor must not play any role in the fitting process, because $\mathbf{R_g}$ only affects the closed loop gain of the amplifier, not the sensor response itself. Thus, it is better to use equation **(3.7)** for the fit instead of Equation **(3.9)**. In order to avoid complex numbers resulting from equation **(3.7)** during the fit, equation **(3.7)** is rewritten in terms of the tanh function as shown below:

$$V_{s1} = -k \tanh\left(\frac{Vo}{m'F + b'}\right) \qquad \textbf{(3.11)}$$

Note that equation **(3.11)** implies a three-dimensional fit in terms of the variables **F**, $\mathbf{V_o}$ and $\mathbf{V_{s1}}$, with coefficients **m'**, **b'** and **k** to be determined.

In practice, the experimental data were gathered in the same way as described in Section 3.2.1. Nevertheless, the fit herein described embraces all variables and coefficients at once (**F**, **Vo**, $\mathbf{V_{s1}}$, **m'**, **b'** and **k**), whereas the fitting process in Section 3.2.1 was split into two independent threads. This is an important difference, because the current fit tries to minimize the overall error, while the process in Section 3.2.1 independently minimizes the error for every exerted force.

Figure 3.7 shows the experimental data points and the surface produced by the three-dimensional fit in equation **(3.11)**. For this case, the values of $\mathbf{R^2}$ were in general lower than for the fits given in section 3.2.1. The minimum value of $\mathbf{R^2}$ for the four sensors under study was $\mathbf{R^2=0.989}$, with an average value of $\mathbf{R^2=0.991}$; this is comprehensible, because all forces and voltages were embraced in a single fit, and thus a single k value was returned.

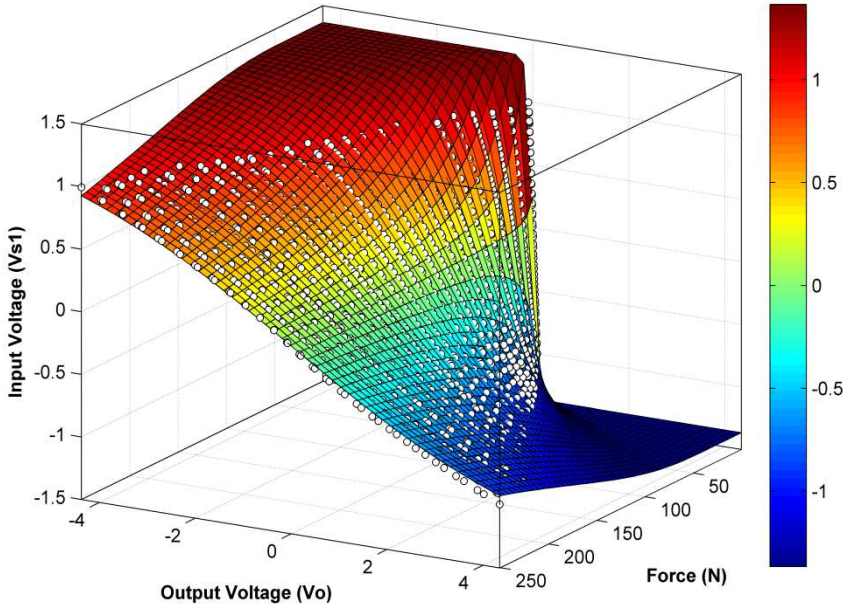

Figure 3.7: Surface resulting from the three dimensional fit of the PFS-general model to the experimental data points shown as empty circles in the plot

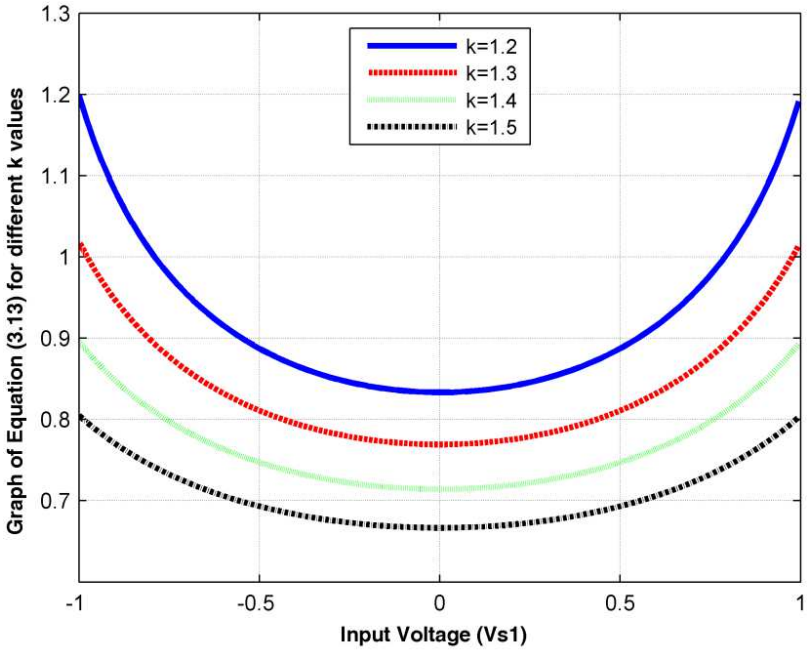

Figure 3.8: Graph of the equation **(3.13)** for different **k** values. Note that as **k** increases the lines flatten

Once the fit is done, it is possible to assemble the general-sensor equation by substituting into equation **(3.9)** the coefficient values returned from the fit (**m'**, **b'** and **k**) and the value of the feedback resistor used during the characterization process, which matches $\mathbf{R_{ref}}$ in equation **(3.9)**. If $\mathbf{R_g}$ or $\mathbf{V_{s1}}$ are changed at any time, it is possible to recalculate m and b from equation **(3.9)**; or, if the feedback resistor, $\mathbf{R_g}$, is fixed by the application circuit, the target sensitivity, $\mathbf{m_t}$, can be obtained by choosing the appropriate $\mathbf{V_{s1}}$ from equation **(3.9)** as shown below:

$$V_{s1} = k \tanh\left(\frac{m_t}{m'}\frac{R_{ref}}{R_g}\right) \qquad \textbf{(3.12)}$$

However, equation **(3.12)** is valid if and only if the predicted input voltage is lower than **1 V**, because only the amplitude nonlinearity for $\mathbf{|V_{s1}| < 1\ V}$ has been studied.

Note that the **k** factor may be taken as a mean of amplitude nonlinearity. To confirm this, Figure 3.8 plots the following function, which is drawn from the sensor-conductance expression, see equation **(3.10)**:

$$f(V_{s1}) = \frac{\operatorname{atanh}(V_{s1}/k)}{V_{s1}R_g} \qquad \textbf{(3.13)}$$

Equation **(3.13)** is a mean of how the sensor conductance is affected by changes in the input voltage. The higher **k** is for a given sensor, the lines flatten in Figure 3.8. This can be understood as a *less-noticeable amplitude nonlinearity* in the sensor.

3.2.3.2 Testing the accuracy of the proposed method.

In order to test the accuracy of the method presented in Section 3.2.3.1, the following tests were carried over four piezoresistive devices.

Forces were applied within the range of **0 N** to **250 N** under seven sourcing conditions, starting at **0.4 V**, with increments of **0.1 V**, up to **1 V**. For every supply voltage, the sensor sensitivity, **m**, and the y-intercept, **b**, were found according to the classical method proposed by the manufacturer [76]. These values of m and b are assumed as references for calculating subsequent errors in them under the different methods studied.

Sensors were then characterized in terms of **m'**, **b'** and **k** as described in Section 3.2.3.1 Doing so enabled equation **(3.9)** to be assembled and **m**, **b** to be estimated for the aforementioned DC voltages.

With the aim of demonstrating the typical error resulting from the assumption of linear-sensor response, the values of **m**, **b** measured at **1 V** and equation **(3.5)** were used to estimate m, b for the remaining six voltages (**0.4 V to 0.9 V**). That is, if the m value measured at **1 V** is **20 mV/N**, use of equation **(3.5)** shows that the estimated value of **m** at **0.4 V** is equal to **8 mV/N**; the same calculation applies to the y-intercept coefficient, **b**.

Table 3.1: Comparison table of the average errors resulting from the estimation of **m**, **b** by means of a linear equation **(3.5)** and a nonlinear equation **(3.9)** under input voltages within the range **(0.4 V, 0.9 V)**

Sensor number	**1**	**2**	**3**	**4**	**Average error for all sensors**
Average error (%) in **m** resulting from equation **(3.9)**	2.79	1.07	2.67	1.62	2.04
Average error (%) in **m** resulting from equation **(3.5)**	10.3	10.3	10.8	14	11.35
Average error (%) in **b** resulting from equation **(3.9)**	9.46	12.5	10.9	8.2	10.27
Average error (%) in **b** resulting from equation **(3.5)**	13.5	20.3	13.3	10.9	14.5

Two facts may be drawn from Table 3.1. First, the errors in the m values predicted by equation **(3.9)** are rather small for all sensors. This means that the nonlinear model presented in Section 3.2.1 produces matches in predicting the sensor sensitivity for any input voltage under **1 V**. In fact, the average error in m for all sensors and all voltages is only **2.04%**. Second, the assumption of linear response in sensor conductance produces a reasonably greater error when predicting m via equation **(3.5)**; an average error of **11.35%** was obtained, which almost six times the error resulting from equation **(3.9)**. Figure 3.9 shows the values of m for sensor number four, under all the discrete applied voltages. Also shown are the trendlines arising from the linear equation **(3.5)** and the nonlinear model, equation **(3.9)**.

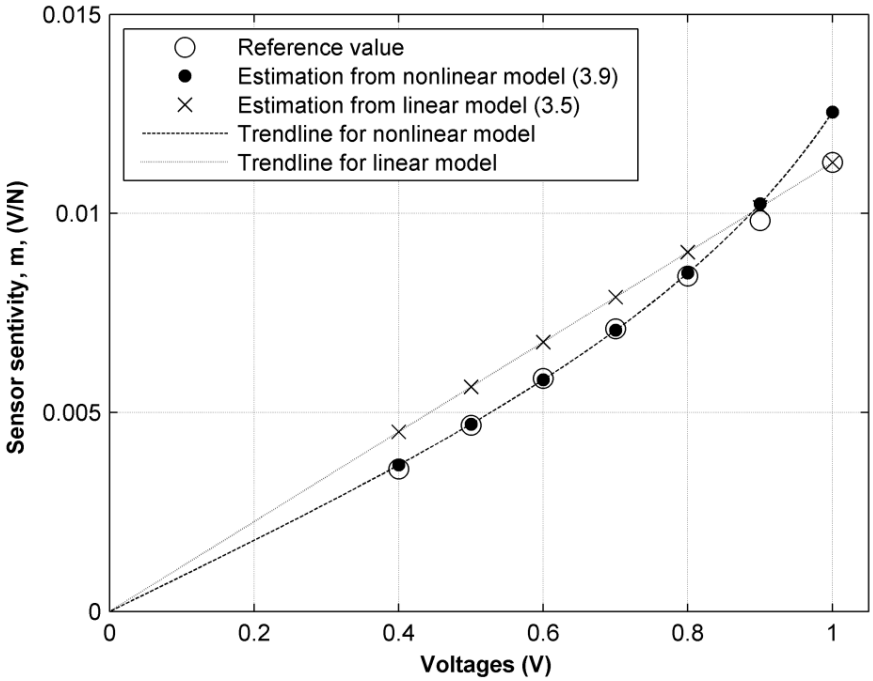

Figure 3.9: Sensor Sensitivity, m, for different input voltages. The prediction from the linear equation **(3.5)** and the nonlinear Equation **(3.9)** models are compared to the reference sensitivity measured at different input voltages

Second, the average error for all sensors resulting from the estimation of the y-intercept coefficient, **b**, was quite high, **10.27%** and **14.5%** for the two models. Despite this fact, *it is declared that equation* **(3.9)** *can effectively model sensor behavior*, because throughout the various optimization processes is has been effectively reduced the estimation error of **b** by discarding the highly noisy data obtained under forces lower than **40 N**. Such data are noisy because of the low amplitude of $\mathbf{V_o}$, resulting from the low-force condition. If the data taken under forces lower than **40 N** are discarded, the average error for the y-intercept estimation is reduced to **6.35%**.

3.2.4 An Approach to Modeling the Amplitude Nonlinearity for DC Input Voltages over 1 V

If the PFS is sourced with voltages above **1 V**, the fitting curve in equation **(3.2)** and the general-sensor model in equation **(3.9)** provide an unsatisfactory fit. Figure 3.10 shows the output and input voltage from data taken under three different forces of **47 N**, **97 N** and **240 N** for driving voltages within the range **(-6 V, 6 V)** with equation **(3.2)** as the trendline. Note that the experimental data points move away from the trendline, especially in the middle-range voltages, $\mathbf{|V_{s1}| < 3\ V}$.

Despite the fact that the coefficient of determination remained high for all sensors under study (exhibiting an average value of $\mathbf{R^2=0.991}$), it is clear that equation **(3.2)** and **(3.9)** require some changes in order to provide a better fit. So far it has not been found a suitable, yet simple, curve for modeling sensor behavior under such driving condition.

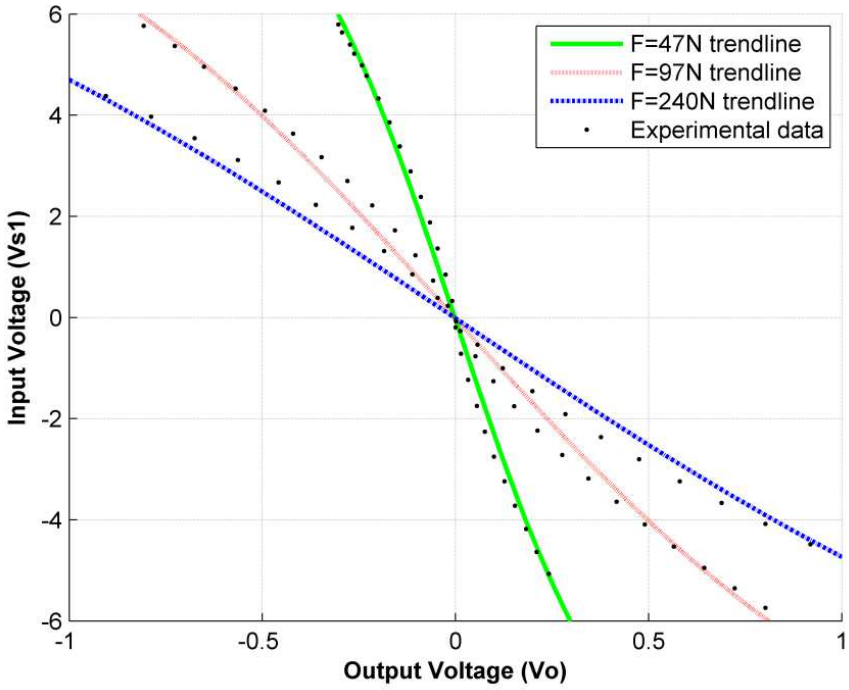

Figure 3.10: Graph representing the relation of $\mathbf{V_{s1}}$ vs. $\mathbf{V_o}$ for input amplitudes within the range **(-6 V, 6 V)** and forces of **47 N**, **97 N** and **240 N**

The derivation of a valid sensor model for DC sourcing over **1 V** is one of the pending tasks of this thesis listed on the future works of this thesis, see Chapter 6. However, a method to bypass the amplitude nonlinearity in the FlexiForce A201-100 is introduced in Section 3.3.3. Bypassing the amplitude nonlinearity is a mandatory task when attempting to read sensor's capacitance.

3.2.5 Identification of sensor model under AC sourcing

In order to obtain a RLC model for the FlexiForce A201-100, it is necessary to apply different type of signals to the sensor and observe the output response of the device, and then compare the sensor output with typical responses of RLC circuits. For such a purpose both signals from the driving circuit of Figure 3.3 were alternatively applied to the sensor under different applied force. The electrical signals can be written as follows:

$$V_{s1} = -5V \tag{3.14}$$

$$V_{s2} = A_s \sin(2\pi ft) \tag{3.15}$$

where **f** and $\mathbf{A_s}$ are the signal frequency and amplitude respectively in the sine wave of equation **(3.15)**. The transfer function of the inverting amplifier of Figure 3.3 is given by the following

$$V_o = -(R_g / Z_{FSR})V_s \tag{3.16}$$

where $\mathbf{Z_{FSR}}$ is the impedance of the FlexiForce sensor and $\mathbf{R_g}$ is a pure resistor used for controlling the amplifier gain.

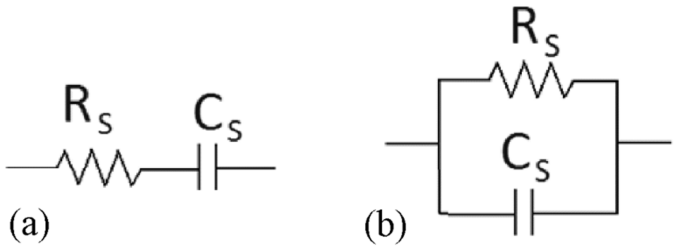

Figure 3.11: Possible electrical models of the FlexiForce sensor. (a) RC series model (b) RC parallel model

When signal $\mathbf{V_{s2}}$ from equation **(3.15)** was selected as the driving signal at low frequencies, a phase shift of **-180º** was observed at the output voltage, **Vo** in Figure 3.3. As the frequency was increased up to a few hundred Kilohertz, the phase shift decreased to a minimum of **-90º**. Considering the minus sign in the amplifier transfer function, see equation **(3.16)**, which caused a **-180º** phase shift, the phase shift due to $\mathbf{Z_{FSR}}$ is consequently of **90º**. This essential clue allowed us to formulate a first order resistor-capacitor (RC) model for the FlexiForce sensors. An electrical model including inductance is not possible since the phase shift introduced by the FlexiForce sensor is always positive. Note that the sensor's capacitance introduces a zero into the system, thereby causing positive phase shifts.

There are two possible variants for a first order RC circuit: RC series or RC parallel, see Figure 3.11. It is simple to discard the RC series as the sensor model by applying $\mathbf{V_{s1}}$, see equation **(3.14)**, as the input signal to the circuit of Figure 3.3. An RC series model would not allow Direct Current to flow through the sensor because of the capacitor effect, $\mathbf{C_s}$, and $\mathbf{V_o}$ would therefore be zero. However, an output voltage was observed experimentally, so the premise of an RC series model was incorrect. *Finally, the appropriate electrical model for the FlexiForce A201-100 is that of a RC parallel circuit with sensor's resistance,* $\mathbf{R_s}$*, and sensor's capacitance,* $\mathbf{C_s}$*, see Figure 3.11b.*

Next section presents a set of validation tests to demonstrate that the RC parallel proposal is a valid model for the sensor under study. Furthermore, it is presented the limitation of such a model to predict sensor behavior under certain operating conditions.

3.2.6 Validation of the RC parallel model for the FlexiForce A201-100.

If the RC parallel model is assumed as valid and the sinusoidal input $\mathbf{V_{s2}}$ is chosen, see equation **(3.15)**, a linear equation may be written to model the behavior of the sensor-OPAMP system from Figure 3.3:

$$\frac{V_{s2}}{R_s} + Cs\frac{dV_{s2}}{dt} = -\frac{V_o}{R_g} \qquad \textbf{(3.17)}$$

Solving equation **(3.17)** for sinusoidal input $\mathbf{V_{s2}}$ gives us the following expression of $\mathbf{V_o}$:

$$V_o = -A_s R_g\left(\frac{\sin(2\pi ft)}{R_s} + 2\pi fC_s\cos(2\pi ft)\right) \qquad \textbf{(3.18)}$$

Equation **(3.18)** may be written as a sine function with output amplitude $\mathbf{A_o}$ and phase shift ϕ as shown next:

$$V_o = A_o \sin(2\pi ft + \phi) \quad \textbf{(3.19)}$$

Linking equations **(3.18)** and **(3.19)** give us a sensor's capacitance expression which will be used later for estimating applied forces to the sensor. An expression for sensor's resistance can also be found.

$$C_s = \frac{A_o \sin(\phi)}{R_g A_s 2\pi f} \quad \textbf{(3.20)}$$

$$R_s = \frac{R_g A_s}{A_o \cos(\phi)} \quad \textbf{(3.21)}$$

A theoretical variation of the phase shift can be found by linking equations **(3.20)** and **(3.21)**, which yields:

$$\phi = \arctan(2\pi f C_s R_s) \quad \textbf{(3.22)}$$

In order to validate the RC parallel electrical model, it was chosen the AC source $\mathbf{V_{s2}}$ as the input of the driving circuit of Figure 3.3. It was varied the input frequency f from **100 Hz** to **40 KHz**, which matches the highest frequency the amplifier can deal with negligible phase shift. It is important to keep the phase shift introduced by the amplifier to at least as possible; otherwise, such phase shifts will add to those introduced by sensor's capacitance, leading to inaccurate results.

On the other hand, it is necessary to choose a small enough input amplitude, $\mathbf{A_s}$, for the AC source $\mathbf{V_{s2}}$ that does not saturate the amplifier output voltage as frequency increases. Notice that equation **(3.18)** states that as frequency increase the same will do the output amplitude. Although, if input amplitude is too small phase readings will be subject to noise and data will be scattered.

It must be kept in mind that sensor resistance $\mathbf{R_s}$ is far from being linear to changes in the driving voltage. This was previously discussed in Sections 3.2.1 through 3.2.4. However, if the driving signal is small enough, the approximation of constant resistance can be taken as valid. This can be ascertained by looking the plot of Figure 3.5 when the input voltage was below **0.5 V**. In such region, the tanh function can be approximated to a line and thus sensor resistance can be taken as constant. So, the driving conditions in the validation test were set to $\mathbf{A_s = 0.5\ V}$ and the frequency swept from **100 Hz** to **40 KHz**.

Figure 3.12 is a phase bode plot of one FlexiForce sensor for three different forces of **50 N**, **125 N** and **250 N**. Experimental data, shown with markers, are superposed over the theoretical curve that was obtained using equation **(3.22)**. Sensor's Resistance, $\mathbf{R_s}$, and Capacitance, **Cs**, were estimated at **2.5 KHz** and then substituted in **(3.22)** for obtaining a trendline for the experimental data. It was deliberated chosen **2.5 KHz** as the frequency for estimating $\mathbf{R_s}$ and $\mathbf{C_s}$ because this way the trendline fits better the experimental results for the three applied forces. Although, very similar trendlines were obtained when $\mathbf{R_s}$ and $\mathbf{C_s}$ were estimated at frequencies between **1 KHz** and **4 KHz**.

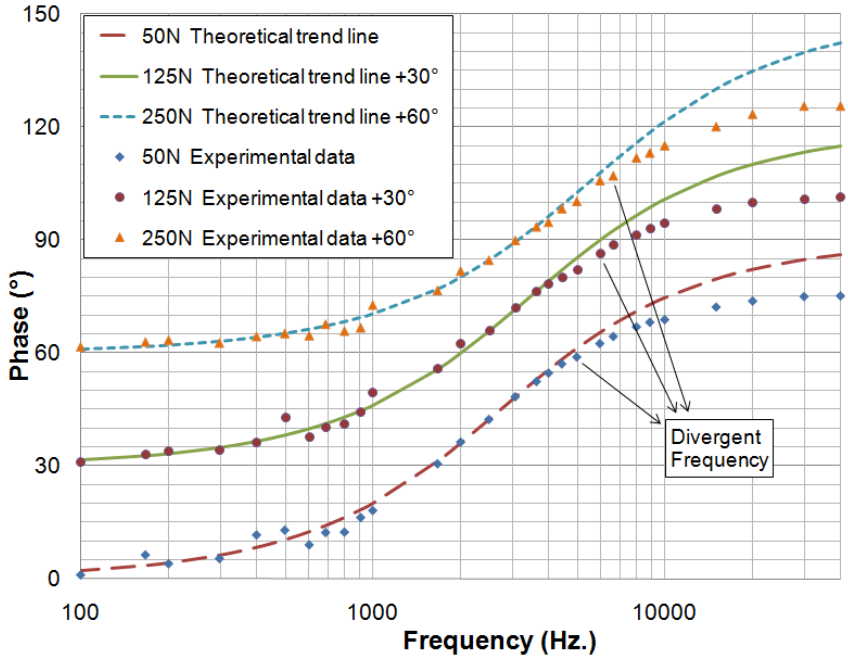

Figure 3.12: Phase bode plot of FlexiForce sensor for three different forces applied of **50 N**, **125 N** and **250 N**. Experimental data are shown with markers and the trendlines are superposed on each one

A series of interesting facts may be taken out from Figure 3.12. First, under low frequency operation (below **1 KHz**) experimental data are more scattered than at higher frequencies. This may happen due to the fact that, under low frequency operation the output voltage is too low, and then, the phase readings are more noise-sensitive. Second, equation **(3.22)** is a fit for the experimental data until reaching a certain frequency, which was conveniently called *divergent frequency*. As frequency increases beyond the divergent point, experimental phase readings saturate and both curves separate from each other. This behavior in sensor's response may be understood as *frequency nonlinearity*, where the RC model is no longer valid, and thus, the equations stated in Section 3.2.5 do not match for sensor's response. Three, Divergence frequency seems to be non-dependent on the applied force; only slight variation of the divergent frequency is noticed as force changes, although, the divergent frequency changes more noticeable from one sensor to another, starting at **4.5 KHz** for some sensors and up to **7 KHz** for others.

It has been demonstrated that sensor model introduced in Section 3.2.5 matches for FlexiForce sensor response in a defined range of frequencies, from DC up to **4.5 KHz**. It is interesting to study why the sensor exhibits such nonlinear response as frequency goes beyond **4.5 KHz**. In order to study that, Figure 3.13 and Figure 3.14 show $\mathbf{C_s}$ and $\mathbf{R_s}$ respectively, as a function of frequency for the three same forces of **50 N**, **125 N** and **250 N**. Sensor's capacitance and resistance were estimated by performing phase, ϕ, and output amplitude readings, $\mathbf{A_o}$, and then using expressions **(3.20)** and **(3.21)** to obtain $\mathbf{C_s}$ and $\mathbf{R_s}$.

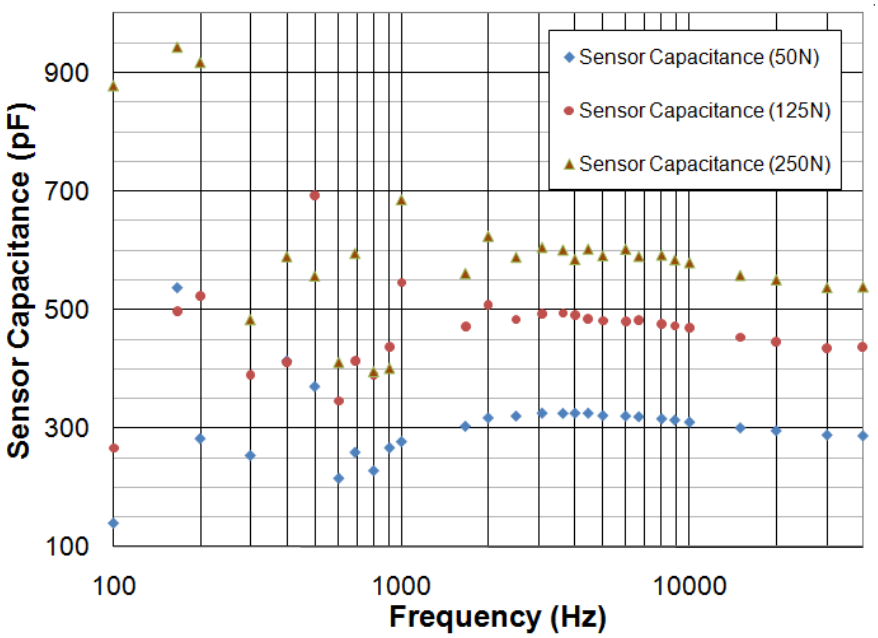

Figure 3.13: Plot of Sensor's Capacitance as a function of input frequency for three different applied forces of **50 N**, **125 N** and **250 N**

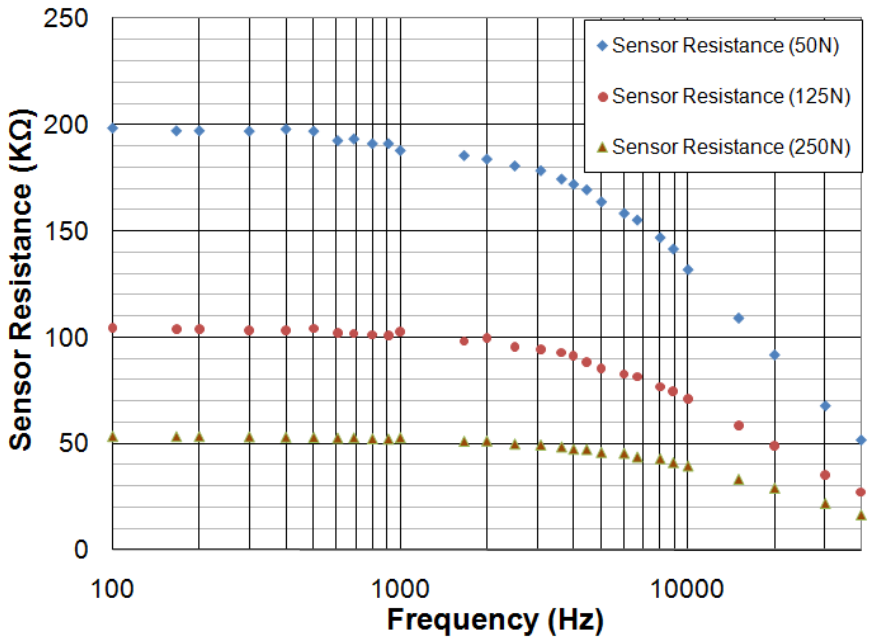

Figure 3.14: Plot of Sensor Resistance as a function of input frequency for three different applied forces of **50 N**, **125 N** and **250 N**

Figure 3.13 yields similar statements as previously did Figure 3.12: First, capacitance data are scattered at small frequency values, this is due to the same reason phase values were scattered on Figure 3.12. Second, capacitance values remain with little variation for a given force despite the frequency changes, whereas resistance values in Figure 3.14 decrease dramatically when the divergence frequency is reached. This behavior explains why the phase readings for the sensor saturate beyond the divergence frequency, but actually, the physical cause of such phenomenon is unknown.

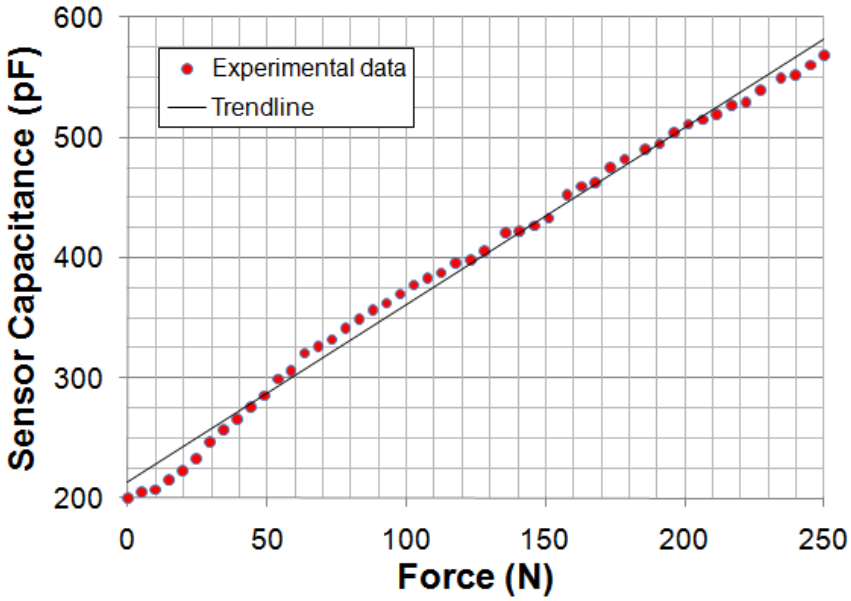

Figure 3.15: Variation of Capacitance as a function of the applied force

An interesting fact can be derived from Figure 3.13, it can be observed that capacitance values actually change as force increases. *This means that the sensors exhibit a piezocapacitive behavior*, such property had been unknown up to now, and only the piezoresistive property of the sensor had been used for estimating forces.

In order to get a full understanding of the piezocapacitive behavior in the sensor, the force was increased in steps of **5 N**, and simultaneously, sensor's capacitance was estimated using phase shift readings and equation **(3.20)**. Experimental results are plotted in Figure 3.15.

The experimental data points were initially adjusted with a line in the plot of Figure 3.15. However, in Section 3.3 a different approach is given for the capacitance values. Also, an in-depth analysis on how to use the piezocapacitive property of the sensor to improve sensor's performance is presented in Section 3.3.

3.3 Usage of the piezocapacitive effect in the FlexiForce A201-100 to improve device's performance

Previous section experimentally demonstrated that the FlexiForce A201-100 exhibits a piezocapacitive response. When attempting to read sensor's capacitance, an AC source must be used, and thus, it is necessary to define a linear region of operation in terms of input amplitude and operating frequency. The linear region of operation for the FlexiForce A201-100 can be classified according to the type of sourcing as next:

Under DC sourcing

- Input amplitude: The DC sourcing is the recommended setup by the manufacturer. The DC voltage can be set to any desired value and the sensor will always exhibit a linear response between the output voltage and the applied force, see Figure 3.4. However if the DC voltage is changed, the sensor must be calibrated again at the new operating voltage, because as earlier demonstrated

in section 3.2.1, sensor conductivity is not linear to changes in the source voltage.

Section 3.2.3 introduced a generalized method for obtaining a specific sensitivity in sensor's response, but such a method is restricted to sourcing voltages below **1 V**, because the amplitude nonlinearity presents a more complex behavior when the source voltage is over **1 V**.

Under AC sourcing

- Input frequency: Must be kept below the divergence frequency, see Section 3.2.6. Unfortunately, each sensor exhibits a different divergence frequency. The lowest value found in the sample of sensors matches **4.5 KHz**, so the recommended operating frequency must be set a bit lower to **4 KHz**.
- Input amplitude: In order to assume sensor conductivity as approximately constant, the operating voltage must be kept as low as possible. The validation tests of section 3.2.6 were done with $\mathbf{A_s = 0.5\ V}$, which is a sufficiently low voltage to ensure a linear behavior in sensor conductivity. This voltage restriction can be yielded from the plot of Figure 3.5.

Unfortunately, the first tests aimed to improve sensor performance were done with an input amplitude of $\mathbf{A_s = 3\ V}$ [129, 134], which is out of the linear range of the sensor, this was done so because the nonlinearity due to the tanh modulation went unnoticed.

Next Section describes the subtle effects of tanh modulation in the sensor's output and then presents the first results aimed to reduce the force estimation error in the FlexiForce A201-100 sensor. Finally, it is presented a method to bypass the amplitude nonlinearity in the sensor when performing Capacitance readings under AC sourcing regardless of the input amplitude.

3.3.1 Effect of Amplitude Nonlinearity under AC Sourcing for the Sensor

It has been demonstrated that sensor conductance is not constant if there are changes in the input voltage. By relating equation **(3.17)** with the conductance model, equation **(3.10)**, the following expression is obtained which is useful for studying the effect of amplitude nonlinearity under AC sourcing:

$$-\frac{V_o}{R_g} = \frac{1}{(m'F + b')R_g}\,\text{atanh}\left(\frac{V_{s2}}{k}\right) + Cs\frac{d}{dt}(V_{s2}) \qquad \textbf{(3.23)}$$

Where $\mathbf{|V_{s2}| < 1\ V, \forall t}$ in order to meet the general-sensor model from equation **(3.9)**.

Under AC sourcing, the nonlinear term, equation **(3.13)**, extracted from equation **(3.10)** causes a modulation effect in sensor conductance which was not accounted for in the tests reported in [129, 134]. It is evident that solving equation **(3.23)** for a sine-wave input yields a set of equations different from equations **(3.20)**, **(3.21)** and **(3.22)** . But, if the input amplitude of the AC signal is low enough, sensor conductance can be taken as approximately constant and consequently, the expressions from Section 3.2.5 and 3.2.6 can be taken as valid.

Specifically, the *frequency analyses* carried out in [129, 134] were done under a sine-wave input with $\mathbf{A_s = 0.5\ V}$, and therefore the results reported by those sources can be trusted. Note from Figure 3.5 that for $\mathbf{|V_{s1}| < 0.5\ V}$, sensor conductance can be taken approximately as constant regardless of changes in $\mathbf{V_{s1}}$. In contrast, the tests carried out in [129, 134] *for estimating the effect of capacitance readings in force-estimation errors* are in principle questionable, because the input signal used for those tests was a sine wave with $\mathbf{A_s = 3\ V}$.

A resume of the results presented in [129, 134] is addressed in the next Section with special focus on the implications of using a sourcing voltage of $\mathbf{A_s = 3\ V}$.

Hyperbolic-tangent nonlinearity was hard to detect in previous work [129, 134], because it produces neither saturation nor exponential growth in the output voltage. An additional circumstance prevents the detection of amplitude nonlinearity; to show this, V_{s2} was replaced in equation **(3.23)** with a sine function, and equation **(3.6)** was used to state equation **(3.23)** in terms of q as shown below:

$$Vo = -\left[\frac{1}{q}\operatorname{atanh}\left(\frac{A_s}{k}\sin(2\pi ft)\right) + 2\pi f C_s R_g A_s \cos(2\pi ft)\right] \qquad \textbf{(3.24)}$$

A close look at equation **(3.24)** reveals that the output voltage, $\mathbf{V_o}$, is the sum of the nonlinear term stemming from sensor conductance and the term stemming from sensor capacitance. It is demonstrated ahead in Section 3.3.4 that sensor capacitance is constant regardless of changes in the input voltage, and therefore the resulting V_o in equation **(3.24)** is the sum of a linear and a nonlinear term. From the time-domain viewpoint, given an input sine wave, the resulting output, equation **(3.24)**, looks rather sinusoidal, because the nonlinear response is diminished by the linear one. From the frequency-domain viewpoint, the output voltage is slightly distorted because of the odd harmonics coming from the high-order terms of the atanh-Taylor series.

3.3.2 Reducing the force estimation error through a combination of conductance and capacitance data.

Recalling the concepts and arguments introduced in Sections 2.2, the Mean Squared Error was employed as the method to compare the performance of the different methods to be presented in this Section. Likewise, the **MSE** of a sensor can be understood as a quantitative evaluation of the combined, hysteresis and non-repeatability error. Several reasons that support the appropriate usage of the **MSE** as a valid metric for the comparison of estimation methods were argued in Sections 2.2.5 and 2.2.6.

The tests presented in this Section were done without preventing the nonlinear behavior of sensor's conductance, and thus, the sine wave amplitude was chosen to be over **0.5 V**. Specifically the following two signals were used to drive the sensor during the tests:

$$V_{s1} = -5V \qquad \textbf{(3.25)}$$

$$V_{s2} = 3V\sin(2\pi 4000t) \qquad \textbf{(3.26)}$$

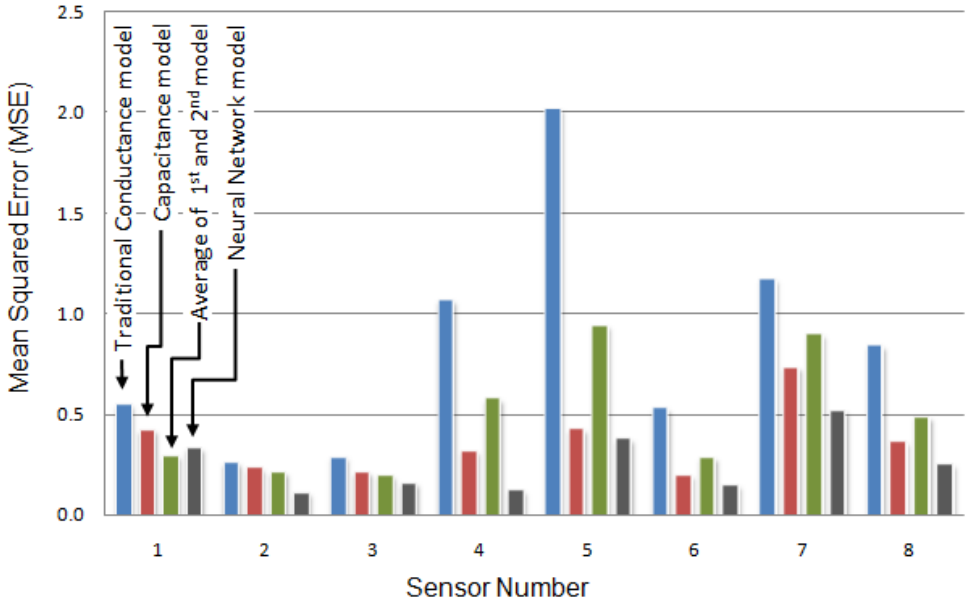

Figure 3.16: Mean Squared Error of the four models proposed for the eight sensors under study

In order to reduce the force estimation error when reading sensor's output, it was developed a set of four empirical models based upon conductance and capacitance changes.

The traditional conductance method, the first of the proposed models, was chosen as reference for further comparison. For such a purpose, the input $\mathbf{V_{s1}}$ from equation **(3.25)** was selected as the input in the circuit of Figure 3.3.

The second model was a linear regression of the capacitance values, so the input $\mathbf{V_{s2}}$, from equation **(3.26)**, was chosen as the input in the circuit of Figure 3.3, and then, expressions **(3.19)** and **(3.20)** were used for estimating $\mathbf{C_s}$. The third model consists of an average of the output forces predicted by the first and the second model.

The fourth model was a feedforward neural network with two inputs ($\mathbf{V_o}$ and $\mathbf{C_s}$), one hidden layer with two neurons, and one neuron output. The same network topology was used for all sensors but training data were taken individually for each sensor; this was necessary because capacitance was different from one sensor to other, just as conductance exhibited different values for each sensor.

The neural network was trained offline with $\mathbf{V_o}$ resulting from the DC source of expression **(3.25)** as the input of the circuit in Figure 3.3. The capacitance values, $\mathbf{C_s}$, were obtained in the same way as earlier described for the second model.

The histogram in Figure 3.16 summarizes the experimental results for each sensor in terms of the mean squared error for the four models under study. An important set of facts can be concluded from Figure 3.16.

First, the capacitance model generated lower errors than the traditional conductance model for all sensors. This is an important fact, because it shows that capacitance readings are more repeatable than conductance measurements.

Second, averaging the predicted forces from the conductance and capacitance always reduced **MSE** when compared with traditional conductance model.

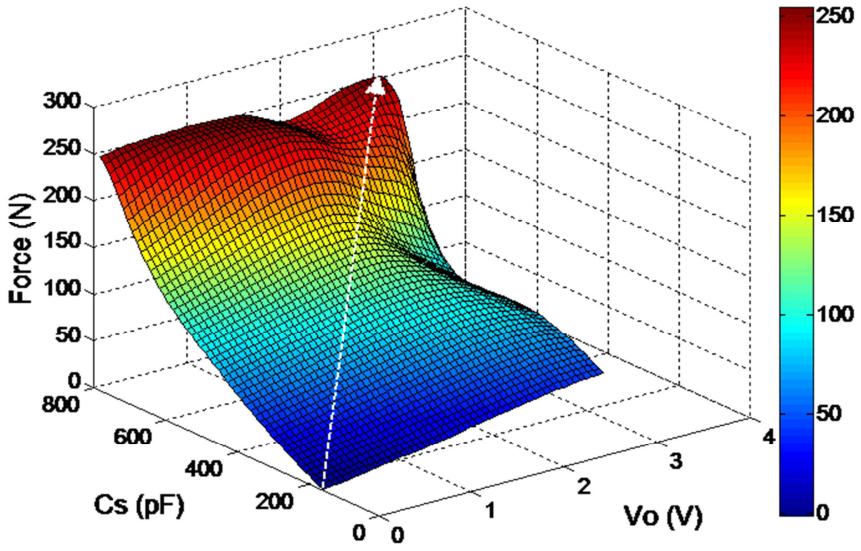

Figure 3.17: 3D plot of the surface generated by the neural network for predicting forces applied to FlexiForce sensors. An ideal variation of $\mathbf{V_o}$ and $\mathbf{C_s}$ as force increases is indicated by a white arrow

Third, the neural network model was the best technique for reducing output errors. This method worked better than the others due to the fact that a two-variable function is built from the $\mathbf{V_o}$ and $\mathbf{C_s}$ values. Conversely, the other three methods only take into account one of the two variables at any given time. Averaging the predicted forces from the conductance and capacitance models seldom produced better results than the neural network model (which was the case with sensor 1, but not the other sensors).

A 3-D plot of the surface generated by the neural network for a given sensor is depicted in Figure 3.17. An arrow superimposed on the surface indicates the typical variation of $\mathbf{V_o}$ and $\mathbf{C_s}$ as force increases. When either $\mathbf{V_o}$ or $\mathbf{C_s}$ values deviate from the ideal trajectory described by the white arrow, force is estimated incorrectly. However, the soft surface generated by the neural network tends to mitigate this error and improve sensor response. Finally, the traditional conductance model produced output errors that were notably different from one sensor to another. These imbalances are a frequent source of problems in applications in which several sensors are used [116]. summarizes the improvements introduced by the neural network, compared with the traditional conductance model for the eight sensors under study.

Note that the neural network model reduced the **MSE** dispersion to a narrower range of **0.107 – 0.515**, whereas the dispersion of the traditional conductance model was noticeable higher **0.258- 2.01**. The percentage of error reduction is computed (PER) from the formula below:

$$\mathrm{PER} = \left(1 - \frac{\text{MSE Neural Network Model}}{\text{MSE Traditional Conductance Model}}\right) \qquad \textbf{(3.27)}$$

A high value of **PER** for a given sensor means that the neural network model has substantially reduced estimation error compared with the traditional conductance model. *The results presented in Figure 3.16 and Table 3.2 demonstrated the effectiveness of capacitance readings to yield an average reduction of* ***64%*** *in the force estimation error.*

Table 3.2: Comparison of Traditional conductance model with Neural Network Model in terms of the Means Squared Error (**MSE**)

Sensor	**1**	**2**	**3**	**4**	**5**	**6**	**7**	**8**
MSE of traditional conductance model	0.547	0.258	0.285	1.06	2.01	0.527	1.17	0.839
MSE of Neural Network Model	0.33	0.107	0.156	0.118	0.374	0.145	0.515	0.249
Percentage of error reduction, **PER** (%)	39.7	58.2	44.9	88.8	81.4	72.4	55.9	70.2
				Average Percentage of error reduction				**64%**

However, an important aspect was left hanging in regard with the magnitude of the sourcing voltage of expression **(3.26)**: *how could be reduced the force estimation error if the amplitude nonlinearity was not taken into account during the data gathering?*

It is not possible to give a straight answer to such a concern, because it is necessary to solve the differential equation **(3.23)** with the inclusion of the amplitude nonlinearity in order to assess the effects of assuming a constant conductance. Unfortunately, it is not possible to *theoretically* estimate the underlying error stemming from the capacitance readings reported in [129, 134] whether the input sine wave has an amplitude of **0.5 V** or **3 V**. Where the input sine wave has an amplitude of **0.5 V**, equation **(3.23)** must be solved analytically in terms of **θ** and $\mathbf{A_o}$, which is a challenging task not to be addressed in this thesis; and where the input sine wave is **3 V**, a comprehensive model of the amplitude nonlinearity must be developed for input voltages above **1 V**, and then such model must be included in the differential equation **(3.17)**.

Neither procedure is addressed in this thesis, because a method is proposed in Section 3.3.3 for bypassing the amplitude nonlinearity under AC sourcing regardless of whether the input voltage is lower or higher than **1 V**. The practical implications of accidentally omitting the amplitude nonlinearity in [129, 134] are presented ahead in Section 3.3.4.

3.3.3 Bypassing Amplitude Nonlinearity for Estimating Sensor Capacitance

Recalling the nonlinearity concepts introduced in Sections 3.2.1 through 3.2.4, the Factors **q** and **k** can be easily determined if the sensor is sourced with a DC signal; there is therefore no interest in estimating **q** and **k** using AC sourcing. Note in equation **(3.24)** that sensor capacitance, $\mathbf{C_s}$, is multiplied only by the term with the cosine function, so if that term can somehow be isolated, it may become possible to read sensor capacitance.

Multiplying $\mathbf{V_o}$ from Equation **(3.24)** by:

$$V_x = A_x \cos(2\pi f t) \tag{3.28}$$

and Low-Pass Filtering (LPF) yields:

$$LPF\,[VoVx\,] = LPF\left[\begin{array}{l} A_x \cos(2\pi f t)\,\dfrac{1}{q}\,\text{atanh}\left(\dfrac{A_s}{k}\sin(2\pi f t)\right) + \\ 2\pi f A_x A_s C_s R_g \cos^2(2\pi f t) \end{array}\right] \tag{3.29}$$

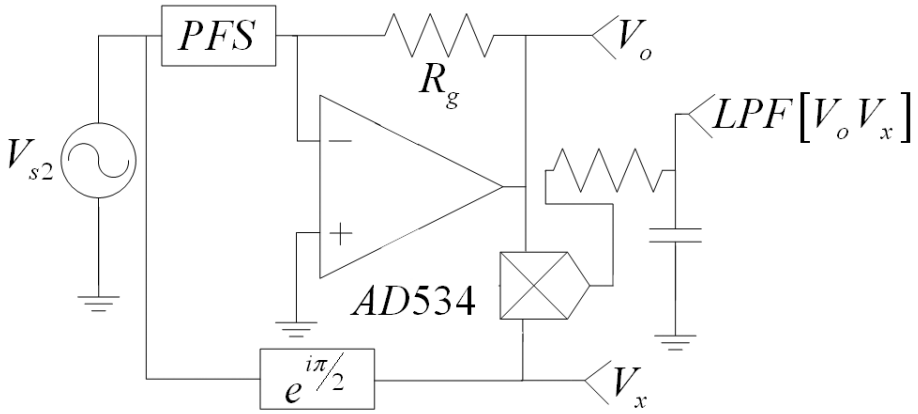

Figure 3.18: General diagram for measuring **Cs** by means of removing the conductance term from the output voltage by performing the operation **LPF [$V_o V_x$]**

Considering that the composition of two odd functions is an odd function, the first term of Equation **(3.24)** is consequently odd (the atanh and sin functions are both odd). Multiplying such a term by an even function, equation **(3.28)**, results an odd function with frequency components at $4\pi nf, \forall n \geq 1 \in N$.

The harmonics come from the decomposition of the atanh function in its Taylor series. Thus, the first term of equation **(3.29)** can be expressed as:

$$A_x \cos(2\pi ft)\frac{1}{q}\operatorname{atanh}\left(\frac{A_s}{k}\sin(2\pi ft)\right) = \frac{A_x \cos(2\pi ft)}{q}\left[\frac{A_s}{k}\sin(2\pi ft) + -\frac{1}{3}\left(\frac{A_s}{k}\sin(2\pi ft)\right)^3 + \frac{2}{15}\left(\frac{A_s}{k}\sin(2\pi ft)\right)^5 + \ldots\right] \quad \textbf{(3.30)}$$

Note that equation **(3.30)** does not have a DC component, and thus the low-pass filter removes the entire signal.

On the other hand, the second term of equation **(3.29)** is an even function and may be rewritten as:

$$2\pi f A_x A_s C_s R_g \cos^2(2\pi ft) = \pi f A_s A_x R_g C_s (1 + \cos(4\pi ft)) \quad \textbf{(3.31)}$$

Equation **(3.31)** has a nonzero mean value and a term with frequency component at **4πf**, which is removed by the LPF, and thus, expression **(3.31)** can be simplified to:

$$LPF[V_o V_x] = -\pi f A_s A_x R_g C_s \quad \textbf{(3.32)}$$

The above expression is useful for reading sensor capacitance, because the other factors in equation **(3.32)** are constants. The mathematical function **LPF [$V_o V_x$]** can be obtained by using a four-quadrant multiplier, such as the *AD534*, and a RC-series circuit in the low-pass configuration. Figure 3.18 summarizes the described process for measuring $\mathbf{C_s}$.

Equation **(3.32)** is inherently different from equation **(3.20)**, because sensor conductance is not present in the former, while in the latter it is, albeit implicitly, due to the ratio $\mathbf{A_o/A_s}$ in equation **(3.20)**. This is an important difference, because the process

herein depicted removes the contribution of sensor conductance from the output signal. So, regardless of what the conductance model is, equation **(3.32)** remains unchangeable. It is not possible to provide a theoretical demonstration of this statement until a model for $\mathbf{1/R_s}$ is developed for sourcing voltages above **1 V**; however, experimental results that support this hypothesis are presented in the next Section.

It must be remarked that different methods for measuring capacitance were evaluated [136, 143, 171], but the fact that a variable resistor, $\mathbf{R_s}$, is placed across the capacitance, $\mathbf{C_s}$, makes reading difficult. The method described above was inspired by the synchronous demodulation of RF signals [94]. Note that $\mathbf{C_s}$ can be considered as the message in equation **(3.31)**, the term $\mathbf{2\pi f R_g A_s cos(2\pi ft)}$ acts like the carrier signal and $\mathbf{A_x cos(2\pi ft)}$ as the demodulating signal.

The effectiveness of capacitance readings to reduce the force estimation error was earlier demonstrated in [129, 134] and summarized in Section 3.3.2. Nonetheless an inappropriate method for reading sensor capacitance was employed in such tests because the amplitude nonlinearity went undetected.

3.3.4 Testing the Feasibility of the circuit of Figure 3.18 for bypassing Amplitude Nonlinearity

In order to test the feasibility of the circuit depicted in Figure 3.18, it was followed a similar procedure to that of Section 3.3.2 with the difference that Capacitance data were collected under *multiple* AC input amplitudes of **0.4 V**, **0.6 V**, **1.5 V** and **2.5 V**, see expression **(3.15)**. All the capacitance data were plotted in for this four input amplitudes.

Input amplitudes were not restricted to be under **1 V** for the AC sourcing experiments, because the intention was to subject the feasibility of the measuring scheme of Figure 3.18 to a thorough test.

Figure 3.19 shows two different sets of capacitance values for the same sensor, taken under sinusoidal excitation at a fixed frequency of **4 KHz**. The black values were taken according to the measuring scheme of Figure 3.18, whereas the red data points were taken from previous work [129, 134], when the amplitude nonlinearity was unknown and the equations from Section 3.2.6 were used to estimate $\mathbf{C_s}$. This set of data was taken at a fixed input amplitude of **3 V**.

Considering:

- That the black data points in Figure 3.19 are rather close to each other for the different driving voltages, and
- That the feasibility of the measuring scheme in Figure 3.18 was theoretically demonstrated in Section 3.3.3;

It may be concluded that sensor capacitance is constant regardless of changes in the driving voltage, with the restriction of $\mathbf{|V_{s1}| < 1\ V}$.

A look at the capacitance values for input voltages of 1.5V and 2.5V (see Figure 3.19) shows that it is reasonable to suggest that $\mathbf{C_s}$ remains constant for $\mathbf{V_{s1}}$ above **1 V**, but this cannot be definitely stated until a model for sensor conductance is developed for

$\mathbf{V_{s1}}$ above **1 V**, because the compatibility of such model with the measuring scheme in Figure 3.18 must first be ascertained.

An attempt was made to fit a linear trendline to the black data points in Figure 3.19. This is a logical approach, considering that previous work reported a linear variation of $\mathbf{C_s}$ in response to force changes [129, 134]. However, the residuals resulting from the fitting process suggested that a linear fit was unsuitable. Thus, different trendline forms were tried. The best, but also simplest, trendline that could model the variation of $\mathbf{C_s}$ was a square-root model dependent on the applied force, **F** as next:

$$C_s = m_c\sqrt{F + b_c{}^2} \tag{3.33}$$

where $\mathbf{m_c}$ and $\mathbf{b_c^2}$ are constants estimated from the fit.

Multiple variations of square-root models were tested over the experimental data points of Figure 3.19 with different results. Some of the tested trendlines are listed next:

$$C_s = m_c\sqrt{F} + b_c \tag{3.34}$$

$$C_s = \sqrt{m_c F + b_c{}^2} \tag{3.35}$$

$$C_s = m_c\sqrt{F + b_c{}^2} + C_o \tag{3.36}$$

Models **(3.34)** and **(3.35)** failed to provide an appropriate fit for the experimental datapoints. On the other hand, the model **(3.36)** showed an outstanding performance, but the constant $\mathbf{C_o}$ was redundant, and consequently, it was removed from the model.

Note from equation **(3.33)** that the factor $\mathbf{m_c b_c}$ can be taken as the initial value of capacitance under no-applied force, **F = 0 N**. If force is different from null, $\mathbf{b_c^2}$ can be taken as an offset factor in the square root function, while $\mathbf{m_c}$ modifies the rate of growth of capacitance. Finally, the simplest but still most realistic model for Capacitance variations was obtained from the equation **(3.33)**.

The red data points in Figure 3.19 -taken from previous work [129, 134]- were fitted with a line as earlier reported in Figure 3.15, and a remarkably good coefficient of determination was obtained, $\mathbf{R^2 = 0.9942}$. This set of data was already presented in Section 3.2.6 when the piezocapacitive behavior was introduced.

Under the same loading conditions for the sensor, but employing the measuring scheme of Figure 3.18, the experimental data were gathered and plotted in black color with expression **(3.33)** as the equation fit. Under such circumstance, the value of $\mathbf{R^2}$ was slightly better, $\mathbf{R^2 = 0.9987}$.

From Figure 3.19, it is clear that one set of data points is incorrect, because it is impossible that different values of capacitance were measured for the same sensor, under the same applied forces and the same mechanical layout. Considering that the red data points were taken under the erroneous supposition of linear conductance, it is logical to suggest that it was the assumption that yielded the incorrect values of capacitance; but, as stated in Sections 3.3.1 and 3.3.3, there are a few steps remaining to be accomplished before this hypothesis can be demonstrated.

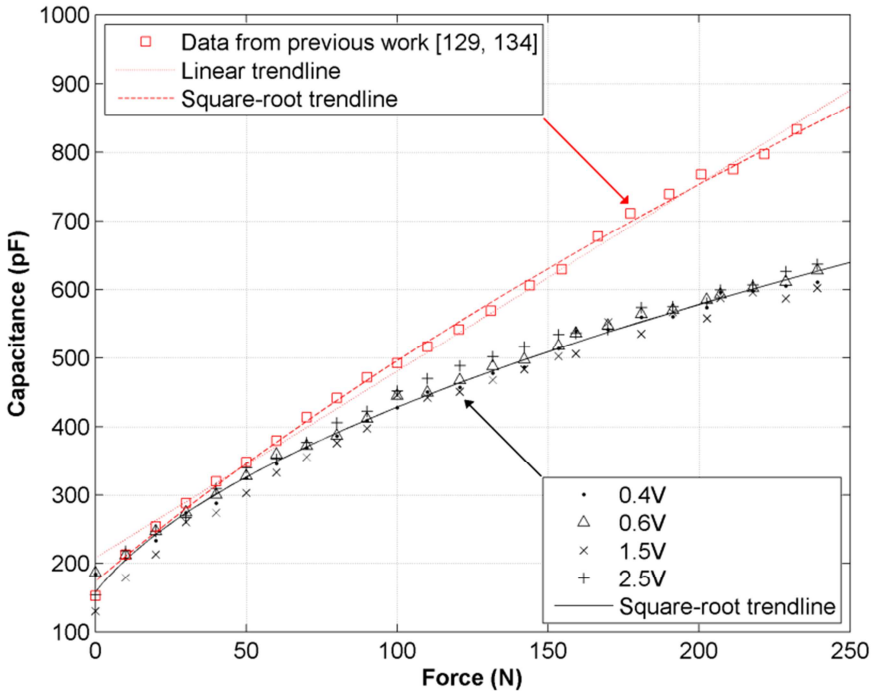

Figure 3.19: Sensor Capacitance, $\mathbf{C_s}$, measured using two different methods under different sourcing voltages

In other words, it has been theoretically and experimentally demonstrated that the black data points from Figure 3.19 are correct at least for $\mathbf{|V_{s1}| < 1\ V}$, but it is not theoretically possible to demonstrate that the error basis from the red data points is due to the assumption of linear sensor conductance despite some experimental results supporting this hypothesis. For instance, a look at the measured capacitance under low applied forces in Figure 3.19 shows that both methods estimate the same $\mathbf{C_s}$. This may be understood if one recalls the piezoresistive behavior of the sensor; so, under low applied forces and AC excitation, sensor resistance can be taken as virtually infinite (see Figure 3.15), and its response is dominated only by capacitive factors. Under these circumstances, the resistive term in equation **(3.17)** may be discarded, and the measured capacitance will be the same, regardless of the conductance model or the method employed for measuring $\mathbf{C_s}$. It is only when the exerted force is increased that the aforementioned conditions start to play an important role in the estimation of sensor capacitance, and consequently, as F increases, the two sets of data points gradually diverge.

3.4 Modelling the variations of sensor's Capacitance and Conductance to changes in the applied Force and the exertion Area.

Sections 3.2 and 3.3 presented a detailed derivation of the electrical model for the FlexiForce A201-100 sensor. The newly found piezocapacitive property demonstrated its effectiveness towards the reduction of force estimation error as reported in Section 3.3.2. Nonetheless, the inclusion of capacitance readings may still provide additional benefits and capabilities to the sensor performance.

From the concepts introduced in Chapter 2 and Chapter 3, the piezoresistive effect is exhibited in Polymer MEMs due to the applied stress over its surface. Recalling the

stress definition summarized in equation **(2.2)**, stress is defined as the relation between the applied force **F** and the cross-sectional area **A**. And so, it is logical-thinking to carry out an empirical study that attempts to identify the relation of conductance and capacitance variations with regard to the cross-sectional area **A** and the applied Force **F**. From now on and due to simplification reasons, the cross sectional area is pointed out as the *exertion area*.

Previous experiments from Section 3.2 and Section 3.3 were done with a constant puck area of **51 mm^2**, this is, the exertion area from equation **(2.2)** remained constant along all the experiments, and consequently the measured output voltage and conductance could be directly related with the applied force **F** because the puck area was treated as a constant. However, in order to study the effect of different exertion areas, a set of nine different pucks were assembled as described next.

3.4.1 Custom design pucks with different exertion Areas and description of the redesigned testbench.

A set of nine different pucks were assembled with increasing sizes starting at **6 mm^2** up to **54 mm^2** in increase steps of **6 mm^2**, see Figure 3.20. Since a larger amount of pucks must be handled together, it was redesigned the puck holder of Figure 3.1 and also the test bench assembly of Figure 3.2 to manage the nine sensors simultaneously. The redesigned puck holder was also thought to reduce the backlash occurring between the puck holder and the pucks. For such a purpose, a set of four notches were added along the puck borders and the puck holder was modified likewise, see Figure 3.21 for a detailed view of the redesigned test bench.

The process for gathering the data was pretty similar to the above described in Section 3.1 with the difference that after every set of data were taken, each sensor was relocated over the pile of sensors such that the bottom side of each puck was exerted over each other, see Figure 3.21c. So after nine swaps, each sensor was tested over all the existing puck sizes and then, it was possible to proceed with the fitting tool process and further sensor modelling.

The hardware employed during the data gathering was based on the schematic presented in Figure 3.18 with the add-on that a multiplexed scheme was employed to reduce the total part count.

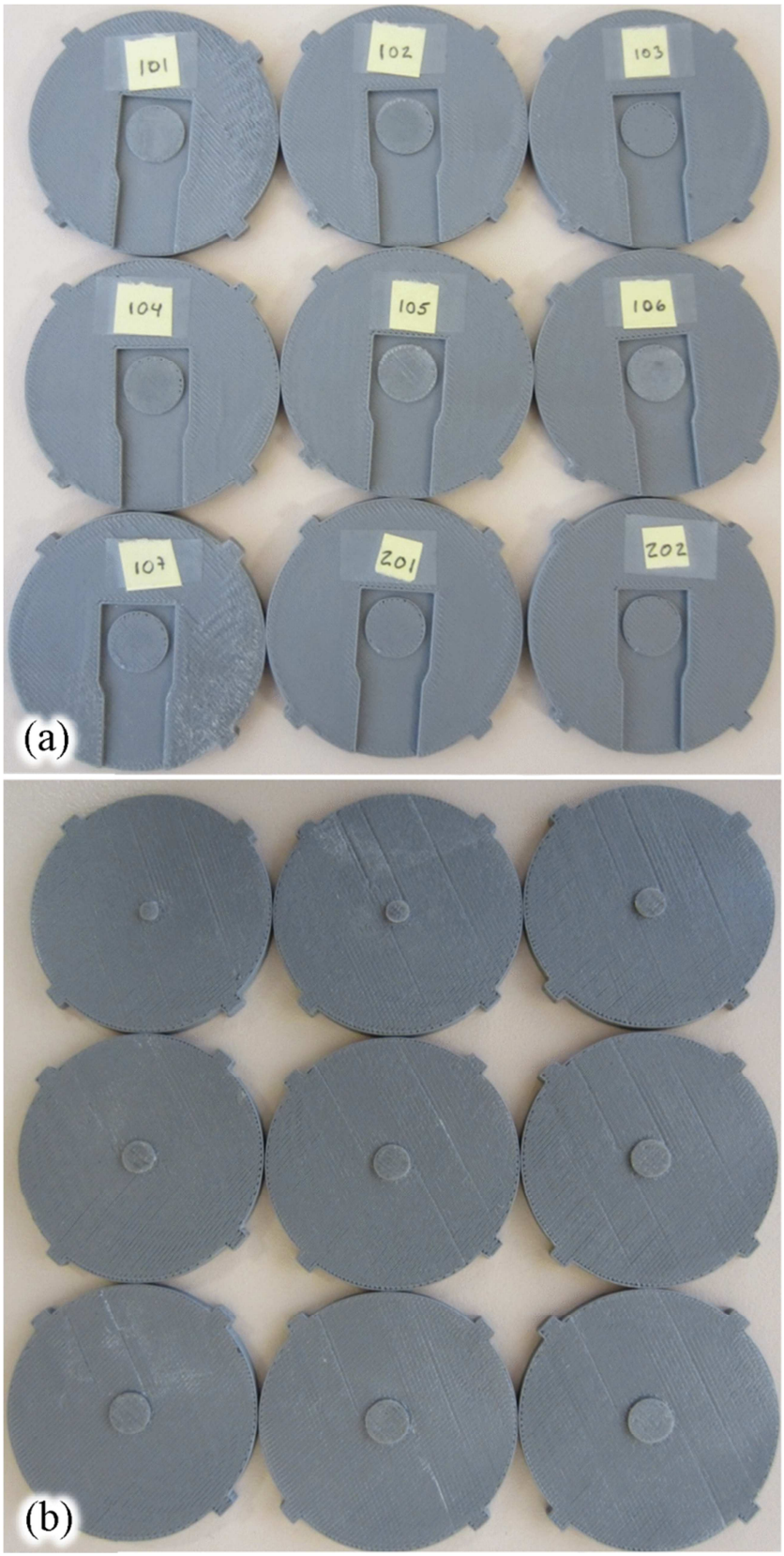

Figure 3.20: Picture of the nine pucks with different cross sectional areas. (a) Top view with a numbered legend for easy identification. (b) Bottom view showing the increasing cross sectional areas

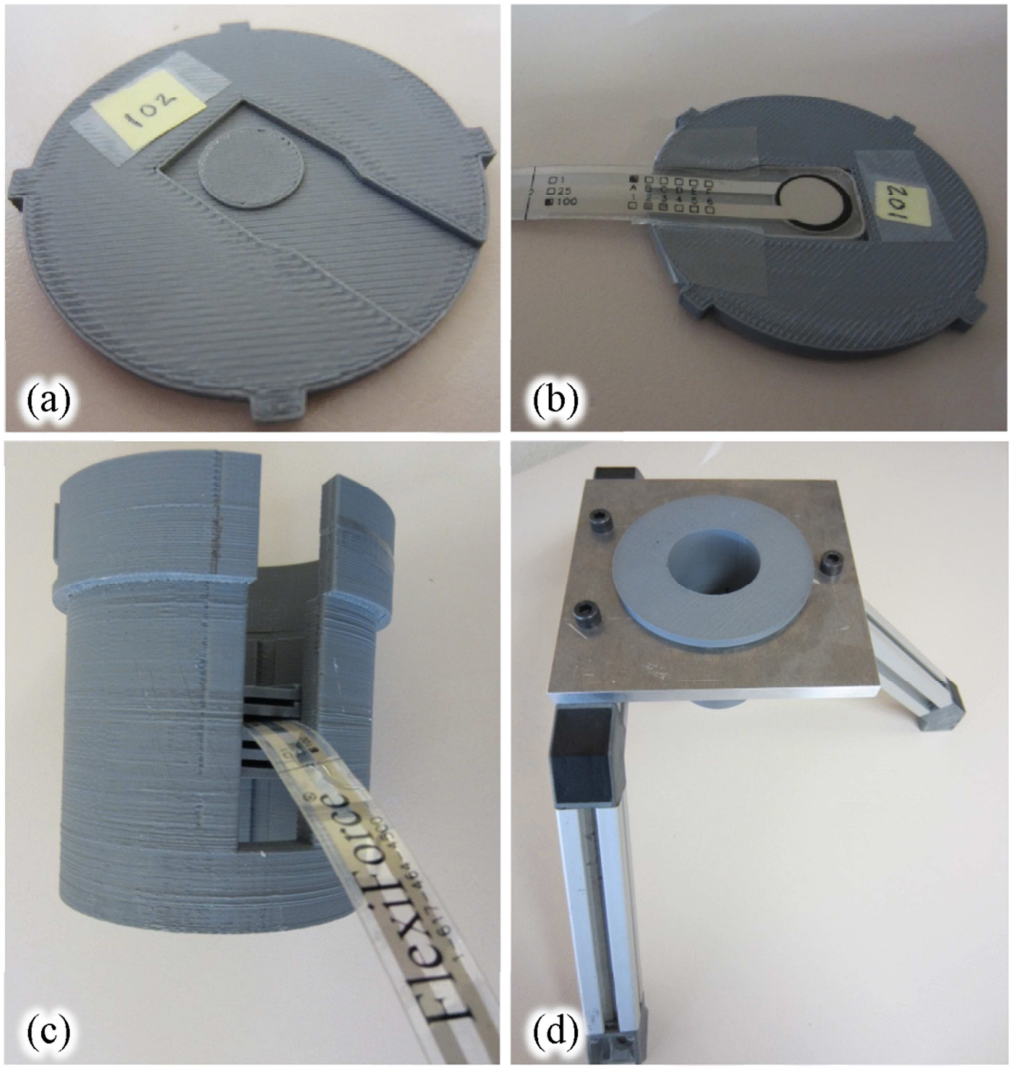

Figure 3.21: Redesigned testbench to handle nine pucks with different cross sectional areas. (a) Isometric view of the puck. (b) Top view of the puck with a bonded A201-100 FlexiForce sensor. (c) Isometric view of the puck holder with five pucks. (d) Final assembly of the testbench

3.4.2 Ideas behind the model proposal

Since a multivariable model was required for the force/area model, it was mandatory that both conductance and capacitance were measured in order to allow the solving of the equation system:

$$C_s(F,A) = \psi_{11(F,A)} + \psi_{12(F,A)} + \psi_{13(F,A)} + \dots \quad \textbf{(3.37)}$$
$$V_o(F,A) = \psi_{21(F,A)} + \psi_{22(F,A)} + \psi_{23(F,A)} + \dots$$

Where $\Psi_{1i(F,A)}$ and $\Psi_{2i(F,A)}$ are each one of the functions relating conductance and capacitance with the applied force **F**, and the exertion area **A** respectively.

The main challenge behind the model proposal was to find the adequate functions, $\Psi_{1i(F,A)}$ and $\Psi_{2i(F,A)}$, that could predict sensor behaviour while keeping to a minimum the system complexity.

Several similarities can be found on the experimental approach between equation **(3.37)** and the identification of amplitude nonlinearity from Section 3.2.1. Likewise, it must be recalled from Section 3.3.4 that sensor's capacitance increases to the squared root of the applied force **F**, see equation **(3.33)**. Next section resumes the experimental results from the above model.

3.4.3 Experimental Results from the MIMO Model.

After attempting to fit the experimental data with different functions while maintaining the overall simplicity to a minimum, it was proposed the following equation system to predict the variations of Capacitance $\mathbf{C_s}$ and the output voltage $\mathbf{V_o}$ to changes in the Force **F** and the exertion area **A**:

$$\begin{cases} C_s = m_c\sqrt{F + b_c{}^2} + m_A A & \textbf{(3.38)} \\ V_o = n_F F + n_A A + b_o & \textbf{(3.39)} \end{cases}$$

The Capacitance variation from equation **(3.38)** was similar to that presented in Section 3.3.4, with the difference that the factor, $\mathbf{m_A A}$, has been added to include the effect of the exertion Area, **A**, over the Capacitance, $\mathbf{C_s}$.

The same extrapolation applies to the sensor's conductance that exhibited a linear relationship with the exertion Area through the factor $\mathbf{n_A A}$. The term $\mathbf{b_o}$ is analogous to b in equation **(3.3)**, and can be understood as the output voltage under null force condition. The equation system of **(3.38)** and **(3.39)** has been proposed and tested after gathering data over the nine FlexiForce A201-100 sensors.

A plot of the Capacitance trendline **(3.38)** together with the experimental data points is shown on Figure 3.22. Likewise, for the Conductance trendline **(3.39)** shown on the plot of Figure 3.23. Both set of data points were randomly chosen among the nine sensors because the performance of each sensor in terms of the $\mathbf{R^2}$ factor was pretty similar among them.

The functions relating Capacitance and Conductance with the applied force, F**,** and the exertion area, **A,** exhibited coefficients of determination equal to $\mathbf{R^2 = 0.9312}$ and $\mathbf{R^2 = 0.9053}$ respectively. These values were not so high compared to previous results from Section 3.2.4 and Section 3.3.4. However, it must be pointed out that the equation system from **(3.38)** and **(3.39)** embraces multiple inputs and outputs, and thus, there is a natural tendency for larger errors to occur.

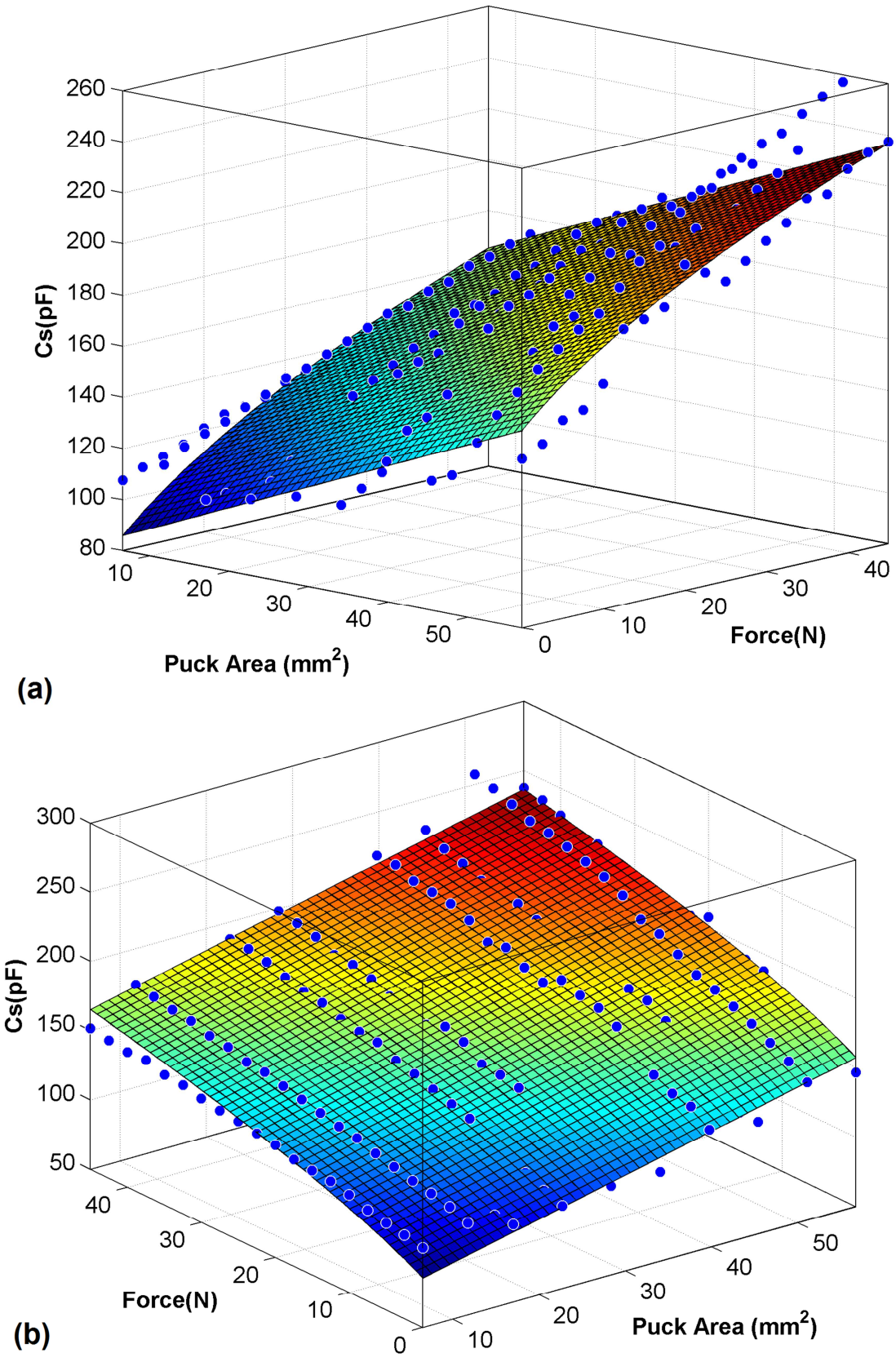

Figure 3.22: Experimental data and trendline for sensor's Capacitance $\mathbf{C_s}$ as a function of the force **F** and the exertion area **A**. (a) Isometric view a. (b) Isometric view b

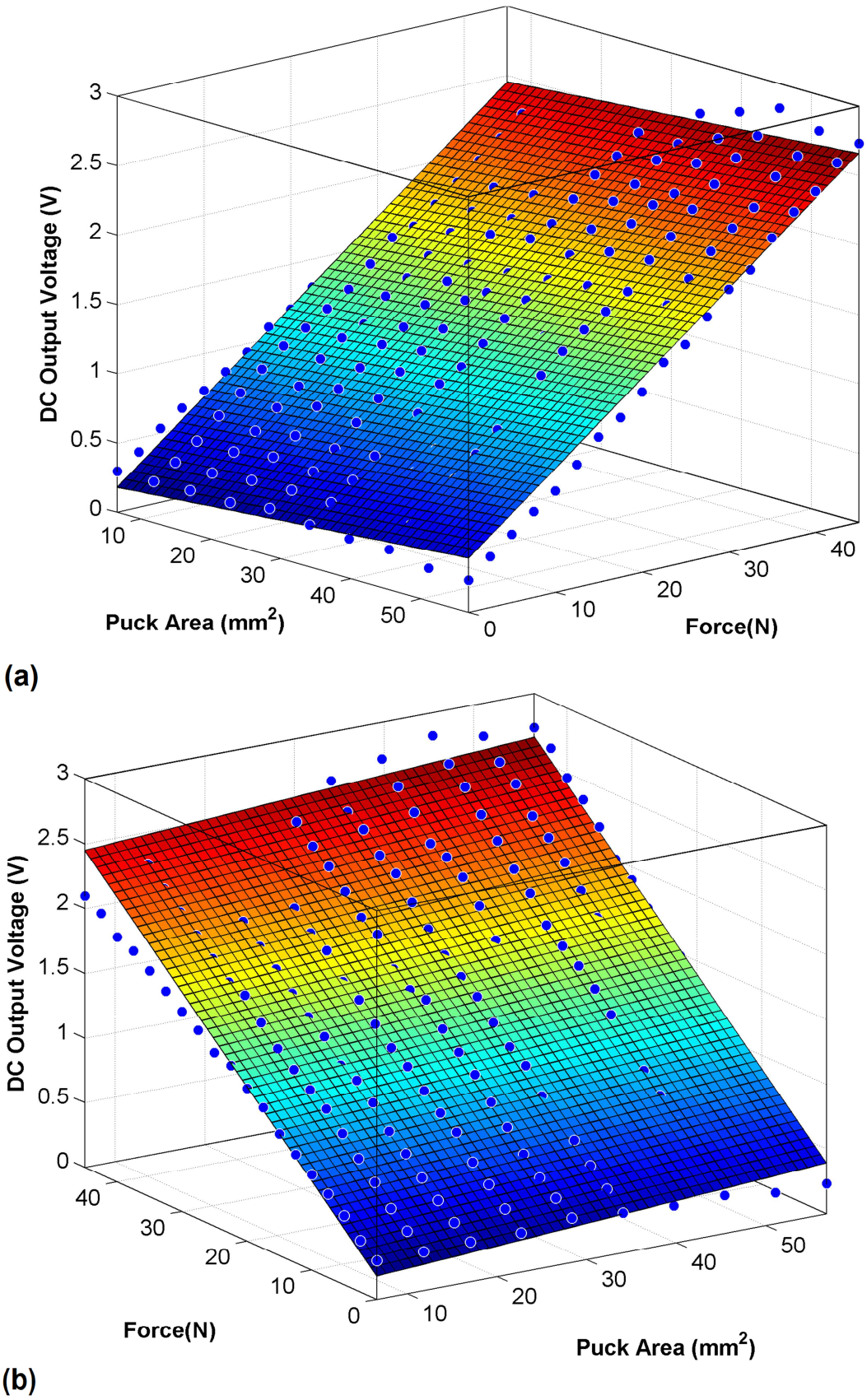

Figure 3.23: Experimental data and trendline for sensor's Conductance $\mathbf{V_o}$ as a function of the force **F** and the exertion area **A**. (a) Isometric view a. (b) Isometric view b

3.5 Conclusion and resume

This Chapter presented the derivation of a model for the piezoresistive sensor model FlexiForce A201-100. The model was developed under an empirical basis using two different testbenches and employing AC and DC sourcing. The following set of highlights found during sensor characterization can be pointed out:

A non-linear behaviour to changes in the input voltage was identified in the FlexiForce sensor model A201-100. A non-linear model relating conductance variations to changes in the input voltage was found for sourcing voltages below **1 V**. However, a more general model for input voltages over **1 V** must be still formulated.

In regard to sensor response under AC sourcing, it was found that the sensor exhibits a piezocapacitive response which implies that capacitance varies when the applied force changes.

It was demonstrated that the combined usage of capacitance and conductance variations in the FlexiForce A201-100 sensor can yield relevant improvements on the device's performance. This thesis has found two remarkable improvements, the first states that the force estimation error can be dramatically reduced, a **64%** in average, when combining conductance and capacitance measurements through multivariable force estimation. The second improvement states that it is possible to estimate the applied force as well as the area where the force is being applied.

Chapter 4

4. Review on the Concepts, Applications and Control Algorithms regarding the Intelligent Assist Devices (IADs)

Cranes, service lifts and mechanical arms are devices traditionally controlled by levers, pushbuttons and more recently by joysticks or handlers. Henceforth, such devices are referred in this text as Manual Assist Devices (MADs) to distinguish with the Intelligent Assist Devices (IADs) to be defined ahead. The MADs are primarily used in industrial assembly processes and have played a crucial role in making such processes more productive. The MADs enable the operator to effortlessly displace heavy payloads using the system control's pushbuttons or levers.

Nonetheless, a high degree of dexterity is required by the operators who handle this equipment, and this skill can only be achieved through months or even years of experience. On top of this, the operators must contend with an industrial setting in which other production workers are controlling other machines. In light of this shared work environment, operators must take great care when performing their tasks so as to avoid collisions or accidents that could jeopardise their physical well-being or decrease the plant's productivity. MADs also have other drawbacks, identified by Peshkin [140, 141] and summarised below:

- Limited manoeuvrability owing primarily to a control interface based on control levers and pushbuttons; components which prove unnatural and require the operator to undertake a lengthy training process.
- The time that the MAD operators need to become familiar with this equipment translates into decreased plant productivity. In a worst case scenario, the operators are forced to take courses or examinations in order to proficiently manoeuvre the MADs.
- In certain situations, motion limits should be programmed so as to prevent operators from entering prohibited areas of the plant. This function cannot be performed with a MAD.
- MADs cannot be programmed for repetitive tasks. The operator must always guide the device's movements.
- MADs are not equipped to mask the inertia of the displaced objects, which poses an issue of plant safety, since the operator might not perceive the proximity of an obstacle sufficiently in advance and could cause a collision or workplace accident.

In a bid to overcome these drawbacks, a group of researchers set about designing systems with improved ergonomic conditions for production workers; systems known as Intelligent Assist Devices (IADs).

In May 1995, Northwestern University and General Motors (GM) began a 5-year project toward designing a series of IADs that would substantially improve working conditions in the GM assembly line. The numerous projects developed at this time allowed for the following prototypes to be built: the Unicycle Cobot [34], Scooter [168], 3-DOF Robot with Continuously Variable Transmission (CVT) [118], Jib Crane [123] and the Rail Cobot [141]. Stanley Assembly also took part in some of these projects that were later launched as spin-off products under the *Cobotics* designation.

Afterwards, Northwestern University continued to develop other IAD projects, including: the Unicycle Two-Link Arm (UTLA) Cobot [170] and the 6DOF Cobotic Hand Controller [47].

Parallel research efforts were carried with the goal of developing Assist Robots by Helms in the Fraunhofer Institute IPA [66] and the *SMErobot* initiative. The idea behind this concept was to design *flexible* robots with *direct interaction* that provides sensor and actuator based mechanism with variable *mechanical impedance* during the robot interaction. It was also desirable that the robot's provided data collecting and further processing abilities with the aim of improving the assembly's performance.

A review of the most relevant implementation of IADs is presented in this Chapter. The IAD Operation Modes and IAD Control Algorithms are also addressed. Passive and Active implementations of assistive robots are explored and compared from the safety and the flexibility standpoints. The notion of non-colocation of actuators and sensors in IADs is introduced together with the complication arising from such condition. Some solutions for the instability problems resulting from the non-colocation are discussed too.

4.1 What Are Intelligent Assist Devices (IADs)?

A broad definition of IADs was presented by Colgate in [33]:

> *Computer-controlled, servo driven tools that enable production workers to lift, move and position payloads quickly, accurately and with ergonomic safety. IADs address the need for a solution that bridges the limitations of conventional material handling equipment and the high capital costs of robots in production environments.*

The IADs are devices that enable a unique collaboration of humans and machines, and thus yield greater levels of productivity, quality and ergonomic safety to manual operations. With the use of sophisticated sensors, controls and proven servo motor technology, the IADs allow operators to manipulate and position loads with speed, precision and ease. The IADs fall within the classification of COlaborative RoBOTS, COBOTS.

The Cobots are specially designed to assist in the manipulation of loads in industrial environments. This assistance is usually carried out in the form of shared control, which implies that the path guidance relies on the robot, whereas the necessary power for load's motion is uniquely delivered by the operator. This turns the *Cobots as inherently passive devices*. On the opposite side, the designation of *IAD* is given to active Cobots that allow *power amplification*. This aspect is discussed later in Section 4.3.

The design of IADs requires the understanding of some concepts which are typically not discussed when dealing with classical robotic manipulators that exhibit a holonomic design. Conversely some IADs are nonholonomic devices that require the understanding of additional concepts. The most relevant definitions are next presented:

4.1.1 Definition of Taskspace Dimensionality and Degrees of Freedom

Both terms have been used interchangeably in articles since, in most practical instances, taskspace dimensionality and degrees of freedom are usually equal in terms of number. That said, the difference between the two concepts must be accounted for when looking to study nonholonomic systems. A comparison of the extent of both definitions was presented by Peshkin [141] as next:

Degrees of freedom are the space of velocities that is mechanically allowed by the robot's, cobot's or organism's mechanism, while taskspace dimensionality refers to the space of endpoint poses (position and orientation) that can be reached over time. A non-redundant holonomic robot requires six degrees of freedom, the same as its taskspace dimensionality.

4.1.2 Holonomic and Nonholonomic Robots

Holonomic devices are defined as those whose controllable degrees of freedom are equal to or greater than the total degrees of freedom. Nonholonomic devices are those whose controllable degrees of freedom are less than the total degrees of freedom.

The following example illustrates the difference between the two definitions: whereas an automobile has a taskspace dimensionality of 3 **(x-y-θ)**, in which **(x-y)** refers to position and **(θ)** to orientation, it only possesses two controllable degrees of freedom, the rolling speed and steering angle of the wheels. As a result, the vehicle is a nonholonomic device.

The human arm, on the other hand, is a redundant holonomic system, since it possesses three degrees of freedom in the shoulder, two in the elbow and two in the wrist: seven altogether. As it has a taskspace dimensionality of six, is has one additional degree of freedom.

All the IADs and Cobots to be described in Section 4.6 are nonholonomic devices. The advantages of using this design concept are addressed in Section 4.7.

4.1.3 Underactuated and Undercontrolled Robots

In [141], Peshkin defined *underactuated robots* as those with fewer actuators than they have taskspace dimensions, i.e. nonholonomic robots are, by definition, underactuated.

Undercontrolled robots are those where the number of control inputs is fewer than the taskspace dimensions. In other words, a car is an undercontrolled device since it only has two control inputs (speed and the steering angle of the wheels) and has a taskspace dimensionality of three. It is also undercontrolled on account of its one single actuator.

The human arm, on the other hand, is fully controlled and actuated. Manipulators with conventional servo driven systems are both fully actuated and fully servo driven. Ahead

in this chapter, are presented the devices that are fully controlled yet underactuated, since they are of great interest in the field of IADs.

4.2 A broad view of the Underactuated, Undercontrolled IADs and the CVTs' Capabilities.

The underactuated, undercontrolled IADs make use of nonholonomic devices such as Continuously Variable Transmissions (CVTs) and steered wheels to generate constraints in the IAD's rolling direction. There are two kinds of CVTs: translational and rotational. The former uses a steered wheel to establish a transmission ratio between two translational velocities, while the latter uses spheres to hold two angular velocities in proportion. Figure 4.1 shows an isometric view of a translational CVT in the plane **(x-y)**

The figure identifies two axes of rotation, a point of contact between the wheel and the plane **(x-y)** and a box in the top left corner in which **(θ)** represents the angle of the wheel's rolling direction from the x axis, an angle known as *caster*. The axis of rotation 1 is the only axis that can be robot-controlled and helps orient the wheel in a given direction in the plane **(x-y)**, by doing this, the wheel's motion is constrained only along the direction defined by the caster angle **θ**. The continuous adaptation of **θ** allows the guidance of wheel's motion and generates desirable constraint effects to be discussed ahead in this section.

Conversely, as the wheel turns on axis of rotation 2, the CVT moves horizontally over the planar rolling surface **(x-y)**. This motion is fully controlled by the operator since he represents the Cobot's sole source of power. Note that there is no motion over the planar rolling surface **(x-y)** when the wheel turns on the axis of rotation 1, hence why CVT-based IADs are inherently passive and do not amplify human power.

Cobots mask inertia when the CVT turns appropriately on axis 1, i.e. by adjusting the caster, subsequently redirecting the Cobot's motion within the taskspace. The stiffness of the CVTs' mechanical properties enables the operator to perform these tasks transparently, even though the rolling speed remains the same, as stopping the object rests solely on the production worker.

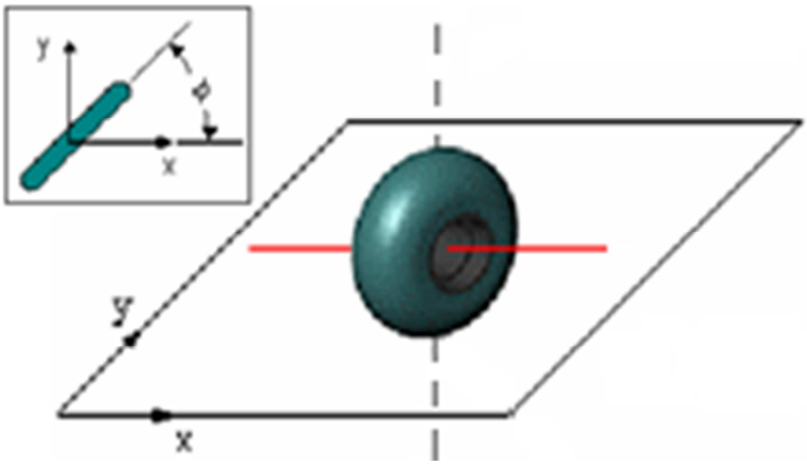

Figure 4.1: Isometric view of a translational CVT. The black dotted line denotes the axis of rotation 1, which is known as the caster angle. The red solid line is the axis of rotation 2, which is not controlled by the robot

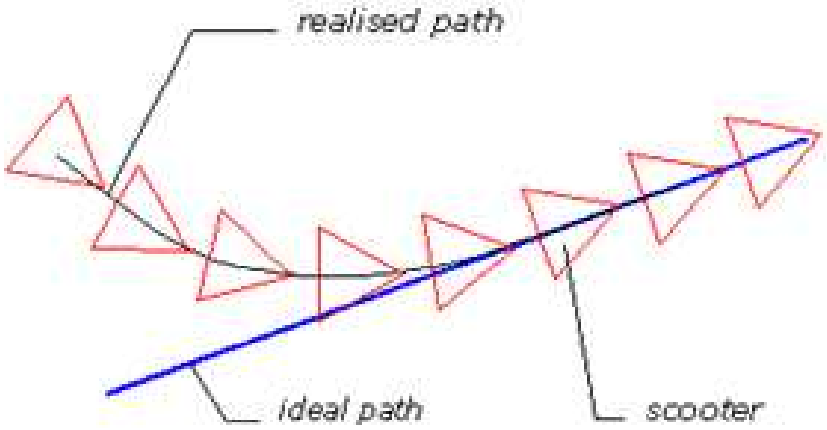

Figure 4.2: Transition from a realized to an ideal path following virtual path guidance. In this case, the scooter robot, from Section 4.6.3, is taken as example

Note that, although the CVT in Figure 4.1 possesses one single degree of freedom (steering angle on axis 1); it has a taskspace dimensionality of two and is therefore a *nonholonomic device*. Peshkin discusses in [141] an alternative definition for the nonholonomic nature of CVTs:

> *The capacity to control position but not speed rather than a reduction ratio based on gears (holonomic) helps regulate both speed and position.*

The IADs were conceived to assist line-production workers in handling tasks that usually require considerable physical efforts and become often repetitive. The IADs perform this role in a number of different manners. To explain them, it must be first presented the most remarkable capabilities resulting from the appropriate control of CVT in Cobots and IADs:

4.2.1 Virtual Path

A virtual path is a 1-D trajectory allowing for IAD motion. It provides the operator guidance via one-dimensional trajectories that expedite the handling of objects and decrease the rate of workplace accidents. A number of control algorithms may be used: force control, follow the carrot, pure pursuit and vector pursuit [33]. They can trace straight or circular trajectories or, in relation to 3-dimensional motion, paths with a smoothly varying curvature known as triple-clothoids. The use of virtual paths helps guide the operator through hazardous areas which require precision when handling large or heavy objects.

The sketch from Figure 4.2 shows the transition from a random initial position to the ideal path and the corresponding realised path. The approach stage from the initial position to the ideal path is soft, so that a slow variation of the curvature is exhibited.

4.2.2 Virtual Surface

Virtual surfaces are 2-D and 3-D renditions of one-dimensional virtual paths. Virtual surfaces constrain the IAD's taskspace to an established area or volume. A broader definition of virtual surfaces was presented by Colgate in [32]:

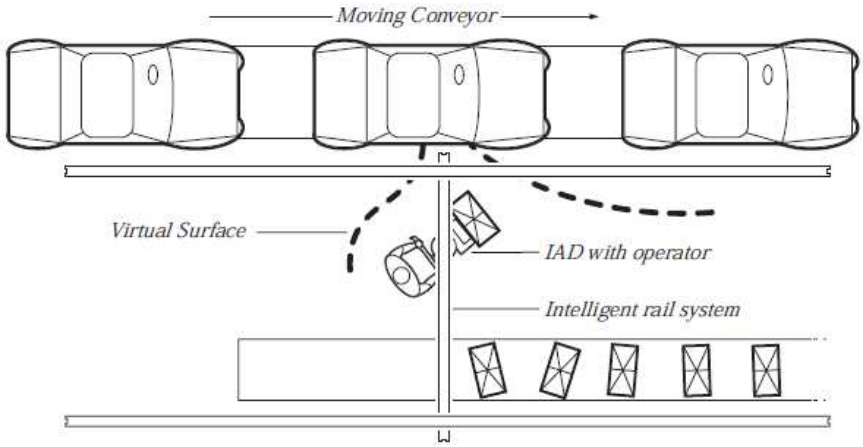

Figure 4.3: Example of virtual surface use in industrial settings. Image taken from [33]

IADs are capable of a much higher level of functionality using what are known as virtual surfaces. Virtual surfaces are so named because they are defined in software, but their effects are quite real. As illustrated in Figure 4.3, they can be used to guide operator and payload motion while preventing unwanted impacts. Virtual surfaces can improve productivity and ergonomics as well. By way of analogy, consider the familiar task of drawing a straight line on a piece of paper. While possible to do freehand, the task is done much faster and better with a ruler. Virtual surfaces are like rulers, only multi-dimensional, and most importantly, user-programmable.

4.2.3 Virtual Window

A virtual window is a small virtual surface forming a 3-D tunnel which enables the production worker to perform a task requiring surgical precision. Figure 4.4 shows an assembly line worker loading accessories into a vehicle while the IAD operates in virtual window mode. In [33], Colgate presented one instance of how virtual windows may be employed based on the situation of Figure 4.4:

As the operator approaches the vehicle, payload motion is guided such that the instrument panel passes through a virtual window aligned with the opening in the side of the vehicle.

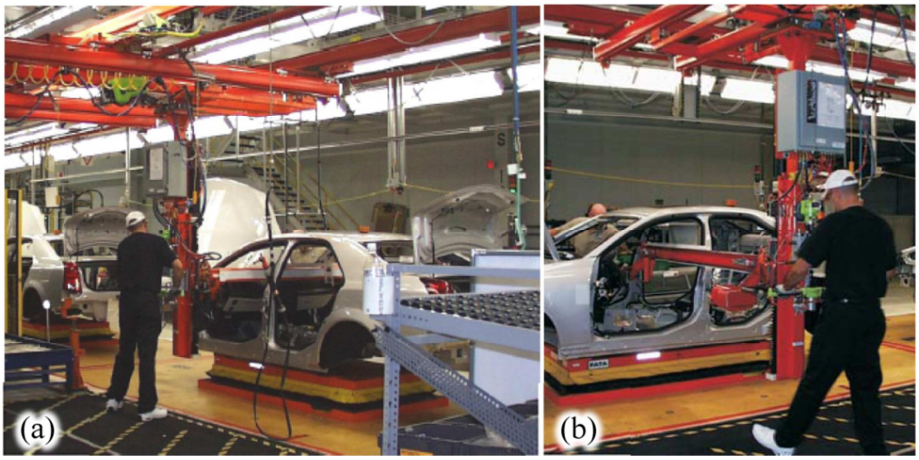

Figure 4.4: Assisted loading of vehicle accessories with IAD in virtual window mode. (a) Full view of the production line and (b) Zoom-in around the virtual window during cockpit installation

4.3 Power Amplification in IADs

As earlier mentioned in this Section the usage of CVTs ensures user safety as the resulting robot is inherently passive; the only available source of power is stemmed from the human operator. This has the advantage of being naturally limited to the user's capabilities, and thus, the exerted power is placed within secure limits. However, in some applications, it is necessary to provide power amplification and to provide inertia masking because the robot's load is simply too heavy for a human operator to be pushed. Also, inertia and gravity masking are desirable when attempting to quickly stop robot's motion and to avoid possible accidents and injuries to the operator.

Examples from Virtual Caster in Figure 4.3 and Virtual Window in Figure 4.4 have employed active versions of CVTs in order to mask the effects of inertia and gravity during cockpit installation in cars. For such a purpose, a modified version of the translational CVT from Figure 4.1 must be conceived in order to allow the assembly of *Serial Link Cobots*; this is the case of rotational CVTs that employ spheres to hold two angular velocities in proportion. Rotational CVTs are often designated in literature as *tetrahedral CVTs*. A detailed explanation on how rotational CVTs operate is out of the scope of this thesis. However a brief description of its operation is next presented.

The concept and the kinematical basis of tetrahedral CVTs were introduced by Moore in [118]. A tetrahedral CVT consists of a sphere held by four rolling discs that conveniently adjust the rotation speed of the sphere in order to rotate the robot's serial link around the sphere's center. A picture of a CVT is shown on Figure 4.5.

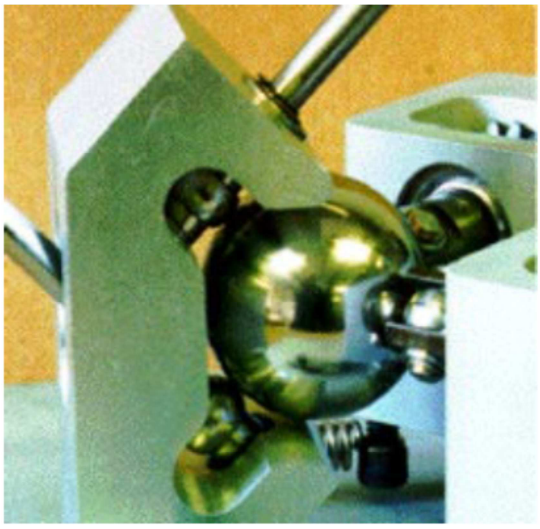

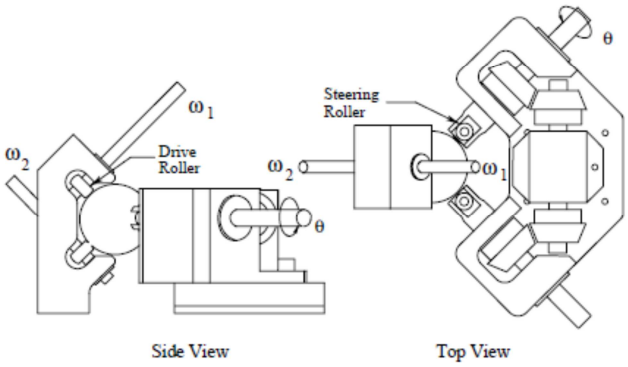

Figure 4.5: Top: Picture of a tetrahedral CVT. Bottom: Sketch of side and top views of a tetrahedral CVT. Both images taken from [118]

Implementations of active CVTs in IADs are highly desirable since they combine the benefits from CVT while providing power amplification. On one side, the CVTs are capable of generating abrupt transitions from free to constrained surfaces, which is a desirable characteristic when providing motion guidance along predefined paths. On the other side, inertia masking and power amplification are desirable when dealing with heavy loads.

Next Chapter deals with the operation modes of Cobots (inherently passive devices) and IADs (active versions of Cobots):

4.4 Operation Modes

The Operation Modes define the *principles and paradigms that the Cobot motion planning must follow*, this is, they are the core of the of the Cobot's intelligence, but do not specify the type of interface existing between the Cobot and the Operator, this issue is described in the *IAD Control Modes* from Section 4.5. The following operation modes can be identified in both: Cobots and IADs:

4.4.1 Virtual Caster

The definition of Virtual Caster applies to Cobots that use CVTs to generate constraints, although its application may also encompass powered IADs. Under this mode, the caster of the CVT's wheels aligns with the operator's applied force on the IAD enabling the Cobot to freely move. This operation mode is later exemplified in Section 4.6.1 when the Unicycle is presented.

Nonetheless, one must remember that since passive Cobots do not mask linear inertia, the operator must apply force in the rolling direction he wishes to travel even though the caster of the wheels is correct. The Cobot senses the operator's intent using force sensors installed at the device's user interface. Section 4.6 presents some examples of Cobots working under this principle.

4.4.2 Virtual Wall Mode

The Virtual Wall Mode only takes effect when the Cobot approaches the boundary of a virtual surface or a virtual wall. When this occurs, the CVT's caster is reoriented such that the only translation permitted is parallel to or away from the wall. In other words, during the contact of the Cobot with the Virtual Wall, the user's forces are classified in two categories: force components that push the Cobot into the wall or away from it. The components of force away from the wall turn the Cobot into *Virtual Caster Mode*, and thus the user can easily push the Cobot along the virtual wall or pull it back into the unconstrained space. Conversely, the components of force into the wall are discarded and the only allowed motion is tangent to it. Section 4.6 presents some application examples of Cobots switching from Virtual Wall Mode to Virtual Caster Mode.

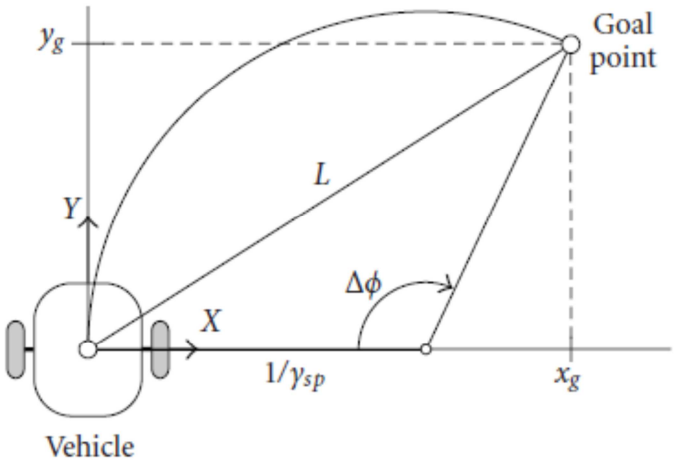

Figure 4.6: Diagram of the Pure-Pursuit strategy. Image taken from [120]

4.4.3 Pure Pursuit

The Pure Pursuit Mode works by calculating the curvature that will move a Cobot/IAD from its current position to any goal position within the taskspace. The idea behind the algorithm is to choose a goal point position that is some distance ahead of the Cobot on the path. The name pure pursuit comes from the analogy that is used to describe the method. Typically, it is common to think of a vehicle as chasing a point on the path some distance ahead of it, i.e., it is pursuing that moving point.

The Pure Pursuit Mode takes into account the current caster angle of the CVT, as well as the current linear speed of the Cobot, and defines a goal point that ensures a smooth trajectory. For the case of Figure 4.6, a circular trajectory is traced between the Vehicle and the Goal Point, but any desired trajectory can be defined. In certain situations, paths with a smoothly varying curvature are defined. Such is the case of clothoids [117], which are able to provide a constant angular acceleration.

4.4.4 Impedance Control in IADs.

Impedance control has been an active research area in robotics throughout the years. Several servo controlled robots have used this control scheme to provide a natural way of interacting with the environment and the user. For the case of Cobots and IADs, impedance control is only possible in the latter devices because the concept of impedance control is inherently associated with power amplification.

On a brief, an impedance controlled manipulator is run on the basis of a mass-spring-damper model, whose respective parameters, Mass **m**, Spring Constant **k** and Viscous Damping Coefficient **b**, affect the natural response of the manipulator to an external applied force $\mathbf{F_{ext}}$. The target manipulator/IAD endpoint position is derived from a differential equation which takes into account the system parameters and the external force as next:

$$F_{ext} = m\ddot{x} + b\dot{x} + k(x - x_0) \quad \textbf{(4.1)}$$

Where $\ddot{x}$, $\dot{x}$ and x are the acceleration, speed and position of the robot's endpoint respectively. The parameter $\mathbf{x_0}$ is the equilibrium position at steady state in the absence of any external force.

The concept of Impedance Control was first introduced by Hogan [67] in the mid 80's, since then, many versions and applications of this control scheme have been developed. Impedance control is a widely used control scheme to deal with robot motion. In fact, all of the IADs reported in Section 4.6 have used the impedance approach to deal with inertia masking, and to generate motion commands under unconstrained space. Chapter 5 presents a 6-DOF manipulator running on the basis of impedance control, so additional considerations regarding this control scheme are later addressed.

4.5 Cobot and IAD Control Modes

Previous Section introduced the principles and paradigms in the motion planning of IADs and Cobots. This section explains the diverse manners in which humans and Cobots/IADs *interact* by the way of *Control Modes*.

4.5.1 Float Mode or Hands-on-Payload

When a Cobot or an IAD is set to the hands-on-payload mode, the operator applies force directly to the payload or the robot. The sensory system is responsible for perceiving and interpreting these commands, while the control system then uses actuators to proportionally coordinate robot's motions.

The hands-on-payload mode operates under the same principle with IADs and Cobots. As regards to the first, the servomotors controlling the joints move in proportion to the operator's applied force. With Cobots, the caster of the CVTs adjusts based on the direction of the applied force.

Despite the natural advantages provided by the Float Mode, it is common that instability problems occur under certain conditions. In [31], Colgate addressed this issue which stems from the fact that the robot's actuators and force sensors are not located in the same place. Instead they are linked by robotic transmissions or structural components, something which could affect force sensing and must be taken into account. For instance, most robots' actuators are positioned at the joints, while the force sensors are positioned on the end-effector. The structure linking the joint to the end-effector should be characterised and taken into account when designing the equipment's control scheme, otherwise the system might become unstable. This circumstance is known as *non-colocation of sensors and actuators*.

4.5.2 Hands-on-Control Mode

In hands-on-control mode, the operator controls the IAD using a joystick or a remote control unit. This is the conventional control method used to guide non-autonomous robots, allowing for teleoperation [159] and, more recently, remote surgery [37].

This type of control has a number of associated drawbacks when attempting to maximize processes' productivity. Dejong touches upon the most significant issues [41],

which include the numerous mental transformations the operator is forced to perform and the lack of an environmental feedback, so when possible, the Float Mode must be preferably used. But in certain applications it is simply not possible that the operator and the robot have a direct interaction and the only solution left is to recur to a Hands-on-Control scheme.

Fortunately, a new field of research called haptic feedback enables the operator to sense texture, restricted motion and vibration through the control element, simulating direct interaction between the operator's hands and the IAD-handled payload. In [41], DeJong uses virtual surfaces to constrain the motion of a telerobot operating in a decommissioned nuclear power plant. The operator controlling the IAD perceives the motion constraints through the joystick at a distance of **16 Km** from the plant. This is an example of how haptic feedback can make robotics substantially more ergonomic.

4.5.3 Hands-off Mode.

This is a semi-autonomous control mode in which repetitive routine movements can be programmed. This property is useful when attempting to get the most from the operator's time by automating the tasks which do not require the operator's supervision.

Typically, an IAD can switch among the 3 described modes depending on the handling requirements at any given time. Recalling the study-case presented by Colgate in Figure 4.3, the following comment can be cited to exemplify the advantages of using the Hands-off Mode [33]:

> *The IAD can also be programmed to perform semi-autonomous functions such as returning to a home or loading position, automatically retrieving a new part or synchronising with a moving assembly line. Semi-autonomous operations allow the operator to focus on value-added tasks (which robots cannot perform), while the IAD takes over routine movements.*

It is important to note that Cobots cannot operate in this mode, as they are inherently passive. Semi-autonomous tasks are possible only on IADs.

4.6 IAD Development through Time. Significant Cobots and IADs

Sections 4.4 and 4.5 went through the Operation and Control Modes of Cobots and IADs; these two concepts have provided a basic guideline for the design and construction of assistive robots, but little has been said about the prototypes developed under such principles. This section comes with such an issue by presenting the most relevant developments of Cobots and IADs which were initially conceived in labs as research projects, and were later brought to industrial environments.

This section presents a brief description of the most significant Cobots and IADs in chronological order of their appearance:

4.6.1 Unicycle

The unicycle was the first Cobot developed by Northwestern University and the first Cobot prototype ever made [141]. The Unicycle is rail-mounted Cobot exhibiting a very

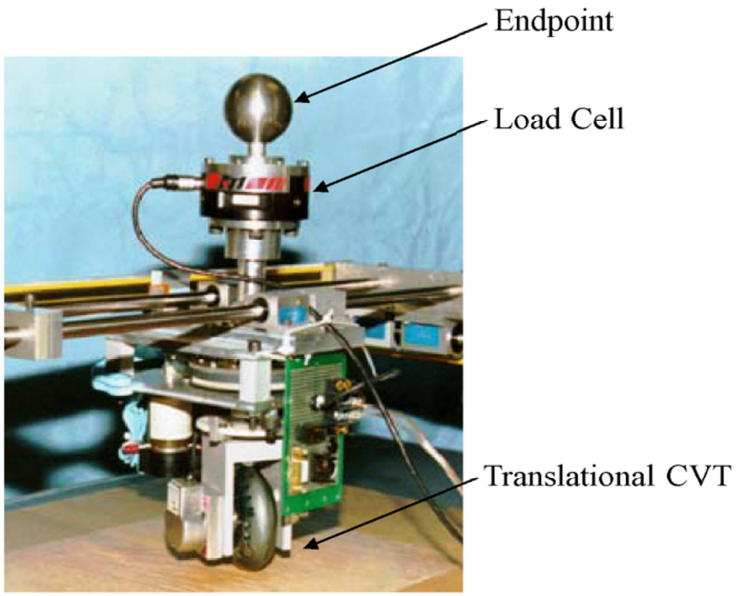

Figure 4.7: Photo of the Unicycle indicating its main components. Image taken from [141]

limited taskspace. However, it allowed testing the feasibility of the concepts of Virtual Paths and Virtual Walls which were previously described in Sections 4.2.1 and 4.2.2 respectively.

It has one single translational CVT that provides a taskspace dimensionality of 2 **(x-y)**; it is inherently passive and possesses a single controllable degree of freedom **(θ)**. Figure 4.7 shows the unicycle and its most important components.

The Force sensor employed in the Unicycle was of load-cell type and collects the user applied forces over the endpoint. The force sensor data and the encoder data were both used to switch between the Operation Modes of Virtual Caster and Virtual Wall as described earlier in Section 4.4.1 and 4.4.2. The lessons learned from the Unicycle operation were of great importance towards the development of more complex and larger IADs.

4.6.2 Unicycle Two Link Arm (UTLA)

This Cobot, the two-joint version of the unicycle, was developed by Northwestern University. Like the unicycle, the UTLA possesses one translational CVT, a taskspace dimensionality of 2 **(x-y)** and one degree of freedom **(θ)**. Figure 4.8 shows the UTLA and its components:

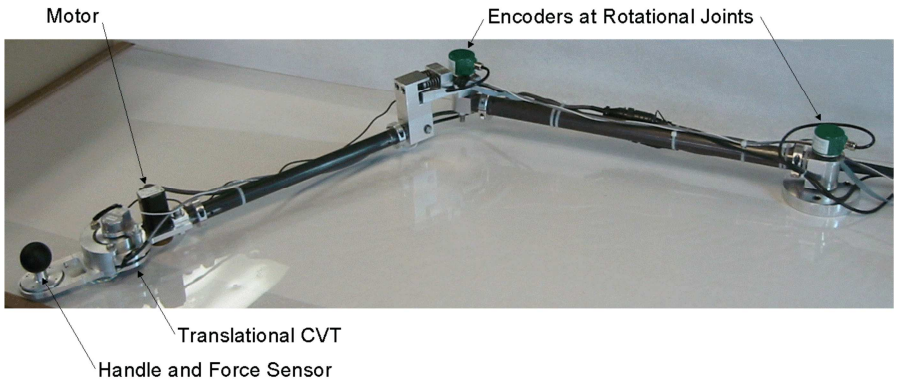

Figure 4.8: Photograph indicating UTLA parts. Image taken from [170]

The two link arm from the UTLA came to solve the limitations imposed by the reduced workspace in the Unicycle [170]. By providing the UTLA with a serial configuration, the workspace was considerably increased and additional tests can be thus performed. The UTLA was especially useful to study the best transition function that most naturally suit to human operators. It must be remembered that CVT can provide hard transitions between constrained and unconstrained spaces, and the study of such transitions requires a test bench for assessing the performance of the different control algorithms. The wide workspace provided by the UTLA resulted ideal to such experimentation.

A detailed formulation of the Operation modes from Section 4.4 was presented by Wornsopp using the UTLA [170]. Such algorithms were previously tested on the Unicycle, but more complex and wider paths were experimented using the UTLA.

Despite the UTLA was merely a research project, the lessons learned from it were of paramount importance towards the development of more complex and useful Cobots, such as the 3-DOF Arm Cobot from Section 4.6.4, and the Jib Crane from Section 4.6.6.

4.6.3 The Scooter or Tricycle Cobot

The scooter is a three wheeled robot with a taskspace dimensionality of 3 **(x-y-ϕ)** and consequently three degrees of freedom **(θ_1-θ_2-θ_3)**, one for each wheel.

Following with the evolution of the Unicycle and the UTLA, the Scooter does not require a stationary support to remain upright, see Figure 4.9a. Also, the addition of a third wheel to the scooter allowed the Cobot to orientate within the taskspace; these improvements provided the Scooter with the required flexibility to operate in industrial environments [168].

A modified Scooter was adapted to assist in the removing of doors from newly paint auto bodies prior to assembly of the cabin. The scooter has demonstrated to be a rugged yet highly manoeuvrable device at the GM facilities, see Figure 4.9b. During the approach stage, a Virtual Surface is created to close the Scooter to the vehicle's rocker panel, guiding the Cobot to the appropriate location to grip the door without scratching the car's paint. The operator is only responsible for providing the required power to move the Scooter and load, and to push the *lock button* when the Scooter and the door are perfectly aligned.

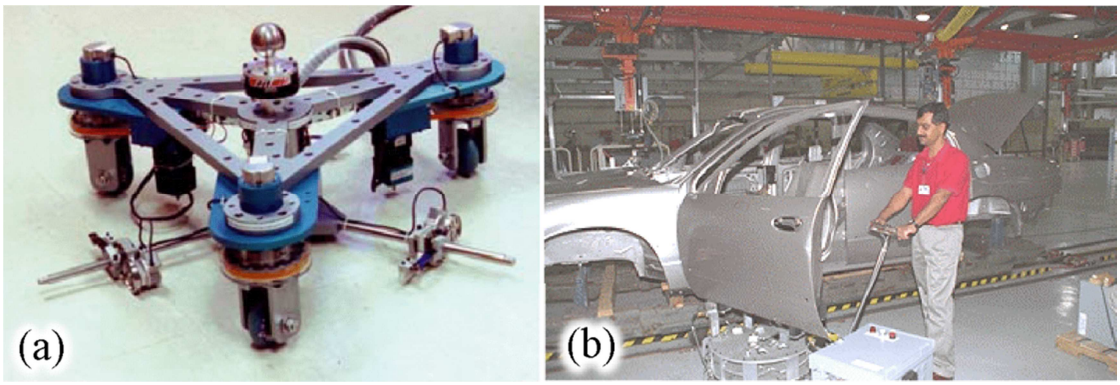

Figure 4.9: Photographs of the tricycle. (a) Photo of the Scooter with three small planimeter wheels to infer the rolling sped of the steered wheels. (b) Industrial implementation of the Scooter in a GM facility. Image taken from [141]

During door disengage; the Scooter operates in Virtual Path Mode [141]. The scape trajectory is defined such that the door remain perpendicular to the car's body at any time, by doing this, the door's bolts naturally separate from the car avoiding backlash and scratches in the paint. This a clear example of *motion assistance* provided by a Cobot.

The Cooperation between Northwestern University and GM brought into industry several Cobots and IADs. Section 4.6.5, describes the IAD known as *Rail Cobot* which was used to install the car's cockpit after the Scooter has removed the door from the newly paint car.

4.6.4 3DOF Arm Cobot

The 3-DOF Arm Cobot uses tetrahedral CVTs to recreate a robot with a conventional serial link configuration. The 3-DOF Arm Cobot is the natural evolution from the UTLA and the earlier Unicycle operating in a 2-D taskspace. However, in order to evolve from a 2-D to a 3-D taskspace **(x-y-z)**, a new type of CVT had to be implemented. This is the case of tetrahedral CVTs which were earlier described in Section 4.3.

The Arm Cobot is a three-joint parallelogram manipulator with a reach of **90 cm**, see Figure 4.10. Following the design concepts from its predecessors, the Arm Cobot interfaces with the user through a force sensor installed at the end effector. The sensor is responsible of gathering the user intention, and then, to allow or block Cobot motion according to the end point position. However, since power amplification is required, each CVT shares contact with a common central wheel which is powered. This turns the 3-D Arm Cobot into an IAD.

Power amplification is required for multiple reasons such as: to overcome the gravity effects over the z-axis, but also to mask linear inertia over the rest of axes. Inertia Masking is of great importance when dealing with heavy loads in industrial environments in order to avoid lower back injuries in operators when stopping heavy loads. An in-depth description of the mechanical design regarding the 3-D Arm Robot is out of the scope of this document, but it is available at [119, 141]. The 3-D Arm Robot operates under the same principles as the above described Cobots with the difference that Virtual Paths can be defined following 3-D trajectories.

The implementation of Virtual Surfaces using CVT in serial link Cobots brings a series of advantages over the traditional servo controlled robots. For instance, when attempting to redirect robot motion under a heavy load condition, a servo controlled robot must exert a considerable great torque over the links to deal with the load and the self-robot inertia; and thus; the greater the load held is, the more powerful motors are required. On the opposite side, a Cobot employing CVTs lies on the mechanical stiffness provided by the CVTs to redirect Cobot's motion. This passive approach yields low power consumption and a greater reduction in the power requirements of the Cobot's motors. From the safety standpoint, the lower the rated power is in the robot actuators, the safer the robot becomes, since less harm can be exerted over the operator in case of robot malfunctioning or operator's inattention.

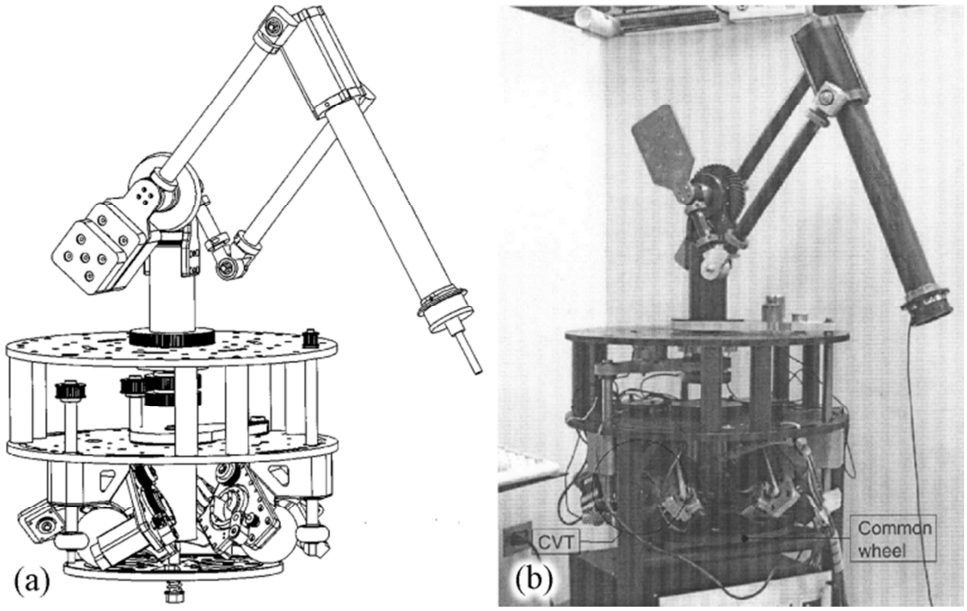

Figure 4.10: The 3D Arm Robot. a) Sketch of the Cobot showing the three tetrahedral CVTs connected in parallel through a common wheel for power amplification. b) Photograph showing the realization the Arm Cobot

4.6.5 The RailCobot

The *RailCobot* is the project name given to an IAD running on the basis of an industrial overhead rail system. It possesses a taskspace dimensionality of 3 **(x-y-z)** and has been designed with the same kind of rotational CVTs as the 3DOF Arm Cobot. It transfers power and generates virtual surfaces by way of belts [32, 141]. Sketches of the RailCobot from different angles are shown on Figure 4.11.

The Rail Cobot project was developed in joint partnership between Stanley Assembly and Northwestern University, and it was the first IAD taken straight into production for assembling tasks. The industrial version of the Rail Cobot was commercialized under the same name, but further additions to the original prototype were made to enhance system flexibility; these improvements embrace specific end effector tools for performing different tasks, but also the possibility to work in Hands-off Mode [32].

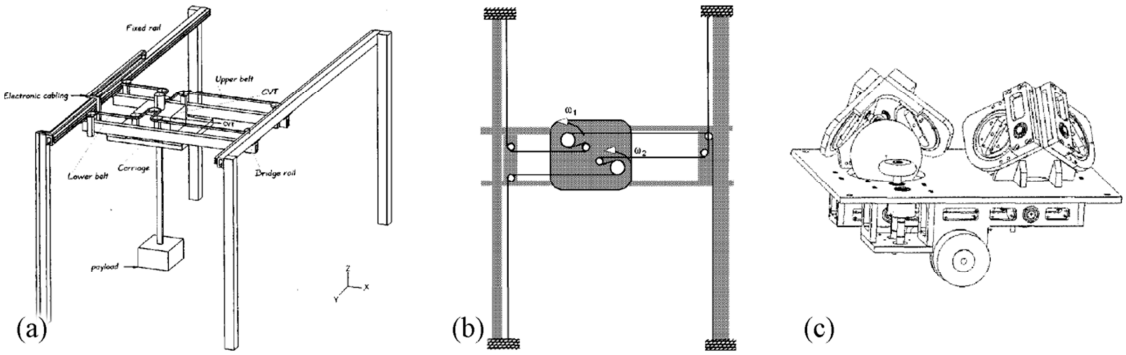

Figure 4.11: Sketches of the Rail Cobot. a) Isometric view of the crane indicating its components. b) Top view of the belt system for the **(x-y)** motion. c) Tetrahedral CVTs to drive the Cobot's belts

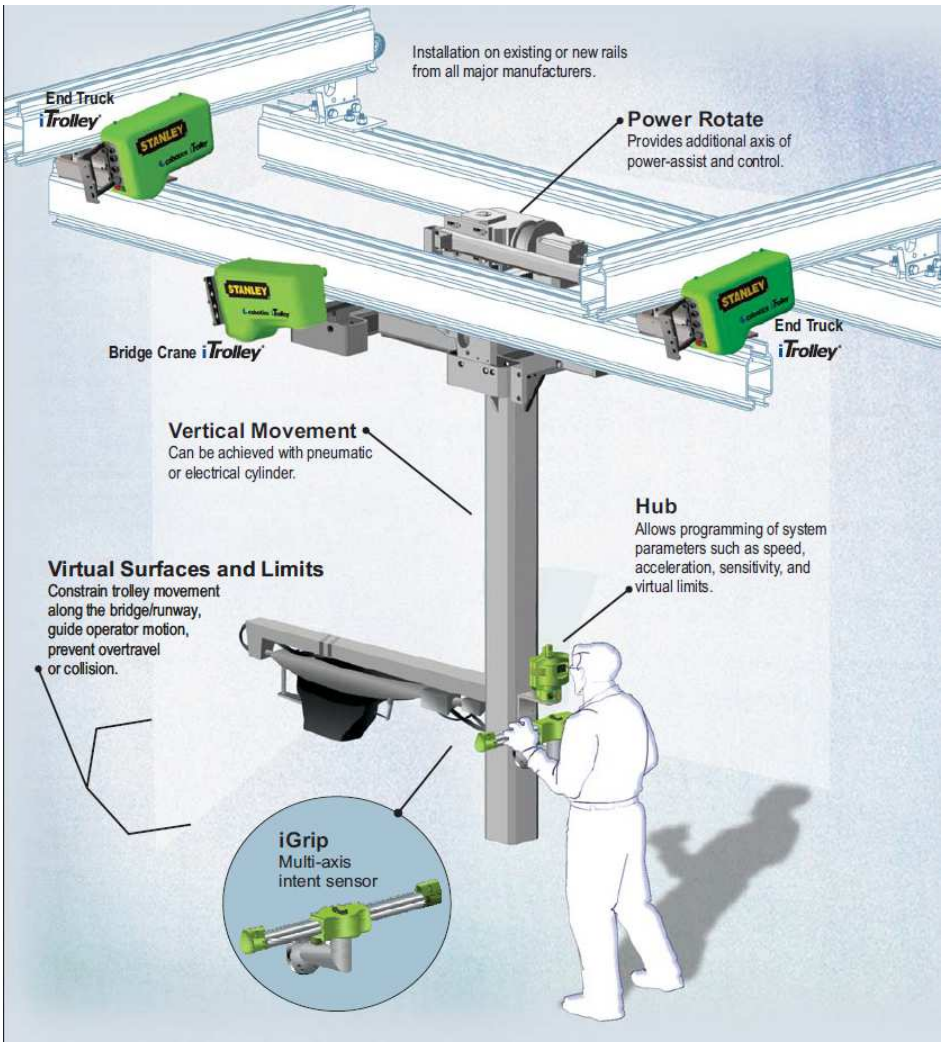

Figure 4.12: The *RailCobot* crane manufactured by Stanley Assembly. Image taken from the Stanley Assembly Cobotics Brochure [155]

The Stanley version of the RailCobot interfaces with the operator through a Multi-Axis Intent sensor mounted on the opposite side of the Cobot's end-effector, see Figure 4.12. This design pattern is consistent with the previously described realizations of the Unicycle, UTLA and the 3D Arm Cobot. It must be recalled from the ideas given at the beginning of this Chapter that the design pattern of user interfaces should avoid the usage of pushbutton or levers, and instead, a more natural way of interaction should be provided. The gripper of Figure 4.12 attempts to provide a straightforward interaction between the load and the operator, in fact, the gripper from the RailCobot falls within the control mode of *hands-on-payload*, which was previously described in the Section 4.5.1.

The RailCobot has been used together with the Scooter Cobot in the GM facilities to install the cockpit during car assembly as earlier shown on Figure 4.4. While the Scooter is used for removing the door after car painting, the RailCobot is used in the next stage for installing the car's cockpit.

The usage of the RailCobot, in combination with the appropriate end-effector tool, gives a huge boost to the overall productivity in production lines. The level of automation is so high and repeatable, that production lines do not need to stop on

each assembly stage, instead, they are continuously running at a constant, yet low, speed as the car is assembled, see Figure 4.4. Under such scenario, the RailCobot can be configured to automatically return to its original (predefined) position, after placing the cockpit in its final position, and then pick a new cockpit for assembling the next car. Since this return-to-origin task is highly repetitive and does not involve an assembly by itself, it is possible to program the RailCobot to perform it autonomously. This is an example of the *hands-off mode*, as earlier described on Section 4.5.3.

4.6.6 Jib Crane

The concept version of the Jib Crane consisted of a floor mounted, free rotating column, with a Hoist Trolley at end for z-axis lift, see Figure 4.13a. The typical control interface for a Jib Crane includes a panel with two buttons (not shown on the figure) for lifting and lowering the load. This button-type panels are commonly encountered on the Manual Assist Devices, MAD, as earlier described at the beginning of this Chapter.

In order to allow a full automation of the Jib Crane and to improve its user interface, a deflection sensor was added at the Hoist Trolley to read the user's intention over the tangential and radial directions. The deflection sensor works by measuring the wire deviation from its vertical position, as summarized in Figure 4.13b. The deflection angle, $\boldsymbol{\delta}$, is proportional to the applied user force, $\mathbf{F}$, and consequently robot motion is initiated depending on its magnitude [123]. The deflection sensor of Figure 4.13b is installed to read only the tangential component of the user applied force with respect to the Crane's Boom, but a second sensor can be added over the Radial direction to move the Hoist Trolley proportionately.

The combination of the Cable Deflection Sensor and the Jib Crane became a successful commercial product resulting from the joint venture between Northwestern University and Stanley Assembly. The Jib Crane is marketed under the designation of *iTrolley* by Stanley Assembly as presented in Figure 4.14. The *iTrolley* was previously cited in Section 2.5 when the importance of load cell to robotic developments was introduced.

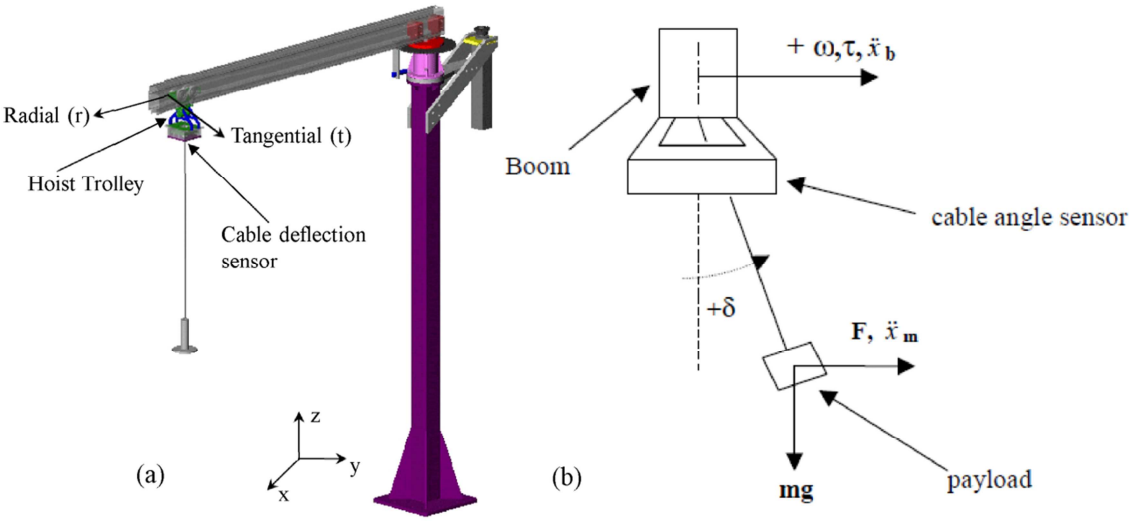

Figure 4.13: Sketch and Diagrams of the Jib Crane. a) Concept version of the Jib Crane. Image taken from [138]. Functioning of the Cable Deflection Sensor over the tangential axis. Image taken from [123]

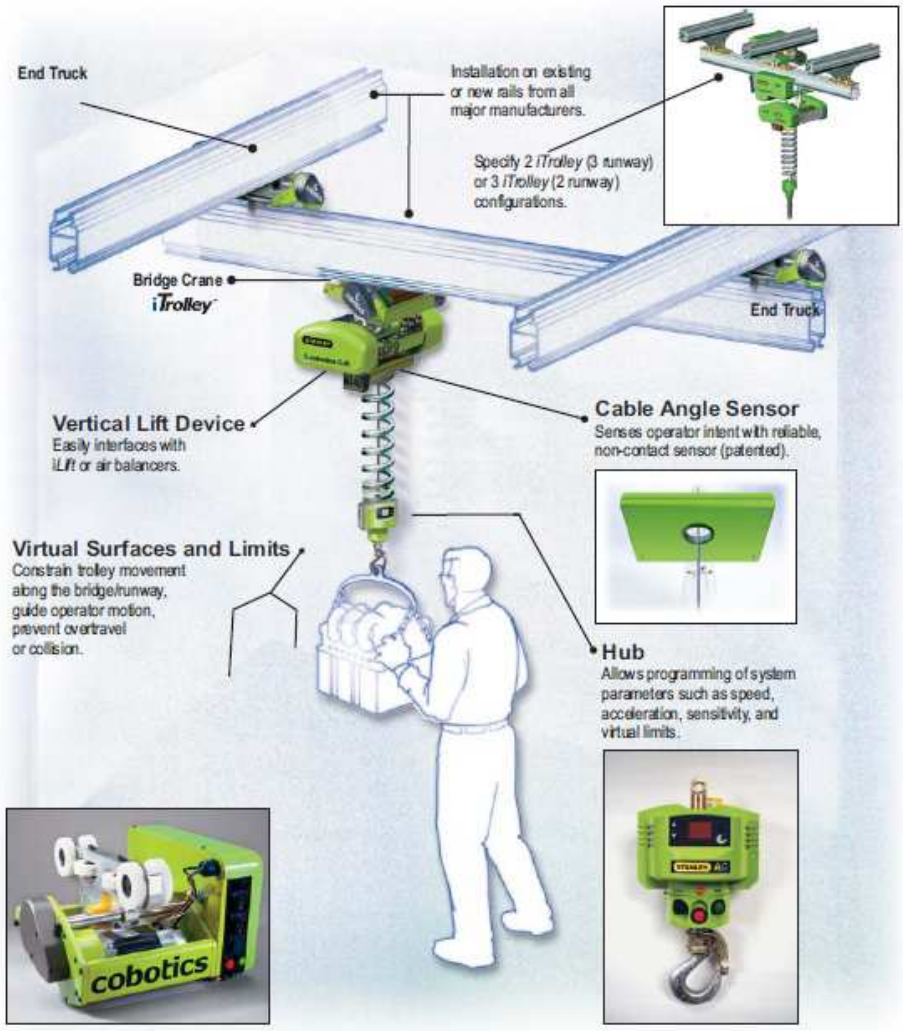

Figure 4.14: The *iTrolley* marketed by Stanley

The free Rotating Column from the Concept version of Figure 4.13a has been replaced by a more robust Overhead Rail System, which is also compatible with several Industrial Rails already installed on factories and assembly facilities. The Overhead Rail System is also compatible with the Rails employed in the *RailCobot*. The standardization of assembly tools yield a productivity increase since more and more tools can share the same workplace while simultaneous tasks can be performed [32]. Also, the production line becomes more versatile since assembly tools can be relocated within the factory at no cost.

However, the most relevant add-on provided by the *iTrolley* is the ability to operate on a handler- and button-less basis when moving over the **(x-y)** plane; this is possible due to the Cable Angle Sensor installed on the Hoist Trolley. This provides the operator a great flexibility and manoeuvrability since direct contact between the load and the operator is possible. This Interface is a clear example of the *hands-on-payload mode*. It must be recalled that the Operation Modes of Virtual Wall and Virtual Path are also applicable to the *iTrolley* as remarked in the sketch of Figure 4.14.

The Cable Angle Sensor allows the human intention detection over the x- and y-axes, but in order to move the robot over the z-axis a different type of sensor must be provided. The joint venture between Northwestern University and Stanley Assembly

came up with a slide handle to overcome this problem. The handle is typically integrated between the hoist and the load, so that the operator must simply hold it and grasp to the desired direction in order to lift or lower the load as shown on Figure 4.15. This solution has been designated as *iLift*. This control scheme is an example of the *hands-on-control Mode* as it uses a handle to interface with the operator.

Nonetheless, once the load is lifted, it is possible to activate the *hands-on-payload* mode because the system is capable of sensing the load's weight and then respond to the user applied forces over the z-axis. For such a purpose, it has been integrated a hub panel with buttons to switch between both control modes.

The *iLift* is typically integrated with an *iTrolley* solution for allowing load motion over the entire workspace. In fact, Figure 4.14 shows an *iTrolley* unit for moving the load over the **(x-y)** plane, and an *iLift* unit for moving the load over the z-axis.

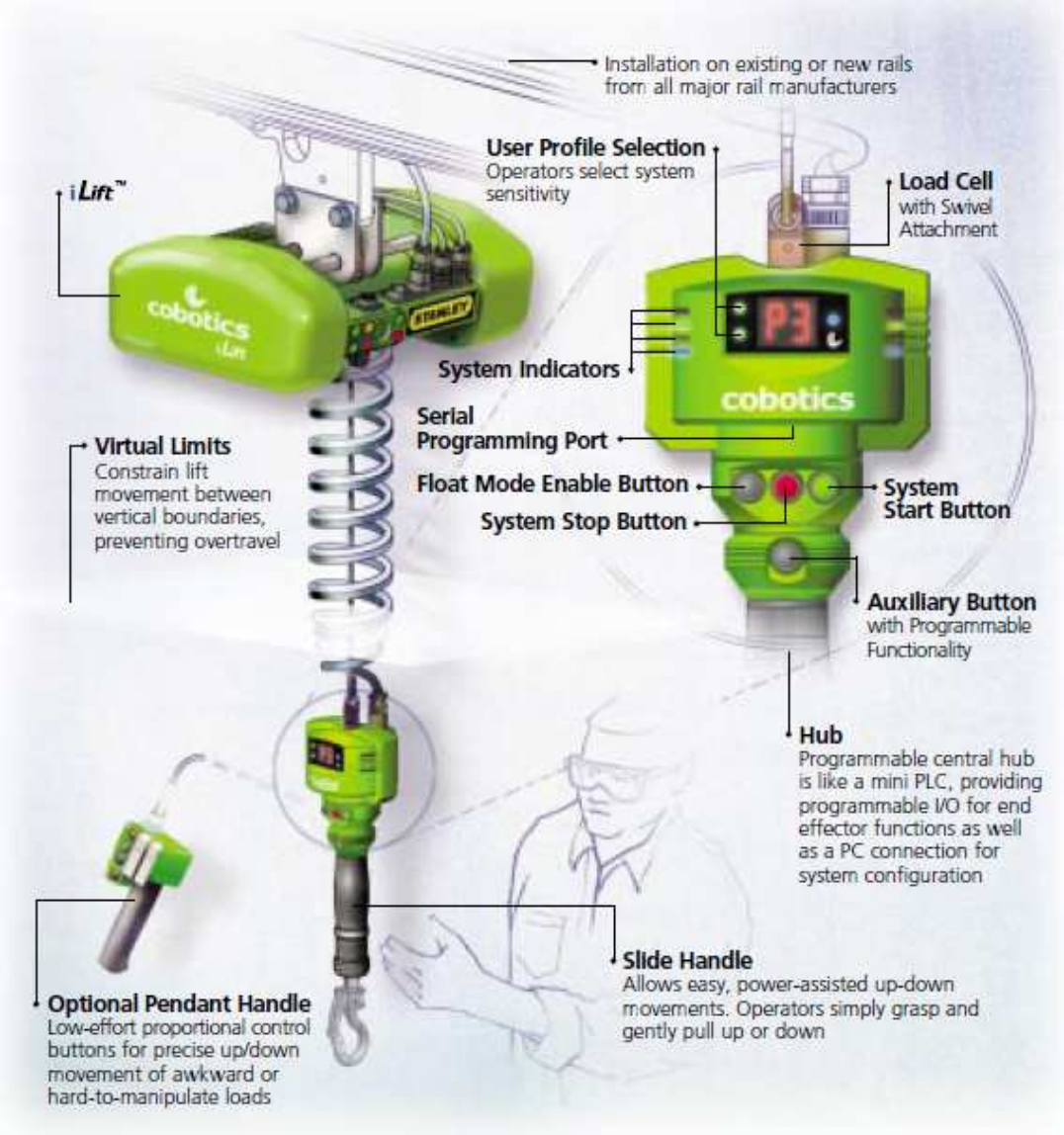

Figure 4.15: The *iLift* marketed by Stanley

4.7 Comparative Analysis of Cobots, IADs and traditional servo controlled robots.

Previous Sections have described the working basis of Cobots and IADs. However, little has been said in regard with the advantages and disadvantages that such systems offer when compared to traditional servo controlled robots. This section comes up with such an issue by providing a comparison of the three technologies under the basis of four criteria: generation of Virtual Surfaces, Safety, Inertia Masking, Efficiency and special remark on the *User's Interface*.

4.7.1 Generation of Virtual Surfaces

This aspect was previously discussed in Sections 4.2 and 4.6. However, in order to emphasis the advantages provided by CVTs over the traditional servo controlled robots, it is cited the following statement from DeJong [41]:

> *By utilising nonholonomic constraints within these transmissions, rather than powerful actuators, it can create haptic virtual surfaces that are very stiff (50kN/m) in the constraint direction yet very smooth tangentially.*

In other words, in order to generate surface tensions of **50 KN/m** with conventional actuators, such actuators have to be powerful and consequently very large. In the case of CVTs, it is the device's inherent mechanical stiffness that generates the constraint, not a powered actuator.

The Generation of Virtual Surfaces is probably the clearest advantage of Cobots and IADs over the traditional servo controlled robots.

4.7.2 Inertia Masking

Whereas the unpowered Cobots are able to reduce steering inertia, they cannot mask linear inertia. Owing to their active nature, IADs can mask both kinds of inertia, giving them a significant advantage over the unpowered Cobots.

Nonetheless, Peshkin remarked a practical drawback inherent in steering on the powered IADs [141]. The example Peshkin sets forth is associated with the above-mentioned Rail Cobot from Section 4.6.5, where although CVTs generate constraints, a drive motor expedites the payload's linear motion, making it an actuated Cobot, i.e., an IAD:

> *The drive motor is adequate to overcome the inherent friction of the rail system and belts, and to considerably ease the human effort required to bring a 150-kg payload from rest to a speed of 2 m/s. For safety reasons, one would not want a motor of greater than human power. By comparison, turning the payload through a 90-degree bend, with a turning radius of 30 cm, when it is travelling at 2 m/s, would require a 4000-W motor, if our virtual walls relied for their strength on motors rather than CVTs.*

Steering inertia is masked with little effort on account of the CVTs' mechanical stiffness. Alternatively, if drive motors were the sole means of generating constraints, the actuators would have to be very powerful.

4.7.3 Safety

Safety is a highly sensitive issue when it comes to designing IADs that interact directly with operators, i.e. under the hands-on control scheme. Whereas an unstable IAD response to the operator's command or a collision could cause harmful physical damage to the workspace and/or operator, the device's stability must be ensured at all times.

Since Cobots are inherently passive, the operator is the only subject that can apply power and move the payload. As a result, the operator's safety depends entirely on his skills and abilities to remain attentive to the displaced objects.

IADs have actuators that amplify power. If the system is stable, safety in the shared workspace is guaranteed but accidents may still occur due to an operator's neglect. Nonetheless, the system is safer if drive motors are of less than the human's power. Yet this solution for ensuring safety is not always viable, as increasingly powerful drive motors are required to move heavier payloads.

From the Safety standpoint, Cobots and IADs provide a greater level of safety compared to the traditional servo controlled robots that employ powerful motor to provide Inertia Masking and Virtual Surfaces.

4.7.4 Efficiency

It is not surprising that IADs result more efficient than traditional servo controlled robots, since typically the latter must employ powerful actuators to provide the effects of Inertia Masking and Virtual Surfaces under heavy load conditions. In other words, less power is required to generate such effects when CVTs are used together with an adequately sized motor rather than relying solely on actuators.

Faulring touches upon certain advantages of holonomic transmissions as regards to efficiency [47]:

> *Cobotic technology provides a highly power and weight efficient transmission architecture that can have minimal dissipation and trivial dynamics. Gear trains, timing belt transmissions, hydraulic and pneumatic systems as well as cable systems all have dissipative losses that result in heat and noise generation. In addition, stiction, friction, compliance and backlash in these transmissions add highly nonlinear dynamics to mechanisms. Cobotic transmissions utilising bearing quality steel components in dry-friction rolling-contact have none of these nonlinearities.*

The efficiency term is not applicable to the passive Cobots, since no power is drawn by any motor to allow load displacement.

4.7.5 User Interface

Special focus has been placed on the designing of friendly user interfaces for Cobots and IADs. This has been a common approach for most IAD designers [26, 33, 41]. Section 4.5 introduced the Hands-on-payload mode and the hands-off mode as two different approaches that attempted to provide a natural way of interaction between humans and IADs. Above examples of the Rail Cobot and the Jib Crane, from Sections

4.6.5 and 4.6.6 respectively, are only some examples that follow the design criteria of Section 4.5. However, such interfaces should not be confused with the IAD design itself, because they can be implemented on a traditional servo controlled robot regardless of whether CVTs or servomotors are employed.

The ideas behind the design of user interfaces are the same regardless of the type of actuators and transmission employed. Conversely, different user interfaces should be designed according to the type of task performed by the robot. For the case of robots that work in direct cooperation with humans, a general design pattern can be summarized based as follows: make more natural the interaction between human and machines by using an intuitive framework demanding little or null training from the user, while ensuring safety in the workplace and providing comfort to the operator.

4.8 Conclusion and resume

An overview of the concepts and ideas regarding the Intelligent Assist Devices was presented in this Chapter. The motivation behind the IAD design was also presented together with plenty of industrial applications that reported the usage of such devices for semi-autonomous tasks under time-shared and shared-workspace conditions. Special interest has been placed on documenting the joint venture between Northwestern University and Stanley Assembly which produces a series of successful developments of IADs such as the *iTrolley* and the *iLift*.

A comparative analysis between the traditional servo controlled manipulators and the more recent Cobots that employ Continuously Variable Transmissions CVTs was presented. The comparison concluded that Cobots employing CVTs are better in multiple aspects ranging from virtual surface generation, inertia masking, safety and efficiency. The outstanding performance of the Cobots running on the CVT-basis lies on the mechanical stiffness of the CVTs to provide motion reorientation using less energy when compared to traditional servo controlled robots.

Multiple forms of interaction between the robot and the user were discussed, ranging from direct interaction approaches, such as the *hands-on-payload mode*, to traditional control techniques based on push button and levers; this is the case of the *hands-on-control mode*. Also, semi-autonomous solutions for repetitive tasks were explored under the *hands-off mode* designation.

Chapter 5

5. Dataglove-based Interface for the Impedance Control of Robotic Manipulators

This section describes the application of an impedance control approach to a 6-DOF Manipulator using the input data provided by a dataglove-based interface which is capable of collecting the user applied force.

The interface uses piezoresistive sensors carefully placed on the palm-side fabric of a 15-DOF dataglove to read contact forces. Based on the dataglove measurements, the force components are transformed and summed to assemble the resultant force vector. Finally, this force vector is translated into the manipulator frame using orientation measurements from an Inertial Measurement Unit (IMU) placed on the dorsal side of the dataglove. *The design and construction of the dataglove-based interface is the main contribution of this thesis.*

For simplification purposes, the dataglove-based is henceforth pointed out as *dataglove interface*.

In order to test the feasibility of the system, the force readings acquired from the dataglove interface were compared with the readings gathered by a load cell installed on the robot end effector. Both readings were compared on a time-shared basis along each axis.

The remainder of this Chapter is organized as follows: it is firstly addressed the motivation for designing the dataglove interface, followed by a description of its main parts and functioning. Finally a set of tests are presented to demonstrate the feasibility of the interface.

5.1 Motivation behind the design of the dataglove interface

Chapter 1 went through the basis of haptic perception and object manipulation. The concepts therein described focused on essential considerations regarding the importance of force measurements in hand-centered studies. Such concepts must be recalled in this section in order to provide a thoroughly description of the motivation behind the dataglove interface.

It must be first recalled the importance of touch for humans. Touch is one of the five human senses. Besides other functions, the sense of touch is important for two main tasks related with the issue of this thesis: identification of objects based on tactile exploration and determination of applied human forces during object manipulation. The former task is known as *haptic perception*, as earlier described on Section 1.2, while the latter is more related with the concept of mechanical impedance, since usually force and object motion come together.

The measurement of environmental forces is necessary in any force-based algorithm. Historically, contact forces were measured by strain gages installed near the robot end effector [54, 146] until sophisticated multi-axis load cells replaced the strain gages [60, 84]. More recently, Torsten et al. [97] and Gamez et al. [60] incorporated accelerometers to extract the forces and torques caused by inertia. This approach takes advantage of multiple sensors to accomplish more complex robotic tasks, especially those tasks requiring adaptive behavior in constantly changing environments [96]. These concepts and examples were in-depth discussed on Chapter *2* when the introduction of load cells into robotic developments was presented.

Improved instrumentation combined with the use of adaptive and interactive algorithms enables human-robot cooperation in many different applications, such as programming by demonstration of contact tasks [135], the manipulation of Jenga game blocks [96] and human-robot cooperation for the installation of heavy construction materials [105]. These examples of human-robot cooperation [96, 105, 135] use impedance control as the basic scheme for interfacing with humans. As in the previously cited works on impedance control along this document [26, 45, 60, 68, 84, 97, 111], these examples share a common method for the measurement of environmental forces: the control schemes rely upon sensors installed on the robot wrist, primarily load cells, to measure such forces. This approach is used in many implementations of impedance control, with some exceptions such as the recognition of the human intent by an interactive algorithm, using the principle of conservation of zero momentum for position-controlled systems [46]. In this approach, the force sensors are replaced by an observer that detects sudden load changes.

Despite impedance control not only focuses on reading the forces applied by humans; it is interesting to note that, in most applications regarding human-robot cooperation, the robot is the only location for the sensory system. Conversely, a different sensor location is addressed in cybernetics researches where usually human-machine systems are analyzed as a whole and sensor location may be shared between them.

In cybernetics research, it is of great interest to understand [61, 83] and track human motion in different activities of daily life [51, 108] to design bioinspired robots capable of emulating human skills in terms of motion [16, 43, 87] and sensory feedback [22, 36]. Whether the human hand [42] or foot [17, 109] or another limb is measured [124], custom-designed hardware is worn by the subjects to gather data under controlled conditions. Although the overall goal of such tests is also to determine the human intention, a significantly different sensory configuration is used for gathering the data than in the aforementioned impedance control applications.

In impedance control applications involving human-robot cooperation, the sensory system is either built into the robot links or mounted on the robot wrist [96, 105, 135]; however, in most cybernetics studies, the sensory system is worn by the subject [17, 42, 109, 124]. This difference is a logical consequence of the research focuses of the two fields.

It should be noted that either approach comes with benefits and disadvantages when attempting to determine the human intention. Sensory systems worn by humans often require a calibration process before each use; usually a new calibration is required for

each subject. This is a clear disadvantage if the calibration process is time consuming. On the other hand, robot-based systems with impedance controllers must degrade its performance in order to ensure safety in cooperative human-robot environments. This performance degradation includes reducing the maximum speed, precision and load capabilities of the robotic system [52, 64, 139]. This tradeoff between safety and performance is the current challenge in impedance control, as initially stated at the beginning of this Chapter.

To overcome these disadvantages, a new concept of impedance control is developed, inspired by cybernetics [130], in which the sensory system used to provide force feedback to the control loop is located on the human hand instead of the robot. This approach allows the human intention to be determined regardless of the robot's size, configuration, instantaneous speed or load. It is also proven that the force measurements acquired from the new interface naturally filter the internal robot forces stemming from inertia, vibration and Coriolis effects. Next section provides a description of the components and functioning of the interface.

5.2 Description of the dataglove interface for determining human-hand intention

The overall structure of the proposed interface is depicted on Figure 5.1 and thoroughly explained on [130, 131, 133]. The interface comprises a right-handed dataglove system, 11 piezoresistive sensors, an Inertial Measurement Unit (IMU) and a robotic manipulator for performing the tests. In this section, each system component is described below. A more comprehensive diagram of the dataglove interface, with emphasis on device interconnection, is presented on Chapter 6.

5.2.1 Dataglove device

Because most of the manipulation performed by humans is done with the hands, it is logical to design the control interface to be hand wearable. The human hand is a kinematically complex gripping tool with 27 degrees of freedom (DOF) [108]. Based on early work by Kamakura on human hand prehension [83], several studies have focused on understanding hand grasping [25, 51, 87] and on simplifying the kinematic model of the hand [23, 24] with the goal of designing robotic hands [16] capable of emulating human skills with the minimum degrees of freedom while maintaining precision. Similarly, in order to track human hand motion [42], it is necessary to optimize the sensors' location based on the most significant degrees of freedom for each finger. This optimization may reduce the total number of bending sensors in the dataglove and thus simplify the kinematic calculations. Additionally, the system cost is reduced, and the resulting device is more comfortable.

The proposed interface for determining hand intention is based on a 16-DOF hand model derived from the original model with 24 DOF. A thorough derivation of the 16-DOF kinematic model for the human hand is given by Cobos in [25] and will not be herein presented. The 16-DOF simplified model comprises three limbs (proximal, middle and distal) and three revolute joints for the index, middle, ring and little fingers; for the thumb, three limbs are considered (metacarpal, proximal and distal) with 4 DOF.

The metacarpal limb is connected by a 2-DOF universal joint with abduction/abduction and flexion/extension rotations. The proximal and distal limbs in the thumb are connected by revolute joints.

A 16-DOF kinematic model was chosen for the proposed interface because the model provides a high level of realism and tracking accuracy while maintaining simplicity [23]. The *X-IST* dataglove [78] was chosen for implementing the interface because it is commercially available at an affordable cost with a 15-DOF tracking capability. *Unfortunately, the X-IST is not capable of tracking the abduction/abduction rotation; consequently, this angle was manually adjusted during the tests.*

5.2.2 Pressure measurement technology

Most of the pressure sensors used in hand-centered applications are of piezoresistive type [20, 92, 104, 174, 175]. The main advantages of these sensors are the good relation between cost and precision as well as the low thickness, which allows the sensors to fit in a dataglove with minimal interference with the hand motion. Integrating pressure sensors into dataglove-based systems is a proven approach for studying manipulation [20, 104] and contact tasks in humans [175]. Additionally, pressure sensors can be integrated into robotic hands [62] to detect contact forces.

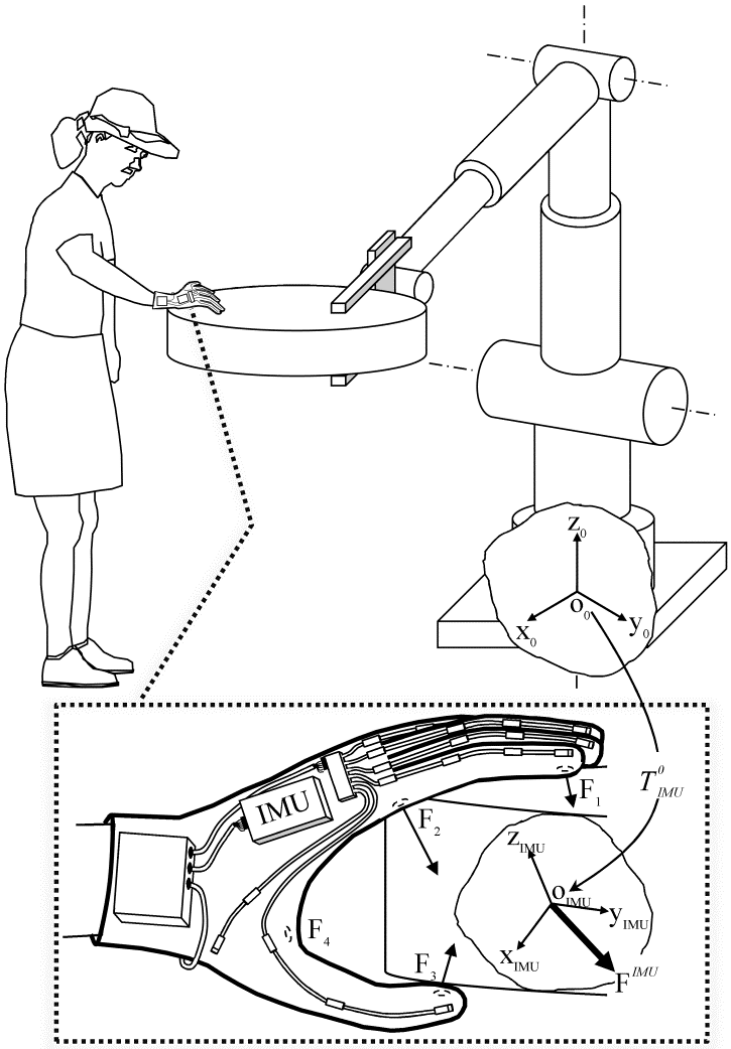

Figure 5.1: General diagram of the dataglove interface

Figure 5.2: Set of photographs showing the tailored fabrics which were pasted to the dataglove for sensor installation. The chronological order is from left to right and up to down

Pressure sensors based on resistive changes are usually known as Force Sensing Resistors (FSR) or simply as piezoresistive sensors. The FSR are two-terminal devices with a hyperbolically varying resistance as a function of the incremental force changes; this property requires a *transimpedance* amplifier as the driving circuit (see Figure 1 in [92]) to obtain a voltage proportional to the exerted pressure.

Several studies have focused on improving the accuracy and on modeling the drift of these devices [69, 92, 127, 165]. Previous work on FlexiForce sensors studied the amplitude nonlinearities and discovered a piezocapacitive response [128, 129, 132, 134], and therefore, FlexiForce devices were chosen as the force sensors for the proposed interface. A total of 11 sensors were located along the palm side of the dataglove interface to measure the applied hand forces. For such purpose a set of tailored fabrics were pasted on the palm side of the dataglove to hold the sensors. Figure 5.2 shows in chronological order the addition of such sensors to the bare dataglove up to the final glove version in the down-right side.

Figure 5.3 shows the sensor locations on the palm. The total number of sensors was determined by a tradeoff between comfort and precision. The sensor distribution was based on previous hand-grip studies that employed the same measurement principle [20, 104]. Initially, it was planned to install a total of nineteen force sensors on the

dataglove, since nineteen tailored fabrics were added to the device, see Figure 5.2. However, the resulting dataglove was too bulky and eight sensors were removed from the middle and proximal phalanges yielding the final form of Figure 5.3.

Before the sensors were located on the palm side of the dataglove, see Figure 5.4, each device was characterized using a linear regression between the pressure and the output voltage. For such purpose, the amplifier circuit of Figure 3.3 was used, and the DC input source, $\mathbf{V_{s1}}$, was tuned with **5 V**. This is a standard procedure followed in previous works and recommended by the sensor manufacturer [76]. However, this version of the dataglove interface does not include piezocapacitive effects in the pressure estimation algorithm.

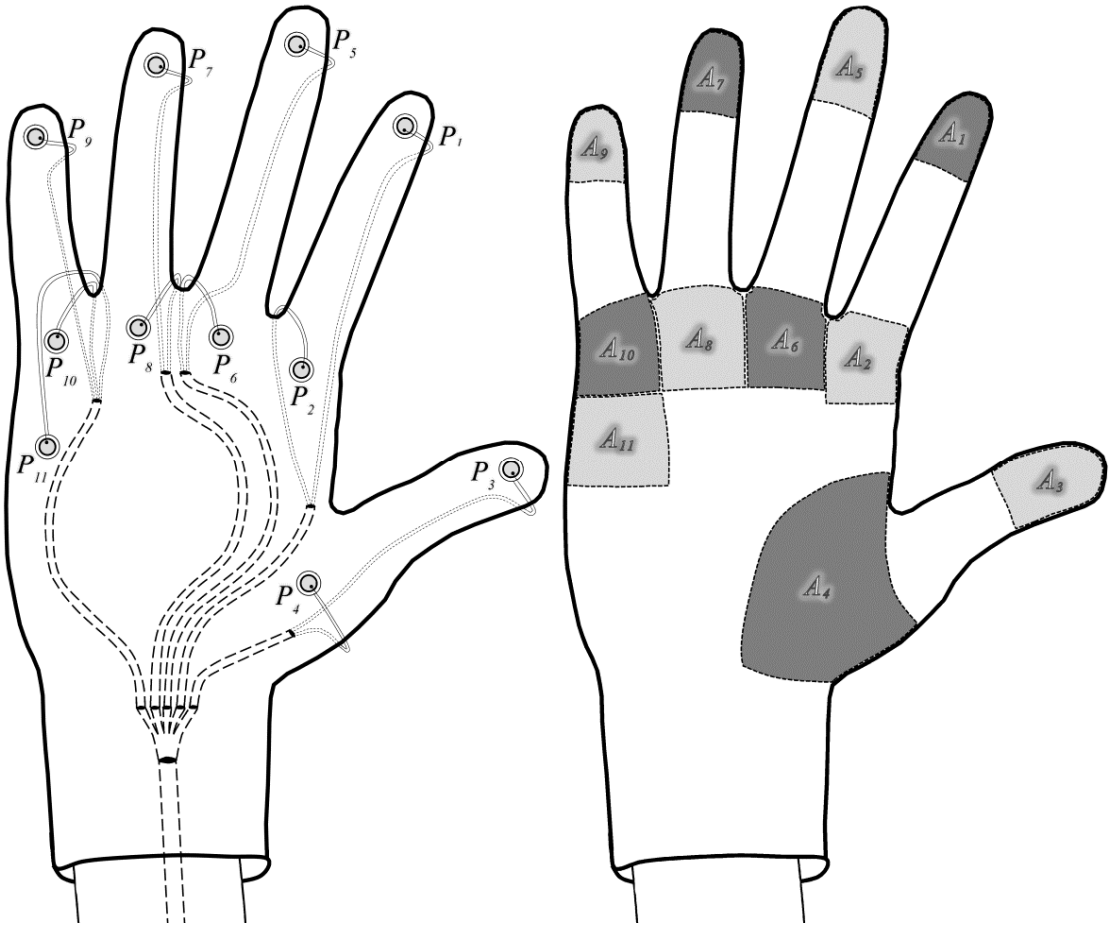

Figure 5.3: Left: Sketch of the FSR distribution, $\mathbf{P_i}$, on the palm side of the dataglove interface used to measure the applied forces. Right: the areas in gray represent the regions with an even distribution of pressure. Each area is associated with a FSR in the left sketch and corresponds to a given limb area $\mathbf{A_i}$ for computing the individual force contributions $\mathbf{F_i}$

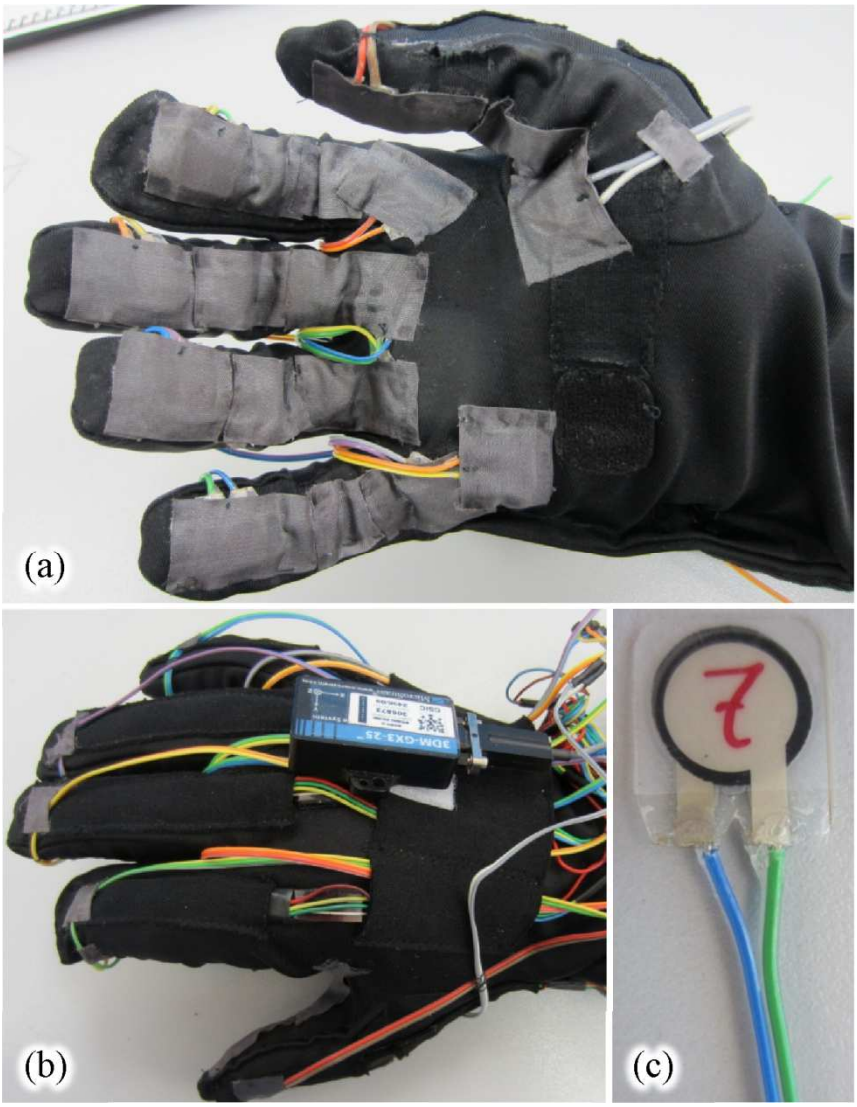

Figure 5.4: Images of the dataglove interface. (a) Palm side of the interface, showing the FSR fitted inside fabric patches to avoid undesired displacement when grasping objects. (b) Dorsal side of the interface, showing the IMU location. (c) The FSR were trimmed to a **1 cm** length and glued to flexible thin wires using a conductive epoxy to ensure comfort for the user

When a given FSR is read and converted to a pressure measurement, it is assumed that the pressure is evenly distributed on the associated region of the finger or the palm. The pressure measurement $\mathbf{P_i}$ can thus be converted to a force contribution $\mathbf{F_i}$ using the formula

$$F_i = P_i A_i \tag{5.1}$$

Where $\mathbf{A_i}$ is the limb area of every contribution, as shown in Figure 5.3. Consequently, there are a total of eleven force contributions, each associated with a FSR. All these force contributions are assumed to be normal to the finger/palm limb. These assumptions may have multiple consequences when determining human intention such as:

- It is necessary to determine all the areas associated with the eleven FSR; this requires measuring the hand to the subject who will wear the dataglove.

Figure 5.5: Photograph of the *3DM-GX3-25* IMU to obtain hand orientation within the task space

- Shear forces are neglected because only normal forces are obtained from equation **(5.1)**.

Both consequences suggest a strong dependency on the subject's hand size and on the hand configuration when pushing the load; experimental results related to these consequences are addressed in the next section.

5.2.3 Measuring Hand Orientation

To track the hand position and orientation within the workspace, an IMU was attached to the dorsal side of the dataglove. The IMU employed is a *3DM-GX3-25* manufactured by Microstrain [115] with a built-in magnetometer; see Figure 5.4b and Figure 5.5. The use of magnetic field compensation in the IMU magnetometer yields orientation measurements that do not diverge with time; this technique provides reliable orientation tracking and it has the advantage of being already implemented in the IMU unit from factory set up.

Typically, the orientation of a given object with respect to the base frame is expressed using the homogeneous orientation matrix $\mathbf{M^0_{obj}}$, with $\mathbf{M} \in \Re^{3X3}$. Similarly, the homogeneous transformation matrix $\mathbf{T^0_{obj}}$, with $\mathbf{T} \in \Re^{4X4}$, encompasses object rotation and position with respect to the base frame. The definition of $\mathbf{T^0_{obj}}$ is

$$T^0_{obj} = \begin{bmatrix} M^0_{obj} & p^0_{obj} \\ 0_{1x3} & 1 \end{bmatrix} \quad \textbf{(5.2)}$$

Where $\mathbf{p^0_{obj}}$ is the coordinate vector of the object with respect to the reference frame $\mathbf{O_0\text{-}x_0y_0z_0}$. For the case summarized in Figure 5.1, the IMU is the object, and the transformation matrix is defined as $\mathbf{T^0_{IMU}}$. Unfortunately, absolute position tracking is not possible using only the accelerometers from the IMU, this is, the vector $\mathbf{p^0_{IMU}}$ cannot be accurately determined over long time periods using the information from the accelerometers exclusively, because of the cumulative errors derived from the integration of acceleration in a 6-DOF task space. Solutions based on vision recognition and ultrasonic sensors were explored, but these solutions required multiple sensors and cameras, which would increase system cost and complexity; consequently, they were not implemented in this version of the dataglove interface.

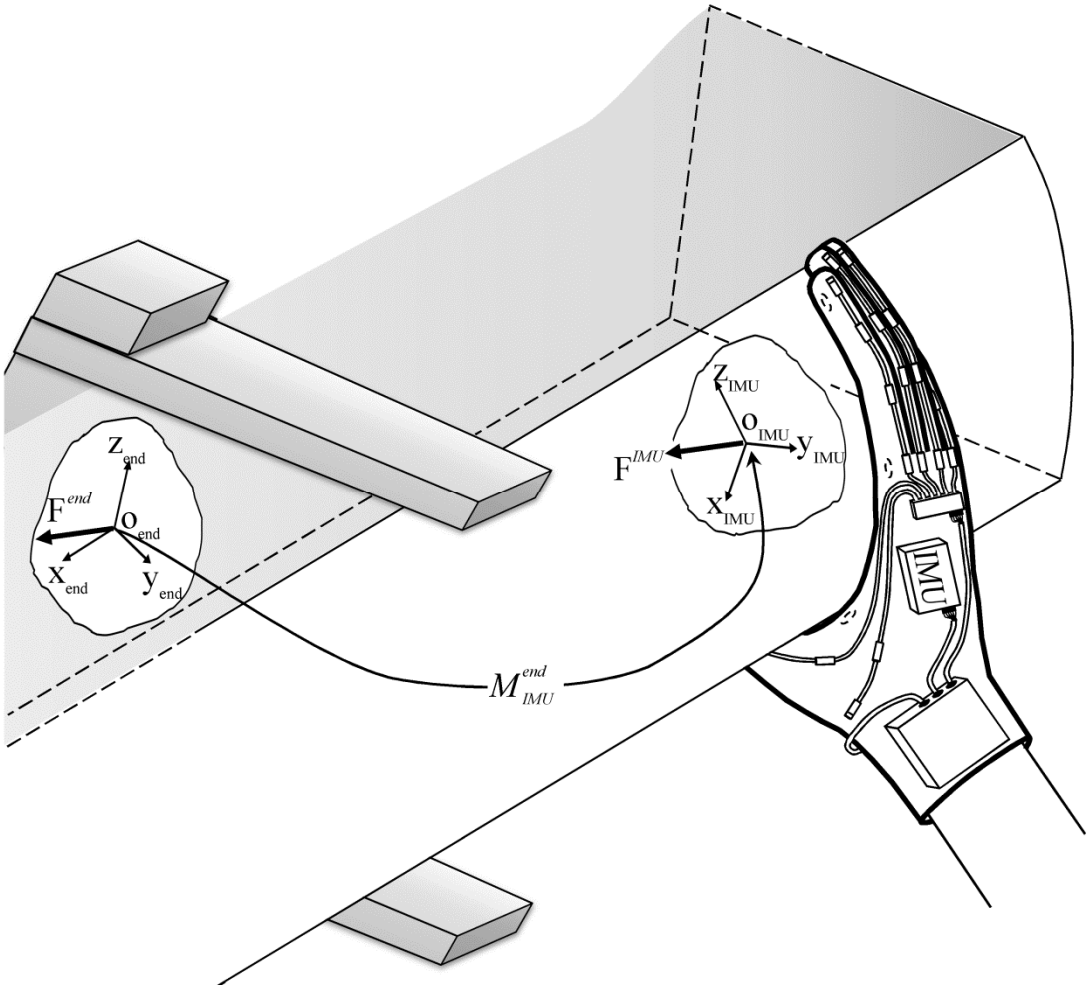

Figure 5.6: Close-up view of Figure 5.1 around the contact point between the dataglove interface and the load, showing the rotation of the vector $\mathbf{F^{IMU}}$ from the IMU reference frame, $\mathbf{O_{IMU}\text{-}x_{IMU}y_{IMU}z_{IMU}}$, to the end effector frame, $\mathbf{O_{end}\text{-}x_{end}y_{end}z_{end}}$

If only hand orientation ($\mathbf{M^0_{IMU}}$) is measured with respect to the base system, the dataglove interface can convert pressure measurements to force commands in a 3-D task space, and so the robot can solely move under position trajectories, **(x-y-z)**. To estimate the applied hand torques, it is necessary to determine the moment arm of the force represented by $\mathbf{p^0_{obj}}$ in $\mathbf{T^0_{IMU}}$. Figure 5.6 illustrates this scenario using a close-up view of Figure 5.1 around the contact point between the dataglove interface and the load, with the difference that the end effector frame $\mathbf{O_{end}\text{-}x_{end}y_{end}z_{end}}$ is used as a reference for easier interpretation of the image. Figure 5.6 depicts the scenario in which $\mathbf{p^{end}_{IMU}}$ is unknown and the force measured by the dataglove interface ($\mathbf{F^{IMU}}$) is only rotated using $\mathbf{M^{end}_{IMU}}$ to the origin frame $\mathbf{O_{end}\text{-}x_{end}y_{end}z_{end}}$.

The reference axes printed on the IMU must be aligned with the robot base frame, $\mathbf{O_0\text{-}x_0y_0z_0}$, every time the IMU is powered. By doing this, the measured forces from the inertial system, dataglove-IMU, can be rotated to the base frame on every control loop using $\mathbf{M^0_{IMU}}$, and proper motion can be achieved.

5.2.4 Converting pressure measurements to robot motion

The process of determining the human intention can be summarized as follows: on each cycle, the pressure sensors are read and the results are converted to force contributions $\mathbf{F_i}$ using equation **(5.1)**. There are a total of eleven force contributions, each from a limb Area $\mathbf{A_i}$ and a pressure sensor $\mathbf{P_i}$, as shown in Figure 5.3. Simultaneously, the dataglove measures the finger flexion in the operator's hand and returns an orientation matrix $(\mathbf{M^{j-1}_j})$ for each revolute joint according to the 16-DOF hand model of Cobos [25]. These matrices allow the transformation of the individual force contributions to the IMU frame to calculate the resultant force. However, note that not every degree of freedom contributes to the total force because there are 16 DOF in the hand model but only eleven FSR. Consequently, the following convention is adopted:

The force contribution $\mathbf{F_{11}}$ is the only referenced to the IMU frame and thus does not require any transformation; this is because $\mathbf{F_{11}}$ is directly exerted by the palm of the hand, where the IMU is mounted on, see Figure 5.3. The paired force contributions $\mathbf{F_2}$-$\mathbf{F_1}$, $\mathbf{F_6}$-$\mathbf{F_5}$, $\mathbf{F_8}$-$\mathbf{F_7}$ and $\mathbf{F_{10}}$-$\mathbf{F_9}$ correspond to the proximal and distal limbs of the index, middle, ring and pinky fingers, respectively. Finally, the force contributions $\mathbf{F_3}$ and $\mathbf{F_4}$ correspond to the distal and metacarpal limb of the thumb, respectively. Once the force contributions have been related to the corresponding finger/palm limb, it is possible to define a general equation to total the contributions. Combining finger limb poses, $\mathbf{M^{IMU}_i}$, and force contributions, $\mathbf{F_i}$, with the formula

$$F^{IMU} = \sum_{i=0}^{11} M_i^{IMU} F_i \tag{5.3}$$

returns a resulting vector, $\mathbf{F^{IMU}}$, referenced to the dataglove-IMU system. The vector $\mathbf{F^{IMU}}$ is then expressed in terms of the frame $\mathbf{O_0}$-$\mathbf{x_0y_0z_0}$ according to the orientation measurements from the IMU using the basic transformation formula:

$$F^0 = M^0_{IMU} F^{IMU} \tag{5.4}$$

The resulting force vector, $\mathbf{F^0}$, represents the user intention and serves as the robot motion command to the impedance controller. Note that $\mathbf{F^0}$ only controls the robot motion in a 3-DOF space **(x-y-z)**.

On the other hand, a general model for a robot driven by actuators that exert a controllable torque can be written in joint coordinates as:

$$I(\theta)\ddot{\theta} + C(\theta,\dot{\theta})\dot{\theta} = \tau_{act} - J^t(\theta)F_{ext} \tag{5.5}$$

Equation **(5.5)** models the robot as an inertial mechanism in which $\mathbf{I}$ is the inertia matrix, $\mathbf{C}$ is the Coriolis matrix, $\boldsymbol{\tau}_{\mathbf{act}}$ is the controllable actuator torque, $\mathbf{J^t}$ is the transposed Jacobian matrix, and $\mathbf{F_{ext}}$ are the environmental forces measured by a load cell installed on the robot wrist.

A typical control law for the robot model **(5.5)** is based on the target impedance approach which was previously mentioned on Section 4.4.4 in the form of equation **(4.1)**. However, since such equation is repeatedly pointed out in this Chapter, it is rewritten below:

$$F_{ext} = m\ddot{x} + b\dot{x} + k(x - x_0) \quad \textbf{(5.6)}$$

Above expression is that of a mass-spring-damper system with constants m, b and k in response to an external force $\mathbf{F_{ext}}$. The quantity $\mathbf{x_0}$ is the nominal equilibrium point of the end effector at steady state in the absence of any external force, and **x** is the endpoint position at any given time.

Equation **(5.6)** is solved on each cycle loop based on the force measurements acquired from the dataglove interface. This saves the formulation of a dynamic robot model, as that of equation **(5.5)**, and instead, the human intention is obtained regardless of the robot model, instantaneous speed or any other parameter related with the robot itself.

In practice, the vector $\mathbf{F_{ext}}$ is updated using the measurements resulting from equation **(5.4)**, this is, the human intention $\mathbf{F^0}$, and then, the reference position along the **(x-y-z)** axes is sent to the robot controller to initiate robot motion. This aspect is discussed with more detail on Section 5.2.6. A set of photographs from the manipulator is depicted on Figure 5.7.

5.2.5 Interface Electronics

The summing process described in Section 5.2.4 was computed on an embedded system running *VxWorks*, a Unix-based Real Time OS. The embedded System is the *Single-Board Reconfigurable Input Output NI-9632* (SBRIO-9632) manufactured by *National Instruments* and programed using *LabVIEW Real Time* and *LabVIEW FPGA*. The embedded system included a **400 Mhz** Power PC processor, a 3 Million Gates FPGA model Spartan 3 plus a set of peripheral interfaces for communication and low level controlling. The most relevant are listed below:

- An Analog to Digital Converter (ADC) with a 16 bit resolution and 16 time multiplexed ports.
- A Digital to Analog Converter (DAC) with a 16 bit resolution and 4 output ports.
- A total of 110 Digital Input/output lines with TTL voltage levels. All these inputs are available through the FPGA which is integrated in the backplane of the embedded system.
- A 10/100BASE-TX Ethernet port.
- A RS232 serial port.

In addition, and considering that multiple sensors are connected to the embedded platform, it was developed a custom condition board as shown on Figure 5.8.

The conditioning board was designed with the same dimensions as the SBRIO-9632 platform and located right on top of it. It performs multiple functions regarding signal conditioning, signal drivers and sourcing, they are detailed next:

- Drive the 11 FSR installed on the palm side of the dataglove. For such a function, every sensor had an amplifier driver similar to that of Figure 3.3 with a DC sourcing of **5 V**. The output of each sensor was multiplexed and then connected to the ADC of the SBRIO-9632

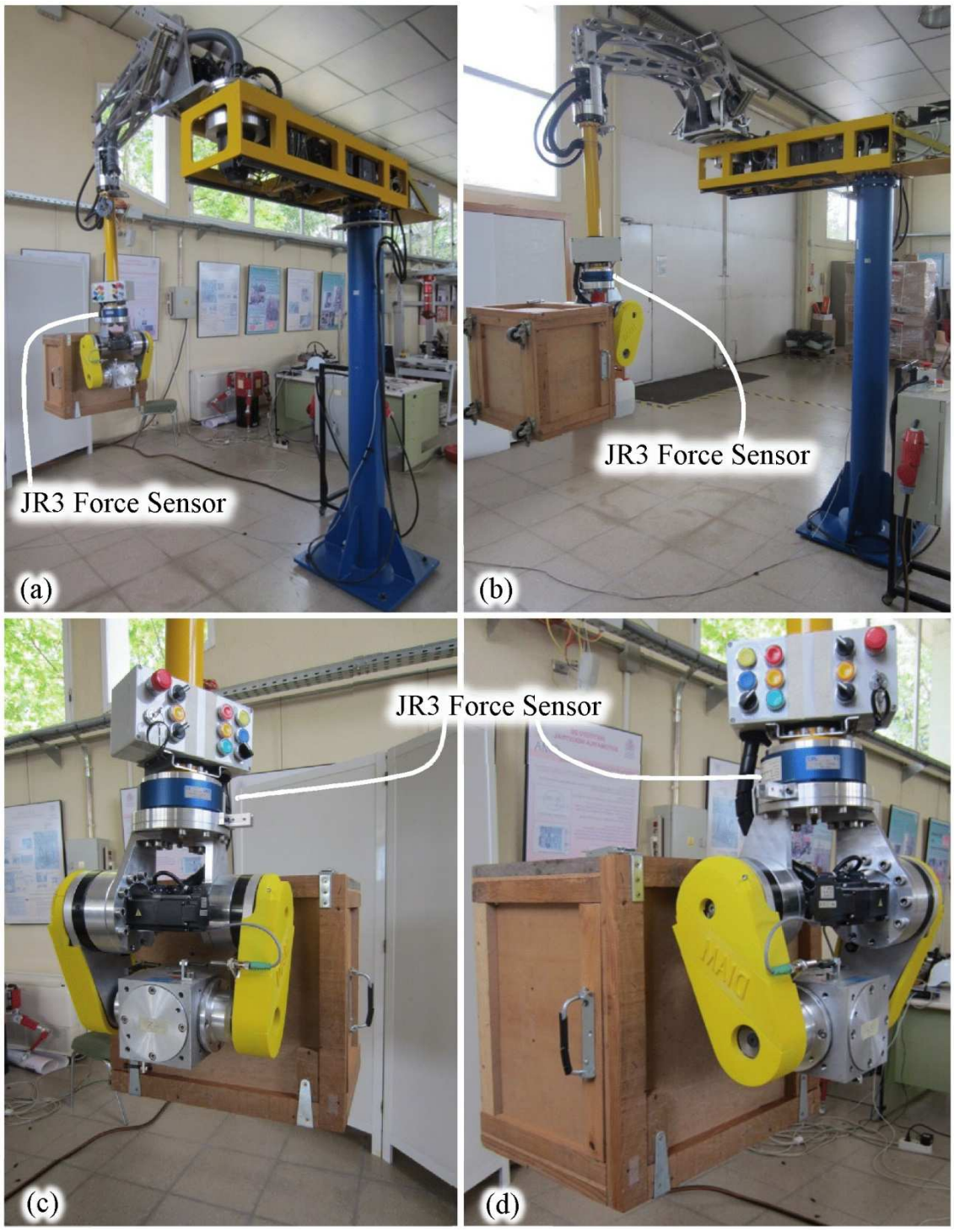

Figure 5.7: Images of (a), (b) the modified 6-DOF SCARA manipulator used to perform the tests of the dataglove interface and (c), (d) close-up views of the end effector and the load showing the JR3 sensor location

- Interface between the TTL voltage levels available in the SBRIO-9632 and the RS232 voltages from the X-IST dataglove [78] and the 3DM-GX3-25 IMU [115].
- Provide the adequate sourcing to the dataglove and the IMU.
- Leds and switches are included for software debugging.

The SBRIO-9632 and the Custom Design Board were placed inside a metal box for Housing and powered by three lithium batteries. The schematic of the conditioning board is shown on the Appendix C.

5.2.6 Robot Controller and Process Summary

The communication between the SBRIO-9632 and the Robot Controller was established through a wired Ethernet connection. The reference position along the **(x-y-z)** axes was sent to the robot controller with an update rate of **60 Hz**. The Robot Controller is a PC running *QNX OS* and mounted on the rear side of the manipulator, see Figure 5.7a and Figure 5.9.

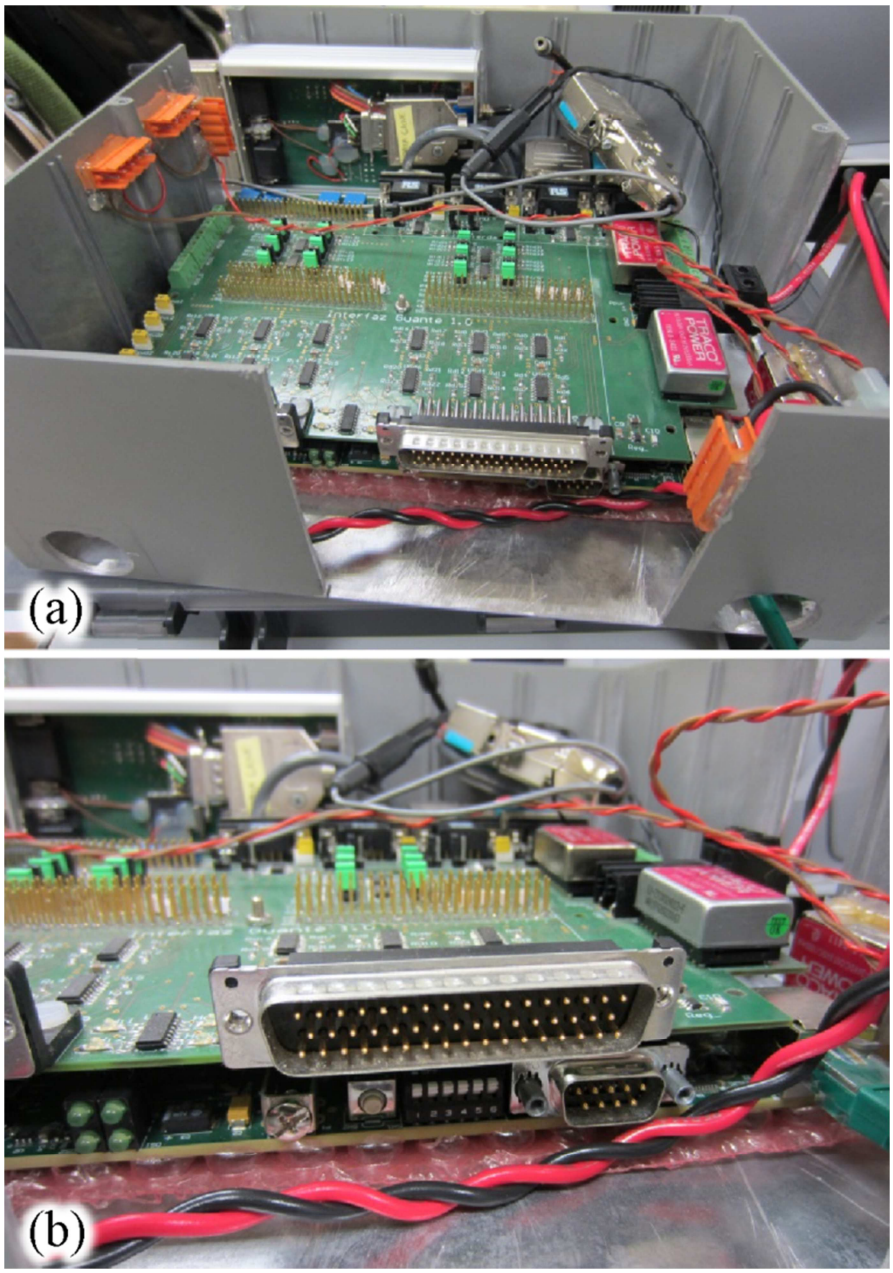

Figure 5.8: Photographs of the Single Board RIO platform (SBRIO-9632) and the custom conditioning board for the analog acquisition and signal drivers. a) Isometric view of the two boards and the metallic tailored box for housing. b) Close-up view showing the on-top location of the conditioning board and the lower SBRIO-9632

Figure 5.9: PC mounted on the rear side of the manipulator working as the robot controller

The PC of Figure 5.9 is responsible for the direct interaction with the robot servo controller through the *DMC-1832 Galil Motion Controller* [55] installed in the PC. One the PC receives the motion commands in the form of **(x-y-z)** coordinates; the Cartesian coordinates must be converted to joint angle positions, for such purpose, the robot's kinematics must be solved within the same control loop. The kinematic calculation is performed by the PC that ensures a deterministic behavior due to the Real Time characteristic of the *QNX OS*. A detail of the robot's kinematics is available at [63].

Once the Cartesian Coordinates are converted to joint angle positions, it is possible to feed the control loop of each degree of freedom in order to initiate robot's motion. Each degree of freedom is controlled by a PID as shown on Figure 5.10. The entire process beginning on the dataglove side can be summarized as follows:

- Read the 11 piezoresistive sensors and convert the analog voltage to pressure readings, see equation **(5.1)**.
- Read the instantaneous finger position from the 15-angle sensors on the *X-IST* dataglove and solve the direct kinematics employing the 16-DOF model for a human hand [23].
- Combine the pressure sensor measurements with the hand instantaneous position in order to assemble a net resulting vector of Force, see equation **(5.3)**.
- Read hand orientation and rotate the net resulting force vector to the manipulator frame, see equation **(5.4)**.
- Solve the impedance control law, see equation **(5.6)**, and calculate the Cartesian reference position for the manipulator. Then, such reference position is sent to the PC controller through the Ethernet network.

The Tasks performed by the PC controller are next listed:

- The PC controller receives the Cartesian reference position and converts them to joint angle positions using the robot's kinematics [63].

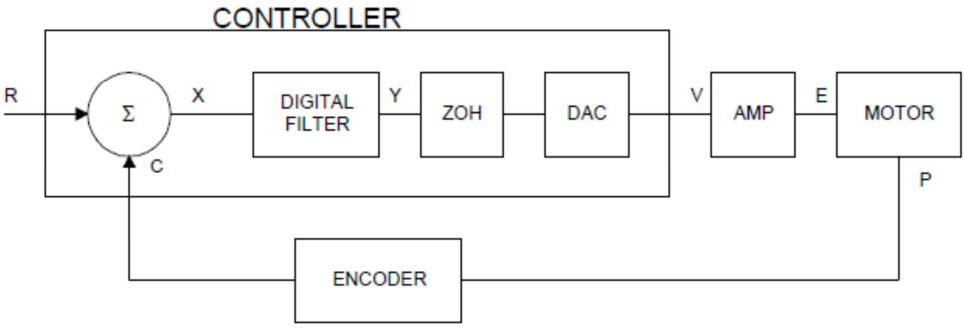

Figure 5.10: Control diagram of each degree of freedom controlled by the *DMC-1832 Galil Motion Controller* [55] which is installed in the robot's PC, see Figure 5.9

- The joint angle positions are fed back to the *DMC-1832 Galil Motion Controller* [55] to initiate robot motion.
- The final robot position is sent back to the SBRIO-9632 for solving the impedance control law on the next iteration.
- In order to assess the performance of the dataglove interface, the measurements from the JR3 Force Sensor are collected and sent back to the SBRIO-9632 for off-line analysis and processing. The JR3 Force Sensor is installed near the robot's end effector, see Figure 5.7.

It must be remarked, that the above described process does not require information regarding the robot's dynamic model, and so, equation **(5.5)** can be skipped from the algorithm, only information for the robot kinematics is required to initiate robot motion but not to estimate the user intention. Such process, as well as the entire dataglove interface, is patent protected [130]. The text of the patent is available at the Appendix B

5.3 Testing the dataglove interface

The test bench for the dataglove interface comprises a 6-DOF manipulator [63]. The configuration of the manipulator is based on the Selective Compliant Articulated Robot Arm SCARA with modifications aimed to reduce the actuator torques, see Figure 5.7. A JR3 force/torque sensor [82] is installed on the wrist to perform validation tests on the dataglove interface. The JR3 sensor measurements, $\mathbf{F}_{JR3}$, are used as reference for computing the errors on every axis:

$$\boldsymbol{e} = \boldsymbol{F}_{JR3} - \boldsymbol{F}^{0} \qquad \textbf{(5.7)}$$

Two types of tests were performed on the interface: static and dynamic. The static was a motionless test to evaluate the accuracy of the interface in terms of the error as defined in equation **(5.7)**; the dynamic test used the control law of equation **(5.6)**. Before each test was performed, a calibration procedure was performed by the wearer of the dataglove interface. The subject was instructed to put on the dataglove interface and replicate ten finger configurations shown on a screen, corresponding to the limit angles of each joint, while the analog data were acquired from the dataglove sensors. The IMU was calibrated by aligning its reference axes with the robot axes. The 11 FSR were calibrated just before the final assembly of the interface was performed. This calibration was done using the test bench and the procedures described in [134]. The

FSR were calibrated only once because it was not practical to constantly remove and replace these devices from the fabric patches on the palm side of the dataglove.

5.3.1 Static Test

During the static test, robot motion was disabled by disconnecting motor power and by activating motor brakes on each joint. The dataglove interface was worn by a 26-year-old subject on his right hand using either the Surrounding Mild Flexion (SMF) grip or the Parallel Mild Flexion (PMF) grip described by Kamakura [83]. These grips were chosen for the test for two reasons:

- These grips are the best suited for the bulky load held by the robot end effector (see Figure 5.7b).
- Using these grips with a bulky load minimizes shear forces because thumb opposition is constrained; this naturally forces the subject to simply push the load rather than to grasp and push it.

Force measurements were simultaneously collected from the JR3 sensor and the dataglove interface on each axis, see Figure 5.11. The subject was instructed to apply step force commands in six directions, comprising two commands on each axis in the positive and negative directions in the following order: $\mathbf{F_z}^+$, $\mathbf{F_z}^-$, $\mathbf{F_x}^+$, $\mathbf{F_x}^-$, $\mathbf{F_y}^+$ and $\mathbf{F_y}^-$.

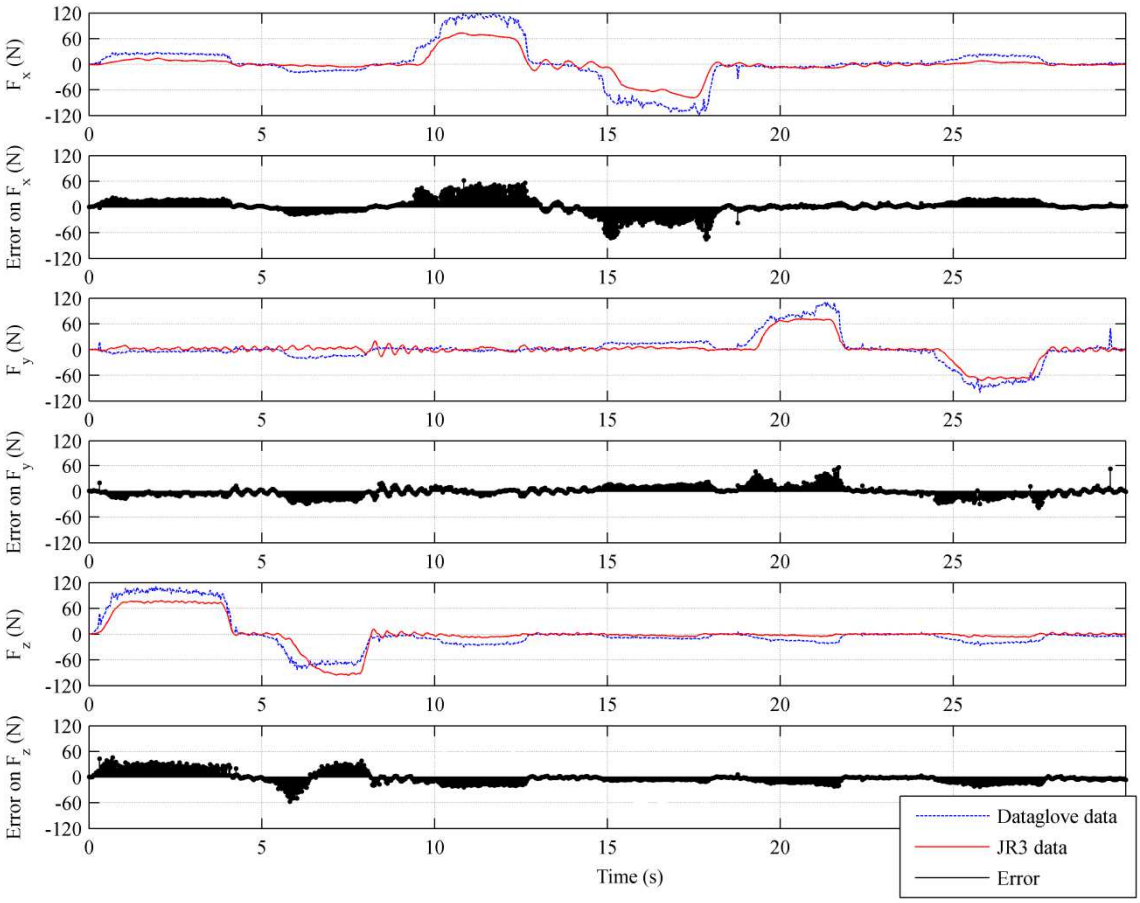

Figure 5.11: Results of the static test comparing force measurements acquired from the dataglove interface (dashed blue lines) and the JR3 sensor (solid red lines). The data are shown in separate plots for each axis ($\mathbf{F_x}$, $\mathbf{F_y}$ and $\mathbf{F_z}$). The errors calculated from equation **(5.7)** (solid black lines) are plotted separately for better comprehension

There are several observations that can be made from Figure 5.11. First, note that the force measurements from the dataglove interface are in general greater than the load cell measurements. This can be explained by the assumption that the pressure is evenly distributed in the finger/palm limbs. This condition causes that every force contribution $\mathbf{F_i}$ is overestimated, resulting in a greater force vector $\mathbf{F^0}$.

Second, note that when the operator exerts force in the **z** direction during the time interval $\mathbf{0\ s \leq t \leq 8\ s}$, a proportional contribution appears in the x axis. This result is a clear evidence of misalignment between the IMU frame and the robot axes. This situation occurs despite of the great effort to align the IMU frame with the robot axes in the beginning of the test. Similar behavior is observed during the interval $\mathbf{19\ s \leq t \leq 27\ s}$, when the subject applies force in the **y** direction and a force contribution appears on the z axis.

Third, a slight saturation response is observed in the dataglove force measurements. At $\mathbf{t = 6\ s}$ in the $\mathbf{F_z}$ plot, the dataglove force measurements saturate as the load cell measurements continue to increase. It is only possible to speculate about the possible sources of this error. The most likely causes of saturation are the saturation to nonlinearities in the FSR and to forces exerted by hand regions that lack pressure sensors, see Figure 5.3.

Finally, when the subject raised his hand from the load, a damped oscillatory response is observed in the load cell measurements. This ringing in the force is caused by the compliant mechanics of the manipulator, which has a large workspace area with a **2 m** radius [63] and is thus capable of storing substantial elastic energy. This phenomenon is observed at all transition points, but it is particularly noticeable at $\mathbf{t = 8\ s}$ in the $\mathbf{F_y}$ and $\mathbf{F_z}$ plots and at $\mathbf{t = 12.5\ s}$ in the $\mathbf{F_x}$ plot. However, note that the measurements from the dataglove interface do not show this behavior because the FSR are not tied to the flexible robot links; they are mounted on the hand instead. This fact is the greatest contribution of the present work because the proposed interface is capable of decoupling the internal robot forces from the applied hand forces in a transparent way. Consequently, it is possible to safely implement any control law for robot motion, such as the impedance control of equation **(5.6)**.

The internal robot forces arise from multiple sources. The main sources are Inertia and Coriolis terms of equation **(5.5)**, but elasticity and gravity also play an important role, especially in large-workspace robots.

Several studies have attempted to distinguish between the internal robot forces and the applied human forces [60, 96, 97, 105, 135]. Figure 5.11 confirms that the dataglove interface can accomplish this goal, but with some imprecision.

5.3.2 Dynamic test

During this test robot motion was enabled, and the impedance equation **(5.6)** was used to control robot motion with parameters $\mathbf{M = 120\ Kg}$, $\mathbf{K = 100\ N/m}$ and $\mathbf{B = 100\ Ns/m}$. The vector $\mathbf{F_{ext}}$ from equation **(5.6)** was updated on every cycle loop with $\mathbf{F^0}$ from equation **(5.4)**, this is, the force estimation resulting from the dataglove interface.

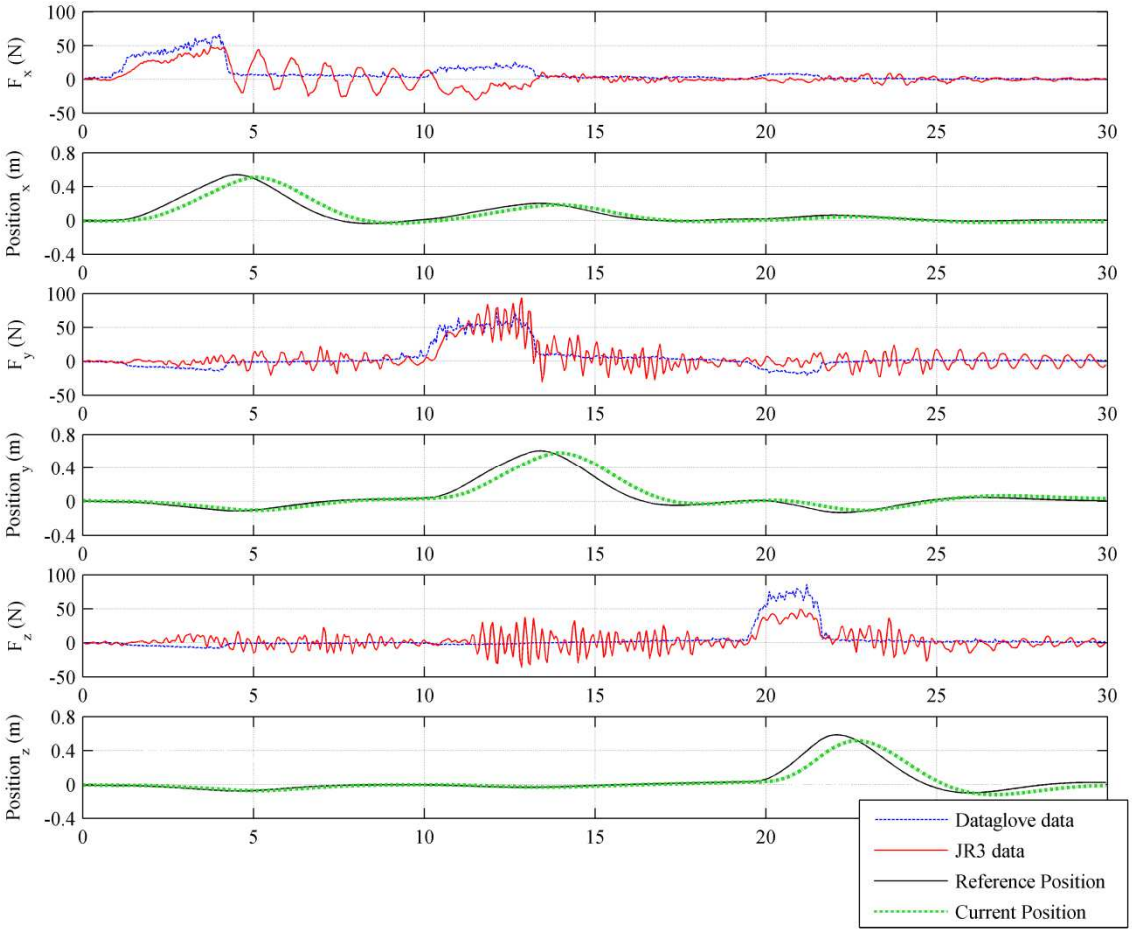

Figure 5.12: Results of the dynamic test comparing the force measurements acquired from the dataglove interface (dashed blue lines) and the JR3 sensor (solid red lines). The force and position data are shown in separate plots for each axis

Simultaneously, JR3 data were collected but not used in the control scheme. It must be remarked that it was ensured the absence of environmental forces caused by physical constraints within the workspace; this was done this way in order to allow an objective comparison of the JR3 and the dataglove force measurements.

The subject was instructed to apply step force commands in the $\mathbf{F_x}^+$, $\mathbf{F_y}^+$ and $\mathbf{F_z}^+$ directions, with a **5 s** interval between consecutive force commands to wait for the robot to return to the equilibrium position.

Figure 5.12 presents the experimental results from the test on separate plots for each axis. A broad view of the plots shows the dataglove data to be a filtered version of the JR3 measurements, particularly of the forces produced by the elasticity due to the compliant mechanics of the manipulator. This filter is especially noticeable when the robot returns to the equilibrium position when the hand force is absent, e.g., during the time interval $\mathbf{4.2\ s \leq t \leq 10\ s}$ in the $\mathbf{F_x}$ plot and during the interval $\mathbf{13.5\ s \leq t \leq 19.2\ s}$ in the $\mathbf{F_y}$ and $\mathbf{F_z}$ plots.

The force-filtering benefits were also observed when the subject exerted a force on the load, resulting in smooth position commands immune to vibrations. However, the inaccuracies reported in the previous section (i.e., the overestimation and misalignment of the force) can be observed in Figure 5.12, mainly during the interval $\mathbf{19.2\ s \leq t \leq 22\ s}$ when the force estimated by the dataglove interface is almost twice as

great as the JR3 measurement along the **z** axis. Additionally, during the interval **13.5 s ≤ t ≤ 19.2 s**, an estimation error of **18 N** in the **x** direction led to a displacement of **0.18 m**; even though the user applied force was concentrated in the **y** direction.

The overestimation of force from the dataglove interface can be corrected by simply scaling the force by a constant factor to be determined from a statistical analysis of the static-test results. However, given the two sources of error observable in Figure 5.11 and Figure 5.12, it is more convenient to solve first the problem of misalignment; this is one of the key improvements of the future work.

5.4 Conclusion and resume

A dataglove interface for determining applied hand forces was presented in this Chapter. The interface comprises a 15-DOF dataglove, 11 force sensing resistors and an Inertial Measurement Unit (IMU). The interface was initially tested on a motionless basis, in which the measurements from the interface were compared with force measurements from a JR3 load cell mounted on the wrist of a 6-DOF manipulator. The experimental results show that the interface can track applied hand forces in a 3-D **(x-y-z)** task space, but with some inaccuracies in magnitude and direction.

The dynamic test demonstrated that the dataglove interface could be used effectively in an impedance control application. The decoupled dynamics of the human hand with respect to the robot structure produced a naturally filtered force signal, which could be used to control robot motion despite the above-mentioned inaccuracies. This result is the main contribution of the interface research.

Chapter 6

6. Examples of Handling Operations with the dataglove interface and the 6-DOF Manipulator

Chapter 5 presented the tests for assessing the performance of the dataglove interface under static and dynamic basses. Given the outstanding performance exhibited throughout the tests, it was possible to perform further maneuvering tasks using a wooden box as dummy load.

Multiple sets of photographs sequences are herein shown as ways of representing the maneuvering tasks performed over the 6-DOF manipulator, such photos were taken from a video which is included together with the digital version of this thesis. Likewise, a software was developed to track finger/hand motion and to debug force sensing during dataglove assembly. Since the software demonstrated to be a powerful tool during load maneuvering, a set of capture screens from the software are also presented in this Chapter.

6.1 Experimental Setup for dummy load maneuvering

Figure 5.7 showed the 6-DOF manipulator together with the JR3 sensor installed near the robot's end effector. However, little has been said in regard with how the tests from Section 5.3 were performed. Likewise, Figure 5.8 showed a photograph of the interface electronics but it was not explained how such electronics was actually held by the user during object maneuvering.

Figure 6.1 shows a complete overview of the experimental setup for the tests herein presented. It comprises the 6-DOF manipulator with the JR3 sensor, the dummy load and the robot controller installed on the manipulator's rear-side. On the user's side, Figure 6.1 shows the operator exerting force over the load with the dataglove interface and a backpack which is used to place all the conditioning electronics and the embedded system. These two elements were previously described on Section 5.2.5 and shown on Figure 5.8.

Additionally, but not shown on Figure 6.1, a second PC -running windows- was often required for supervision tasks and to save the data generated by the dataglove interface and the JR3 sensor; henceforth the PC running windows is pointed out as the *monitoring PC* and the software running on it as the *monitoring software*. This PC is a non-mandatory component because direct communication was established between the robot controller -running *QNX OS*- and the *SBRIO-9632* running *VxWorks OS*. However, as previously mentioned, the debug software running on the *monitoring* PC demonstrated to be a high valuable resource during the interface assembly and later during load maneuvering, and so, most of the carried out experiments required the usage of both PCs. A comprehensive diagram of the dataglove interface and the 6-DOF manipulator is available on Figure 6.2. Special effort has been placed on representing

device interconnection with the appropriate symbols. Next section presents a description of the software running on the monitoring PC.

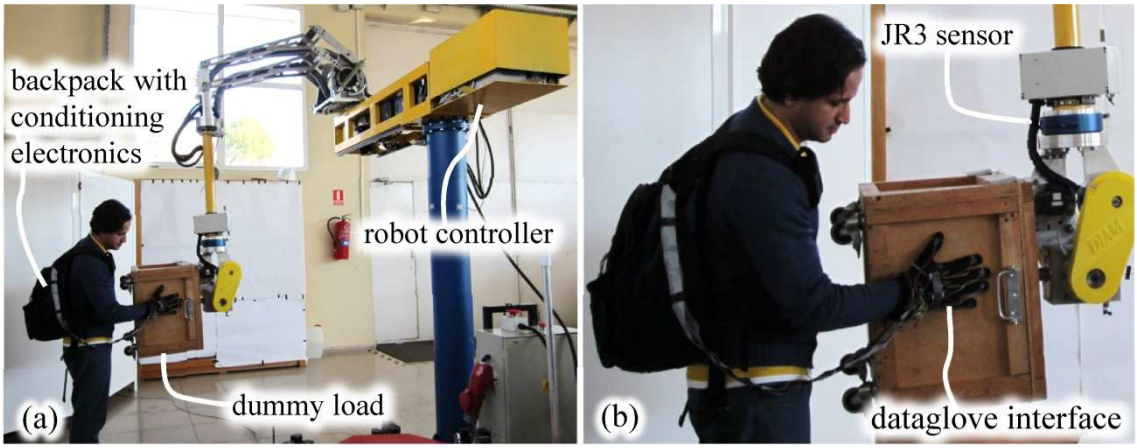

Figure 6.1: Photographs of an operator interacting with the 6-DOF manipulator through the dataglove interface. a) Overview of the experimental setup for load maneuvering. b) Zoom around robot's end effector

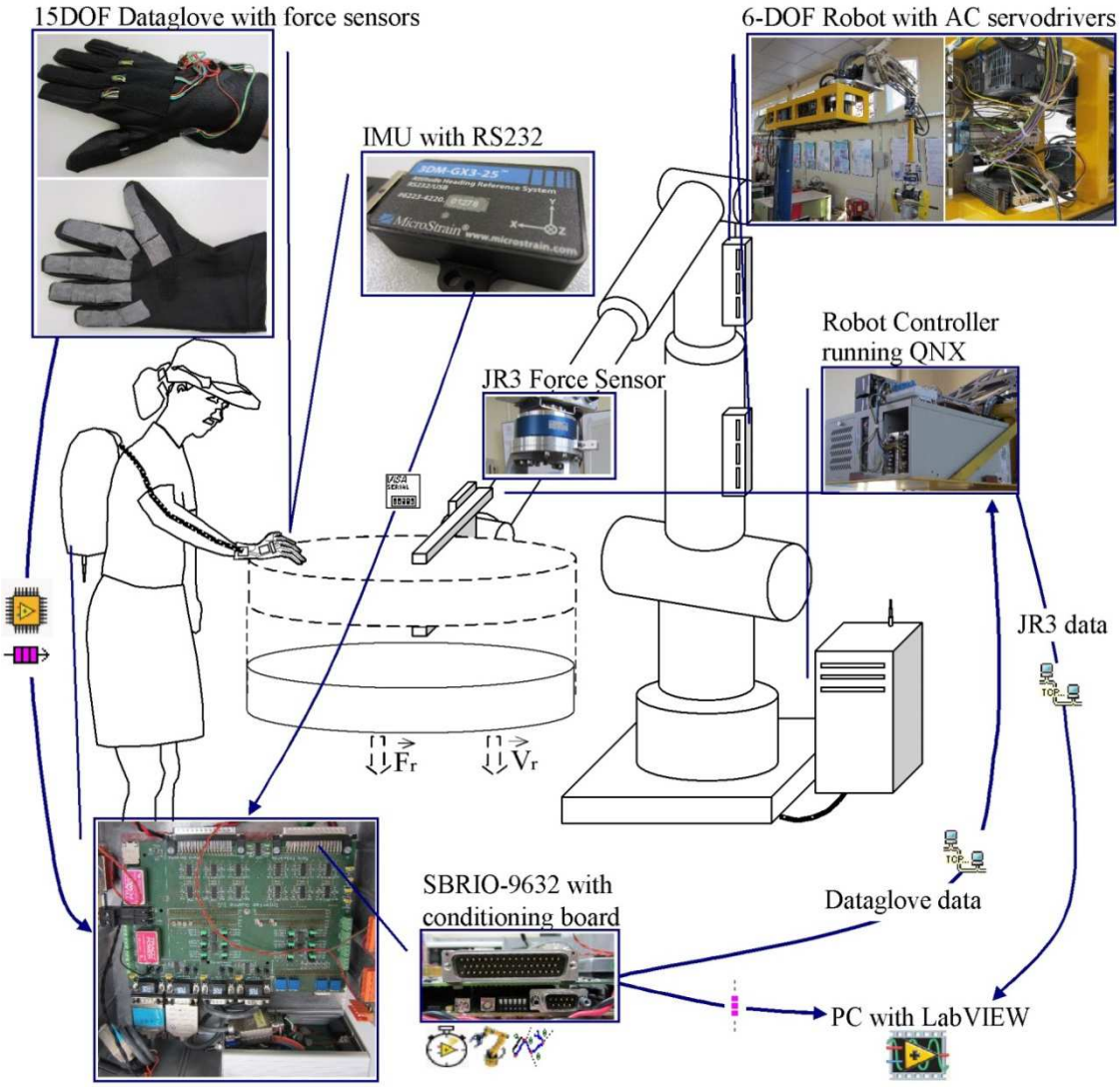

Figure 6.2: Detailed diagram of the dataglove interface and the 6-DOF manipulator with special emphasis on device interconnection

6.2 Software for the debugging and supervision of the dataglove interface

The software running on the monitoring PC embraced three operation modes towards debugging and supervision tasks of the entire system; this is; the dataglove interface and the 6-DOF manipulator. They are next listed:

6.2.1 Console Mode

Before deploying software at the SBRIO-9632 platform and operating the robot under dataglove-force commands, it was necessary to perform a large amount of tests over the 6-DOF manipulator. For such purpose, it was necessary to provide a simple control mode to move the robot according to Cartesian speed commands. Therefore a console mode was developed to interface with the robot, see Figure 6.3. It uses *TCP/IP* protocol to communicate between *LabVIEW* and the *QNX OS*. The *TCP/IP* link between both devices can be observed on Figure 6.2.

Multiple functionalities are available under Console Mode; they are all focused to test the 6-DOF manipulator and the JR3 sensor. The most remarkable are: simulate applied external forces, draw force profiles on each axis and reset the JR3 sensor.

6.2.2 Dataglove Mode

Under Dataglove Mode, a communication is established between the *SBRIO-9632* and the monitoring PC through a Network Stream connection; see Figure 6.2. This mode enabled the 6-DOF manipulator to be controlled under an impedance control basis. However, it was also possible to simply read the user applied forces and disable robot motion.

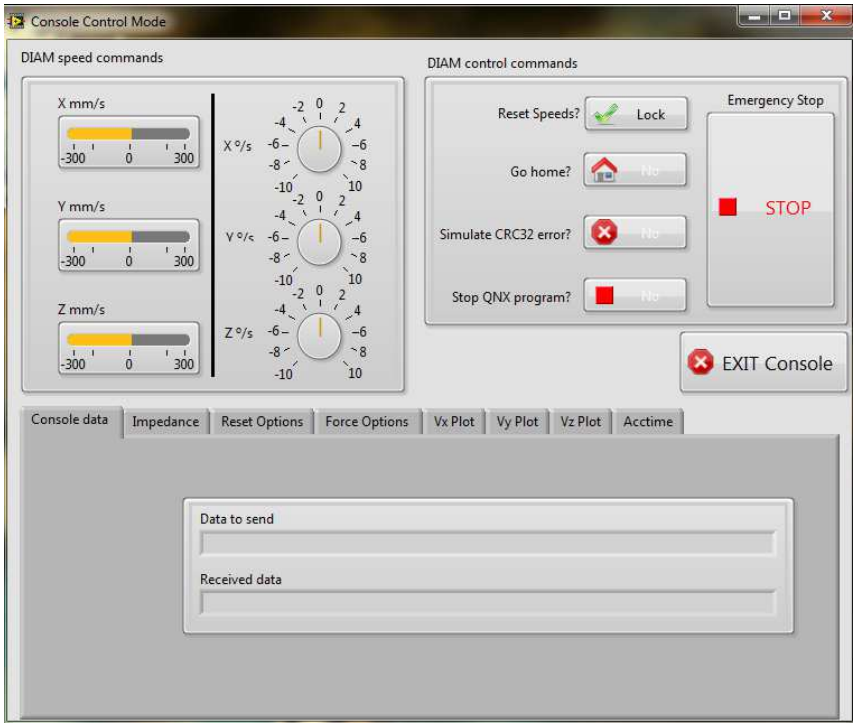

Figure 6.3: Screen Capture of the Console-Mode window

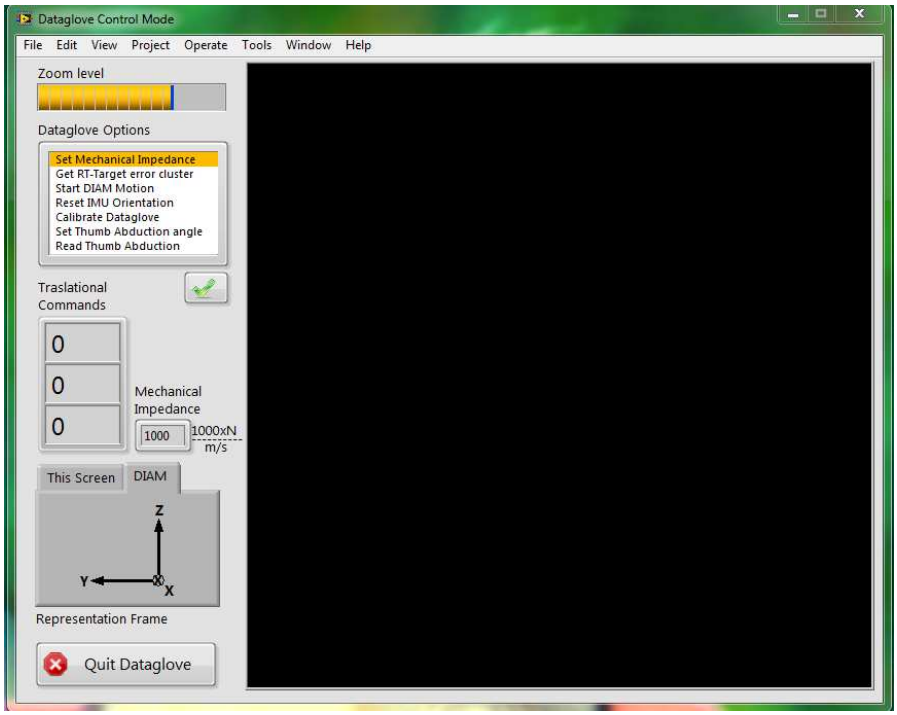

Figure 6.4: Screen Capture of the dataglove-mode window

The net applied force by the user is represented on the screen with a blue arrow and is also numerically shown on the screen. The flat version of the dataglove-mode window is shown on Figure 6.4, but an image sequence showing its full set of functionalities is available in Figure 6.5.

Under dataglove mode, it is also possible to set the **m**, **k**, **b** parameters of the impedance control algorithm, see equation **(5.6)**, and thus change the transient response of the manipulator. Likewise, it is possible to reset IMU orientation and to perform a calibration of the dataglove sensors. This is of great usefulness when the operator is changed, and also, to compensate for the thermal drifts occurring in the dataglove flex sensors.

6.2.3 Debug Mode

The debug mode is based on the dataglove mode from Section 6.2.2, with the difference that two additional screens are provided to allow debugging and supervision tasks.

Under debug mode, a window -with a hand sketch- represents with color changes the user applied forces on each of the individual force spots occurring on the dataglove palm side. The second window shows a 3-D rendering hand that represents finger and hand rotation. This is of great usefulness to assess the calibration of the individual flex sensors of the dataglove. Since both windows are strongly dependent on user's inputs, they are shown in the sequence of photographs from Section 6.3.

6.3 Sequence of photographs from the monitoring software during dataglove operation and robot motion disabled

The sequence of photographs from Figure 6.5 shows the dataglove interface which is worn by a subject under different finger configurations. The software running on the monitoring PC is displayed in background; meanwhile the subject changes his hand configuration and exerts forces over a wooden wedge located in the photos' right side. Debug mode was enabled during this sequence of photographs, see Section 6.2.3. Some comments from each photo are next presented:

Photographs a) and b): The subject's hand is rotated and the *monitoring software* replicates such motion on the 3-D rendering hand. Since no force is applied to any object, the blue arrow is not displayed on the screen. Likewise, the force spots on the hand sketch are all in blue, meaning that no force is being applied.

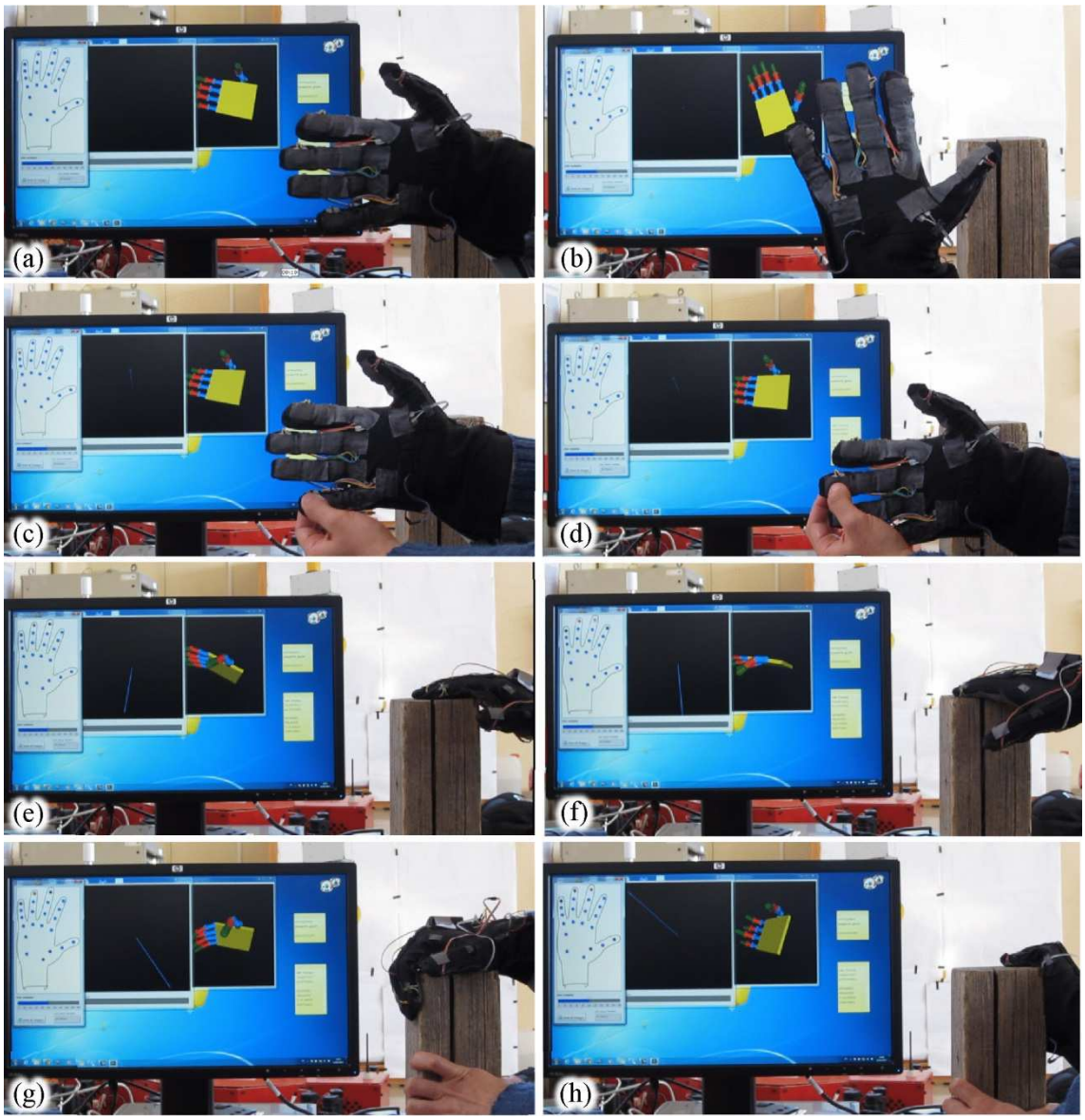

Figure 6.5: Sequence of photographs from the dataglove interface and the monitor software working under debug mode

Photographs c) and d): Different force spots are tested on the dataglove palm side meanwhile hand position remains invariable. The hand sketch shows in red the force spots with representative force contributions; this is, the pinky finger in Photo c, and the middle finger in Photo d. Also, a blue force vector pointing out of the screen is displayed.

Photographs e) and f): The subject applies forces to the wooden wedge with the hand extended, and thus, some force spots on the hand sketch turn into red color. Note that the blue vector is pointing accordingly with the user intention.

Photographs g) and h): The user applies forces while grasping the object. The 3-D rendering hand is accordingly rotated on the screen. However, some misalignment between the real and the rendering hand is observed, especially in Photo h). A similar phenomenon was observed in the static test summarized on Figure 5.11, in which the force data from the JR3 sensor and the dataglove interface was compared on a time basis.

6.4 Sequence of photographs from the entire system working under dataglove force commands and robot motion enabled

Following the format of Figure 6.5, two sequences of photographs are presented separately in Figure 6.6 and Figure 6.7. Both photographs were shot at different moments since a single camera was available.

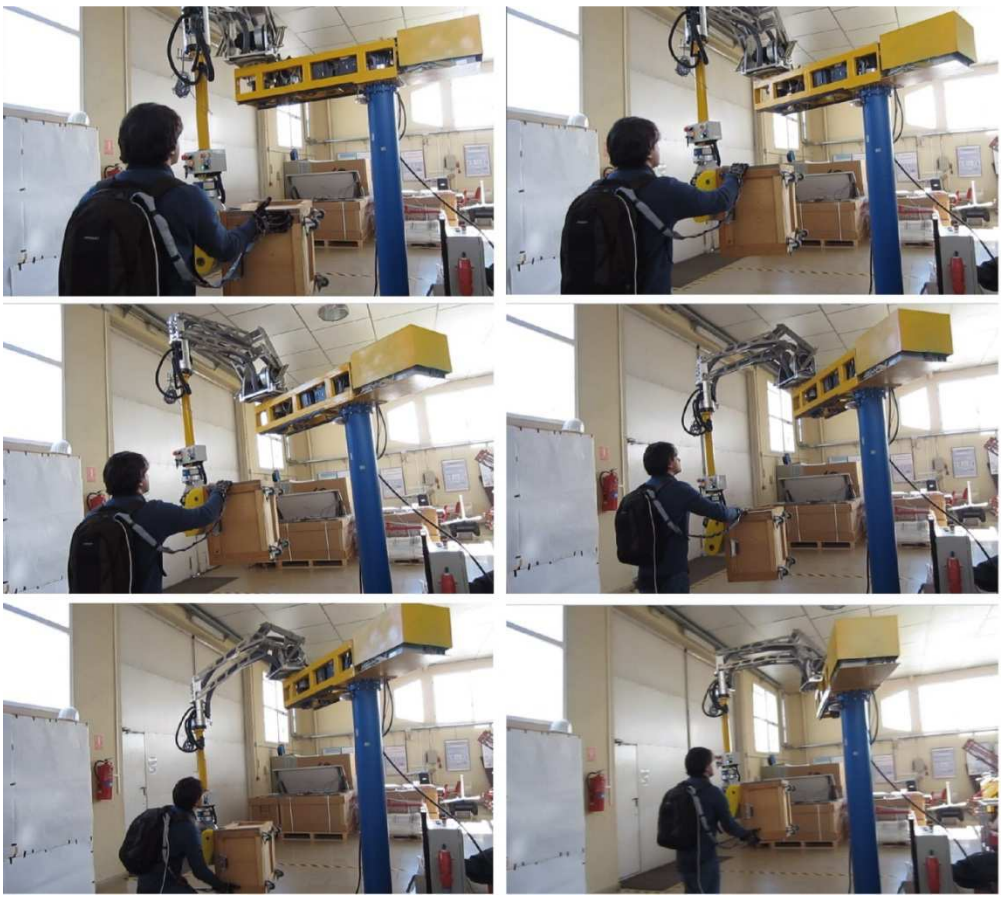

Figure 6.6: Sequence of photographs 1/2 showing the operation of the dataglove interface and the 6-DOF manipulator under an impedance control basis

Nonetheless, the maneuvers performed over the 6-DOF were basically the same in both instances. It must be remarked that the impedance law of equation Figure 5.6 was set as the rule to control robot motion in both cases.

Figure 6.7: Sequence of photographs 2/2 showing the operation of the dataglove interface and the 6-DOF manipulator under an impedance control basis

6.5 Conclusion and resume

This Chapter presented sequences of photographs from the combined operation of the dataglove interface and the 6-DOF manipulator under an impedance control basis. The sequences of photographs were captured from a set of videos included together with the digital version of thesis.

The test framework included: the dataglove interface, the 6-DOF manipulator, a dummy box-shaped load held at the manipulator end effector, the JR3 sensor and a subject with a backpack in which all the interface electronics -from the dataglove interface- were placed. Special emphasis was placed in this chapter to technically describe the interconnection among the aforesaid components.

A monitoring software capable of individually testing the electronic parts from the dataglove interface was also presented in this Chapter. This software tool was widely used during the development of the dataglove interface, but also demonstrated to be of great usefulness for later robot operation, since it could detect error sources such as hand orientation misalignment. Screen shots of the monitoring software were also presented with the aim of demonstrating its usefulness.

Chapter 7

7. Conclusions, contributions and future work

This Chapter summarizes the most remarkable facts and findings presented in this thesis. It is also presented some ideas for future developments and improvements regarding the contributions herein presented. Since this thesis has two differentiated, but highly related focuses; the conclusions and the possible future works are presented separately.

7.1 Conclusions regarding the modeling of the piezoresistive sensor model FlexiForce A201-100

An equivalent electrical model was presented and validated for the FlexiForce sensor model A201-100 with some restrictions. An operational amplifier, in inverting configuration, was used along all the tests herein described according to the recommendations given by the device's manufacturer.

7.1.1 Sensor Modeling and identification of non-linearities

The best match model was a parallel Resistor-Capacitor (RC), but some non-linearities were found in sensor's response that restricted the extensive usage of the proposed equivalent circuit. Specifically, two types of non-linearities were found:

Frequency non-linearity: The RC parallel model is a match for the FlexiForce sensor until a certain frequency, conveniently named as divergent frequency, is reached. For driving signals running over such magnitude, saturation in sensor's output is observed and the output phase shift is clamped to **70º** regardless of frequency increases. Slight changes were observed in the magnitude of the divergence frequency from one device to another, as well as little dependency between the applied force and the divergence frequency; this implies that no matter what the applied force is, the divergence frequency remains unchanged. It can be concluded that in order to ensure sensor operation within its linear region, the driving frequency must be held below **4 KHz**.

Amplitude non-linearity: This was probably the hardest to detect non-linearity in the FlexiForce sensor, since it neither produces saturation, nor exponential growth in the output signal of the amplifier circuit. When dealing with amplitude non-linearity, it must be understood as a non-linearity in sensor's resistance, because sensor's resistance is directly responsible for the output voltage under DC sourcing condition.

The type of amplitude non-linearity is that of a hyperbolic tangent function (**tanh**), i.e., the input and output voltage of the conditioning circuit running the FlexiForce sensor is related by a **tanh** function, so incremental input voltages produce hyperbolic tangent variations in the output signal. Nonetheless, and similarly to the frequency non-linearity, the **tanh** model is not comprehensive, and it is only capable of modeling the sensor's non-linearity when the magnitude of the driving voltage is held below **1 V**. For

sourcing voltages over **1 V**, it has not been yet found a suitable function capable of modeling sensor's resistance.

7.1.2 Linear Region of Operation for the FlexiForce sensor

Once the aforementioned non-linearities were delimited, it was possible to define a linear region of operation for the sensor. This is one of the contributions of the present work that could help others to further research in the understanding of piezoresistive sensors. So, in order to operate the FlexiForce sensor within its linear region, the DC voltage must be held constant meanwhile the force is varied. This statement adds no knowledge to the information already given by the manufacturer. However, by recalling that the amplitude non-linearity can be modeled when the sourcing voltage is held below **1 V**, it was demonstrated that it is possible to predict the changes in sensor's sensitivity produced by changes in the driving voltage using the **tanh** model; this yields an accurate force estimation whether the driving voltage is held constant or not during the force estimation process.

Changing the driving voltage is one of the two possible ways to trim a desired sensor's sensitivity. The second way is to change the value of the feedback resistor in the driving circuit.

For such cases that the input voltage is taken off from the range **(-1 V, 1 V)**, it has not been yet developed a sensor's model capable of correcting the amplitude nonlinearity, and consequently, the only way to perform force measurements is to held the input voltage constant meanwhile the force is varied.

Under the case of AC sourcing, the frequency of the driving signal must be held below **4 KHz** with the aim of operating the sensor within its linear region. The amplitude non-linearity is also present under AC sourcing, and thus, the AC-input amplitude was initially held below **1 V**. Nonetheless, a method to bypass the amplitude non-linearity was presented. The proposed method allows the decoupling between the non-linear conductance and the linear capacitance regardless of the magnitude of the AC input signal. This method is another of the main contributions presented in this thesis.

7.1.3 Piezocapacitive response and reduction in the force estimation error

A piezocapacitive response was found in the FlexiForce sensor A201-100. This is a novel property found on the device, and it is clearly another of the main contributions herein presented. The piezocapacitive property demonstrated to be useful to increase sensor's accuracy by means of performing a two-variable estimation of force. The reduction in the force estimation error is of paramount importance for the extensive usage of FlexiForce sensors in robotics applications which demand accurate and noninvasive force measurements.

Three different models working on the basis of combined conductance-capacitance estimation were presented. The traditional conductance model was also implemented for comparison purposes. The results reported an average reduction of **64%** in the force estimation error when compared with the conductance model proposed by the manufacturer. The method for computing the estimation error was based on the Mean Squared Error.

A decoupling method was used to perform capacitance readings over the sensors. For such purpose, the output signal from the driving circuit is multiplied by a cosine function which is then low-pass filtered to produce a DC signal which is only dependent on sensor's capacitance. This method was above declared as one of the contributions from this thesis. Despite all the aforesaid improvements, there is still a long road ahead for polymer piezoresistive sensors to match the sensitivity of load cells.

7.1.4 Combined estimation of the applied force and the exertion area

It was demonstrated that a combined estimation of the applied force and the exertion area is possible. For such purpose, a characterization involving different puck areas and force sweep was performed; meanwhile, sensor's conductance and capacitance were collected. With the data collected and the previous knowledge of capacitance and conductance variations, it was possible to arrange an equation system which could estimate both: the exertion area of the applied force and the force itself. This development is also claimed as one of the contributions of this thesis.

7.2 Future work regarding the modeling of the piezoresistive sensor model A201-100

Within the field of piezoresistive sensing technology, there are multiple approximations to follow on future researches. Next are addressed only some of the possible lines of research in regard with the contributions herein presented. However, a broader scope of the possible approximations was presented by Liu [107], with special focus on the new polymer materials and its usage on the manufacturing of piezoresistive sensors.

In order to follow the research lines summarized in Section 7.1, it should be first modeled the amplitude non-linearity of the FlexiForce sensor for input amplitudes greater than **1 V**. This is probably the most straightforward task to perform in the short term since the amplitude non-linearity was only studied for input voltages under **1 V**. A comprehensive sensor model without voltage restrictions is necessary for multiple reasons, e.g., to match a desired sensitivity in a multi sensor development or to develop more realistic models that include the temperature drift as input variable.

Modeling amplitude non-linearity for any input voltage would also allow to theoretically demonstrate the feasibility of the measuring scheme presented in Section 3.3.3, which is able to bypass the nonlinear behavior of sensor's conductance. This is important because only a partial demonstration was presented with the restriction of $\mathbf{|V_s| < 1\ V}$.

This thesis has presented plenty of empirical and theoretical data to support the usage of capacitance variation as an effective way to reduce the force estimation error. As above mentioned, a method to read sensor's capacitance through the bypass of conductance non-linearity was also presented. Later efforts can either focus on improving the performance of such devices or in providing additional functionalities to them, e.g., a combined estimation of the applied force and the exertion area. This property was already presented but there are many others available such as: the development of a thermal model to estimate the sensitivity variations produced by temperature changes. It is also possible to further research in the reduction of the force

estimation error through the proposal of new relationships between conductance and capacitance changes.

A combined estimation of the applied force and the exertion area was presented. However, no results were offered regarding the accuracy of such method because not enough experimental data were collected. Further researches could take as start point the framework for performing the combined estimation of force and area; this would include the set of pucks with different puck areas, the testbench and the equation system itself. The combined estimation of force and area is probably the most challenging task within the field of piezoresistive sensing because it demands full knowledge of resistive and capacitive variations as a function of the applied force.

Formulating a unifying model that embraces the exertion area, the applied force and temperature under a wide range of voltages is also a challenging task to perform. The model should be able to predict capacitance and conductance changes for the four mentioned variables. This could make available a wide range of capabilities to the sensor and yield a broader usage on robotic applications. However, it cannot be ascertained that such a model is possible to be formulated because the relationship between temperature, capacitance and conductance has not been yet explored.

Finally, it must be recalled that the modeling and methods presented in Chapter 3 have been developed for the sensor FlexiForce A201-100. However, there are multiple manufacturers of piezoresistive sensors as reported in Chapter 4. A broader study could embrace the application of the techniques learned in Chapter 3 to the Interlink sensor or to any other sensor working on the basis of piezoresistive sensing.

7.3 Conclusions regarding the dataglove interface for the impedance Control of Robotic Manipulators

The dataglove interface demonstrated to be a valid solution for determining the hand applied forces during object manipulation. Multiple applications can be encountered to the interface; this thesis has focused on only of them, the impedance control of a robotic manipulator.

7.3.1 Interface Functioning and Overview

The dataglove interface is a multi-sensor development capable of gathering the hand applied forces during object manipulation through the 11 piezoresistive sensors installed on the palm side. The instantaneous finger position is collected through the X-IST dataglove with a resolution of 15 DOF. Finally, the hand orientation within the task space is provided by an Inertial Measurement Unit, IMU, with magnetic field compensation. The IMU has been conveniently located on the dorsal side of the dataglove for comfort purposes.

The force sensor distribution along the palm side of the dataglove was based on previous hand grip studies and on the size of the robot's load. A match between the load size and the optimum sensor distribution was made with the goal of maximizing the user's comfort while reducing sensor number to a minimum. Given the bulky

characteristics of the load, the Surrounding Mild Flexion (SMF) and the Parallel Mild Flexion (PMF) grips were chosen to exert forces during load manipulation [83].

Through the combination of the information provided by the multiple sensors, it was possible to estimate, in a real-time basis, the hand applied forces meanwhile the operator manipulates the robot's endpoint or the robot's load. The hand applied forces are taken as the user's intention of motion, and thus, they are used to perform an impedance control scheme over the 6-DOF manipulator. Nonetheless, robot motion is only possible under a 3D (**x-y-z**) task space in this version of the interface.

This control scheme is based on the hands-on-payload concept, which states that the control interfaces of Intelligent Assist Devices should be as natural as possible, and likewise, the robot's maneuvers, levers or push button should be replaced by direct contact interfaces. The tests performed during this thesis demonstrated the feasibility of the dataglove interface to operate under the hands-on-payload concept.

It must be remarked that robot motion was done only with information from the dataglove interface and the robot kinematics. No information regarding the dynamic model of the manipulator was required. This is the most remarkable contribution of the dataglove interface, since the formulation of the robot dynamic model can be skipped.

When attempting to control a robotic manipulator under the hands-on-payload scheme, a load cell is usually installed near the robot's end point to collect the user applied forces. However, a robot dynamic model is required to discriminate among the user applied forces and the self-robot forces. The dataglove interface avoids the formulation of the robot dynamic model because the user's forces are directly obtained through the sensors installed on the palm side of the dataglove. Considering the decoupled dynamics that exists between the hand-dataglove system and the robot's structure, the self-robot forces do not affect the force readings acquired from the dataglove interface, and thus, they can be directly fed back to the impedance control loop. This is a clear advantage provided by the dataglove interface.

7.3.2 Resume of the tests performed over the dataglove interface

The force readings acquired from the dataglove interface were compared with the force measurements collected from a JR3 sensor installed near the end point of the 6-DOF manipulator. The JR3 sensor is a multi-axis load cell capable of collecting the forces and torques over all the axes with remarkable accuracy due to its built-in strain gauges. Considering that the JR3 readings were affected by the self-robot forces, two types of tests were performed.

First, a motionless test was performed and the force readings from the dataglove were compared with the JR3 force readings. The comparison was made on a time basis in separate plots for each axis. A separate plot was presented with the error along each axis. Considering that robot motion was disabled, the inertial forces were absent in the force plots from the JR3 sensor, and an objective comparison could be performed. The test results demonstrated the feasibility of the dataglove interface to track the hand applied forces over all the axes, but with certain inaccuracies in the force magnitude and direction.

One of the key advantages demonstrated during the motionless test was the ability of the dataglove interface to filter the hand applied forces from the forces produced by the robot's compliance. To understand this, it must be recalled that after the operator stopped from applying forces over the load, the manipulator kept oscillating for a few seconds due to the robot's compliance. This oscillating behavior was collected by the JR3 sensor, and was represented in the force plots with an oscillation pattern right after lifting the hand from the load. On the opposite side, the force readings collected by the interface exhibited a smooth decay when the hand force faded; this occurred due to the decoupled dynamics between the robot's structure and the hand-dataglove system.

The Second test applied to the dataglove interface was of dynamic type; this test embraced the usage of the real-time force measurements for the impedance control of a 6-DOF manipulator. In this case, the JR3 readings could no longer be considered as reference because the self-robot forces stemming from inertia affected the force measurements. Similar to the results stemmed from the static test, the experimental results demonstrated the feasibility of the interface to operate under the hands-on-payload mode by providing smooth force profiles and consequently adequate robot motion.

7.3.3 Broad usage of the dataglove interface in other research fields

The dataglove interface is an effective way of assessing the human intention during object's grasping and manipulation. The results herein presented demonstrated the feasibility of the interface for the impedance control of a 6-DOF manipulator. However, there are multiple applications that the dataglove interface could encounter. First of all, the force information stemmed from the interface could be used to control any type of manipulator. The only information required from the manipulator is the kinematic model to control the joint trajectories of each axis, but no information from the dynamic model is required. This fact eases the integration of the interface to any type of robotic manipulator.

The dataglove interface also finds possible applications within the field of rehabilitation. The force information gathered from the piezoresistive sensors, together with the finger flexion information is highly valuable when tracking patient's progress after any type of hand disease.

Within the field of sport researches, the dataglove interface could be used to track the hand applied forces together with hand motion during the holding stage of specific instruments of each sport, such as: golf sticks, tennis racquets and balls. Force tracking in unstructured environments is possible with the proposed interface since it is portable and battery sourced. Likewise, force and motion tracking is of paramount importance in multiple research fields which are hand-centered and demand reliable measuring solutions with little or null interference to the user's activity (noninvasive force readings). This statement is on the same trend with the above conclusions regarding the research over the FlexiForce sensor.

7.4 Future work regarding the dataglove interface

There are multiple approaches for future developments related with the dataglove interface, they are next listed:

7.4.1 Different Finger Configurations

The tests presented in this thesis were done using the Surrounding Mild Flexion (SMF) and the Parallel Mild Flexion (PMF) grips. These were the most appropriate grips for the bulky load held by the manipulator. With the aim of exhaustively testing the interface, it is necessary to change the load, for a less bulky one, and then use different grips to interact with it. Under such scenario, it could be necessary to either add more force sensors, or change its distribution over the hand.

If multiple hand grips are to be implemented, or if manipulation with precision grip is required, it would be necessary to use a more realistic dataglove capable of measuring finger abduction over all the fingers. This would require a minimum of 21DOF to achieve a realism level capable of coping with the precision grips. The X-IST dataglove, employed in this research, is capable of measuring up to 15 DOF but only finger flexion is measured.

7.4.2. Allow full robot motion over a 6-D taskspace.

The forces gathered by the dataglove interface were done on the basis of a 3-D taskspace, ($\mathbf{F_x}$-$\mathbf{F_y}$-$\mathbf{F_z}$). Consequently, robot motion was performed in a 3-D taskspace (**x-y-z**). In order to allow full robot motion in a 6-D taskspace, the measured forces must be converted to torques. This requires a conversion convention that may have multiple possibilities.

One of the possible solutions is to employ a second dataglove on the left hand. This would allow torque estimation on the basis of two force vectors applied over a free load in the space. The pivot point for the moment torque calculation could be located in the middle of both forces; that is, in the middle of both hands. An in-depth analysis of this approach is available on the Appendix B of this thesis.

7.4.3 Implement capacitive measurements over the piezoresistive sensors.

This thesis has demonstrated the advantages of combined conductance-capacitance estimation towards the reduction of the force estimation error in piezoresistive devices. The most straightforward way of improving the accuracy of the dataglove interface is, therefore, to implement capacitance readings on the piezoresistive sensors, and then, implement a combined conductance-capacitance estimation of the exerted force.

Considering that both research lines have been performed in parallel, the most remarkable improvements on force sensing were discovered right after the dataglove interface was designed and built. This caused that many of the force sensing improvements could not be implemented on this version of the dataglove interface.

References

[1] D Aarno and D Kragic. Motion intention recognition in robot assisted applications. *Robotics and Autonomous Systems*, 56(8):692–705, 2008.

[2] J Akizono, T Hirabayashi, T Yamamoto, H Sakai, and H Yano. Teleoperation of construction machines with haptic information for underwater applications. *Automation in Construction*, 15(5):563–70, 2006.

[3] M Aliaga, A Rubio, and E Sanchez. Experimental quantitative comparison of different control architectures for master-slave teleoperation. *IEEE Transactions on Control Systems Technology*, 12(1):2–11, 2004.

[4] M Arnouldus. Determination of the piezoresistive properties of strained silicon. Master's thesis, Technical University of Denmark, 2006.

[5] C Ashruf. Thin flexible pressure sensors. *Sensor Review*, 22:322–7, 2002.

[6] L Barbe, B Bayle, E Laroche, and M de Mathelin. User Adapted Control of Force Feedback Teleoperators: Evaluation and Robustness Analysis. In *Proc. IEEE/RSJ Int. Conf. Robots and Intelligent Systems*, pp. 418–23, 2008. Nice, France.

[7] Barrett Technology Inc. BarrettHand datasheet. Available at: http://web.barrett.com/support/BarrettHand_Documentation/BH8-280_Datasheet.pdf.

[8] J Baumhauer, R Wervey, J McWilliams, G Harris, and M Shereff. A comparison study of plantar foot pressure in a standardized shoe, total contact cast, and prefabricated pneumatic walking brace. *Foot & Ankle Int.*, 18(1):26–33, 1997.

[9] L Beccai, S Roccella, A Arena, F Valvo, P Valdastri, A Menciassi, M Carrozza, and P Dario. Design and Fabrication of a Hybrid silicon three-axial Force Sensor for Biomechanical Applications. *Sensors and Actuators A: Physical*, 120(2):370–82, 2005.

[10] M Beyer. Do You Know the Accuracy of your Pressure Sensor? Find your Way Out of the Waze of Accuracy Data? *Sensor Magazin*, 4:54–6, 2008.

[11] K Bisshopp and D Drucker. Large Deflection of Cantilever Beams. *Quarterly of Applied Mathematics*, 3(1), 1945.

[12] H Bolandi and S M Esmaeilzadeh. Exact Tip Trajectory Tracking Control of a Flexible Robot Arm. *Int. Journal of Robotics & Automation*, 26(1):100–9, 2011.

[13] C Borst, M Fischer, S Haidacher, H Liu, and G Hirzinger. DLR hand II: Experiments and experiences with an anthropomorphic hand. In *Proc. IEEE Int. Conf. Robotics and Automation*, pp. 702–7, 2003. Taipei, Taiwan.

[14] T Bretl, S Lall, J Latombe, and S Rock. Multi-step Motion Planning for Free-climbing Robots. In *Workshop on the Algorithmic Foundations on the Robotics (WAFR)*, pp. 1–16, 2004. Utrecht, Netherlands.

[15] Busch Electronics. Understanding accuracy ratings in melt pressure sensors, 2009. Available at: http://www.buschelectronics.com/uploads/Understanding_Accuracy_Ratings_in_Melt_Pressure_Sensors_Rev_F.pdf.

[16] M Carrozza, G Cappiello, S Micera, B Edin, L Beccai, and C Cipriani. Design of a Cybernetic Hand for Perception and Action.

[17] M Carrozza, A Persichetti, C Laschi, F Vecchi, R Lazzarini, P Vacalebri, and P Dario. A Wearable Biomechatronic Interface for Controlling Robots with Voluntary Foot Movements. *IEEE-ASME Transactions on Mechatronics*, 12(1):1–11, 2007.

[18] J Carusone, K Buchan, and G D'Eleuterio. Experiments in End-Effector Tracking Control for Structurally Flexible Space Manipulators. *IEEE Transactions on Robotics and Automation*, 9(5):553–60, 1993.

[19] J Castellanos-Ramos, R Navas-Gonzalez, H Macicior, T Sikora, E Ochoteco, and F Vidal-Verdu. Tactile sensors based on Conductive Polymers. *Microsystem Technologies*, 16(5, SI):765–76, 2010.

[20] M Castro and A Jr Cliquet. A low-cost instrumented Glove for Monitoring Forces during Object Manipulation. *IEEE Transactions on Rehabilitation Engineering*, 5(2):140–7, 1997.

[21] M Chalon, M Grebenstein, T Wimboeck, and G Hirzinger. The thumb: Guidelines for a Robotic Design. In *Proc. IEEE/RSJ Int. Conf. Intelligent Robots and Systems*, pp. 5886–93, 2010. Taipei, Taiwan.

[22] P Chappell and J Elliott. Contact Force Sensor for Artificial Hands with a Digital Interface for a Controller.

[23] S Cobos, M Ferre, and R Aracil. Simplified Human Hand Models based on Grasping Analysis.

[24] S Cobos, M Ferre, J Ortego, and M A Sanchez-Uran. Simplified hand configuration for object manipulation. In *Haptics: Perception, Devices and Scenarios*, volume 5024 of *Lecture Notes in Computer Science*, pp. 730–5. Springer Berlin / Heidelberg, 2008. ISBN 978-3-540-69056-6.

[25] S Cobos, M Ferre, M A Sanchez-Uran, J Ortego, and R Aracil. Human Hand Descriptions and Gesture Recognition for Object Manipulation. *Computer Methods in Biomechanics and Biomedical Engineering*, 13(3):305–17, 2010.

[26] R Colbaugh, H Seraji, and K Glass. Adaptive Compliant Motion Control for Dexterous Manipulators. *Int. Journal of Robotics Research*, 14(3):270–80, 1995.

[27] J Colgate. *The Control of Dynamically Interacting Systems*. PhD thesis, Massachusetts institute of Technology, 1988.

[28] J Colgate and N Hogan. Robust control of dynamically interacting systems. *Int. Journal of Control*, 48(1):65–88, 1988.

[29] J Colgate and N Hogan. *Advanced Robotics*, chapter The Interaction of Robots with Passive Environments: Application to Force Feedback Control. Springer-Verlag, 1989.

[30] J Colgate and N Hogan. An analysis of contact instability in terms of passive physical equivalents. In *Proc. IEEE Int. Conf. Robotics and Automation*, pp. 404–9, 1989. Scottsdal, AZ.

[31] J Colgate and N Hogan. The Interaction of Robots with Passive Environments: Application to Force Feedback Control. In Kenneth J. Waldron, editor, *Advanced Robotics: 1989*, pp. 465–474. Springer Berlin Heidelberg, 1989.

[32] J Colgate and M Peshkin. Intelligent Assist Devices. Revolutionary Technology for Material Handling, 2002. The New Standard in Material Handling Technology. Cobotics IAD White Paper, Stanley.

[33] J Colgate, M Peshkin, and S Klostermeyer. Intelligent Assist Devices in industrial applications: A review. In *Proc. IEEE. Int. Conf. Intelligent Robots and Systems*, volume 3, pp. 2516–21, 2003. Las Vegas, NV.

[34] J Colgate, M Peshkin, and W Wannasuphoprasit. Nonholonomic haptic display. In *Proc. IEEE Int. Conf. Robotics and Automation*, pp. 539–44, 1996. Minneapolis, MN.

[35] J Craig and M Raibert. A systematic method of hybrid position/force control of a manipulator. In *Proc. IEEE Computer Society's Third International Conf. Computer Software and Applications COMPSAC*, pp. 446–51, 1979. Chicago, IL.

[36] A Cranny, D Cotton, P Chappell, S Beeby, and N White. Thick-film force, slip and temperature Sensors for a Prosthetic Hand.

[37] M Culjat, C King, M Franco, C Lewis, J Bisley, and E Dutson. A tactile feedback system for robotic surgery. In *Proc. 30th Int. Conf. IEEE Engineering in Medicine and Biology Society EMBS*, pp. 1930–4, 2008. Vancouver, Canada.

[38] Cyber Glove Systems. *Cyberglove Datasheet*. Available at: http://www.cyberglovesystems.com/sites/default/files/CyberGloveII_Brochure_2009.pdf.

[39] Cyber Glove Systems. *Cybergrasp Datasheet*. Available at: http://www.cyberglovesystems.com/sites/default/files/CyberGrasp_Brochure_2009_1.pdf.

[40] Hao Dang, J Weisz, and P Allen. Blind grasping: Stable robotic grasping using tactile feedback and hand kinematics. In *Proc. IEEE Int. Conf. Robotics and Automation*, pp. 5917–22, 2011. Shanghai, China.

[41] B DeJong, E Faulring, J Colgate, M Peshkin, H Kang, Y Park, and T Ewing. Lessons learned from a novel teleoperation testbed. *Industrial Robot: An Int. Journal*, 33:187–93, 2006.

[42] L Dipietro, A Sabatini, and P Dario. A Survey of glove-based Systems and their Applications. *IEEE Transactions on Systems, Man, and Cybernetics. Part C-Applications and Reviews*.

[43] S Ekvall and D Kragic. Learning and evaluation of the approach vector for automatic grasp generation and planning. In *Proc. IEEE Int. Conf. Robotics and Automation*, 2007. Rome, Italy.

[44] K Emancipator and M Kroll. A quantitative Measure of Nonlinearity. *Clinical Chemistry*, 39(5):766–72, 1993.

[45] S Eppinger and W Seering. Modeling Robot Flexibility for Endpoint Force Control. In *Proc. IEEE Int. Conf. on Robotics and Automation*, pp. 165–70, 1988. Leuven, Belgium.

[46] M Erden and T Tomiyama. Human-Intent Detection and Physically Interactive Control of a Robot without Force Sensors. *IEEE Transactions on Robotics*, 26(2):370–82, 2010.

[47] E Faulring, J Colgate, and M Peshkin. High Performance Cobotics. In *Proc. IEEE Int. Conf. Rehabilitation Robotics*, pp. 143–8, 2005. Chicago, IL.

[48] M Ferguson-Pell, S Hagisawa, and D Bain. Evaluation of a Sensor for low Interface Pressure Applications. *Medical Engineering & Physics*, 22:657–63, 2000.

[49] M Ferre, I Galiana, and R Aracil. Design of a Lightweight, Cost Effective Thimble-Like Sensor for Haptic Applications Based on Contact Force Sensors. *Sensors*, 11(12):11495–509, 2011.

[50] M Ferre, I Galiana, J Barrio, P Garcia-Robledo, A Gimenez, and J Lopez. Two-Hand Virtual Object Manipulation Based on Networked Architecture. In *Proc. EuroHaptics Int. Conf. on Generating and Perceiving Tangible Sensations*, Lecture Notes in Computer Science, pp. 130–5, 2010. Amsterdam, Netherlands.

[51] J Flanagan, M Burstedt, and R Johansson. Control of Fingertip Forces in Multidigit Manipulation. *Journal of Neurophysiology*, 81(4):1706–17, 1999.

[52] International Organization for Standardization. *ISO 10218-1:2011. Robots and robotic devices – Safety requirements for industrial robots – Part 1: Robots*. 2011.

[53] A Forouzantabar, H Talebi, and A Sedigh. Bilateral control of master-slave manipulators with constant time delay. *ISA Transactions*, 51(1):74–80, 2011.

[54] H Fowler and S Eppinger. Bandwidth Performance of a Direct Drive Manipulator Under Joint Torque and end-point Force Control. In *Proc. IEEE Int. Conf. on Robotics and Automation*, pp. 230–7, 1991. Sacramento, CA.

[55] Galil Motion Control Inc. *DMC-18x2 User Manual*, 2008. Available at: http://irtfweb.ifa.hawaii.edu/ tcs3/tcs3/vendor_info/Galil_rio/Aug2009/manuals/man18x2.pdf.

[56] J Galvez, J Estremera, and P De Santos. SILO4 - A versatile quadruped Robot for Research in Force Distribution. In *3rd Int. Conf. Climbing and Walking Robots (CLAWAR)*, pp. 371–83, 2000. Madrid, Spain.

[57] E Garcia, P Gonzalez de Santos, and F Matia. Dealing with internal and external perturbations on walking robots. *Autonomous Robots*, 24(3):213–27, 2008.

[58] E Garcia and P Gonzalez de Santos. Controlling dynamic stability and active compliance to improve quadrupedal walking. In *8th Int. Conf. Climbing and Walking Robots (CLAWAR)*, pp. 205–12, 2006. London, England.

[59] J Garcia, A Robertsson, J Ortega, and R Johansson. Force and Acceleration Sensor Fusion for Compliant Robot Motion Control. In *Proc. IEEE Int. Conf. Robotics and Automation*, pp. 2709–14, 2005. Barcelona, Spain.

[60] J Garcia, A Robertsson, J Ortega, and R Johansson. Sensor Fusion for Compliant Robot Motion Control. *IEEE Transactions on Robotics*, 24(2):430–41, 2008.

[61] R Gentner and J Classen. Development and evaluation of a low-cost sensor glove for assessment of human finger movements in neurophysiological settings. *Journal of Neuroscience Methods*, 178(1):138–47, 2009.

[62] G Gomez, A Hernandez, and P Hotz. An adaptive neural controller for a tendon driven robotic hand. In *9th Int. Conf. Intelligent Autonomous Systems*, pp. 298–307, 2006. Tokyo, Japan.

[63] P Gonzalez de Santos, E Garcia, J Sarria, R Ponticelli, and J Reviejo. A new Manipulator Structure for power-assist devices. *Industrial Robot: An International Journal*, 37(5):452–8, 2010.

[64] S Haddadin, A Albu-Schaeffer, and G Hirzinger. Safe Physical Human-Robot Interaction: Measurements, Analysis and New Insights. In *13th Int. Symp. on Robotics Research*, pp. 439–50, 2007. Hiroshima, Japan.

[65] R Hannah and S Reed. *Strain Gage User's Handbook*. Springer, 1992. ISBN 978-0-412-53720-2.

[66] E Helms, R D Schraft, and M Hagele. rob@work: Robot assistant in industrial environments. In *Proc. 11th IEEE Int. Workshop on Robot and Human Interactive Communication*, pp. 399–404, 2002. Berlin, Germany.

[67] N Hogan. Impedance Control: An Approach to Manipulation Part I - Theory, Part II - Implementation, Part III - Applications. *Journal of Dynamic Systems, Measurement, and Control*, 107(1):1–24, 1985.

[68] N Hogan. Stable execution of contact tasks using impedance control. In *Proc. IEEE Int. Conf. on Robotics and Automation*, pp. 1047–54, 1987. Raleigh, NC.

[69] A Hollinger and M Wanderley. Evaluation of Commercial Force-Sensing Resistors. In *Int. Conf. on new interfaces for musical expression NIME06*, 2006. Paris, France.

[70] K Houston, A Sieber, C Eder, O Tonet, A Menciassi, and P Dario. Novel Haptic Tool and Input Device for real time Bilateral Biomanipulation addressing Endoscopic Surgery. In *Proc. Annual Int. Conf. IEEE Eng. Medicine and Biology Society*, pp. 198–201, 2007. Lyon, France.

[71] H Y Hu, X H Gao, J W Li, and H Wang. Calibrating human hand for teleoperating the HIT/DLR hand. In *Proc. IEEE Int. Conf. Robotics and Automation*, pp. 4571–6, 2004. New Orleans, LA.

[72] H Y Hu, J W Li, Z W Xie, B Wang, H Liu, and G Hirzinger. A robot arm/hand teleoperation system with telepresence and shared control. In *IEEE/ASME Int. Conference Advanced Intelligent Mechatronics*, pp. 1312–7, 2005. Monterey, CA.

[73] Q J Huang and K Nonami. Humanitarian mine detecting six-legged walking robot and hybrid neuro walking control with position/force control. *Mechatronics*, 13(8-9):773–90, 2003.

[74] A Hussong, T Rau, H Eilers, S Baron, B Heimann, M Leinung, T Lenarz, and O Majdani. Conception and Design of an Automated Insertion Tool for Cochlear Implants. In *Proc. IEEE Ann. Int. Conf. Engineering in Medicine and Biology Society*, pp. 5593–6, 2008. Vancouver, Canada.

[75] A Hussong, T S Rau, T Ortmaier, B Heimann, T Lenarz, and O Majdani. An automated insertion tool for cochlear implants: another step towards atraumatic

cochlear implant surgery. *Int. Journal of Computer Assisted Radiology and Surgery*, 5(2):163–71, 2010.

[76] Tekscan Inc. *FlexiForce®, Standard Force & Load Sensors Model A201*. Available at: http://www.tekscan.com/pdf/FlexiForce-Sensors-Manual.pdf.

[77] ATI Industrial Automation. *Multi-Axis Force/Torque Sensors Brochure*. Available at: http://www.ati-ia.com/products/ft/sensors.aspx.

[78] Inition. *X-IST Data-Glove Datasheet*. Available at: http://www.inition.co.uk/3D-Technologies/x-ist-data-glove.

[79] Interlink Electronics. *FSR400 Series Datasheet*. Available at: http://www.interlinkelectronics.com/FSR402.php.

[80] H Iwata and S Sugano. Design of Anthropomorphic Dexterous Hand with Passive Joints and Sensitive Soft Skins. In *IEEE/SICE Int. Symp. System Integration*, pp. 129–34, 2009. Tokyo, Japan.

[81] W Y Jiang, A M Liu, and D Howard. Optimization of legged robot locomotion by control of foot-force distribution. *Transactions of the Institute of Measurement and Control*, 26(4):311–23, 2004.

[82] JR3 Inc. *Six axis force and torque transducer model 160M50A*. Available at: http://www.jr3.com/documents/datasheets/MSeries/160M50A3.pdf.

[83] N Kamakura, M Matsuo, H Ishii, F Mitsuboshi, and Y Miura. Patterns of Static Prehension in Normal Hands. *American Journal of Occupational Therapy*, 34(7):437–45, 1980.

[84] R Kamnik, D Matko, and T Bajd. Application of model Reference Adaptive Control to Industrial Robot Impedance Control. *Journal of Intelligent & Robotic Systems*, 22(2):153–63, 1998.

[85] B Kane, M Cutkosky, and G Kovacs. A traction stress sensor array for use in high-resolution robotic tactile imaging. *Journal of Microelectromechanical Systems*, 9(4):425–34, 2000.

[86] M Kaneko, A Mizuno, and K Harada. Torque distribution for achieving a hugging walk. In *Proc. IEEE/RSJ Int. Conf. Intelligent Robots ans Systems*, pp. 2613–8, 2002. Lausanne, Switzerland.

[87] S B Kang and K Ikeuchi. Toward automatic robot instruction from perception - Mapping human grasps to manipulator grasps. *IEEE Transactions on Robotics and Automation*, 13(1):81–95, 1997.

[88] S Katsura, W Iida, and K Ohnishi. Medical mechatronics - an application to haptic forceps. *Annual Reviews in Control*, 29(2):237–45, 2005.

[89] S Katsura, Y Matsumoto, and K Ohnishi. Analysis and experimental validation of force bandwidth for force control. *IEEE Transactions on Industrial Electronics*, 53(3):922–8, 2006.

[90] H Kazerooni, D Fairbanks, A Chen, and G Shin. The magic glove. In *Proc. IEEE Int. Conf. on Robotics and Automation*, pp. 757–63, 2004. New Orleans, LA.

[91] F Khalil, P Payeur, and A Cretu. Integrated Multisensory Robotic Hand System for Deformable Object Manipulation. In *Proc. IASTED Int. Conf. Robotics and Applications*, pp. 159–66, 2010. Cambridge, MA.

[92] E R Komi, J R Roberts, and S J Rothberg. Evaluation of thin, flexible sensors for time-resolved grip force measurement. *Proc. Institution of Mechanical Engineers, Part C: Journal of Mechanical Enginnering Science*, 221(12):1687–99, 2007.

[93] Y-K Kong and B Lowe. Optimal cylindrical handle diameter for grip force tasks. *Int. Journal of Industrial Ergonomics*, 35(6):495–507, 2005.

[94] C Koukourlis, V Trigonidis, and J Sahalos. Differential synchronous demodulation for small signal amplitude estimation. *IEEE Transactions on Instrumentation and Measurement*, 42(5):926–1, 1993.

[95] B Krivopal. Us patent number 5,989,700. pressure sensitive ink means, and method of use, 1999.

[96] T Kroeger, B Finkemeyer, S Winkelbach, L Eble, S Molkenstruck, and F Wahl. A manipulator plays Jenga - Applying multisensor integration in industrial manipulation control. *IEEE Robotics & Automation Magazine*, 15(3):79–84, 2008.

[97] T Kroeger, D Kubus, and F Wahl. Force and acceleration sensor fusion for compliant manipulation control in 6 degrees of freedom. *Advanced Robotics*, 21(14):1603–16, 2007.

[98] J Kruger, T Lien, and A Verl. Cooperation of human and machines in assembly lines. *CIRP Annals - Manufacturing Technology*, 58(2):628–46, 2009.

[99] V Kumar and K J Waldron. Force Distribution in Walking Vehicles. *Journal of Mechanical Design*, 112(1):90–9, 1990.

[100] X Lamy, F Colledani, F Geffard, Y Measson, and G Morel. Robotic Skin Structure and Performances for Industrial Robot Comanipulation. In *IEEE/ASME Int. Conf. Advanced Intelligent Mechatronics*, pp. 427–32, 2009. Singapore.

[101] X Lamy, F Colledani, F Geffard, Y Measson, and G Morel. Overcoming Human Force Amplification Limitations in Comanipulation Tasks with Industrial Robot. In *8th World Congr. on Inteliigent Control and Automation*, pp. 592–8, 2010. Jinan, China.

[102] C Lebosse, B Bayle, M de Mathelin, and P Renaud. Nonlinear modeling of low cost force sensors. In *Proc. IEEE Int. Conf. Robotics and Automation*, pp. 3437–42, may 2008. Pasadena, CA.

[103] C Lebosse, P Renaud, B Bayle, and M de Mathelin. Modeling and evaluation of low-cost force sensors. *IEEE Transactions on Robotics*, 27(4):815–22, 2011.

[104] J H Lee, Y S Lee, S H Park, M C Park, B K Yoo, and S M In. A Study on the Human Grip Force Distribution on the Cylindrical Handle by Intelligent Force Glove (I-Force Glove). In *Int. Conf. Control, Automation and Systems*, pp. 858–61, 2008. Seoul, South Korea.

[105] S Y Lee, K Y Lee, S H Lee, J W Kim, and C S Han. Human-robot Cooperation Control for Installing Heavy Construction Materials. *Autonomous Robots*, 22(3):305–19, 2007.

[106] T Lenzi, N Vitiello, S M M De Rossi, A Persichetti, F Giovacchini, S Roccella, F Vecchi, and M C Carrozza. Measuring human-robot Interaction on wearable Robots: A distributed approach. *Mechatronics*, 21(6):1123–31, 2011.

[107] C Liu. *Foundations of MEMS*. Illinois Ece Series. Pearson Prentice Hall, 2006. ISBN 9780131472860.

[108] H Liu. Exploring human hand capabilities into embedded multifingered object manipulation. *IEEE Transactions on Industrial Informatics*, 7(3):389–98, 2011.

[109] T Liu, Y Inoue, and K Shibata. A wearable force plate system for the continuous measurement of triaxial ground reaction force in biomechanical applications. *Measurement Science & Technology*, 21(8):1–9, 2010.

[110] M Lowe, A King, E Lovett, and T Papakostas. Flexible tactile sensor technology: bringing haptics to life. *Sensor Review*, 24:33–6, 2004.

[111] M-L Lu, T James, B Lowe, M Barrero, and Y-K Kong. An investigation of hand forces and postures for using selected mechanical pipettes. *Int. Journal of Industrial Ergonomics*, 38(1):18–29, 2008.

[112] O Majdani, D Schurzig, A Hussong, T Rau, J Wittkopf, T Lenarz, and R F Labadie. Force Measurement of insertion of Cochlear Implant Electrode Arrays in vitro: Comparison of surgeon to automated Insertion Tool. *Acta Oto-laryngologica*, 130(1):31–6, 2010.

[113] J Makal. The combined sensor using bridge circuit supplied by current sources for simultaneous measurement of two parameters. *Journal of Vibroengineering*, 11(4):729–36, 2009.

[114] M Marzke. Evolutionary Development of the Human Thumb. *Hand Clinics*, 8(1):1–8, 1992.

[115] Microstrain. *3DM-GX3®-25 Data Communications Protocol*. Available at: http://files.microstrain.com/3DM-GX3-Data-Communications-Protocol.pdf.

[116] M Monroy, M Ferre, J Barrio, V Eslava, and I Galiana. Sensorized Thimble for Haptic Applications. In *Proc. IEEE Int. Conf. Mechatronics*, pp. 201–6, 2009. Malaga, Spain.

[117] N Montes, M Mora, and J Tornero. Trajectory Generation based on Rational Bezier Curves as Clothoids. In *Proc. IEEE Intelligent Vehicles Symp.*, pp. 505–10, 2007. Istambul, Turkey.

[118] C Moore. Continuosly Variable Transmission for Serial Link Cobot Architecture. Master's thesis, Department of Mechanical Engineering, Northwestern University, IL, 1997.

[119] C Moore, M Peshkin, and J Colgate. Cobot Implementation of Virtual Paths and 3D Virtual Surfaces. *IEEE Transactions on Robotics and Automation*, 19(2):347–51, 2003.

[120] J Morales, J Martinez, M Martinez, and A Mandow. Pure-Pursuit Reactive Path Tracking for Nonholonomic Mobile Robots with a 2D Laser Scanner. *EURASIP Journal of Advances in Signal Processing*, 2009. ID 935237.

[121] J Morgado De Gois, D Germann, and M Hiller. Sensor-based ground detection in unstructured terrain for the walking machine ALDURO. In *6th Int. Conf. Climbing and Walking Robots (CLAWAR)*, pp. 911–8, 2003. Catania, Italy.

[122] I Muller, R de Brito, C Pereira, and V Brusamarello. Load Cells in Force Sensing Analysis – Theory and a Novel Application. *IEEE Robotics & Automation Magazine*, 13(1):15–9, 2010.

[123] A Narayan. Design of Intelligent Controller Jib Crane. Master's thesis, Department of Mechanical Engineering, Northwestern University, IL, 2000.

[124] K D Nguyen, I M Chen, Z Luo, S H Yeo, and H L Duh. A Wearable Sensing System for Tracking and Monitoring of Functional Arm Movement. *IEEE-ASME Transactions on Mechatronics*, 16(2):213–20, 2011.

[125] A Nihal, J Goldstein, J Haas, R Hiebert, F Kummer, M Liederbach, and E Trepman. Toe flexor forces in dancers and non-dancers. *Foot & Ankle Int.*, 23(12):1119–23, 2002.

[126] K Nonami, Q J Huang, D Komizo, N Shimoi, and H Uchida. Humanitarian mine detection six-legged walking robot. In *Proc. 3rd Int. Conf. Climbing and Walking Robots (CLAWAR)*, pp. 861–8, 2000. Madrid, Spain.

[127] J Otto, T Brown, and J Callaghan. Static and Dynamic Response of a multiplexed-array Piezoresistive Contact Sensor. *Experimental Mechanics*, 39(4):317–23, 1999.

[128] L Paredes-Madrid, L Emmi, E Garcia, and P Gonzalez de Santos. Detailed Study of Amplitude Nonlinearity in Piezoresistive Force Sensors. *Sensors*, 11(9):8836–54, 2011.

[129] L Paredes-Madrid, L Emmi, and P Gonzalez de Santos. Improving the performance of piezoresistive force sensors by modeling sensor capacitance. In *Proc. IEEE Int. Symp. Industrial Electronics*, pp. 458–63, 2010. Bari, Italy.

[130] L Paredes-Madrid and P Gonzalez de Santos. Patente nro. 2351143. Sistema y Procedimiento de Control para Manipuladores. In *Oficina Española de Patentes y Marcas*, 2009.

[131] L Paredes-Madrid and P Gonzalez de Santos. *Sistema de interacción persona-manipulador mediante guantes de datos*, Chapter X, pp. 129–46. Editorial Universidad Nacional de Educación a Distancia, 2009. Interacción Persona-Robot, ISBN: 978-84-692-5987-0.

[132] L Paredes-Madrid and P Gonzalez de Santos. Comprehensible Model of Amplitude Nonlinearities in Piezoresistive-force Sensors. In *Proc. 8th Int. Conf. Informatics in Control Automation and Robotics*, pp. 405–10, 2011. Noordwijkerhout, The Netherlands.

[133] L Paredes-Madrid and P Gonzalez de Santos. Dataglove-based interface for impedance control of manipulators in cooperative human–robot environments. *Measurement Science and Technology*, 24(2), 2013. 025005.

[134] L Paredes-Madrid, P Torruella, P Solaeche, I Galiana, and P Gonzalez de Santos. Accurate modeling of low-cost piezoresistive force sensors for haptic interfaces. In *Proc. IEEE Int. Conf. Robotics and Automation*, pp. 1828–33, 2010. Anchorage, AK.

[135] C Park, J H Kyung, and D I Park. Development of an industrial robot manipulator for the easy and safe human-robot cooperation. In *Int. Conf. Control Automation Systems*, pp. 678–81, 2010. Gyeonggi-do, South Korea.

[136] Y E Park and K D Wise. An MOS switched-capacitor readout Amplifier for Capacitive Pressure Sensors. In *Proc. of the IEEE Custom Integrated Circuits Conference*, pp. 380–4, 1983. Rochester, NY.

[137] I Payo, V Feliu, and O D Cortazar. Force control of a very lightweight single-link flexible arm based on coupling torque feedback. *Mechatronics*, 19(3):334–47, 2009.

[138] H Pearce. The Design and Construction of an Intelligent Power Assist Jib Crane. Master's thesis, Department of Mechanical Engineering, Northwestern University, IL, 1999.

[139] A Pervez and J Ryu. Safe physical human robot interaction-past, present and future. *Journal of Mechanical Science and Technology*, 22(3):469–83, 2008.

[140] M Peshkin and J Colgate. Cobots. *Industrial Robot: An Int. Journal*, 26(5):335–41, 1999.

[141] M Peshkin, J Colgate, W Wannasuphoprasit, C Moore, R Gillespie, and P Akella. Cobot Architecture. *IEEE Transactions on Robotics and Automation*, 17(4):377–90, 2001.

[142] J Plummer. *Silicon VLSI Technology: Fundamentals, Practice, and Modeling*. Pearson Education, 2009. ISBN 9788131726044.

[143] D Preethichandra and K Shida. A simple interface circuit to measure very small capacitance changes in capacitive sensors. *IEEE Transactions on Instrumentation and Measurement*, 50(6):1583–6, 2001.

[144] Pressure Profile Systems. Robotouch Overview. Available at: http://www.pressureprofile.com/products-robotouch.

[145] Pressure Profile Systems. TactArray Devices: Products Overview. Available at: http://www.pressureprofile.com/products.php.

[146] J Salisbury. Active Stiffness Control of Manipulator in Cartesian Coordinates. In *19th IEEE Conf. Decision and Control including Symp. Adaptive Processes*, pp. 95–100, 1980. Albuquerque, NM.

[147] N Sawaguchi, T Majima, T Ishigaki, N Mori, T Terashima, and A Minami. Mobile-Bearing Total Knee Arthroplasty Improves Patellar Tracking and Patellofemoral Contact Stress. *The Journal of Arthroplasty*, 25:920–5, 2010.

[148] A Schneider and U Schmucker. Forced legged platform 'Katharina' for service operations. In *Proc. 3rd Int. Conf. Climbing and Walking Robots (CLAWAR)*, pp. 1029–36, 2001. Karlsruhe, Germany.

[149] A Schneider and U Scmucker. *Force Sensing for Multi-Legged Walking Robots: Theory and Experiments Part 1: Overview and Force Sensing*, chapter 23, page 576. Fraunhofer Institute for Factory Operation and Automation, 2006.

[150] L Sciavicco and B Siciliano. *Modeling and Control of Robot Manipulatos*. McGraw-Hill Int. Editions, 1996. ISBN 978-1-85233-221-1.

[151] B Shimano. Force control. In *Exploratory Study of Computer Integrated Assembly Systems, Binford, T O, et. al.* Stanford Artificial Intelligence Laboratory Memo 285.4, June, 1977.

[152] B Siciliano and L Villani. *Robot force control*. Kluwer Academic Publishers, 1999. ISBN 0-7923-7733-8.

[153] P Silva, P Pinto, O Postolache, and J Dias. Tactile Sensors for Robotic Applications. *Measurement*, 46(3):1257–71, 2013.

[154] C S Smith. Piezoresistance Effect in Germanium and Silicon. *Physical Review*, 94:42–9, 1954.

[155] Stanley Assembly. Stanley Assembly Cobotics Brochure. Available at: http://pdf.directindustry.com/pdf/stanley-assembly-technologies/stanley-assembly-cobotics-brochure/22234-240739-_6.html.

[156] J Steuer and F Pfeiffer. Control of a six-legged-walking-machine working in uneven terrain. In *5th IFAC Symposium on Robot Control*, pp. 97–103, 1998. Nantes, France.

[157] B G Streetman and S Kumar. *Solid State Electronic Devices*. Prentice Hall, 2009. ISBN 9788120330207.

[158] T Sugaiwa, K Iwamoto, H Iwata, and S Sugano. Pressure control on whole surface of human-mimetic multi-fingered hand with tactile sensing. In *Proc. SICE Annual Conf.*, pp. 436–8, 2010. Taipei, Taiwan.

[159] A Talasaz, R Patel, and M Naish. Haptics-enabled Teleoperation for Robot-assisted Tumor Localization. In *Proc. IEEE Int. Conf. Robotics and Automation*, pp. 5340–5, 2010. Anchorage, AK.

[160] K Tarchanidis and J Lygouras. Data Glove with a Force Sensor. *IEEE Transactions on Instrumentation and Measurement*, 52(3):984–9, 2003.

[161] P Tuffield and H Elias. The Shadow robot mimics human actions. *Industrial Robot: An Int. Journal*, 30(1):56–60, 2003.

[162] O Tufte and E Stelzer. Piezoresistive Properties of Silicon Diffused Layers. *Journal of Applied Physics*, 34(2):313–8, 1963.

[163] J Ueda and T Yoshikawa. Force-reflecting bilateral teleoperation with time delay by signal filtering. *IEEE Transactions on Robotics and Automation*, 20(3):613–9, 2004.

[164] F Vidal-Verdu, M Barquero, J Castellanos-Ramos, R Navas-Gonzalez, J Sanchez, J Seron, and A Garcia-Cerezo. A Large Area Tactile Sensor Patch Based on Commercial Force Sensors. *Sensors*, 11(5):5489–507, 2011.

[165] F Vidal-Verdu, O Oballe-Peinado, J Sanchez-Duran, J Castellanos-Ramos, and R Navas-Gonzalez. Three Realizations and Comparison of Hardware for Piezoresistive Tactile Sensors. *Sensors*, 11(3):3249–66, 2011.

[166] R Voyles, J Merrow, and P Khosla. Including sensor bias in shape from motion calibration and sensor fusion. In *Proc. IEEE/SICE/RSJ Int. Conf. Multisensor Fusion and Integration for Intelligent Systems*, pp. 93–9, 1996. Washington D.C.

[167] M Walter. Structural load measurements on complex aircraft components using strain-gage summation circuits. *Journal of the Aeronautical Sciences*, 18(2):101–6, 1951.

[168] W Wannasuphoprasit, R Gillespie, J Colgate, and M Peshkin. Cobot Control. In *Proc. IEEE Int. Conf. Rehabilitation Robotics*, pp. 3571–6, 1997. Albuquerque, NM.

[169] E Wood, I Leusen, and H Warner. Comparison of aortic pressure pulses recorded by strain-gauge and capacitance nanometer-catheter systems in man. *American Journal of Physiology*, 171(3):780, 1952.

[170] T Worsnopp. Design of an Unicycle Cobot Controller. Master's thesis, Department of Mechanical Engineering, Northwestern University, IL, 2003.

[171] L Xiujun and G Meijer. An accurate interface for capacitive sensors. *IEEE Transactions on Instrumentation and Measurement*, 51(5):935–9, 2002.

[172] K Yamada, M Nishihara, S Shimada, M Tanabe, M Shimazoe, and Y Matsuoka. Nonlinearity of the piezoresistance effect of p-type silicon diffused layers. *IEEE Transactions on Electron Devices*, 29(1):71–77, 1982.

[173] S Yaniger. Force Sensing Resistors: A Review of The Technology. In *Electro Int. Conf. Record*, pp. 666–8, 1991. New York, NY.

[174] M H Yun, D Cannon, A Freivalds, and G Thomas. An instrumented glove for grasp specification in virtual-reality-based point-and-direct telerobotics. *IEEE Transactions on Systems, Man and Cybernetics. Part B: Cybernetics*, 27(5):835–46, 1997.

[175] R Zollner, O Rogalla, R Dillmann, and M Zollner. Understanding users intention: programming fine manipulation tasks by demonstration. In *Proc. IEEE/RSJ Int. Conf. Intelligent Robots and Systems*, pp. 1114–9, 2002. Lausanne, Switzerland.

Appendices

Appendix A

A. Review and discussion on the concepts of non-linearity, non-repeatability and hysteresis

It is next presented a brief, yet complete, overview of the most accepted metrics to assess the performance of sensors. However, it must be remarked that there is not a universally-accepted definition for all of the metrics herein presented.

A.1 Non-linearity error

It measures how curved or non-linear a characteristic curve is. This definition is accepted by all authors; however the calculation of the non-linearity error may vary from one author to another depending on the method used, it is presented next the three-most widely accepted approaches:

1. Maximum Deviation from the **BFSL**: The term **BFSL** stands for Best Fit Straight Line; it implies that a linear trendline **h(x)** is traced in a way that the maximum positive deviation and the maximum negative deviation are identical. This concept can be understood from Figure A.1 in which the following condition is met:

$$f(x_a) - h(x_a) = h(x_b) - f(x_b) \tag{A.1}$$

Given the **BFSL** of Figure A.1, the **BFSL** non-linearity error **BFSL-NLE** can be estimated as a function of the full scale maximum $\mathbf{h(x_M)}$:

$$BFSL - NLE = \frac{h(x_b) - f(x_b)}{h(x_M)} \cdot 100\% \tag{A.2}$$

The BFSL effectively halves the error at $\mathbf{x = x_a}$ and at $\mathbf{x = x_b}$, but nothing is said about the non-linearity error at the remaining datapoints; this requires an integral formulation of the error function along the entire function range. Another drawback of the BFSL method lies in the condition of equation **(A.1)**, which is easy to satisfy if the output plot of the transducer is given. However, if the data is given in a table format, the BFSL method is no longer straightforward, because it is neither statistical nor systematic.

2. Maximum Deviation from the **TBL**: It is similar to the **BFSL** method with the difference that a Terminal Base Line (**TBL**) is traced between the end datapoints of the sensor output. Once the **TBL** line has been found it is possible to obtain the TBL non-linearity error by determining the maximum deviation between the trendline and experimental data; this occurs at $\mathbf{x = x_c}$ for the plot of Figure A.2. The TBL non-linearity error **TBL-NLE** can thus be estimated from:

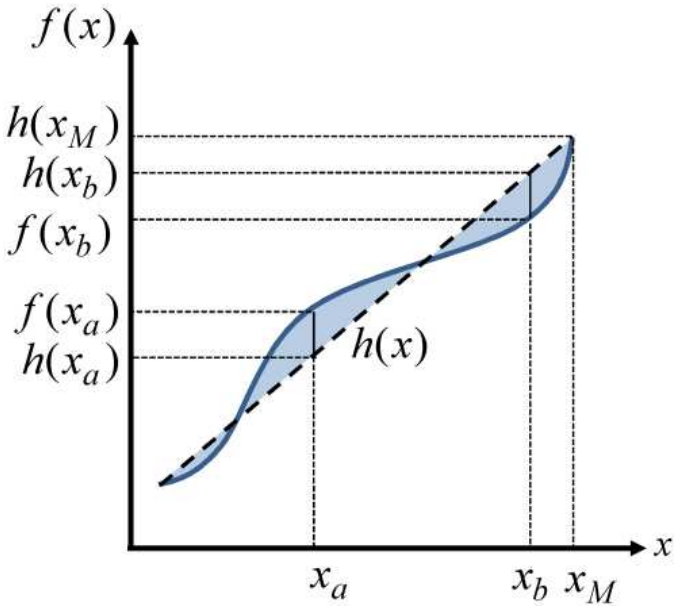

Figure A.1: Output plot of a sensor with a trendline estimated from the BFSL method

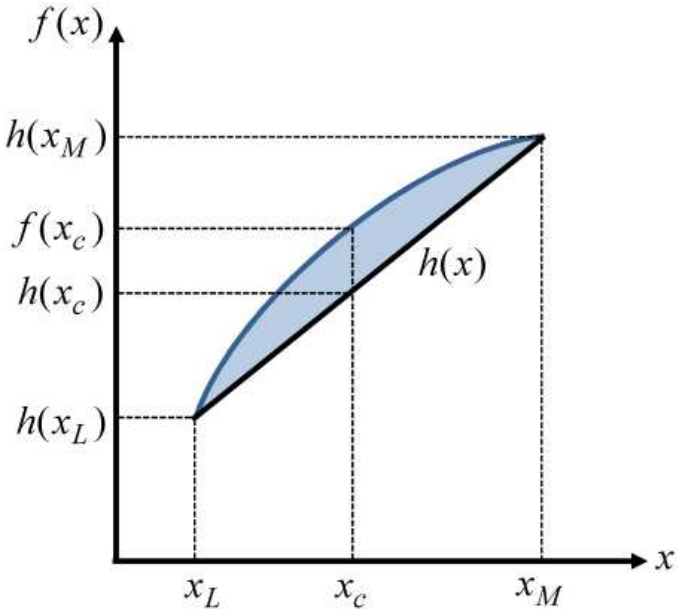

Figure A.2: Output plot of a sensor with a trendline estimated from the TBL method.

$$TBL - NLE = \frac{f(x_c) - h(x_c)}{h(x_M)} \cdot 100\% \qquad \textbf{(A.3)}$$

Sensor manufacturers choose either the **BFSL** or the **TBL** method according to the best-suited metric for his product. For the special case of Figure A.1, either method would produce the same error estimation, but for Figure A.2, the non-linearity error-**BFSL** would be halved compared to the **TBL** estimation.

The **TBL** method is of great importance because it is common to find sensors that perform periodic or user-requested tuning based on the **TBL** method. But just as the **BFSL** method, it falls to provide information about the non-linearity error along the entire sensor range, or over a specific region of operation. The **BFSL** and **TBL** methods

only provide information of the maximum possible error, and thus it is common to find in sensor literature, designations such as:

Non-linearity: *±0.5% of full scale maximum (**BFSL**), or either ±2% of full scale maximum (TBL).*

Note from the definition of both errors, that the **TBL** non-linearity error is at the-best case, equal or lower than the BFSL non-linearity error.

3. Integral formulation of the nonlinearity error: The integral formulation of error accounts for the non-linearity along the entire range of operation, and thus, a more representative estimation of nonlinearity is provided [44]. This is of great importance especially for those sensors that exhibit output responses such as those of Figure A.3. Note from the figure, that both sensors exhibit the same **BFSL** non-linearity error, but for the sensor of Figure A.3b the net error resulting from the equation below is effectively lower than for that of Figure A.3a, this is, the shaded region of Figure A.3b is smaller than that of Figure A.3a:

$$L = \frac{1}{x_u - x_l}\int_{x_l}^{x_u} |f(x) - h(x)|dx \qquad \textbf{(A.4)}$$

Where **f(x)** is the sensor output and **h(x)** is the best-fit trendline for the datapoints.

Equation **(A.4)** is useful to assess the total error within the range $\mathbf{x_l < x < x_u}$, however, the absolute value formulation of the equation is mathematically intractable, thus, it is better to calculate the mean squared value of **f(x) – h(x)** and then take the squared root of the integral. The final form of the integral non-linearity error $\mathbf{I\text{-}NLE_c}$ calculated over the range $\mathbf{x_l < x < x_u}$ can be written as:

$$I - NLE_c = \frac{1}{x_u - x_l}\sqrt{\int_{x_l}^{x_u} [f(x) - h(x)]^2 dx} \qquad \textbf{(A.5)}$$

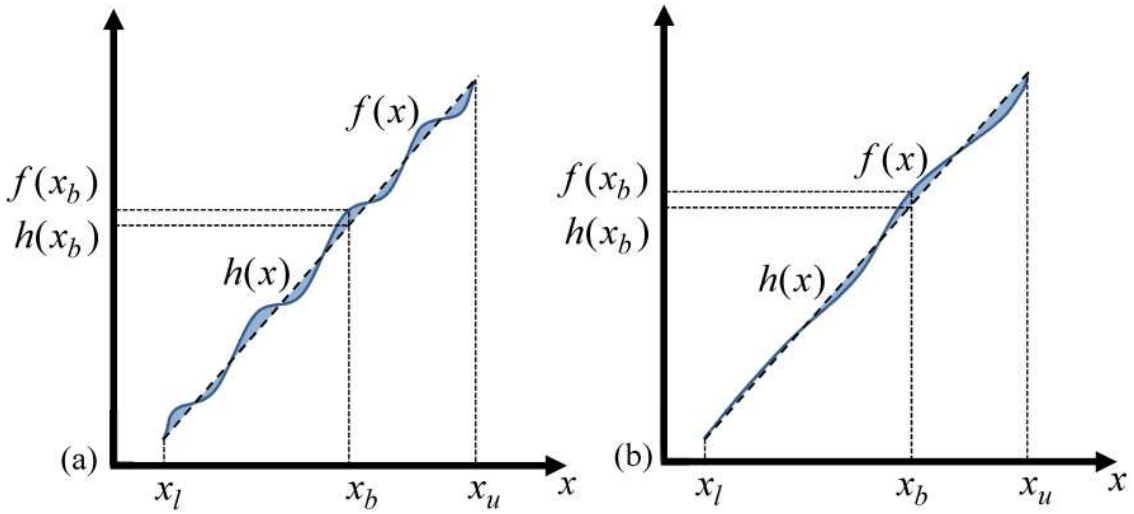

Figure A.3: Comparison between two sensors with the same BFSL nonlinearity but with different values of integral non-linearity.

Equation **(A.5)** is said to be the *Root Mean Square* (RMS) of the deviation of a function **f(x)** from the best-fit trendline **h(x)** in the continuous domain. The best-fit trendline can be estimated my minimizing the error function of **I-NLEc**. So for the case of a discrete (finite) set of datapoints, finding **h(i)** is merely a linear regression of the datapoints; this is probably the most encountered situation in closed-loop control systems. Typically, the sensors are first characterized on a testbench by emulating the normal operating conditions. Based on the readings acquired during the characterization (y_i, x_i), with $y_i = f(x_i)$, the best-fit transfer function of the sensor **h(i)** is built using linear fitting techniques. The general form of **h(i)** is that of a line with slope m and y-intercept b. So, the transfer function of the sensor can be obtained from the equations of a linear regression:

$$m = \frac{\sum_{i=1}^{n} x_i y_i - \frac{1}{n}\left(\sum_{i=1}^{n} x_i \sum_{i=1}^{n} y_i\right)}{\sum_{i=1}^{n} x_i^2 - \frac{1}{n}\left(\sum_{i=1}^{n} x_i\right)^2}, \quad b = \frac{\sum_{i=1}^{n} y_i - m\sum_{i=1}^{n} x_i}{n} \tag{A.6}$$

Where **n** is the amount of datapoints collected during the characterization.

Finally, the Integral non-linearity of a discrete domain function $\mathbf{I\text{-}NLE_d}$ can be computed from:

$$I - NLE_d = \frac{1}{(x_u - x_l)n}\sum_{i=1}^{n}[f(x_i) - h(x_i)]^2 = \frac{1}{(x_u - x_l)n}\sum_{i=1}^{n}[y_i - h(x_i)]^2 \tag{A.7}$$

A.2 Discussion about the metrics for assessing the non-linearity error

Three important differences lie in calculation of the **I-NLEd** compared to the **BFSL-NLE** and **TBL-NLE** approaches. First, it must be recalled the comprehensive analysis of the non-linearity derived from the integral approach $\mathbf{I\text{-}NLE_d}$, this feature is not provided by either the **BFSL-NLE** or the **TBL-NLE**. Second, the linear regression method of equation **(A.6)** provides a statistical, systematic and programmable-friendly method to characterize sensor in either industrial or research environments, and third. Given that the best-fit transfer function **h(i)** is obtained through an optimization procedure, further usage of **h(i)** as an estimator yields the lowest possible error, this minimizes the so-called non-repeatability error, refer to Section A.4 for a detailed description of the non-repeatability error.

Despite all the aforementioned advantages of the $\mathbf{I\text{-}NLE_d}$ approach, sensor manufacturers seldom specify such a metric. When specifying sensor linearity, manufacturers mostly rely on the **BFSL-NLE**, and when dealing with accuracy, the non-repeatability error is preferably chosen over the measurement error. The reason for opting for a given metric is simple; manufacturers want to show his products as the best market solution so typically the lowest-error metric is chosen to appear on the sensor datasheet. Given the *integral* approach of the $\mathbf{I\text{-}NLE_d}$, this value is usually greater than the *single-point* estimation of the **BFSL-NLE**. Similar conclusions are

derived for the non-repeatability error; see Section A.4, and the measurement error as previously shown on Section 2.2.1.

A.3 Hysteresis

Hysteresis is the tendency of the transducer's output to not change in proportion to a change in the input depending on the starting value and direction of change. In other words, the sensor's output depends on the previous state(s) [15]. For the case of Figure A.4, different readings are produced during the loading and unloading stage, the maximum difference between each trajectories occurs at $\mathbf{x = x_a}$. The hysteresis error **HE** can be computed as a percentage of the full scale output $\mathbf{f(x_M)}$ from the formula below:

$$HE = \frac{f(x_a)_l - f(x_a)_u}{f(x_M)} \cdot 100\% \qquad \textbf{(A.8)}$$

A.4 Non-repeatability error

The repeatability must be taken as expression of precision. It is an indication of how close the sensor's output is to previously measured output values for the same input value. Beyer defines the non-repeatability error as *the largest deviation obtained in three measurements under identical conditions* [10]. The circumstance of identical conditions is of great importance because, as previously shown, sensors exhibit memory effect and thus different readings are produced depending on whether the sensor is under a loading or unloading stage, see Figure A.4. Likewise, temperature variations also affect the sensor output. So, in order to properly estimate the non-repeatability error, each measurement must be performed consistently.

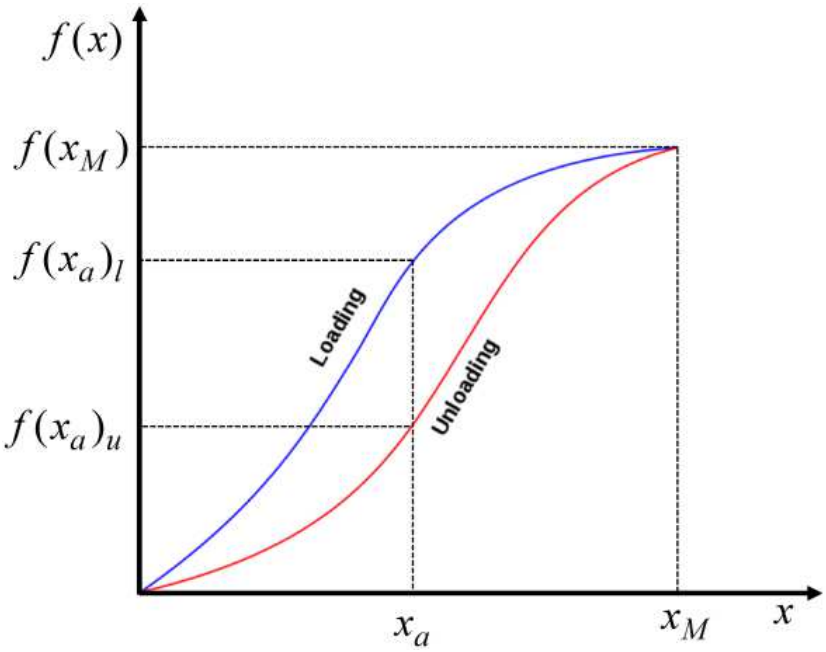

Figure A.4: Plot representing the output **f(x)** of a sensor with hysteresis.

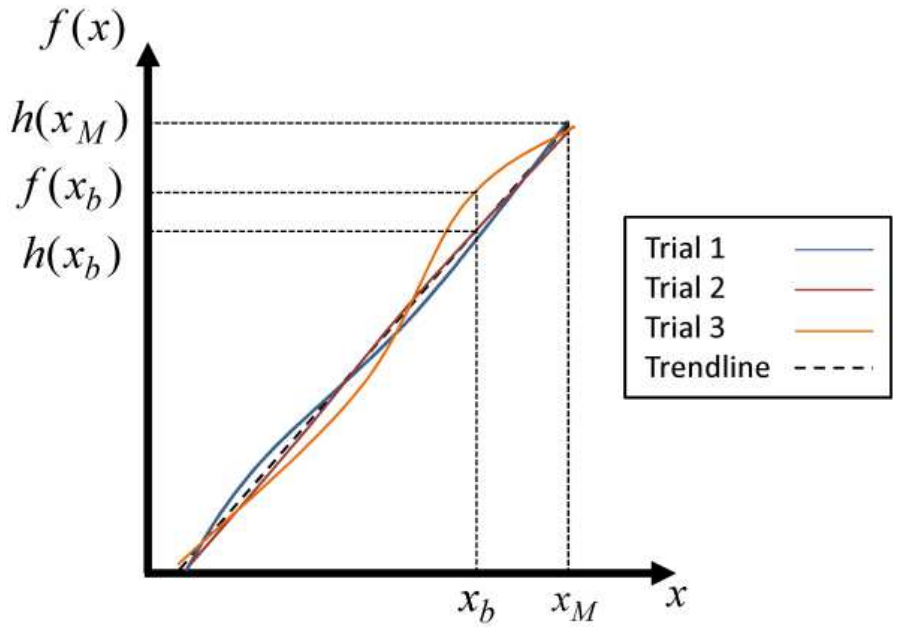

Figure A.5: Plot showing three sets of datapoints for a sensor with output **f(x)** and trendline **h(x)**. The non-repeatability error is estimated at $\mathbf{x = x_b}$ for the trial 3 using equation **(A.9)**.

The plot of Figure A.5 shows the sensor output **f(x)** for three sets of data points. The trendline **h(x)** has been plotted together with the experimental data to illustrate the calculation of the non-repeatability error, **NRE**. Given the maximum difference between **h(x)** and the experimental data at $\mathbf{x = x_b}$ occurring at trial 3, the non-repeatability error can be estimated from the formula below:

$$NRE = \frac{f(x_b) - h(x_b)}{h(x_M)} \cdot 100\% \qquad \textbf{(A.9)}$$

However, an undetermined aspect lies in equation **(A.9)**: *how should be determined the trendline **h(x)**?* Probably, the most straightforward approach is to determine **h(x)** through a linear least squares regression that takes into account the entire set of datapoints from the three trials, see equation **(A.9)**. This is a valid solution, in fact the most used, but in some cases sensor output is not linear, and different fitting techniques may be used. In any case, the definition of non-repeatability error remains unchanged but it must declared what type of trendline was used to model sensor response.

In sensor literature, the following metrics are typically used to evaluate sensor performance:

- Best Fit Straight Line Non-Linearity Error **BFSL-NLE**
- Hysteresis error **HE**
- Non-repeatability Error **NRE**

When dealing with hysteresis **HE** and non-repeatability error **NRE**, it is practically impossible to separate both error sources from the sensor's output; this is so because both error sources go coupled. This fact reduces the expectancy of achieving a **NRE**

lower or similar to that presented in the sensor's datasheet even if temperature is held constant throughout the test. It must be recalled from the **NRE** definition that such metric was estimated based on *identical conditions* along three sets of measurements. This is not possible to reproduce in practice, because the measured variable changes under a random basis, so then, *what is the expected average error when reading sensor output?*

To answer above concern the definition of measurement error must be addressed. The measurement error is the most straightforward way to estimate the expected error when working with sensors because it embraces all error sources on a single reading. However, a formal definition of the measurement error is not next presented because it was already given on Section 2.2.1.

Appendix B

B. Patent: *Sistema y procedimiento de Control para Manipuladores* [130]

(19) OFICINA ESPAÑOLA DE PATENTES Y MARCAS

ESPAÑA

(11) Número de publicación: **2 351 143**

(21) Número de solicitud: 200930173

(51) Int. Cl.:
G06F 3/01 (2006.01)

(12) PATENTE DE INVENCIÓN B1

(22) Fecha de presentación: **14.05.2009**

(43) Fecha de publicación de la solicitud: **01.02.2011**

Fecha de la concesión: **07.11.2011**

(45) Fecha de anuncio de la concesión: **18.11.2011**

(45) Fecha de publicación del folleto de la patente: **18.11.2011**

(73) Titular/es:
CONSEJO SUPERIOR DE INVESTIGACIONES CIENTÍFICAS (CSIC)
SERRANO 117
28006 MADRID, ES

(72) Inventor/es:
PAREDES MADRID, LEONEL y
GONZALEZ DE SANTOS, PABLO

(74) Agente: **Pons Ariño, Ángel**

(54) Título: **SISTEMA Y PROCEDIMIENTO DE CONTROL PARA MANIPULADORES**

(57) Resumen:
Sistema y procedimiento de control para manipuladores.
Basado en guantes (5) dotados de sensores, que permite a un operario (6) controlar cualquier manipulador (4) con uno o más grados de libertad, coordinando su movimiento de acuerdo con la magnitud, dirección y sentido de la fuerza aplicada por el operario (6), ejercida sobre la estructura del manipulador (4) o sobre la carga movilizada (406). Dicho sistema de control comprende al menos un guante (5) dotado de sensores, un computador (411), un receptor inalámbrico (412) y unos variadores de frecuencia (413). Cada guante (5) posee en su zona dorsal un sistema de posicionamiento dactilar (2) que mide la flexión y abducción de los cinco dedos, un sistema de posicionamiento espacial (7) que mide la posición y orientación absoluta del guante (5) y por ende de la mano (1) en el espacio, y en su zona palmar un sistema de medición de fuerza (3) que mide las fuerzas aplicadas por el operario (6).

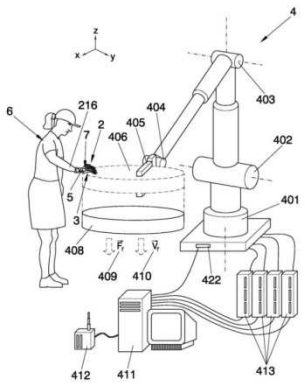

FIG. 4

ES 2 351 143 B1

DESCRIPCIÓN

Sistema y procedimiento de control para manipuladores.

Objeto de la invención

La presente invención pertenece al campo de los sistemas y dispositivos de medición de fuerza y tensiones en general, y más concretamente a una interfaz de control para manipuladores, robots industriales o grúas que funcionan en colaboración directa con los operarios.

El objeto principal de la presente invención es un sistema de control basado en guantes dotados de sensores, que permitan al operario controlar cualquier manipulador con uno o más grados de libertad, coordinando su movimiento de acuerdo con la magnitud, dirección y sentido de la fuerza aplicada por el operario, ejercida sobre la estructura del manipulador o sobre la carga movilizada.

Antecedentes de la invención

Las grúas y manipuladores son comunes en instalaciones industriales que requieren movilizar cargas elevadas. Típicamente la interfaz de usuario de dichos sistemas consiste en palancas de mandos, botones y más recientemente asideros con sensores de fuerza incorporados tal como se describe en los documentos US 6,738,691 y US 6,204,620. Dichos sistemas son conocidos como "Dispositivos Inteligentes de Ayuda a la Manipulación" (DIAM) y tienen como finalidad proveer de amplificación de potencia humana, logrando consecuentemente mejorar la interfaz de control entre el operario y la grúa en términos de: ergonomía, seguridad y productividad de la planta.

Su arquitectura es muy similar a las grúas tradicionales controladas por botones y palancas de mando, pero incorporan nuevos sensores y elementos de realimentación de esfuerzo destinados a proveer de sensaciones hápticas al operario, así como nuevos algoritmos de control. La arquitectura de los DIAM que funcionan en cooperación directa con el operario, se encuentra en documentos como US 6,813,542 y US 6,928,336 mientras que en el campo de la teleoperación con realimentación de esfuerzo pueden encontrarse documentos como: US 6,184,868, US 6,985,133 y US 5,184,319. La Compañía Virtual Realities con sede en Galveston TX, USA, ha desarrollado dispositivos para teleoperación con realimentación de esfuerzo, tal es el caso del CyberGlove II y CyberGrasp. El CyberGlove II es un guante de datos, (*data glove*), dotado con goniómetros resistivos. Los guantes de datos son dispositivos que permiten medir los movimientos de los grados de libertad de la mano, dichos movimientos pueden clasificarse en: flexión y abducción de los dedos y rotación de la muñeca. No obstante, la mayoría de los guantes de datos no están dotados de sensores para medir la rotación de la muñeca.

Incorporando al CyberGlove II una Unidad de Medidas Inerciales, UMI, puede obtenerse la posición y orientación de la mano en el espacio y utilizar dicha información para múltiples tareas, una de ellas consiste en controlar robots remotamente. Si además se incorpora el módulo CyberGrasp puede proveerse de realimentación de esfuerzo sobre la mano, lo que mejora significativamente la interfaz hombre-máquina en el sistema teleoperado.

Además de los goniómetros resistivos usados en el CyberGlove II y CyberGrasp, existen otras tecnologías para estimar la flexión y abducción de los dedos. El documento US 5,184,009 emplea fibra óptica y sensores de intensidad colocados convenientemente en las falanges para medir su flexión y abducción. La utilización de fibra óptica para este fin es muy conveniente, dado que puede mimetizarse con facilidad en un guante debido a la propia flexibilidad de la fibra y al poco espacio que ocupa.

El documento "A Survey of Glove-Based Systems and Their Applications" de Dipietro Laura, Sabatini Angelo y Dario Paolo, IEEE Transactions on Systems, Man and Cybernetics, pp. 461-482, hace un recuento tanto de las aplicaciones de los guantes de datos, como de las distintas versiones de los mismos, dicho estudia abarca desde el año 1994 hasta la fecha de publicación del artículo en julio de 2008.

Las aplicaciones de los guantes de datos son muy variadas, algunos de los campos de investigación que comprenden son: diseño y manufactura en la industria, visualización de información en entornos computacionales de diseño gráfico, asistencia en el proceso de reconocimiento de lenguaje para sordomudos, rehabilitación de pacientes afectados por lesiones motrices y en el campo de robótica, los guantes de datos se utilizan para diversos fines tales como: aprendizaje basado en memorización de los movimientos realizados por un humano, control de robots mediante posiciones gestuales de los dedos y control teleoperado de robots en sistemas con o sin realimentación de esfuerzo, para este último caso el documento "Data Glove With a Forcé Sensor" de Tarchanidis Kostas, Lygouras John, IEEE Transactions on Instrumentation and Measurement, pp. 984-989. describe un guante de datos dotado con sensores de fuerza en la zona palmar y en la zona dorsal con un sistema de medición de la flexión de los dedos.

Las interfaces de control para los DIAM que funcionan en cooperación directa con el operario son variadas dependiendo del número de grados de libertad que se desee controlar. En los documentos US 5,865,426 y US 5,915,673 se exponen interfaces de control para los DIAM con un grado de libertad, en ellos se utilizan sensores de fuerza en un asidero para detectar la intención de movimiento del operario, por consiguiente, la velocidad de movimiento del manipulador cambiará proporcionalmente dependiendo de la magnitud de la fuerza aplicada. El movimiento del manipulador es posible solo verticalmente, debido al tipo de manipulador empleado. Mediante la programación de

trayectorias predefinidas y usando un manipulador adecuado, puede utilizarse la invención descrita en el documento US 5,915,673 para mover cargas en más de un grado de libertad.

Un aspecto que debe tratarse con sumo cuidado es el estudio de la estabilidad de los DIAM que funcionan en cooperación directa con el operario. Dicho tema se aborda en el documento US 7,043,337 para una grúa suspendida. En dicho DIAM, el sensor de fuerza ha sido reemplazado por otro, que detecta la desviación del cable suspendido de su posición vertical; posteriormente, y de forma proporcional al ángulo de desviación, se origina movimiento en el plano horizontal. Entiéndase que el movimiento se realiza en dos grados de libertad *x, y*.

El problema de la estabilidad en los DIAM constituye una complicación importante en aquellos sistemas dotados de sensores de fuerza en el elemento final del manipulador. Este tipo de DIAM funciona bajo la modalidad manos en la carga (*hands on payload*), lo que elimina la necesidad de contar con asideros o botones, basta con que el operario ejerza fuerza sobre el elemento final del manipulador para originar movimiento. Es por ello que este tipo de DIAM provee de las mejoras prestaciones ergonómicas al operario, no obstante, la "no-colocación" de sensores de fuerza y actuadores conlleva a problemas de estabilidad en su operación. La "no-colocación" de sensores y actuadores significa que los actuadores y sensores no residen en la misma ubicación física, encontrándose separados por elementos dinámicos. En el caso de robots, los actuadores están generalmente ubicados en las articulaciones y los sensores de fuerza se encuentran cerca del elemento final, separados de los actuadores por la dinámica de las transmisiones y la dinámica estructural de los eslabones. El artículo "The Interaction of Robots with Passive Environments: Application to Forcé Feedback Control", de Colgate Edward, Hogan Neville, Advanced Robotics 1989, aborda el problema de estabilidad originado por la "no-colocación" de sensores y actuadores.

Por otra parte los sensores de fuerza colocados en los DIAM que funcionan en el modo manos en la carga, requieren de alta resolución para poder detectar la fuerza aplicada por el operario y de un amplio rango dinámico para soportar el peso de la carga, lo que implica usar sensores de elevado costo.

Una versión mejorada del asidero descrito previamente en el documento US 5,915,673 involucra el uso de un guante donde se incorpora un sensor de fuerza que detecta la presión ejercida por el operario sobre el manipulador. Dicha invención se describe en el documento US 6,681,638. El diseño de dicho guante permite al operario mover el manipulador hasta en tres grados de libertad *x, y, z*. El movimiento se realiza únicamente a través de trayectorias definidas previamente, programadas vía software. El único sensor de fuerza que incorpora el guante, indica al sistema de control del manipulador la rapidez con que debe moverse, en tal sentido, la fuerza aplicada por el operario y la rapidez del DIAM son magnitudes proporcionales, no obstante, la dirección de la fuerza aplicada por el operario no necesariamente corresponde con la trayectoria descrita por el robot, ya que la única información recopilada por el guante es la magnitud de la fuerza aplicada, mas no su dirección y sentido.

Descripción de la invención

En la presente invención se describe un sistema de control basado en al menos un guante dotado de sensores, que permite a un operario controlar el movimiento de un manipulador (grúa o robot industrial) con uno o más grados de libertad adaptado para manipular una carga, coordinando su movimiento de acuerdo con la magnitud, dirección y sentido de la fuerza aplicada por dicho operario, pudiendo ejercer dicha fuerza sobre el manipulador o sobre la carga movilizada. Al incorporar un segundo guante en la otra mano, es posible detectar momentos de giro y consecuentemente orientar la carga en el espacio.

Dicho sistema de control consta de uno o dos guantes a ser instalados en las manos del operario, que recogen información tanto de la posición y orientación del guante en el espacio como del módulo, dirección y sentido de la fuerza aplicada, un receptor inalámbrico que recibe información del guante, un computador asociado al receptor inalámbrico, que genera unas consignas de velocidad para cada grado de libertad del manipulador, y unos variadores de frecuencia que reciben órdenes del computador para controlar el manipulador.

Asimismo cada guante posee en la zona dorsal un sistema de posicionamiento dactilar que mide la flexión y abducción de los cinco dedos, y en la zona palmar un sistema de medición de fuerza dotado de al menos un sensor de fuerza.

El sistema de posicionamiento dactilar consta preferentemente de unos emisores de luz, preferentemente seis, instalados en una caja opaca para evitar la interferencia de luz proveniente del exterior. Estos emisores de luz están conectados cada uno a un segmento de fibra óptica. Para medir la flexión y abducción de los dedos de la mano se mide la atenuación de la onda propagada a través del segmento de fibra óptica, siendo esta atenuación proporcional al ángulo de flexión propio de cada segmento de fibra óptica.

También es posible que, para la medición del arco palmar, flexión y abducción de los cinco dedos, el sistema de posicionamiento espacial disponga de medios tales como: goniómetros resistivos, electrogoniómetros, sensores de efecto hall, sensores capacitivos, sensores de inducción magnética, elastómeros conductores piezorresistivos, y/o un sistema de cámaras instaladas en los linderos del espacio de trabajo del operario.

En dicha caja opaca se encuentra también instalado un convertidor analógico digital que digitaliza las magnitudes de unos sensores de intensidad presentes en cada uno de los segmentos de fibra, que preferentemente son veintiuno,

y transmite mediante un cable los paquetes de datos hasta una unidad de comunicación, que preferentemente consiste en una unidad inalámbrica.

Dicha unidad de comunicación envía la información recopilada al receptor inalámbrico mediante unos medios seleccionados entre: ondas electromagnéticas, un cable, fibra óptica, señales de infrarrojo y señales ultrasónicas.

Con el fin de medir la posición y orientación del guante en el espacio, se dispone de una Unidad de Medidas Inerciales (UMI), dotada preferentemente con acelerómetros y giróscopos que permite posicionar y orientar la mano en un espacio de tareas de hasta seis dimensiones, x, y, z, guiñada, cabeceo y balanceo. Preferentemente la UMI se ubica en el plano formado por la zona dorsal del guante, pudiéndose reconstruir tanto la posición y orientación de la mano en el espacio, como la flexión y abducción de los dedos. Dicha UMI se comunica con la unidad de comunicación inalámbrica mediante un cable.

También es posible que dicha unidad de medidas inerciales esté dotada de unos medios seleccionados entre: emisores y receptores infrarrojos, emisores y receptores de ultrasonido, o un sistema de posicionamiento global mediante satélites que orbitan alrededor de la tierra.

Por otra parte el sistema de medición de fuerza está conformado por una serie de sensores de fuerza distribuidos uniformemente en toda la superficie palmar y una unidad de medición de resistencia que se encarga de efectuar mediciones sobre todos los sensores de fuerza instalados en el guante. Esta información se envía a la unidad de comunicación inalámbrica ubicada en la zona dorsal del guante a través de un cable.

Preferentemente el sistema de medición de fuerza presenta veintiséis sensores de fuerza. Asimismo es posible que dichos sensores se seleccionen entre: sensores piezorresistivos, galgas extensiométricos y contactos eléctricos.

Cada sensor de fuerza presenta preferentemente dos terminales cuya conductividad cambia proporcionalmente conforme la magnitud de la fuerza aplicada. Estos terminales se dirigen hacia la unidad de medición de resistencia.

En una realización preferente de la invención, para mejorar la ergonomía del guante, los terminales de los sensores de fuerza están agrupados convenientemente y se encuentran en envolturas para facilitar el traslado de los mismos hasta la unidad de medición de resistencia.

El computador se encarga de procesar los datos recopilados por los sistemas de sensores instalados en cada guante. El procesamiento de dichos datos involucra coordinar el movimiento del manipulador de acuerdo a la magnitud, dirección y sentido de la fuerza aplicada por el operario.

Para controlar al manipulador, el operario se coloca un guante en cualquiera de sus manos y ejerce presión sobre la carga en la dirección de movimiento deseada.

El módulo de la fuerza aplicada por el operario sobre la carga o el manipulador se obtiene a partir de las mediciones efectuadas en los sensores de fuerza del guante. La dirección y sentido de cada contribución de fuerza se obtiene a partir de la reconstrucción de la posición y orientación de la mano en el espacio. Dicha reconstrucción involucra conocer tanto la posición y orientación de la mano como la de los dedos, para ello el sistema se vale tanto de la unidad de medidas inerciales como del sistema de posicionamiento que mide la abducción y flexión de los dedos.

Con dicha información se obtiene una serie de vectores de fuerza (tantos como sensores de fuerza haya en el guante) los cuales se suman vectorialmente para conseguir un vector fuerza resultante, dicho vector es consecuentemente colineal con la intención de movimiento del operario.

Para controlar la rapidez del manipulador, el sistema se vale del módulo de la fuerza resultante, de tal forma que un incremento en la fuerza resultante produzca proporcionalmente un aumento en la rapidez del manipulador. El vector fuerza resultante provee de información suficiente al computador para controlar hasta tres grados de libertad de movimiento del manipulador x, y, z, con esto se logra posicionar la carga en tres dimensiones.

Para orientar la carga en el espacio es necesario contar con un segundo guante con las mismas prestaciones descritas. Los movimientos de orientación se coordinan a partir de los momentos de fuerza, cuya reconstrucción se realiza a partir del vector fuerza resultante de cada guante y de su posición en el espacio.

El eje de giro que se considera fijo para la medición de los pares de giro y vectores directores, puede encontrarse en cualquier punto de la distancia entre ambos guantes. Una realización preferente de la invención sitúa dicho punto equidistantemente de ambos guantes con lo que se obtienen dos vectores directores de igual magnitud.

La velocidad de giro de la carga depende de la sumatoria vectorial de los momentos de giro medidos para cada guante. A mayor momento de giro, la velocidad rotacional crecerá proporcionalmente. Al igual que sucede con los movimientos traslacionales, los movimientos de rotación también son colineales respecto al momento resultante aplicado.

Al incluir un segundo guante, se puede orientar la carga en el espacio de tareas con dimensión seis: x, y, z, guiñada, cabeceo y balanceo, ya que la lógica residente en el computador puede discernir entre los momentos de giro que causan rotación y las fuerzas que causan traslación. Para tal fin el algoritmo de control residente en el computador tiene en cuenta un modelo del comportamiento dinámico del sólido rígido en el espacio.

El eje de giro fijado para la medición de los momentos de fuerza, no coincide necesariamente con el eje de giro del manipulador ubicado en su elemento final, ya que el operario no debe aplicar necesariamente fuerza sobre la carga para moverla; el operario también puede ejercer presión sobre la estructura del propio manipulador, bien sea para ocasionar movimientos de traslación o rotación de la carga.

El manipulador controlado por el operario incorpora adicionalmente como elemento de seguridad un detector de contacto, que preferentemente es de tipo electromagnético, con el fin de determinar cuándo el operario efectivamente ejerce fuerza sobre la carga o el propio manipulador. La lógica de seguridad debe permitir el movimiento del manipulador única y exclusivamente cuando el operario ejerza fuerza sobre la carga o bien sobre el propio manipulador. Con esto se evitan movimientos involuntarios de éste, provocados por descuidos del operario al ejercer fuerza sobre algún elemento distinto a los mencionados. También es posible que dicho detector de contacto sea electrostático.

Se resume a continuación las etapas del procedimiento de control para manipuladores descrito anteriormente, para el caso en que se emplee un solo guante:

- comprobación de si el detector de contacto del manipulador está activado,
- inhabilitación para controlar el manipulador en caso de que el detector de contacto no esté activado,
- reconstrucción de la posición y orientación de la mano en el espacio en caso de que el detector de contacto sí esté activado,
- lectura de los sensores de fuerza instalados en el guante,
- generación de los vectores de fuerza individuales de cada sensor de fuerza,
- cálculo de la suma vectorial de los vectores de fuerza individuales para generar el vector fuerza resultante Fr.
- aplicación de la ley proporcional $Vr = k \cdot Fr$ para generar los perfiles de velocidad correspondientes de cada grado de libertad,
- transmisión de cada perfil de velocidad al variador de frecuencia correspondiente para generar movimiento en el manipulador en hasta tres grados de libertad.

Asimismo para el control de manipuladores empleando dos guantes el procedimiento de control comprende las siguientes etapas:

- comprobación de si el detector de contacto del manipulador está activado,
- inhabilitación para controlar el manipulador en caso de que el detector de contacto no esté activado,
- reconstrucción de la posición y orientación de las manos izquierda y derecha en caso de que el detector de contacto sí esté activado,
- lectura de los sensores de fuerza instalados en cada uno de los dos guantes,
- generación de los vectores de fuerza individuales de los sensor de fuerza de cada guante,
- cálculo de la suma vectorial de los vectores de fuerza individuales para generar el vector de fuerza resultante de cada guante, Fri, Frd,
- comprobación de si alguno de los dos vectores de fuerza Fri, Frd son iguales a cero,
- determinación de los vectores directores ri, rd de cada vector de fuerza resultante en caso de que los dos vectores de fuerza Fri, Frd sean distintos de cero,
    i. aplicación de las leyes de la dinámica de cuerpos en el espacio para determinar la velocidad rotacional y traslacional de la carga,
    ii. transmisión de cada perfil de velocidad al variador de frecuencia correspondiente para generar movimiento en el manipulador en hasta seis grados de libertad,

- aplicación de la ley proporcional Vr = k · Fr para generar los perfiles de velocidad correspondientes para cada grado de libertad, en caso de que alguno de los dos vectores de fuerza Fri, Frd sean iguales a cero,

  i. transmisión de cada perfil de velocidad al variador de frecuencia correspondiente para generar movimiento en el manipulador en hasta tres grados de libertad.

Descripción de los dibujos

Con el fin de mejorar la comprensión sobre el funcionamiento de la invención presentada y de acuerdo con un ejemplo preferente de realización práctica de la misma, se incluye como parte integrante de la descripción una serie de dibujos donde con carácter ilustrativo y no limitativo, se ha presentado lo siguiente:

Figura 1.- Muestra la zona palmar y dorsal de una mano derecha humana.

Figura 2.- Vista de la zona dorsal del guante de acuerdo con una realización preferente de la invención donde se muestra el sistema de medición de la posición, orientación y abducción de los cinco dedos de la mano.

Figura 3.- Vista de la zona palmar del guante de acuerdo con una realización preferente de la invención donde se muestra el sistema de medición de fuerza para los cinco dedos y la palma de la mano.

Figura 4.- Muestra a un operario utilizando el guante descrito en la presente invención para movilizar una carga sostenida por un manipulador.

Figura 5.- Muestra la distribución de las fuerzas individuales aplicadas por un operario sobre la carga, las cuales son medidas por el sistema de medición de fuerza instalado en el guante.

Figura 6.- Diagrama de flujo para controlar el movimiento de un manipulador con hasta tres grados de libertad x, y, z, empleando el guante descrito en la presente invención como interfaz entre el operario y el manipulador.

Figura 7.- Muestra la distribución de las fuerzas individuales aplicadas por un operario sobre la carga, cuando emplea ambas manos para orientar al objeto en el espacio, siendo las fuerzas resultantes de cada mano de igual módulo y dirección pero sentido contrario.

Figura 8.- Muestra la distribución de las fuerzas individuales aplicadas por un operario sobre la carga, cuando emplea ambas manos para orientar al objeto en el espacio, siendo las fuerzas resultantes de cada mano de diferente módulo, dirección y sentido.

Figura 9.- Diagrama de flujo para controlar el movimiento de un manipulador con hasta seis grados de libertad x, y, z, guiñada, cabeceo y balanceo, empleando un guante en cada mano.

Realización preferente de la invención

Se describen a continuación algunas realizaciones preferentes de la invención. La figura 1 muestra la zona palmar (102) y dorsal (101) de una mano (1) derecha humana, asimismo se distingue la falange distal (103), la falange media (104) y la falange proximal (105) del dedo índice.

En la figura 2 se observa la zona dorsal de un guante (5) donde se encuentra instalado un sistema de posicionamiento espacial (7) y un sistema de posicionamiento dactilar (2). El sistema de posicionamiento dactilar (2) consta de seis emisores de luz instalados en un compartimiento opaco (204) para evitar la interferencia de luz proveniente del exterior. Los seis emisores de luz están conectados cada uno a un segmento de fibra óptica (202, 209, 219, 220, 221, 222). Para medir la flexión y abducción de los dedos de la mano (1) se mide la atenuación de la onda propagada a través del segmento de fibra óptica (230), la atenuación es proporcional al ángulo de flexión propio de cada segmento de fibra óptica (230).

Para el caso particular del dedo índice, la señal transmitida por el emisor instalado en la caja opaca (204) se propaga a través del primer segmento de fibra (202) hasta el primer sensor de intensidad (203) que convierte la potencia de la señal luminosa a una señal eléctrica la cual se mide mediante un conversor analógico digital instalado en la caja opaca (204). El primer sensor de intensidad luminosa (203) del dedo índice genera una señal eléctrica que es transmitida por un cable de par trenzado que subyace debajo del segmento de fibra óptica (202).

La onda que se propaga a través del primer segmento de fibra (202) continúa su propagación a través del segundo segmento (207) y en caso de haber flexión entre la falange proximal (105) y el plano formado por la zona dorsal de la mano (101), el segundo sensor de intensidad (211) arrojará una medición inferior a la del primer sensor (203). Dicha diferencia en magnitud corresponde proporcionalmente con el ángulo de flexión entre la falange proximal (105) del dedo índice y el plano formado por la zona dorsal de la mano (101).

El mismo procedimiento se repite para las falanges media (104) y distal (103), el tercer (212) y cuarto segmento (214) de fibra, el tercer (213) y cuarto sensor de intensidad (215). En el caso del cuarto sensor de intensidad (215) se ha

incorporado una terminación acoplada convenientemente para evitar reflexiones. Con las magnitudes de los sensores de intensidad (203, 211, 213, 215) se logra reconstruir espacialmente la flexión de las tres falanges del dedo índice (103, 104, 105) respecto al plano formado por la zona dorsal de la mano (101). Este procedimiento se repite de igual forma para las tres falanges de los dedos anular, medio y meñique.

El dedo pulgar posee únicamente dos falanges y por tanto requiere únicamente de tres segmentos de fibra óptica (219, 226, 227) y tres sensores de intensidad (201, 206, 208) para determinar su flexión.

Los segmentos de fibra ubicados sobre los músculos abductores (209) y oponentes del pulgar (224) miden la abducción del pulgar con el mismo principio que para el resto de los dedos. De acuerdo a una realización preferente de la invención, se emplean únicamente dos sensores de intensidad (223, 225) para estimar la abducción del pulgar, no obstante pudieran incorporarse más sensores tanto en el pulgar como en el resto de los dedos con el fin de medir todos los grados de libertad con los que cuenta la mano (1) humana, incluyendo los movimientos de la muñeca.

En la medida en que se coloquen más sensores para medir el movimiento en las articulaciones de la mano (1), se mejorarían las prestaciones de la invención bajo los criterios de: ergonomía y correspondencia de la fuerza aplicada por el operario (6) con la velocidad del manipulador (4), no obstante la esencia de la invención seguiría siendo la misma.

El convertidor analógico digital instalado en la caja opaca (204) digitaliza las magnitudes de los veintiún sensores de intensidad (201, 203, 206, 208, 211, 213, 215, 223, 225) con los que cuenta el sistema de posicionamiento dactilar (2) y transmite mediante un cable (205) los paquetes de datos hasta la unidad de comunicación (210), que para la realización preferente de la invención consiste en una unidad inalámbrica.

Para posicionar y orientar a la mano (1) en un espacio de tareas de seis dimensiones x, y, z, guiñada, cabeceo y balanceo es necesario contar con un sistema de posicionamiento espacial (7), de acuerdo a una realización preferente de la invención se emplea una Unidad de Medidas Inerciales, UMI (701) de seis grados de libertad dotada con acelerómetros y giroscopios. La UMI (701) se ubica en el plano formado por la zona dorsal del guante (5) respecto al cual se referencian las mediciones de flexión y abducción de los dedos, pudiéndose reconstruir tanto la posición y orientación de la mano (1) en el espacio, como la flexión y abducción de los dedos. La UMI (701) se comunica con la unidad de comunicación inalámbrica (210) mediante un cable (702).

En la figura 3 se muestra la zona palmar de un guante (5) diestro en donde se encuentra instalado un sistema de medición de fuerza (3). Este sistema está conformado por sensores de fuerza (301, 305, 306, 307, 308, 309, 310, 312, 313, 314) piezorresistivos. Para el caso del dedo índice se cuenta con tres sensores de fuerza (301, 306, 307) ubicados respectivamente en la zona palmar de la falange distal (103), media (104) y proximal (105). Los dedos medio, anular y meñique cuentan cada uno con tres sensores de fuerza (312, 313, 314). Dado que el dedo pulgar posee únicamente dos falanges, éste sólo cuenta con dos sensores de fuerza (308, 309). De igual forma se dispone de sensores para medir la fuerza ejercida por los músculos abductor (305) y oponente (310) del dedo pulgar. Adicionalmente el sistema cuenta con doce sensores para medir la distribución de fuerza en la palma de la mano (1), repartidos uniformemente sobre ella.

Los dos cables (302) del sensor de fuerza ubicado en la falange distal (103) del dedo índice son los terminales del sensor piezorresistivo (301) cuya conductividad cambia proporcionalmente conforme la magnitud de la fuerza aplicada. La unidad de medición de resistencia (304) se encarga de efectuar mediciones sobre todos los sensores de fuerza instalados en el guante (5). Dicha información se envía a la unidad de comunicación inalámbrica (210) ubicada en la zona dorsal del guante (5) a través de un cable (217).

Para mejorar la ergonomía del guante (5), los terminales de los sensores de fuerza están agrupados convenientemente en grupos (311) de varios cables y se encuentran en envolturas (303) para facilitar el traslado de los mismos hasta la unidad de medición de resistencia (304).

En la figura 4 se muestra a un operario (6) usando en su mano derecha (216) el guante (5) descrito en la presente invención para controlar un manipulador (4) de estructura angular de cuatro grados de libertad x, y, z, balanceo; para ello se usan unos actuadores (401, 402, 403, 404) convenientemente instalados en las articulaciones correspondientes. La pinza (405) instalada en el manipulador (4) sujeta a la carga (406) que se desplaza hasta su posición final (408) por acción de la fuerza resultante Fr (409) ejercida por el operario (6). Para estimar la magnitud, dirección y sentido de la fuerza resultante Fr (409), el guante (5) sensorizado descrito en la presente invención debe valerse del sistema de posicionamiento espacial (7), del sistema de posicionamiento dactilar (2) y del sistema de medición de fuerza (3); mediante ellos puede reconstruirse la magnitud, dirección y sentido de las veintiséis contribuciones individuales de fuerza correspondientes a cada sensor. Luego bastará con sumar vectorialmente dichas contribuciones para obtener el vector fuerza resultante Fr (409).

En la figura 5 se ilustra un caso particular donde sólo intervienen siete contribuciones individuales de fuerza (F_1, F_2, F_3, F_4, F_5, F_6, F_7), las contribuciones individuales F_5, F_6, F_7 corresponden a los sensores de fuerza del dedo índice (301, 306, 307). La contribución individual F_1, correspondiente al sensor de fuerza (309) de la falange distal del dedo pulgar también existe, por encontrarse la carga (406) en contacto con dicho punto. Lo mismo sucede con la contribución F_4. No obstante las contribuciones F_2 y F_3 correspondiente a un sensor del dedo pulgar (308) y otro de la palma (305) son nulas, debido a que no existe contacto entre ellas y la carga (406).

Después de generar las contribuciones individuales F_1, F_2, F_3, F_4, F_5, F_6, F_7, se procede a realizar su suma vectorial y generar el vector fuerza resultante Fr (409), a partir del cual, aplicando la ley proporcional $Vr = K \cdot F_r$ se obtiene la velocidad resultante Vr (410), donde K es un escalar que representa la sensibilidad del guante (5) a la fuerza aplicada por el operario (6), nótese que tanto Fr como Vr son colineales y están relacionados mediante K.

La fuerza resultante Fr (409) y la velocidad resultante Vr (410) se transmiten desde la unidad de comunicación inalámbrica (210) instalada en la zona dorsal del guante (5) hasta el receptor inalámbrico (412) ubicado en las cercanías del manipulador (4). En la figura 4 se observa además un computador (411) que controla un manipulador (4) de cuatro grados de libertad. Dicho computador (411) recibe las coordenadas del vector velocidad resultante Vr (410) provenientes del receptor inalámbrico (412) y genera las consignas de velocidad para cada grado de libertad, las cuales se transmiten a los variadores de frecuencia (413) que manejan cada uno de los cuatro actuadores (401, 402, 403, 404) del manipulador (4).

Las figuras 4 y 5 muestran a un operario (6) ejerciendo presión directamente sobre la carga (406), no obstante y de acuerdo a una realización preferente de la invención, también se permite el movimiento de la carga (406) por acción de una fuerza ejercida por el operario (6) sobre el manipulador (4), con esto se amplía considerablemente el área sobre la cual el operario (6) puede ejercer presión para controlar al manipulador (4).

Con el fin de evitar movimientos involuntarios del manipulador (4) se instala un detector de contacto distribuido (422), el cual de acuerdo a una realización preferente de la invención ha consistido en uno del tipo electromagnético. El campo electromagnético generado por el detector está confinado a la estructura metálica del manipulador (4) y la carga (406), dicho campo se altera únicamente cuando el operario (6) toca al manipulador (4) o a la carga (406), bajo tal condición está permitido el movimiento del manipulador (4). En aquellos casos en los cuales el operario (6) ejerza presión sobre algún elemento diferente a los mencionados, el detector de contacto distribuido (422) no se activará y por consiguiente el movimiento del manipulador (4) se inhabilitará. El procedimiento descrito se resume mediante el diagrama de flujo de la figura 6.

El operario (6) de la figura 4 al emplear un guante (5) sensorizado en su mano derecha (216) puede controlar el movimiento del manipulador (4) y por ende de la carga (406) hasta tres grados de libertad x, y, z. Para poder orientar a la carga (406) y proveer de seis grados de libertad de movimiento: x, y, z, guiñada, cabeceo y balanceo, es necesario contar con un segundo guante (5) en la mano izquierda (216i) tal como se muestra en la figura 7. Los guantes (5) derecho e izquierdo son semejantes el uno del otro y poseen las mismas funcionalidades y características descritas previamente en la realización preferente de la invención donde se emplea un solo guante (5), mostrada en las figuras 1, 2, 3, 4 y 5.

Los sistemas de posicionamiento dactilar (2d, 2i) situados en el guante derecho e izquierdo, conjuntamente con los sistemas de medición de fuerza (3d, 3i) instalados en el guante derecho e izquierdo, permiten generar dos vectores de fuerza resultante; Fri (409i) y Frd (409d) con sus respectivos vectores directores Ri (417i) y Rd (417d), lo que permite obtener un par T(419) y por consiguiente una velocidad angular ω (420) cuya dirección y sentido va a depender de las fuerzas aplicadas por el operario (6).

La fuerza resultante para cada guante (5): Fri (409i) para el izquierdo y Frd (409d) para el derecho, se obtienen de la misma forma para el caso donde se emplea un solo guante (5); en tal sentido se obtienen los vectores individuales de fuerza correspondientes a cada sensor y luego se efectúan las dos sumas vectoriales.

Los vectores directores Ri (417i) y Rd (417d) son considerados de acuerdo a una realización preferente de la invención como de igual magnitud y dirección pero en sentido contrario, lo que implica que el punto imaginario de giro de la carga (406), O_G (418), se sitúa espacialmente en el punto medio de la distancia entre ambos guantes (5).

El par T (419) y la velocidad angular ω (420) medidos por los sistemas instalados en los guantes (5) de la mano derecha (216d) e izquierda (216i) del operario (6), permiten mover la carga (406) hasta en tres grados de libertad: guiñada, cabeceo y balanceo. Para proveer de seis grados de libertad de movimiento (x, y, z, guiñada, cabeceo y balanceo) a partir de las fuerzas resultantes Fri (409i), Frd (409d) y los vectores directores Ri (417i) y Rd (417d) es necesario aplicar a la carga (406) las leyes dinámicas de sólido rígido en el espacio con el fin de determinar la velocidad traslacional y angular ω (420) de la carga (406).

Para el caso particular mostrado en la figura 7, tanto las fuerzas resultantes Fri (409i) y Frd (409d) como los vectores directores Ri (417i) y Rd (417d) son iguales en magnitud y dirección pero en sentido contrario; al aplicar las leyes dinámicas de sólido rígido en el espacio se deduce que la velocidad traslacional es nula existiendo únicamente componente angular ω (420).

La figura 8 muestra un caso donde el operario (6) emplea dos guantes (5) para controlar a la carga (406) y coexisten tanto velocidades de rotación ω (420) como de traslación Vt (421). Nótese que para este caso las componentes de fuerza resultante de cada guante (5), Fri (409i) y Frd (409d), son ortogonales entre sí y generan cada una componentes de velocidad de rotación ω (420) y traslación Vt (421) que deben determinarse a través de las leyes dinámicas de sólido rígido en el espacio.

Al igual que sucede para la modalidad de control donde el operario (6) emplea una sola mano (1), los vectores fuerza resultante de cada guante (5), Fri (409i), Frd (409d), y los vectores directores Ri (417i), Rd (417d) se transmiten desde las unidades de comunicación inalámbrica de cada guante (210i, 210d) hasta el receptor inalámbrico (412) que luego envía al computador (411), el cual se encarga de generar las consignas de velocidad para cada grado de libertad. Dichas consignas se transmiten a los variadores de frecuencia (413) que manejan cada uno de los cuatro actuadores (401, 402, 403, 404) del manipulador (4). La realización preferente de la invención emplea un manipulador (4) con sólo cuatro grados de libertad de movimiento: x, y, z, balanceo, lo que implica que aún cuando el guante (5) sensorizado descrito en la presente invención pueda controlar hasta seis grados de libertad, las características propias del manipulador (4) permiten movimiento únicamente en cuatro grados; para saldar esta aparente incompatibilidad, en el computador (411) se anulan las componentes de guiñada y cabeceo generadas al aplicar las leyes dinámicas de sólido rígido en el espacio a las fuerzas medidas por los guantes (5), Fri (409i), Frd (409d).

Aún cuando las figuras 7 y 8 muestren a un operario (6) ejerciendo presión directamente sobre la carga (406) con ambas manos (216i, 216d) para originar movimientos traslacionales y rotacionales; es posible de acuerdo a una realización preferente de la invención, generar dichos movimientos mediante acción directa del operario (6) sobre la estructura metálica del manipulador (4), esto se hace para mantener la compatibilidad con la modalidad de operación bajo un solo guante (5), en cuyo caso el movimiento del conjunto está permitido bien sea que el operario (6) ejerza presión sobre la carga (406) o el manipulador (4).

El eje de giro O_G (418), fijado para la medición de los momentos de fuerza T (419), no necesariamente coincide con el eje de la carga (406) o con su centro de masa, esta peculiaridad constituye una realización preferente de la invención para permitir los movimientos rotacionales de la carga (406) en aquellos casos en los cuales el operario (6) no ejerza presión sobre ella sino sobre el manipulador (4). En cualquier caso, el eje de giro O_G (418) se considera ubicado en el punto medio de la distancia entre ambos guantes (5), bien sea que el operario (6) actúa sobre la carga (406) o sobre el manipulador (4).

También es necesario para la modalidad de control donde se emplean dos guantes (5) el uso del detector de contacto distribuido (422), con el fin de evitar movimientos involuntarios del manipulador (4). La lógica de seguridad es la misma independientemente si se usan uno dos guantes (5) para controlar al manipulador (4), en tal sentido el movimiento del manipulador (4) se permite únicamente cuando el detector de contacto (422) se encuentra activado. De acuerdo a una realización preferente de la invención, en aquellos casos en los cuales el detector de contacto (422) se encuentre activado y alguno de los dos vectores fuerza resultante sea nulo, los movimientos del manipulador (4) se permiten sólo en tres grados de libertad x, y, z, y se asume el vector fuerza resultante de la mano derecha Frd (409d) o izquierda Fri (409i) según sea el caso, como el único existente y a partir de dicho vector se genera la velocidad resultante Vr (410) correspondiente, usándose los mismos criterios para la modalidad de control de un solo guante (5).

El diagrama de flujo de la figura 9 resume el algoritmo de operación para movilizar a un manipulador (4) hasta en seis grados de libertad cuando se emplean dos guantes (5) sensorizados.

REIVINDICACIONES

1. Sistema de control para manipuladores que permite a un operario (6) controlar el movimiento de un manipulador (4) con uno o más grados de libertad adaptado para manipular una carga (406), ejerciendo presión con una o ambas manos (1) en la dirección de movimiento deseada sobre el manipulador (4) o la carga (406) **caracterizado** porque el sistema comprende al menos un guante (5) dotado de sensores que recoge información tanto de la posición y orientación del guante (5) como del módulo, dirección y sentido de la fuerza aplicada, un receptor inalámbrico (412) que recibe información del guante (5), un computador (411) asociado al receptor inalámbrico (412), que genera unas consignas de velocidad para cada grado de libertad del manipulador (4), y unos variadores de frecuencia (413) que reciben órdenes del computador (411) para controlar el manipulador (4).

2. Sistema de control para manipuladores de acuerdo con reivindicación 1, **caracterizado** porque el guante (5) posee en su zona dorsal un sistema de posicionamiento dactilar (2) que mide la flexión y abducción de los cinco dedos.

3. Sistema de control para manipuladores de acuerdo con reivindicación 1, **caracterizado** porque el guante (5) posee en su zona palmar un sistema de medición de fuerza (3) que mide las fuerzas aplicadas por el operario (6) sobre el manipulador (4) o sobre la carga (406) movilizada.

4. Sistema de control para manipuladores de acuerdo con reivindicación 2, **caracterizado** porque el sistema de posicionamiento dactilar (2) está constituido por una unidad de comunicación (210) que emite la información recogida por el guante (5) al receptor inalámbrico (412) y una caja opaca (204) que presenta en su interior unos emisores de luz instalados, los cuales están conectados a unos segmento de fibra óptica (7) que contienen unos sensores de intensidad (201, 203, 206, 208, 211,213, 215, 223, 225).

5. Sistema de control para manipuladores de acuerdo con reivindicación 4, **caracterizado** porque la unidad de comunicación (210) es inalámbrica.

6. Sistema de control para manipuladores de acuerdo con reivindicación 4, **caracterizado** porque la unidad de comunicación (210) utiliza, para el envío de la información recogida por el/los guantes (5), unos medios seleccionados entre:

ondas electromagnéticas,

un cable,

fibra óptica,

señales de infrarrojo, y

señales ultrasónicas.

7. Sistema de control para manipuladores de acuerdo con reivindicación 4, **caracterizado** porque la caja opaca (204) contiene adicionalmente un convertidor analógico digital.

8. Sistema de control para manipuladores de acuerdo con reivindicaciones 4 ó 7, **caracterizado** porque la caja opaca (204) contiene en su interior seis emisores de luz conectados con seis segmentos de fibra óptica (202, 209, 219, 220, 221, 222).

9. Sistema de control para manipuladores de acuerdo con reivindicación 4, **caracterizado** porque el sistema de posicionamiento dactilar (2) presenta veintiún sensores de intensidad (201, 203, 206, 208, 211,213, 215, 223, 225).

10. Sistema de control para manipuladores de acuerdo con una cualquiera de las reivindicaciones 2, 4 ó 9 **caracterizado** porque el sistema de posicionamiento espacial (7) dispone adicionalmente de una Unidad de Medidas Inerciales, (UMI), (701) que permite posicionar y orientar la mano (1) en un espacio de tareas de hasta seis dimensiones, x, y, z, guiñada, cabeceo y balanceo.

11. Sistema de control para manipuladores de acuerdo con reivindicación 10, **caracterizado** porque la Unidad de Medidas Inerciales (701) está ubicada en el plano formado por la zona dorsal del guante (5).

12. Sistema de control para manipuladores de acuerdo con una cualquiera de las reivindicaciones 10 ó 11, **caracterizado** porque la Unidad de Medidas Inerciales (701) está dotada de medios seleccionados entre:

acelerómetros y giroscopios,

emisores y receptores infrarrojos,

emisores y receptores de ultrasonido, y

sistema de posicionamiento global mediante satélites que orbitan en torno a la tierra.

13. Sistema de control para manipuladores de acuerdo con reivindicación 3, **caracterizado** porque el sistema de medición de fuerza (3) comprende una unidad de medición de resistencia (304) y una serie de sensores de fuerza (301, 305, 306, 307, 308, 309, 310, 312, 313, 314) distribuidos uniformemente en toda la superficie palmar.

14. Sistema de control para manipuladores de acuerdo con reivindicación 13, **caracterizado** porque el sistema de medición de fuerza (3) dispone de veintiséis sensores de fuerza (301, 305, 306, 307, 308, 309, 310, 312, 313, 314).

15. Sistema de control para manipuladores de acuerdo con una cualquiera de las reivindicaciones 13 ó 14, **caracterizado** porque cada sensor de fuerza (301, 305, 306, 307, 308, 309, 310, 312, 313, 314) presenta al menos un par de terminales (302) cuya conductividad cambia proporcionalmente conforme la magnitud de la fuerza aplicada.

16. Sistema de control para manipuladores de acuerdo con reivindicación 15, **caracterizado** porque los terminales (302) se encuentran dentro de unas envolturas (303).

17. Sistema de control para manipuladores de acuerdo con reivindicación 1, **caracterizado** porque el manipulador (4) incorpora unos actuadores (401, 402, 403 y 404) que generan el movimiento de la carga (406) en hasta tres grados de libertad cuando el operario (6) ejerce presión con una sola mano (1), y en hasta seis grados de libertad cuando el operario (6) ejerce presión con ambas manos (1).

18. Sistema de control para manipuladores de acuerdo con una cualquiera de las reivindicaciones 1 ó 17, **caracterizado** porque el manipulador (4) incorpora un detector de contacto (422) para evitar movimientos involuntarios del manipulador (4).

19. Sistema de control para manipuladores de acuerdo con reivindicación 18, **caracterizado** porque el detector de contacto (422) es de un tipo seleccionado entre:

detector de contacto (422) electromagnético, y

detector de contacto (422) electrostático.

20. Sistema de control para manipuladores de acuerdo con reivindicación 2, **caracterizado** porque el sistema de posicionamiento dactilar (2) dispone para la medición del arco palmar, flexión y abducción de los cinco dedos, de medios seleccionados entre:

goniómetros resistivos,

electrogoniómetros,

sensores de efecto hall,

sensores capacitivos,

sensores de inducción magnética,

elastómeros conductores piezorresistivos, y

sistema de cámaras instaladas en los linderos del espacio de trabajo del operario (6).

21. Sistema de control para manipuladores de acuerdo con una cualquiera de las reivindicaciones 13, 14 ó 15 **caracterizado** porque el sistema de medición de fuerza (3) dispone para la medición de las fuerzas aplicadas de sensores de fuerza (301, 305, 306, 307, 308, 309, 310, 312, 313, 314) seleccionados entre:

sensores piezorresistivos,

galgas extensiométricas, y

contactos eléctricos.

22. Procedimiento de control para manipuladores para el sistema de control descrito en una cualquiera de las reivindicaciones 1-21, cuando se emplea un solo guante (5) **caracterizado** porque comprende las siguientes etapas:

- comprobación de si el detector de contacto (422) del manipulador (4) está activado,

- inhabilitación para controlar el manipulador (4) en caso de que el detector de contacto (422) no esté activado,

- reconstrucción de la posición y orientación de la mano (1) en el espacio en caso de que el detector de contacto (422) sí esté activado,

- lectura de los sensores de fuerza (301, 305, 306, 307, 308, 309, 310, 312, 313, 314) instalados en el guante (5),

- generación de los vectores de fuerza individuales de cada sensor de fuerza (301, 305, 306, 307, 308, 309, 310, 312, 313, 314),

- cálculo de la suma vectorial de los vectores de fuerza individuales para generar el vector fuerza resultante Fr (409),

- aplicación de la ley proporcional Vr = k · Fr para generar los perfiles de velocidad correspondientes de cada grado de libertad,

- transmisión de cada perfil de velocidad al variador de frecuencia (413) correspondiente para generar movimiento en el manipulador (4) en hasta tres grados de libertad.

23. Procedimiento de control para manipuladores para el sistema de control descrito en una cualquiera de las reivindicaciones 1-21, cuando se emplean dos guantes (5) **caracterizado** porque comprende las siguientes etapas:

- comprobación de si el detector de contacto (422) del manipulador (4) está activado,

- inhabilitación para controlar el manipulador (4) en caso de que el detector de contacto (422) no esté activado,

- reconstrucción de la posición y orientación de las manos (1) izquierda y derecha en caso de que el detector de contacto (422) sí esté activado,

- lectura de los sensores de fuerza (301, 305, 306, 307, 308, 309, 310, 312, 313, 314) instalados en cada uno de los dos guantes (5),

- generación de los vectores de fuerza individuales de los sensor de fuerza (301, 305, 306, 307, 308, 309, 310, 312, 313, 314) de cada guante (5),

- cálculo de la suma vectorial de los vectores de fuerza individuales para generar el vector de fuerza resultante de cada guante (5), Fri, Frd,

- comprobación de si alguno de los dos vectores de fuerza Fri, Frd son iguales a cero,

- determinación de los vectores directores ri, rd de cada vector de fuerza resultante en caso de que los dos vectores de fuerza Fri, Frd sean distintos de cero,

  i. aplicación de las leyes de la dinámica de cuerpos en el espacio para determinar la velocidad rotacional y traslacional de la carga (406),

  ii. transmisión de cada perfil de velocidad al variador de frecuencia (413) correspondiente para generar movimiento en el manipulador (4) en hasta seis grados de libertad,

- aplicación de la ley proporcional $Vr = k \cdot Fr$ para generar los perfiles de velocidad correspondientes para cada grado de libertad, en caso de que alguno de los dos vectores de fuerza Fri, Frd sean iguales a cero,

  i. transmisión de cada perfil de velocidad al variador de frecuencia (413) correspondiente para generar movimiento en el manipulador (4) en hasta tres grados de libertad.

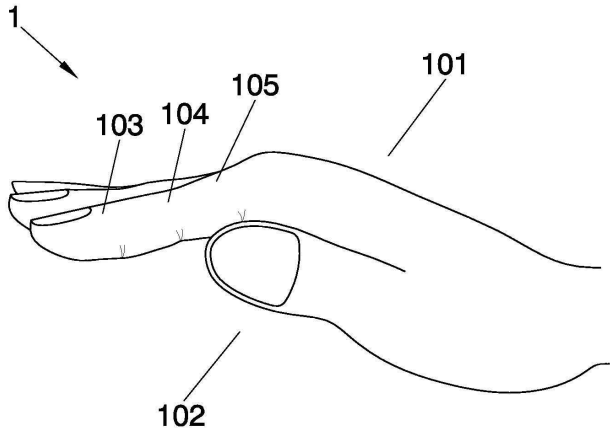

FIG. 1

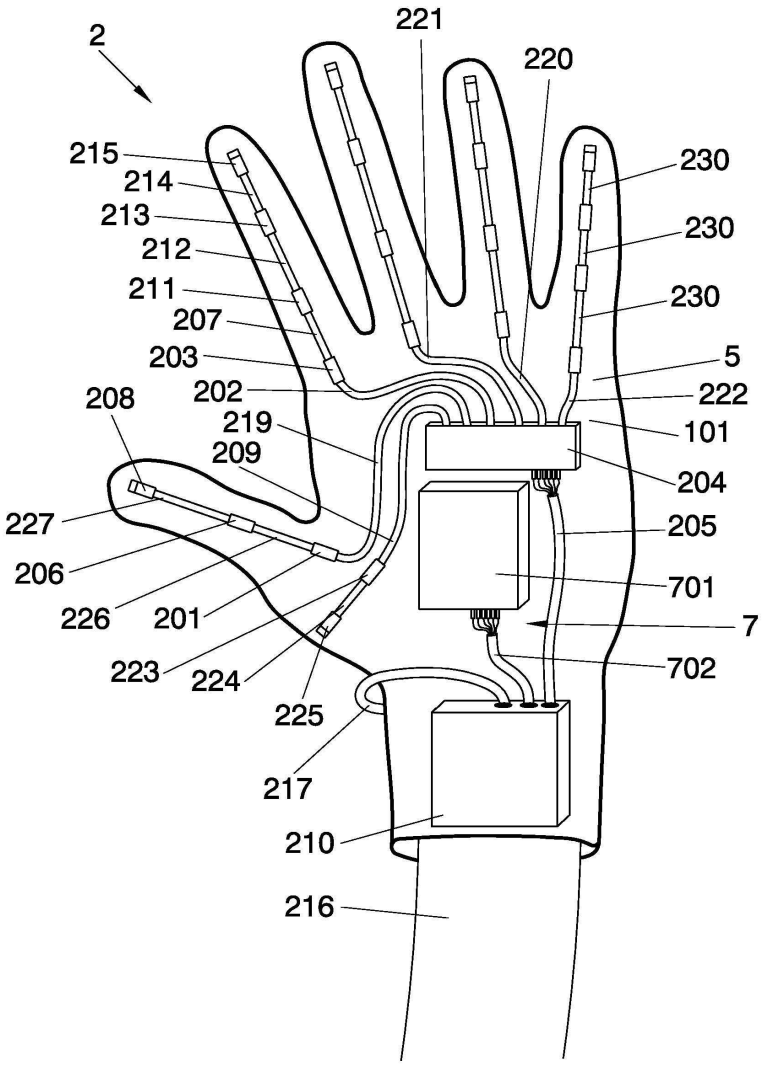
2
221
220
215
214
213
212
211
207
203
202
208
219
209
227
206
226
201
223
224
225
217
210
216
230
230
230
5
222
101
204
205
701
7
702

FIG. 2

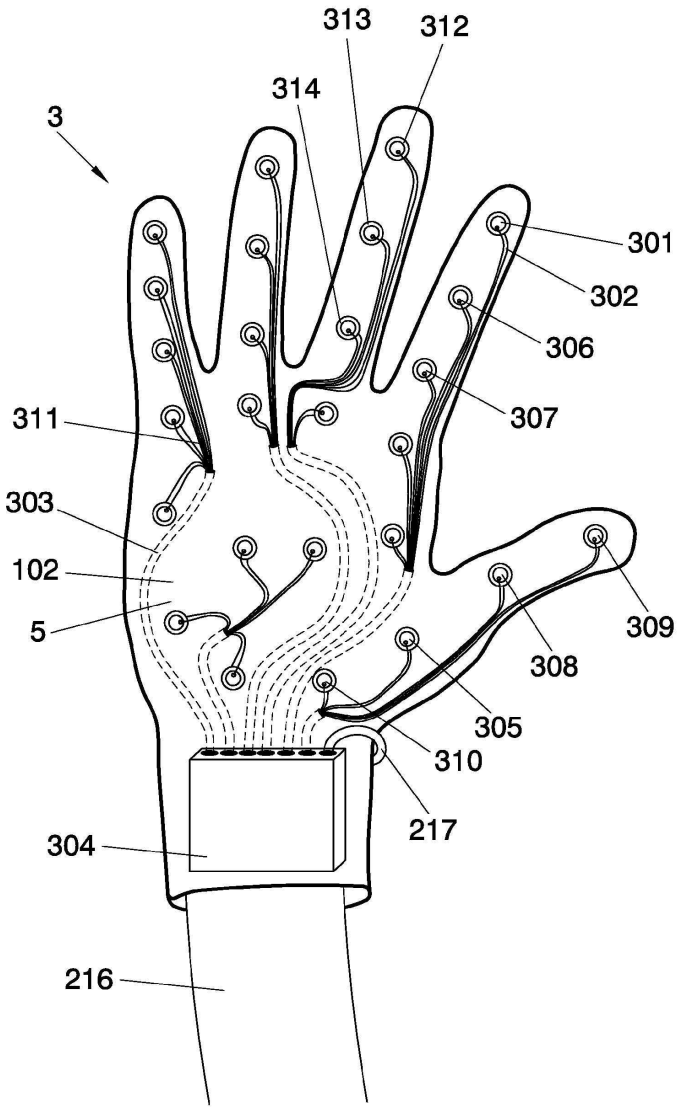
313
312
314
3
301
302
306
307
311
303
102
5
309
308
305
310
217
304
216

FIG. 3

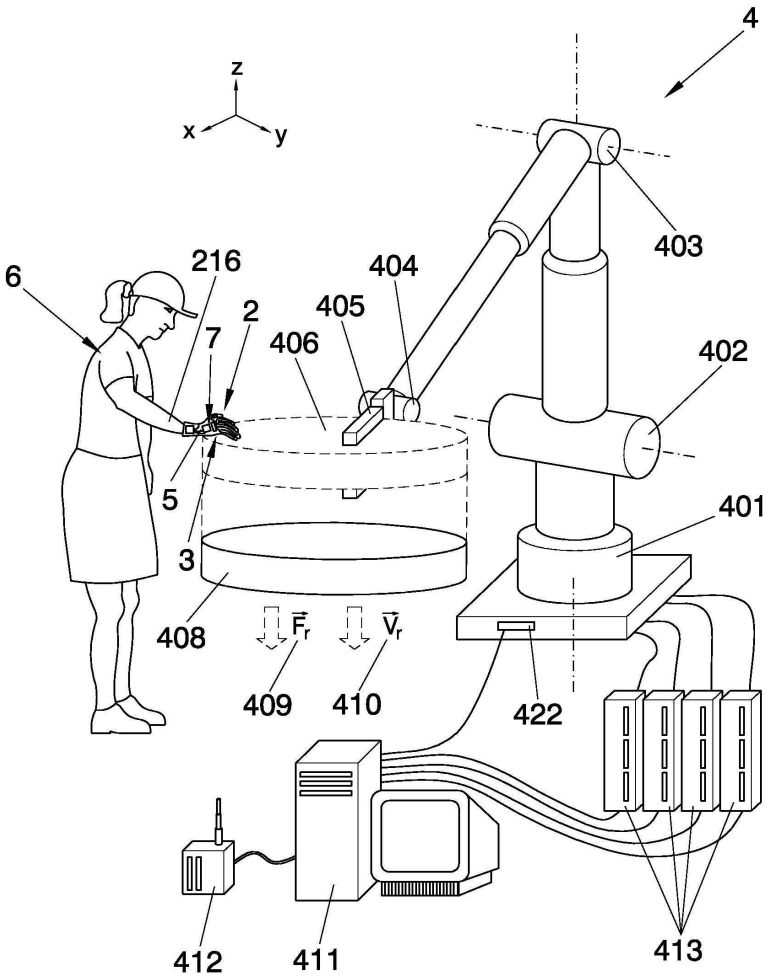
4
z
x
y
403
6
216
404
405
2
7
406
402
5
401
3
408
$\vec{F}_r$
$\vec{V}_r$
409
410
422
412
411
413

FIG. 4

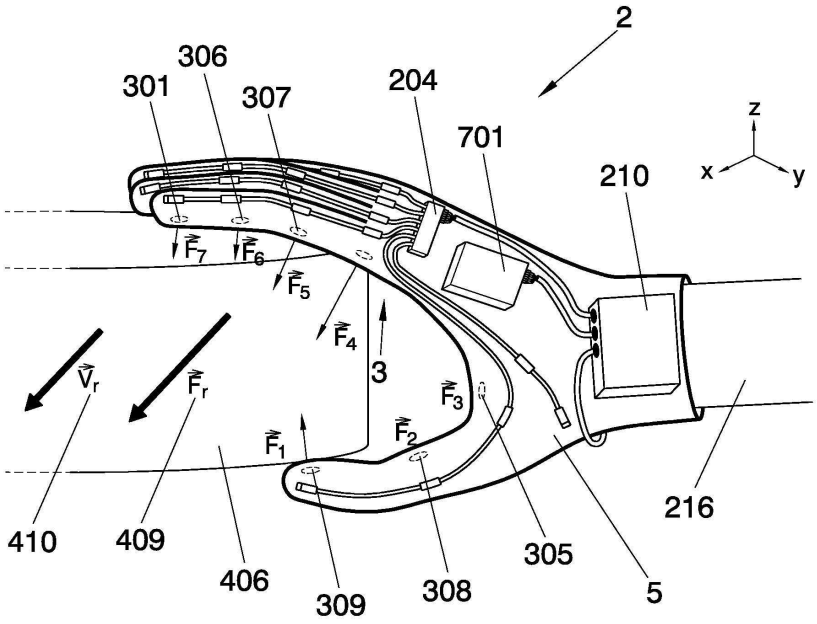
2
306
301
307
204
701
210
z
x
y
$\vec{F}_7$
$\vec{F}_6$
$\vec{F}_5$
$\vec{F}_4$
3
$\vec{V}_r$
$\vec{F}_r$
$\vec{F}_3$
$\vec{F}_2$
$\vec{F}_1$
216
410
409
406
309
308
305
5

FIG. 5

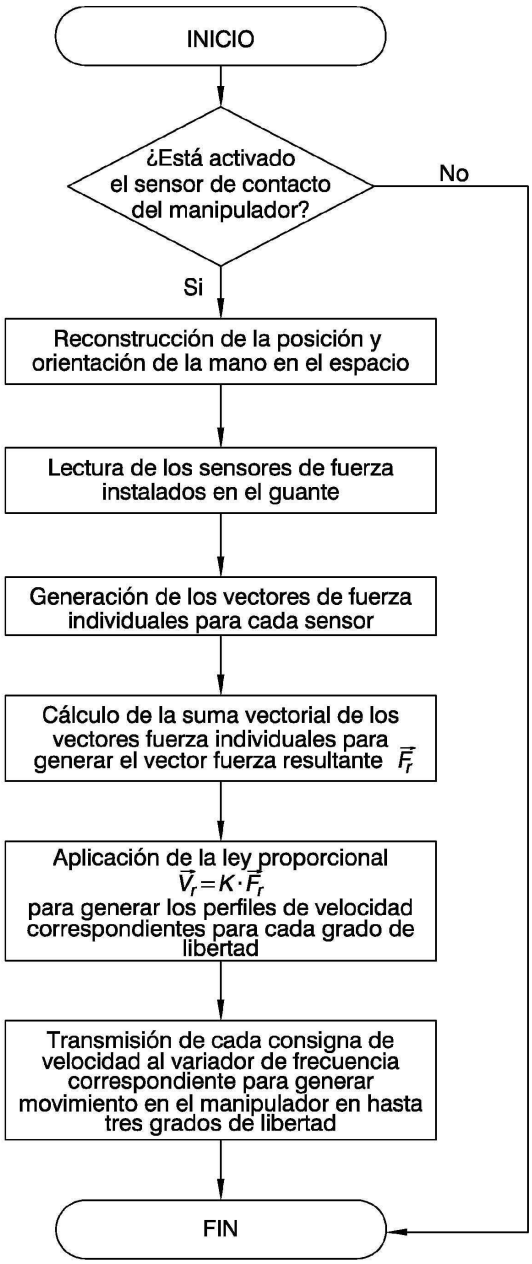
INICIO
¿Está activado el sensor de contacto del manipulador?
No
Si
Reconstrucción de la posición y orientación de la mano en el espacio
Lectura de los sensores de fuerza instalados en el guante
Generación de los vectores de fuerza individuales para cada sensor
Cálculo de la suma vectorial de los vectores fuerza individuales para generar el vector fuerza resultante $\vec{F}_r$
Aplicación de la ley proporcional $\vec{V}_r = K \cdot \vec{F}_r$ para generar los perfiles de velocidad correspondientes para cada grado de libertad
Transmisión de cada consigna de velocidad al variador de frecuencia correspondiente para generar movimiento en el manipulador en hasta tres grados de libertad
FIN

FIG. 6

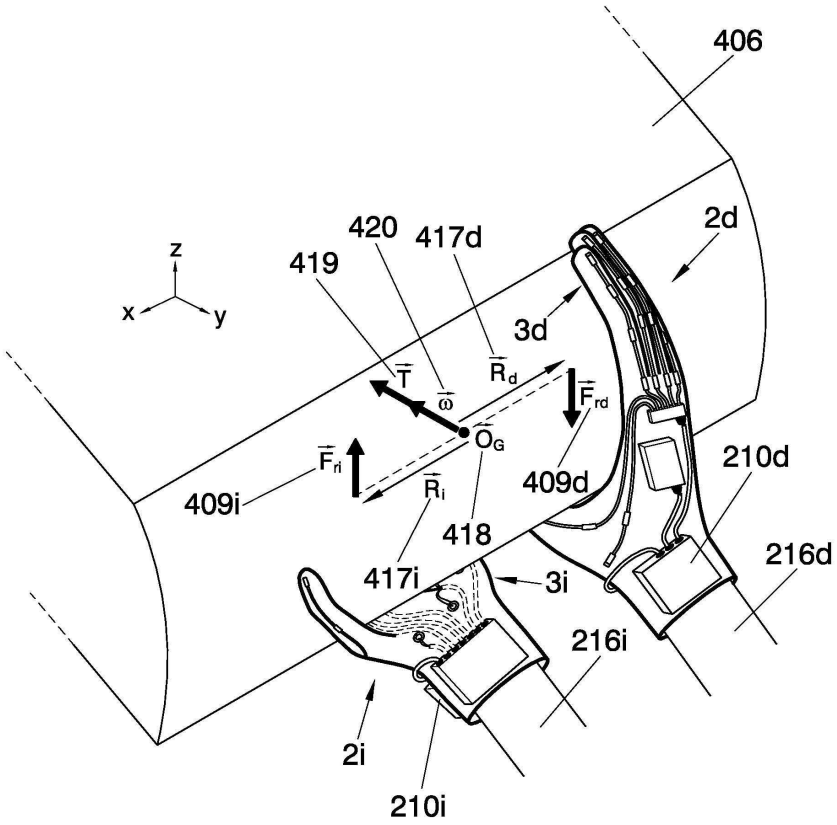
406
2d
420
417d
419
z
x
y
3d
$\vec{T}$
$\vec{\omega}$
$\vec{R}_d$
$\vec{F}_{rd}$
$\vec{O}_G$
$\vec{F}_{ri}$
$\vec{R}_i$
409i
409d
210d
418
216d
417i
3i
216i
2i
210i

FIG. 7

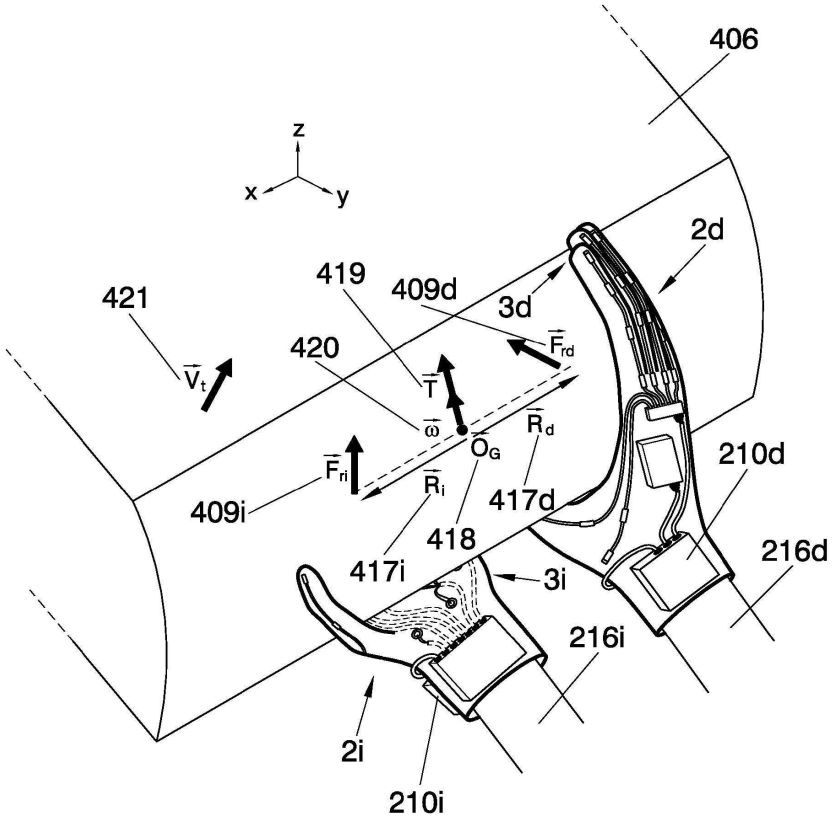
406
z
x
y
2d
421
419
409d
3d
420
$\vec{F}_{rd}$
$\vec{V}_t$
$\vec{T}$
$\vec{\omega}$
$\vec{O}_G$
$\vec{R}_d$
$\vec{F}_{ri}$
$\vec{R}_i$
210d
409i
417d
418
216d
417i
3i
216i
2i
210i

FIG. 8

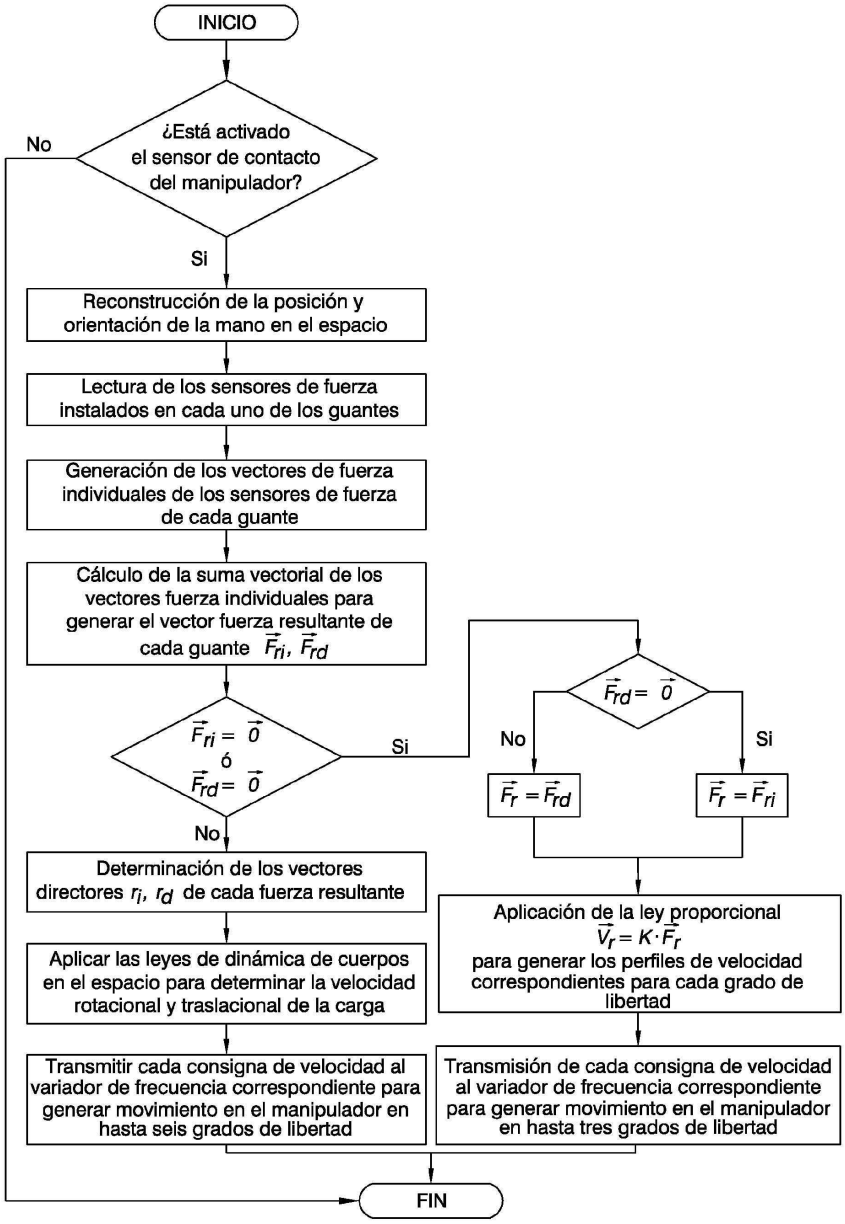
INICIO
¿Está activado el sensor de contacto del manipulador?
No
Si
Reconstrucción de la posición y orientación de la mano en el espacio
Lectura de los sensores de fuerza instalados en cada uno de los guantes
Generación de los vectores de fuerza individuales de los sensores de fuerza de cada guante
Cálculo de la suma vectorial de los vectores fuerza individuales para generar el vector fuerza resultante de cada guante $\vec{F}_{ri}$, $\vec{F}_{rd}$
$\vec{F}_{ri} = \vec{0}$ ó $\vec{F}_{rd} = \vec{0}$
Si
No
$\vec{F}_{rd} = \vec{0}$
No
Si
$\vec{F}_r = \vec{F}_{rd}$
$\vec{F}_r = \vec{F}_{ri}$
Determinación de los vectores directores r_i, r_d de cada fuerza resultante
Aplicación de la ley proporcional $\vec{V}_r = K \cdot \vec{F}_r$ para generar los perfiles de velocidad correspondientes para cada grado de libertad
Aplicar las leyes de dinámica de cuerpos en el espacio para determinar la velocidad rotacional y traslacional de la carga
Transmitir cada consigna de velocidad al variador de frecuencia correspondiente para generar movimiento en el manipulador en hasta seis grados de libertad
Transmisión de cada consigna de velocidad al variador de frecuencia correspondiente para generar movimiento en el manipulador en hasta tres grados de libertad
FIN

FIG. 9

OFICINA ESPAÑOLA
DE PATENTES Y MARCAS

ESPAÑA

(21) N.º solicitud:200930173

(22) Fecha de presentación de la solicitud: 14.05.2009

(32) Fecha de prioridad:

INFORME SOBRE EL ESTADO DE LA TECNICA

(51) **Int. Cl. :** ***G06F3/01*** (01.01.2006)

DOCUMENTOS RELEVANTES

Categoría	Documentos citados	Reivindicaciones afectadas
X	US 5184009 A (WRIGHT et al.) 02.02.1993, columna 7, línea 34 – columna 9, línea 41; figuras 1-3.	1-8
A		9-23
A	US 6452584 B1 (WALKER et al.) 17.09.2002, columna 6, línea 6 – columna 9, línea 51; figuras.	1-9,13-20
A	US 6141643 A (HARMON) 31.10.2000, columna 2, línea 18 – columna 6, línea 47; figuras.	1-8,17,18
A	LAURA DIPRIETO, ANGELO M SABATINI, PAOLO DARIO "A Survey of Glove-Based Systems and Teir Applications", IEEE TRANSACTIONS ON SYSTEMS, MAN AND CIBERNETICS-PART C: APPLICATIONS AND REVIEWS, VOL 38, Nº 4, Julio 2008.	

Categoría de los documentos citados

X: de particular relevancia
Y: de particular relevancia combinado con otro/s de la misma categoría
A: refleja el estado de la técnica
O: referido a divulgación no escrita
P: publicado entre la fecha de prioridad y la de presentación de la solicitud
E: documento anterior, pero publicado después de la fecha de presentación de la solicitud

El presente informe ha sido realizado

☒ para todas las reivindicaciones ☐ para las reivindicaciones nº:

Fecha de realización del informe	Examinador	Página
14.12.2010	P. Pérez Fernández	1/4

INFORME DEL ESTADO DE LA TÉCNICA

Nº de solicitud:200930173

Documentación mínima buscada (sistema de clasificación seguido de los símbolos de clasificación)

G06F

Bases de datos electrónicas consultadas durante la búsqueda (nombre de la base de datos y, si es posible, términos de búsqueda utilizados)

INVENES, EPODOC

OPINIÓN ESCRITA

Nº de solicitud:200930173

Fecha de Realización de la Opinión Escrita: 14.12.2010

Declaración

Novedad (Art. 6.1 LP 11/1986)	Reivindicaciones	1-23	**SI**
	Reivindicaciones		**NO**
Actividad inventiva (Art. 8.1 LP11/1986)	Reivindicaciones	9-23	**SI**
	Reivindicaciones	1-8	**NO**

Se considera que la solicitud cumple con el requisito de aplicación industrial. Este requisito fue evaluado durante la fase de examen formal y técnico de la solicitud (Artículo 31.2 Ley 11/1986).

Base de la Opinión.-

La presente opinión se ha realizado sobre la base de la solicitud de patente tal y como se publica.

OPINIÓN ESCRITA

Nº de solicitud:200930173

1. Documentos considerados.-

A continuación se relacionan los documentos pertenecientes al estado de la técnica tomados en consideración para la realización de esta opinión.

Documento	Número Publicación o Identificación	Fecha Publicación
D01	US 5184009 A (WRIGHT et al.)	02.02.1993

2. Declaración motivada según los artículos 29.6 y 29.7 del Reglamento de ejecución de la Ley 11/1986, de 20 de marzo, de Patentes sobre la novedad y la actividad inventiva; citas y explicaciones en apoyo de esta declaración

Falta de Actividad Inventiva
Reivindicación nº 1
Se establece el documento D01 como el más próximo del Estado de la Técnica.
El documento D01 describe un sistema de medida de la atenuación óptica para la obtención de señales proporcionales al movimiento del sistema a que va unido. Dicho documento contiene:
-un guante de control (11) con unidades de detección (12) para detectar los movimientos individuales del mismo (ver columna 7, líneas 33-43; figura 1).
-un sistema de control óptico (42) que procesa las señales recibidas de cada uno de los sensores (14) del guante (11) para generar señales que se trasmiten que se trasmiten para controlar máquinas inteligentes, robots o semejantes (ver columna 8, líneas 39-59; figura 2).
-el sistema también dispone de información táctil proporcional a la fuerza (ver columna 9, líneas 21-24; figura 3).
-se dispone de medios de control de la posición (64) que sensan la posición y la orientación de la mano del operador (ver columna 9, líneas 30-33; figura 3).
Las diferencias entre el documento D01 y la reivindicación nº 1 residen en que en la reivindicación nº1 la información del guante es transmitida de forma inalámbrica y que las órdenes del computador se envían a unos variadores de frecuencia para controlar el manipulador.
Se considera que estas características son simplemente una de las varias posibilidades evidentes que un experto en la materia seleccionará según las circunstancias, sin el ejercicio de Actividad Inventiva, para resolver el problema planteado.
Por consiguiente, la reivindicación nº 1 carece de Actividad Inventiva (Art 8 LP).
Reivindicación nº 2
Esta característica ya aparece recogida en D01 (ver columna 7, líneas 34-40; figura 1). En consecuencia, la reivindicación nº2 carece de Actividad Inventiva (Art 8 LP).
Reivindicación nº 3
Esta característica también aparece reflejada en D01 (ver columna 9, líneas 21-24). Por tanto, la reivindicación nº 3 también carece de Actividad Inventiva (Art 8LP).
Reivindicación nº 4
Esta reivindicación sería obvia para un experto en la materia a la vista de la figura 2 del documento D01. Por consiguiente, la reivindicación nº 4 carece de Actividad Inventiva (Art 8 LP).
Reivindicación nº 5
Esta característica es simplemente una de las varias posibilidades evidentes que un experto en la materia seleccionará según las circunstancias, sin el ejercicio de Actividad Inventiva , para resolver el problema planteado. En consecuencia, la reivindicación nº 5 carece de Actividad Inventiva (Art 8 LP).
Reivindicación nº 6
Esta característica ya aparece recogida en D01 (ver columna 8, líneas 39-45; figura 2). Por lo tanto, la reivindicación nº6 carece de Actividad Inventiva (Art 8 LP).
Reivindicación nº 7
Esta característica se encuentra recogida en D01 (ver columna 8, líneas 6-9). Por consiguiente, la reivindicación nº7 carece de Actividad Inventiva (Art 8 LP).
Reivindicación nº 8
Esta característica ya aparece recogida en D01 (ver columna 7, línea 64-columna 8, línea 6). En consecuencia, la reivindicación nº8 carece de Actividad Inventiva (Art 8 LP).

Appendix C

C. Schematics. Conditioning board of the dataglove interface

C.1 Control Stage of Analog Inputs

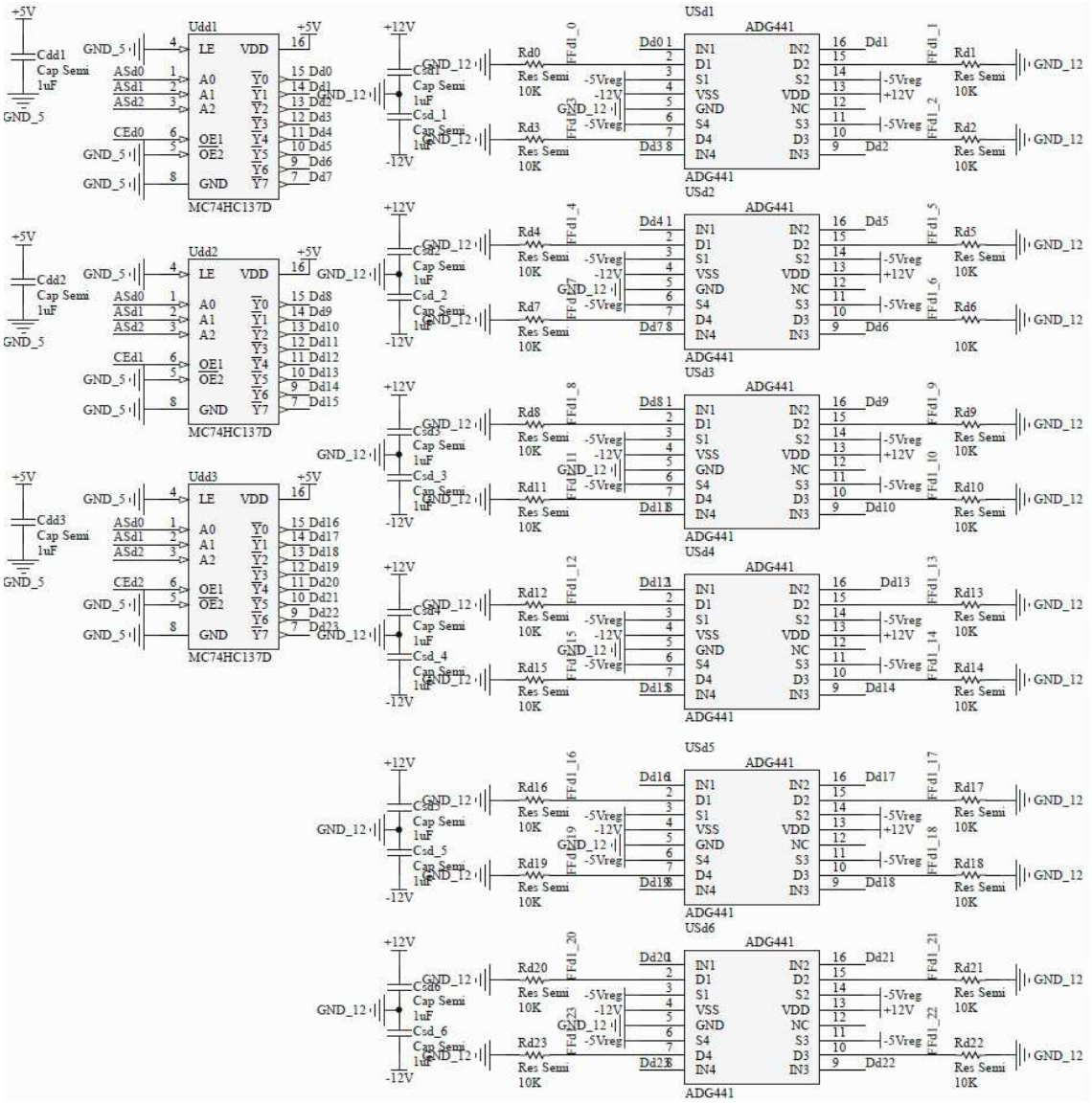

C.2 Stage of Analog Signal Conditioning

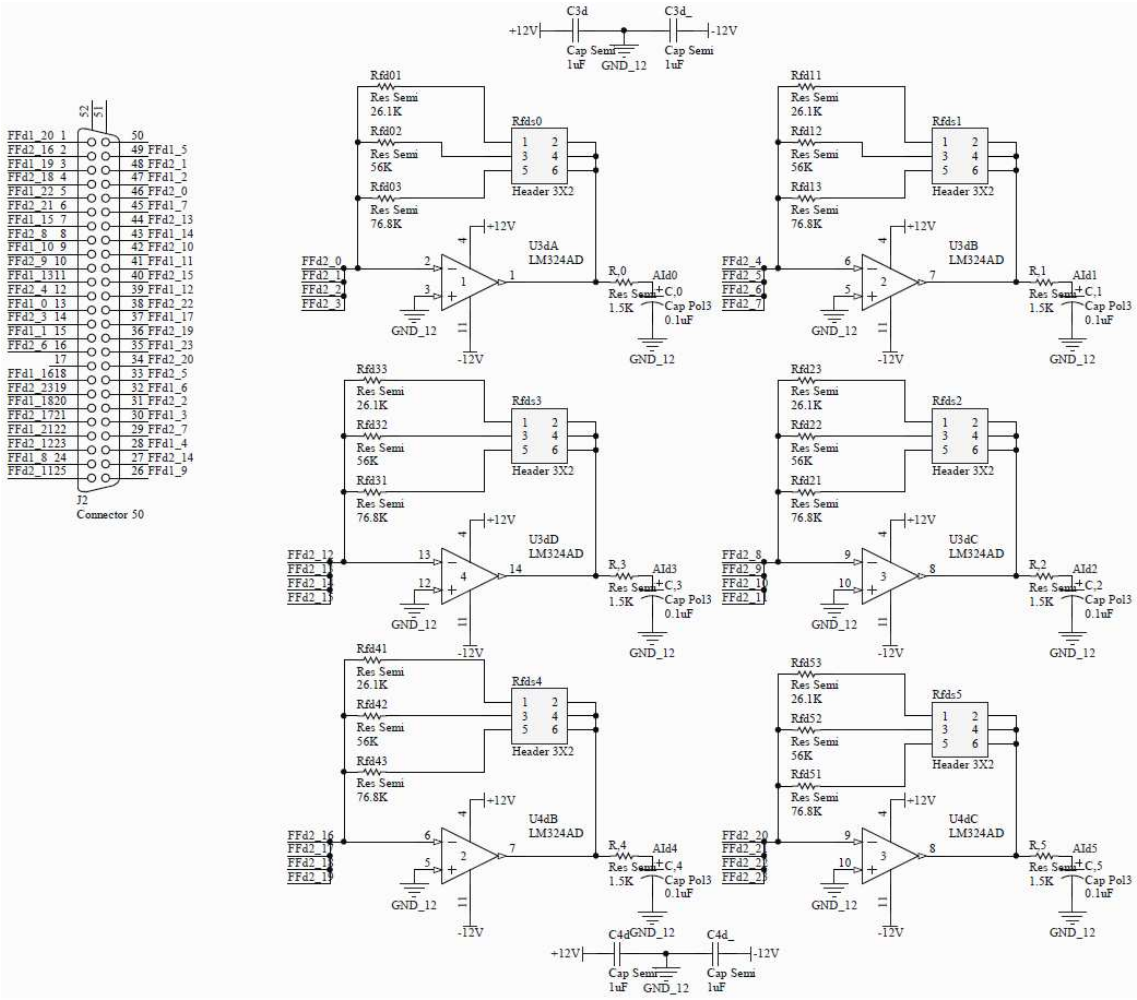

C.3 Stage of Serial Communication

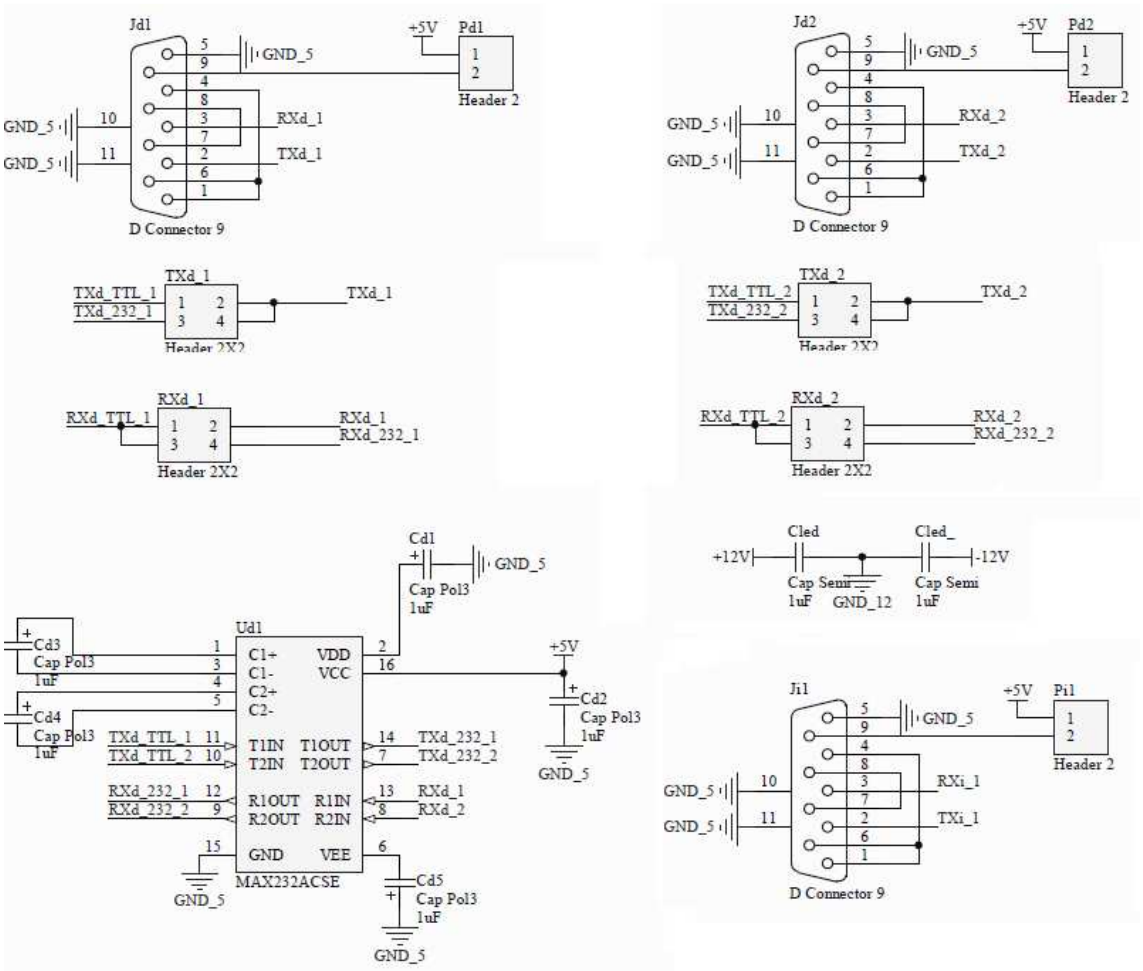

C.4 Pinout map of the SBRIO-9632 Platform

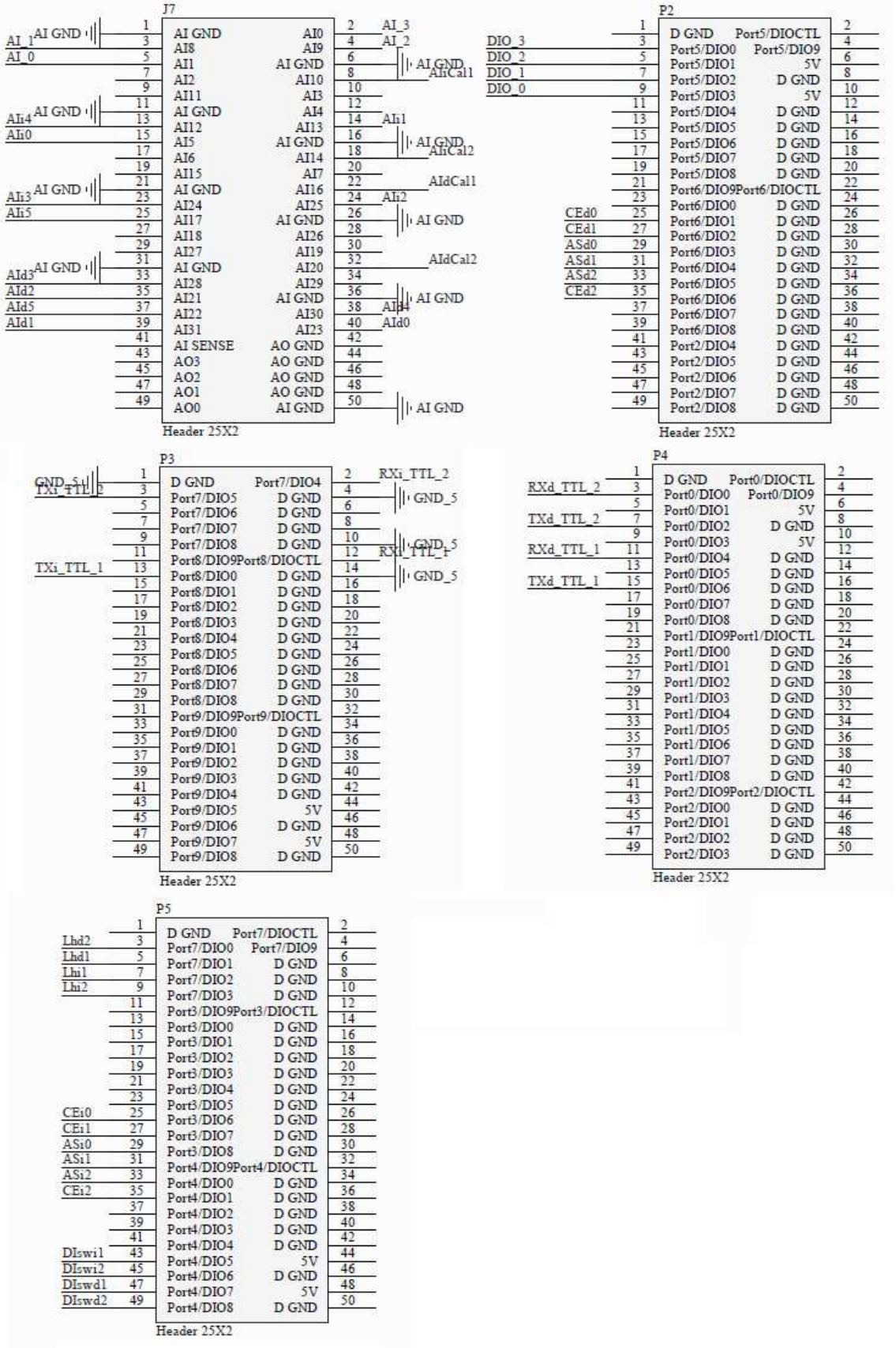

Resumen en Castellano

Resumen

Esta memoria de tesis presenta una interfaz basada en guantes de datos para el control de impedancia en manipuladores robóticos. La interfaz comprende un guante de datos comercial para medir la posición de los dedos, una Unidad de Medidas Inerciales (UMI) para medir la orientación de la mano en el espacio y por último, un total de 11 sensores piezoresistivos encargados de medir la fuerza aplicada por el operador. El banco de pruebas de la interfaz incluyó un manipulador de 6 GDL dotado de una celda de carga instalada cerca de su elemento final. El desempeño de la interfaz se evaluó inicialmente mediante pruebas estáticas, en la cuales las lecturas de fuerza de la celda de carga fueron usadas como referencia. La prueba final de la interfaz comprendió la implementación de un algoritmo de control de impedancia, en el cual las lecturas de fuerza arrojadas por la interfaz fueron usadas para controlar el movimiento del manipulador.

Adicionalmente esta memoria de tesis abarca el modelado del sensor piezoresistivo FlexiForce modelo A201-100. El sensor, usado en la interfaz basada en guantes de datos, fue ampliamente caracterizado en condiciones de excitación de Corriente Continua (CC) y Alterna (CA) bajo múltiples fuerzas y empleando diferentes concentradores de fuerza con diferentes áreas. Se encontraron tres nuevas propiedades que amplían las capacidades del sensor y mejoran su desempeño. La primera mejora abarca el estudio de la no linealidad de amplitud bajo condiciones de excitación inferiores a **1 V**. El estudio detallado de la no linealidad de amplitud, también conocida como no linealidad resistiva, permitió formular un método para estimar la sensibilidad del sensor bajo condiciones de excitación inferiores a **1 V**. La segunda mejora abarca el descubrimiento y uso de la propiedad piezocapacitiva para disminuir el error de estimación de fuerza y por último, se demostró que mediante una estimación que abarque lecturas de capacitancia y conductancia es posible estimar tanto la fuerza aplicada como el área de esfuerzo.

Capítulo 1

1. Introducción: Descripción de las bases teóricas sobre percepción háptica y manipulación de objetos

La identificación y manipulación de objetos mediante la exploración táctil es una actividad cotidiana para los seres humanos. Girar el picaporte de una puerta es una actividad recurrente, sin embargo complicada, que involucra la combinación de múltiples fuentes de información de los dominios visual, táctil y motriz. Tal destreza, casi exclusiva de los seres humanos, reside en su mayoría en la vista y en el sistema somatosensorial, los cuales en conjunto con el sistema nervioso central generan las trayectorias adecuadas para la mano y los dedos. Las tareas de aproximación al picaporte de la puerta y su posterior apertura, son los temas de estudio a ser discutidos en este Capítulo con el objetivo de entender y posteriormente emular las destrezas humanas en robots *bioinspirados*.

1.1 La importancia de las mediciones de fuerza en los estudios de manipulación manual

La mano humana es un miembro completo con un total de 27 Grados De Libertad (GDL) [108]. Esta provee a los humanos con una gran variedad de agarres que pueden ser clasificados en 4 grandes categorías: agarres de potencia, intermedio, precisión y agarre sin dedo pulgar [83]. La habilidad de la mano humana es bastante elevada si se compara con el resto de las especies, especialmente por su capacidad de oponer completamente el pulgar con el resto de los dedos [21]. Análogamente, algunos primates como los chimpancés y orangutanes son capaces de *oponer parcialmente* sus pulgares con el resto de los dedos, lo que les permite utilizar sofisticadas herramientas [114]. La restricción de *oposición parcial* del pulgar implica que el contacto yema con yema entre el pulgar y el resto de los dedos no es posible, no obstante, los primates poseen relevantes habilidades de manipulación de objetos si se comparan con otras especies de mamíferos. Estas habilidades están aún lejos de ser conseguidas en manos robóticas, por consiguiente, se ha puesto un gran esfuerzo en monitorear y entender los patrones de agarre de humanos y primates con el objetivo de emular sus destrezas.

Existen dos propiedades básicas que una mano *cibernética* debe poseer: un conjunto adecuado de sensores y actuadores diseñados en función de la tarea a efectuar y la habilidad para analizar los datos generados por el conjunto de sensores de forma óptima y poder generar así trayectorias adecuas de movimiento.

Si se desean obtener niveles de destreza similares a los de una mano humana, debe procurarse que las manos cibernéticas estén provistas con sistemas de sensores *bioinspirados*. Esta tarea resulta, a día de hoy, muy complicada, porque los sensores son típicamente voluminosos, costosos e incapaces de medir ciertas propiedades de los objetos, tales como su rigidez, temperatura y si éstos poseen bordes cortantes o no. De

igual forma, los músculos de la mano poseen densidades de potencia que aún no son capaces de ser emulados por los servomotores más avanzados. Esta condición conlleva que, en muchas ocasiones, las manos cibernéticas sean *subactuadas*, con el fin de ahorrar espacio, o en su defecto que los servomotores no sean colocados en las estructura interna de la mano cibernética. En cualquier caso, el movimiento de los dedos en manos cibernéticas es torpe si se compara con el observado en una mano real, incluso para la *shadow hand* [158], que es sin duda alguna el desarrollo más realista de mano cibernética jamás realizado con un total de 24 GDL.

El desarrollo de algoritmos flexibles y adaptativos para el control de manos cibernéticas es, a día de hoy, un campo activo de investigación en robótica. Algunas técnicas tales como Modelos Ocultos de Markov (*Hiden-Markov models)* y redes neuronales son a menudos usadas para emular comportamientos humanos en manos cibernéticas [1]. La capacidad de operar en ambientes poco estructurados y de manipular objetos que cambian continuamente de forma es el factor clave a tomar en cuenta en el desarrollo de algoritmos de control. Sin embargo, hay un largo camino por recorrer para conseguir el nivel de destreza de una mano humana. La falta de destreza en los desarrollos cibernéticos actuales no radica exclusivamente en los algoritmos de control de movimiento para la mano y los dedos; el sistema somatosensorial juega también un papel importante en dicha tarea, dado que, tal como se mencionó previamente, los sistemas somatosensores de las manos cibernéticas no son aún capaces de medir ciertas propiedades de los objetos, por consiguiente, los algoritmos de control de movimiento generan trayectorias utilizando información incompleta o impresa sobre el objeto.

1.2 Emulando la percepción háptica en desarrollos robóticos: Una tarea desafiante para la tecnología de punta en sensores de fuerza.

El proceso de reconocimiento de objetos a través de la exploración táctil es conocido como *percepción háptica*. Esta habilidad es posible en los humanos gracias a los propioceptores y receptores kinestésicos. Los propioceptores y los sensores kinestésicos son también responsables de una gran variedad de habilidades humanas, tales como: sentido del equilibrio, habilidades de ubicación espacial de miembros del cuerpo, así como la habilidad para detectar si algún miembro del cuerpo se ha desplazado o no.

Las personas pueden detectar rápida y precisamente objetos tridimensionales a través del tacto. Esta asombrosa capacidad combina dos procesos: *percepción propioceptiva* (relativa a la posición de manos y dedos) y la *percepción somatosensora de patrones* (relativa a la textura, bordes y curvatura de los objetos). La piel humana juega un papel clave en la percepción somatosensora de patrones dado que los *mecanoreceptores* y *nociceptores* se encuentran en la piel; dichos receptores son responsables de las mediciones de presión y dolor respectivamente.

Una piel cibernética bioinspirada debería ser capaz, al menos, de poder medir las mismas propiedades que una mano humana es capaz de hacer. Carrozza y Lamy han presentado soluciones parciales para dicho problema, empleando para tal fin galgas extensiométricas y sensores de tipo piezoresistivo [16, 100]. Las soluciones de Carrozza

y Lamy resuelven parcialmente el problema porque son capaces únicamente de medir contacto y fuerza. Sin embargo, mediante un adecuado algoritmo de control que incorpore la información somatosensora, se puede conseguir mejoras importantes en la destreza de las manos cibernéticas en términos de nuevas habilidades, tales como: detección de deslizamiento del objeto, agarres de precisión y detección de haber levantado el objeto de su posición de reposo [16].

De igual forma, las pieles cibernéticas bioinspiradas pueden ayudar a mejorar las condiciones de seguridad en ambientes cooperativos de robots y humanos mediante la detección de colisiones accidentales que ocurren durante tareas de comanipulación [100]. La seguridad constituye una condición fundamental en el campo de los Robots Colaborativos (Cobots) [98]. En un ambiente de cooperación humano-robot, ambos se encuentran compartiendo el mismo espacio de trabajo y por tanto interactúan físicamente. La comanipulación es usada frecuentemente para combinar las mejores prestaciones de los humanos, tales como:

- Excepcional sistema sensorial.
- Habilidad para aprender tareas complejas.
- Adaptabilidad a ambientes cambiantes y desestructurados.

Con los beneficios ofrecidos por los robots:

- Precisión y fuerza en el movimiento, sin incurrir en fatiga después de horas de incesante trabajo.
- Capacidad para repetir trayectorias sin aburrirse, esto resulta de gran importancia cuando se realizan tareas repetitivas que requieren de mucha precisión.

No obstante, las ventajas de humanos y robots deben combinarse en un marco de trabajo que garantice el confort y la seguridad para el operador. Por consiguiente, resulta natural que las variables de fuerza y velocidad sean continuamente monitoreados y controlados en los ambientes cooperativos humano-robot. Este planteamiento introduce el concepto de *control de impedancia de robots*, que ha sido sin lugar a dudas, un área de investigación relevante a lo largo de las últimas décadas.

Los codificadores ópticos (*encoders)*, celdas de carga y acelerómetros han sido utilizados ampliamente en aplicaciones de control de impedancia como parte del sistema de realimentación fuerza/posición. Una revisión exhaustiva de la literatura sobre control de impedancia muestra que los sensores de fuerza han sido instalados tradicionalmente cerca del elemento final del robot, mientras que los sensores de posición y velocidad se instalan típicamente en las articulaciones del mismo. Sin embargo, esta disposición de los sensores no garantiza siempre la seguridad del operario porque, tal como se mencionó previamente, pueden ocurrir colisiones accidentales durante tareas de comanipulación. Debe señalarse que el control de impedancia es únicamente efectivo en torno al elemento final del robot, y no en torno a la estructura completa del manipulador; por tal motivo, las colisiones que ocurran entre el operador y la estructura del robot no serán detectadas por el sistema de control pudiendo infligirse daños al operario.

Las pieles cibernéticas bioinspiradas son una solución prometedora en aras de garantizar la seguridad en los ambientes cooperativos humano-robot, debido a que

éstas son capaces de detectar colisiones indeseadas con la estructura del robot durante las tareas de comanipulación. Sin embargo, no se ha desarrollado aún una aplicación de control en la cual la única fuente de realimentación de fuerza se realice a través de una piel cibernética bioinspirada. Para ilustrar esto, se pone como ejemplo el caso hipotético en el cual *un voluntario mudo guía a una persona ciega a cruzar la calle cogiendo el voluntario mudo el brazo del sujeto ciego*. Bajo tal escenario de ausencia de realimentación visual y auditiva, el ciego responde a los comandos de fuerza de manera flexible (*compliant response)* basando su respuesta motora únicamente en los estímulos de los mecanoreceptores de su piel, de igual forma, un robot debería responder a las fuerzas aplicadas sobre su estructura por un operador.

Es normal que ocurran colisiones espontáneas entre el voluntario mudo y la persona ciega durante el proceso de guiado. No obstante, éstas no representan un riesgo serio para ninguno de los dos debido al sofisticado sistema propioceptivo de ambos sujetos y a su inteligencia que los hace capaces de sortear eventos inesperados. Por consiguiente, es lógico que buena parte de los actuales desarrollos en robótica se enfoquen en proveer a los robots con las dos propiedades anteriormente descritas (sofisticado sistema propioceptivo e inteligencia); esta condición es la motivación principal para la escritura de esta memoria de tesis.

1.3 Declaración de Intenciones

Esta memoria de tesis aborda dos problemas que surgen de la interacción de humanos y robots en ambientes cooperativos de trabajo. Por consiguiente, se plantean dos objetivos como alternativas para superar estas restricciones.

El primer problema es la falta de un modelo detallado para la mayoría de los sensores usados en pieles cibernéticas disponibles. Esta condición es uno de los aspectos clave para el bajo rendimiento de estos dispositivos y su consecuente subutilización en aplicaciones robóticas. Los sensores usados en pieles cibernéticas son en su mayoría de tipo piezoresistivo, lo que significa que fuerzas incrementales producen cambios proporcionales en su conductancia.

El primer objetivo de la presente investigación es mejorar el rendimiento de los sensores piezoresistivos mediante el desarrollo de un modelo capaz de predecir el comportamiento del sensor bajo condiciones de excitación de Corriente Continua (CC) y Corriente Alterna (CA). La caracterización de los sensores es meramente empírica, y se presenta en términos de conductancia y capacitancia. El sensor de fuerza elegido para la investigación es el *A201-100 FlexiForce*, fabricado por Tekscan Inc, con un rango nominal de fuerza **440 N** y un área de sensado de **71 mm^2** (similar al tamaño de una moneda de 1 céntimo de Euro).

El segundo problema es el uso exclusivo de sensores piezoresistivos en una aplicación de control de impedancia que involucre a un manipulador y a un operario. Este desarrollo es un reto dentro de la línea de investigación de los espacio cooperativos de trabajo humano-robot, especialmente si se desea que la respuesta del manipulador sea similar a la exhibida por un humano ante fuerzas externas.

El segundo objetivo es implementar un esquema de control de impedancia en un manipulador utilizando sensores piezoresistivos como la única fuente de

realimentación para el bucle de control. La aplicación desarrollada utiliza control de impedancia como algoritmo subyacente para el control de movimiento del robot. Sin embargo, existe una diferencia importante con el enfoque de pieles cibernéticas bioinspiradas. En lugar de colocar los sensores de fuerza a lo largo de la estructura del robot, el operador lleva un dispositivo en su mano derecha con los sensores piezoresistivos integrados en la zona palmar de un guante de datos (*dataglove*) de 15 GDL. Adicionalmente, una unidad de medidas inerciales (UMI) se integra en la zona dorsal del guante de datos para medir la orientación de la mano dentro del área de trabajo.

La propuesta de interfaz de guantes de datos es capaz de medir las contribuciones individuales de fuerza a través de una combinación de la posición de los dedos, los sensores de fuerza y la orientación de la mano. Después se calcula un vector de fuerza resultante y se consigue así un movimiento coordinado del manipulador. El vector fuerza, estimado por la interfaz, representa la intención del operador, así como una piel cibernética bioinspirada mediría las fuerzas aplicadas por un operador sobre la estructura del manipulador.

1.4 Resumen de los Capítulos restantes

El Capítulo 2 revisa el estado de la técnica en las tecnologías de medición de fuerza. Se presenta un análisis comparativo de los pros y contras ofrecidos por cada tecnología, con especial atención a las técnicas de medición de fuerza no invasivos. Se presenta una revisión profunda del sensor A201-100 con ejemplos representativos de aplicaciones industriales y de investigación.

En el Capítulo 3 las capacidades del sensor A201-100 son exploradas mediante la realización de una serie de pruebas empíricas. Asimismo, se presenta un modelo eléctrico para el sensor obtenido a través de resultados empíricos y de técnicas de ajuste de curvas. Posteriormente, se demuestra la utilidad de dicho modelo para mejorar las prestaciones del dispositivo, ya que al realizar mediciones de conductancia y capacitancia sobre el sensor se logra disminuir el error cuadrático medio a la mitad. De igual forma, se formula un método para estimar la sensibilidad del sensor bajo condiciones específicas de alimentación.

La capacidad para determinar el área de esfuerzo es una nueva propiedad encontrada en el dispositivo, ésta implica que el sensor A201-100 no sólo es capaz de medir la fuerza aplicada, sino que también es capaz de estimar el área donde se aplica la fuerza, es decir, el área de esfuerzo.

En el capítulo 4 se presenta una revisión de los desarrollos más importante en el campo de los Dispositivos Inteligentes de Ayuda a la Manipulación, DIAM. Se abordan los modos de funcionamiento y los algoritmos de control para los DIAM. Posteriormente se analizan implementaciones pasivas y activas de DIAM y se les comparan desde los puntos de vista de seguridad y flexibilidad. El concepto de no colocación de sensores y actuadores es analizado a la luz de las complicaciones que surgen bajo tal condición. Por último, se discuten algunas soluciones para los problemas de inestabilidad derivados de la condición de no colocación de sensores y actuadores.

Una descripción detallada de la interfaz de guantes de datos se presenta en el Capítulo 5. Se muestran los resultados de pruebas estáticas y dinámicas aplicadas al sensor con el fin de demostrar la viabilidad de la interfaz para operar en un entorno cooperativo humano-robot. El banco de pruebas para la realización de las pruebas de validación y rendimiento abarca un manipulador de 6 GDL y una celda de carga. La celda de carga de 6 GDL se encuentra instalada convenientemente en las cercanías del elemento final del manipulador.

En el Capítulo 6 se presentan pruebas adicionales en las que la interfaz basada en guantes de datos es utilizada en conjunto con el manipulador de 6 GDL para mover una carga. Se muestran allí secuencias de imágenes que exhiben el modo de interacción entre el manipulador, el operario y la interfaz. Finalmente, el Capítulo 7 presenta las conclusiones y posibles trabajos futuros con especial énfasis al uso de las técnicas presentadas en esta memoria de tesis.

Capítulo 7

7. Conclusiones, aportaciones y trabajo futuro

Este Capítulo resume los hechos más destacados y los resultados presentados en esta memoria de tesis. También se presenta algunas ideas para posibles mejoras y futuros desarrollos con respecto a las contribuciones presentadas en esta memoria. Dado que esta tesis tiene dos enfoques diferenciados, pero altamente relacionados, las conclusiones y los posibles trabajos futuros se presentan por separado para cada tópico.

7.1 Conclusiones relacionadas con el modelado del sensor piezoresistive FlexiForce A201-100

Un modelo eléctrico equivalente es presentado y validado para el sensor FlexiForce modelo A201-100, con algunas restricciones. Un amplificador operacional, en la configuración inversora, se utilizó a lo largo de todos los ensayos descritos en este documento de acuerdo con las recomendaciones dadas por el fabricante del dispositivo.

7.1.1 Modelado del sensor e identificación de no linealidades

El mejor modelo equivalente encontrado para el sensor FlexiForce A201-100 es el de Resistencia-Condensador (RC) en paralelo, no obstante, algunas no linealidades se encontraron en la respuesta del sensor que restringen el uso extensivo del modelo equivalente propuesto. Específicamente, se encontraron dos tipos de no linealidades:

No linealidad de Frecuencia: El modelo RC paralelo resultó ser el más acertado para el sensor FlexiForce A201-100 hasta que se alcanza una determinada frecuencia en la señal de excitación, dicho umbral ha sido convenientemente denominado como *frecuencia de divergencia*. Para señales de excitación por encima de la frecuencia de divergencia, se observó saturación en la salida del sensor y un corrimiento de fase fijo e independiente de incrementos en la frecuencia de la señal de entrada. Se observaron ligeros cambios en la magnitud de la frecuencia de divergencia de un dispositivo a otro, no obstante existe poca correlación entre la magnitud de la fuerza aplicada y la frecuencia de divergencia. Esto implica que la frecuencia de divergencia es una propiedad característica de cada dispositivo que poca relación tiene con la magnitud de la fuerza aplicada. Se puede concluir que con el fin de garantizar el funcionamiento del sensor dentro de su región lineal, la frecuencia de la señal de excitación debe mantenerse por debajo de **4 KHz**.

No linealidad de amplitud: Esta fue sin duda alguna la condición de no linealidad más difícil de detectar y modelar en el sensor FlexiForce, debido a que ésta no produce ni saturación, ni crecimiento exponencial a la salida del circuito amplificador. El concepto de no linealidad de amplitud implica que la resistencia del sensor exhibe un

comportamiento no lineal, esto es así porque la resistencia del sensor es directamente responsable de la tensión de salida bajo condiciones de excitación de Corriente Continua CC.

La no linealidad de amplitud es del tipo tangente hiperbólica **(tanh)**, lo que quiere decir que las tensiones de salida y de entrada están relacionadas mediante la función **tanh**. Sin embargo y siguiendo el mismo patrón observado en la no linealidad de frecuencia, el modelo **tanh** no es exhaustivo y es capaz únicamente de predecir la respuesta del sensor para amplitudes de la señal de excitación inferiores a **1 V**. Para excitaciones superiores a **1 V**, no se encontró una función matemática adecuada capaz de predecir la respuesta del sensor.

7.1.2 Región de operación lineal del sensor FlexiForce

Una vez que las no linealidades antes mencionadas se delimitaron, fue posible definir una región lineal de funcionamiento para el sensor. Esta es una de las aportaciones del presente trabajo que podría ayudar a otros a seguir investigando en la comprensión de los sensores piezoresistivos. Por tanto, con el fin de operar al sensor FlexiForce dentro de su región lineal, la tensión de CC debe mantenerse constante mientras la fuerza es medida. Esta sentencia no añade ningún conocimiento a la información ya facilitada por el fabricante. Sin embargo, recordando que la no linealidad de amplitud se puede modelar cuando la tensión de suministro se mantiene por debajo de **1 V**, se demostró que es posible predecir los cambios en la sensibilidad del sensor producidos por los cambios en la tensión de excitación utilizando el modelo **tanh**; esto permite obtener una estimación precisa de la fuerza aplicada bien sea que la tensión de excitación se mantenga o no constante durante el proceso de estimación de fuerza.

Cambiar la tensión de excitación es una de las dos formas posibles para ajustar la sensibilidad del sensor a un rango deseado. La segunda forma es cambiar el valor de la resistencia de realimentación en el circuito de acondicionamiento.

Para aquellos casos en los cuales la tensión de excitación es llevado fuera del rango **(-1 V, 1 V),** no se ha encontrado un modelo capaz de predecir y por tanto corregir el efecto causado por la no linealidad en el dispositivo, por tanto, la única forma de operar al sensor bajo tal condición es la de mantener la tensión de entrada constante mientras la fuerza es medida.

En aquellos casos que se utilice el sensor con excitación de CA, la frecuencia de la señal de excitación debe mantenerse por debajo de los **4 KHz** con el fin de operar al sensor dentro de su región lineal. Debe recordarse que los efectos de la no linealidad de amplitud son también observables bajo excitación CA y por tanto la amplitud de la señal de CA se mantuvo, en las primeras pruebas, por debajo de **1 V**. No obstante, se presentó un método para sobrepasar los efectos causados por la no linealidad de amplitud bajo condiciones de excitación de CA. El método propuesto permite el desacople entre la conductancia no lineal y la capacitancia lineal, el desacople se realiza con independencia de la magnitud de la tensión aplicada. Dicho método es otra de las principales aportaciones descritas en la memoria de tesis.

7.1.3 Respuesta piezocapacitiva y reducción en el error de estimación de fuerza

Al realizar pruebas bajo excitación de CA se encontró que el sensor FlexiForce A201-100 exhibe una respuesta *piezocapacitiva*. Esto constituye un hecho relevante y novedoso y es sin duda alguna, otra de las contribuciones principales de la presente investigación. La propiedad piezocapacitiva demostró ser una herramienta poderosa en aras de aumentar la precisión del dispositivo; esto fue posible gracias a la estimación de fuerza usando modelos combinados de resistencia y capacitancia. La reducción del error de estimación de fuerza es de gran importancia para el uso extensivo de sensores piezoresistivos en aplicaciones robóticas, las cuales requieren mediciones de fuerza precisas y no invasivas.

Se presentaron tres modelos de estimación de fuerza bajo el esquema combinado resistencia-capacitancia. El modelo tradicional de conductancia, propuesto por el fabricante, fue también implementado para servir de patrón de comparación. Los resultados arrojaron una reducción promedio del error de un **64%** cuando se compara con el modelo tradicional de conductancia. El error cuadrático medio fue el patrón de comparación empleado para evaluar los diferentes métodos usados.

Las mediciones de capacitancia fueron realizadas por un método de desacople entre la conductancia no lineal y la capacitancia lineal. Para tal fin, la señal de salida del circuito de acondicionamiento se multiplica, en el tiempo, por una función coseno que es entonces filtrada paso bajo para producir una señal de CC que sólo depende de la capacitancia del sensor. Este método fue anteriormente declarado como una de las aportaciones de esta memoria de tesis. Sin embargo y a pesar de todo el esfuerzo realizado para mejorar la precisión del sensor, todavía hay un largo camino por recorrer para que los sensores piezoresistivos de polímeros exhiban niveles de precisión similares a las celdas de carga.

7.1.4 Estimación conjunta del área de esfuerzo y de la fuerza aplicada

Se demostró que es posible la estimación conjunta del área de esfuerzo y de la fuerza aplicada. Para tal fin se realizó una caracterización del sensor que involucró diferentes tamaños de concentradores de fuerza (*pucks*), mientras que a la par, se midió la conductancia y la capacitancia del sensor. Con los datos recolectados, fue posible formular un sistema de ecuaciones capaz de relacionar la fuerza aplicada y el área de esfuerzo con las variaciones conductancia y capacitancia, permitiendo así una estimación conjunta del área de esfuerzo y de la fuerza aplicada. Este desarrollo constituye otra de las contribuciones principales de la presente investigación.

7.2 Posibles trabajos futuros relacionados con el modelado del sensor FlexiForce A201-100

Dentro del campo de sensores piezoresistivos, hay múltiples caminos a seguir en futuras investigaciones. Se abordan a continuación sólo algunas de las posibles líneas de investigación relacionadas con los aportes presentados en este documento. Sin embargo, un abanico más amplio de posibles investigaciones fue presentado por Liu

[107], con especial énfasis en los nuevos polímeros para la fabricación de sensores piezoresistivos.

Con el fin de seguir con las líneas de investigación resumidas en la Sección 7.1, debe primero modelarse la no linealidad de amplitud del sensor A201-100 para tensiones de entrada superiores a **1 V**. Esta es probablemente la tarea más lógica de realizar en el corto plazo, ya que la no linealidad de amplitud sólo se estudió para tensiones de entrada inferiores a **1 V**. Un modelo exhaustivo y sin restricciones en la tensión de excitación es necesario por múltiples razones, tales como, conseguir que múltiples sensores posean una determinada sensibilidad; esto es especialmente cierto para desarrollos que involucren el uso de varios sensores a la vez. Otro de los posibles desarrollos relacionados con la obtención de un modelo exhaustivo puede incluir la inclusión de parámetros como la deriva térmica (*thermal drift*).

Un modelado exhaustivo de la no linealidad de amplitud, sin restricciones de amplitud, permitiría también demostrar, desde un enfoque teórico, la validez del esquema de medición presentado en la Sección 3.3.3. Debe recordarse que dicho método es capaz de sobrepasar el comportamiento no lineal de la conductancia del sensor. Esto resulta de gran importancia porque una demostración parcial de su validez fue presentada pero con la restricción de $\mathbf{|V_s| < 1\ V}$.

En esta memoria de tesis se han presentado una gran cantidad de datos empíricos y teóricos que apoyan el uso de variaciones de capacitancia como una manera eficaz de reducir el error de estimación de fuerza. Tal como se mencionó previamente, se presentó un método para leer la capacitancia del sensor mediante un método que permite sobrepasar la no linealidad de amplitud. Existen dos enfoques diferentes para futuras investigaciones en el área.

El primero consiste en mejorar las prestaciones del dispositivo, el segundo se basa en ampliar el abanico de funcionalidades que éstos pueden proporcionar, como por ejemplo, realizar una estimación combinada del área de esfuerzo y de la fuerza aplicada. Esta propiedad ya fue presentada en esta memoria, pero existen muchas otras posibilidades tales como: desarrollo de un modelo térmico para el sensor que pueda añadir la variable de deriva térmica a los cambios de sensibilidad del sensor. También es posible ahondar esfuerzos en aras de reducir el error de estimación de fuerza mediante nuevos modelos multivariable que combinen lecturas de conductancia y capacitancia.

Se presentó una estimación combinada de la fuerza aplicada y el área de esfuerzo. Sin embargo, no se ofrecieron resultados con respecto a la exactitud de estos métodos dado que no se recogieron suficientes datos experimentales. Posteriores investigaciones podrían tomar como punto de inicio el marco de desarrollo presentado en esta memoria de tesis para la estimación combinada de ambas variables, el marco de desarrollo incluye el conjunto de concentradores de fuerza con diferentes áreas, el banco de pruebas y el sistema de ecuaciones propuesto. La estimación combinada de fuerza y área es probablemente el reto más desafiante dentro del campo de mediciones piezorresistivos, ya que exige un conocimiento completo de las variaciones resistivas y capacitivas en función de la fuerza aplicada.

La formulación de un modelo unificador que abarque la zona de esfuerzo, la fuerza aplicada y la temperatura bajo una amplia gama de tensiones eléctricas es quizás la tarea más desafiante de realizar. El modelo unificador debe ser capaz de predecir los cambios de capacitancia y conductancia de las cuatro variables mencionadas. Esto podría poner a disposición una amplia gama de capacidades para el sensor y darle un uso más amplio en aplicaciones robóticas. Sin embargo, no se pueda afirmar que dicho modelo sea posible de formularse porque la relación entre la temperatura, la capacitancia y la conductancia no se ha explorado aún.

Por último, debe recordarse que el modelo y los métodos presentados en el Capítulo 3 de esta memoria de tesis han sido desarrollados para el sensor FlexiForce A201-100. No obstante, existen múltiples fabricantes de sensores piezoresistivos tal como se reportó en el Capítulo 4 de esta memoria. Un estudio más amplio podría abarcar la aplicación de las técnicas descritas en el Capítulo 3 al sensor *Interlink* o bien a cualquier otro dispositivo de medición de fuerza que funcione bajo el principio piezoresistivo.

7.3 Conclusiones relacionadas con la interfaz de guantes de datos para el control de impedancia en manipuladores industriales.

La interfaz basada de guantes de datos demostró ser una solución válida para determinar la fuerza aplicada por un operario durante tareas de manipulación de objetos. Se pueden encontrar múltiples aplicaciones para la interfaz, esta memoria de tesis sólo se ha enfocado en presentar una de ellas, la relacionada con el control de impedancia de manipuladores robóticos.

7.3.1 Resumen de funcionamiento de la interfaz

La interfaz basada en guantes de datos es un desarrollo multi-sensor capaz de medir las fuerzas aplicadas por el operador durante tareas de manipulación de objetos, esto es posible gracias a los 11 sensores piezoresistivos instalados en su zona palmar. La posición instantánea de los dedos se mide a través de un guante de datos comercial modelo X-IST con una resolución de 15 GDL. Por último, la orientación de la mano dentro del campo de trabajo se mide a través de una Unidad de Medidas Inerciales (UMI), la cual posee compensación con respecto al campo magnético de la tierra. La UMI ha sido convenientemente ubicada en la zona dorsal del guante de datos para garantizar el confort al operario.

La distribución de los sensores piezoresistivos a lo largo de la zona palmar del guante de datos se basó en estudios previos de agarre en manos humanas y en el tamaño de la carga del robot. Se realizó un compromiso entre el tamaño de la carga y la distribución óptima de los sensores con el objetivo de maximizar la comodidad del usuario, manteniendo el número de sensores bajo mínimos. Dadas las características voluminosas de la carga, se eligieron las siguientes configuraciones de agarre para realizar las tareas de manipulación de objetos: *Surrounding Mild Flexion (SMF)* y *Parallel Mild Flexion (PMF)* [83].

Mediante la combinación de la información suministrada por los múltiples sensores, fue posible estimar, en tiempo real, las fuerzas aplicadas por la mano del operador, mientras que éste realizaba las tareas de manipulación sobre el elemento final del

robot o sobre la propia carga. Las fuerzas aplicadas por el operador se asumen como su intención de movimiento y por tanto, son usadas como entradas por el control de impedancia para realizar movimientos coordinados en el manipulador de 6 GDL. Sin embargo, para esta versión de la interfaz, el movimiento del manipulador sólo fue posible bajo movimientos en 3 D **(x-y-z)**.

La interfaz de control de guantes de datos está basada en el concepto de manos en la carga, *hands-on-payload*, el cual declara que las interfaces de usuario de los Dispositivos Inteligentes de Ayuda a la Manipulación, DIAM, deben ser lo más natural posible, y por tanto, las interfaces de usuario basadas en botones y palancas deben reemplazarse con interfaces en las cuales el operario tenga contacto directo y natural con el manipulador. Las pruebas realizadas sobre la interfaz basada en guantes de datos demostraron su eficiencia para operar bajo el principio de *hands-on-payload*.

Debe recordarse que para realizar movimientos en el manipulador se requirió sólo de la información proveniente de la interfaz de guantes de datos y de la cinemática del robot. En ningún caso fue necesario contar con la información del modelo dinámico del manipulador. Esta es sin duda la ventaja más importante que brinda dicha interfaz, ya que la formulación del modelo dinámico puede ahorrarse y esto resulto de gran utilidad dada la complejidad intrínseca asociada a la formulación y solución de dicho modelo en tiempo real.

Cuando se desea controlar el movimiento de un manipulador bajo el concepto de *hands-on-payload,* es común instalar una celda de carga cerca del elemento final del manipulador para recoger las fuerzas aplicadas por el operador. Sin embargo, es necesaria la formulación de un modelo dinámico para discriminar entre las fuerzas aplicadas por el operario y las propias fuerzas generadas por el robot durante el movimiento. La interfaz basada en guantes de datos evita la formulación de dicho modelo dado que las fuerzas aplicadas por el operario son directamente medidas por los sensores de fuerza instalados en la zona palmar del guante. Dado que el guante y el manipulador se encuentran dinámicamente desacoplados, las propias fuerzas del robot (Inercia y Coriolis) no afectan las lecturas de fuerza realizadas por la interfaz de guantes de datos, y por consiguiente, sus lecturas pueden usarse como entradas al algoritmo de control de impedancia que gobierna el movimiento del manipulador. Esta es, sin duda alguna, la ventaja comparativa más importante que provee dicha interfaz.

7.3.2 Resumen de las pruebas realizadas sobre la interfaz basada en guantes de datos

Las lecturas de fuerza adquiridas desde la interfaz de guantes de datos se compararon con las mediciones de fuerza recogidas por un sensor JR3 instalado cerca del elemento final de un manipulador de 6 GDL. El sensor JR3 es una celda de carga de varios ejes capaz de recoger las fuerzas y momentos sobre todos los ejes con una precisión notable debido a su tecnología basada en galgas extensiométricas. Teniendo en cuenta que las lecturas de fuerza provenientes del sensor JR3 se ven afectadas por las fuerzas propias fuerzas del robot, se realizaron dos tipos de pruebas.

En primera instancia, se llevó a cabo una prueba estática, sin movimiento, que involucró la comparación de las fuerzas estimadas por la interfaz de guantes de datos y los datos de fuerza recogidos por la celda de carga JR3. Se presentaron gráficos separadas para

cada eje y un gráfico de error, el cual se calculó restando las lecturas de fuerza del sensor JR3 y de la interfaz desarrollada. Tomando en cuenta que la prueba fue realizada de forma estática, las fuerzas inerciales no están presentes en las lecturas tomadas por el sensor JR3, y por tanto, la comparación presentada puede tomarse como objetiva. Un análisis minucioso de los resultados obtenidos permite afirmar que la interfaz basada en guantes de datos es capaz de estimar las fuerzas aplicadas por la mano del operador, sin embargo, se observan ciertas imprecisiones en cuanto a la magnitud y dirección de las lecturas de fuerza.

Una de las ventajas claves que puede concluirse de las pruebas estáticas es el hecho que la interfaz basada en guantes de datos es capaz de filtrar las vibraciones producidas por la flexibilidad del robot (*robot's compliance*). Para ilustrar esto, debe recordarse que después de que el operario dejara de aplicar fuerzas sobre el manipulador, éste siguió oscilando por un par de segundo debido a su estructura flexible. Este comportamiento oscilatorio afectó naturalmente a las lecturas de fuerza del sensor JR3, y por tanto, pudo observarse en los gráficos de fuerza un comportamiento oscilatorio justo después que el operario dejó de aplicar fuerzas sobre la carga. En cambio, las lecturas de fuerza estimadas mediante la interfaz de guantes de datos, mostraron una caída suave después de que el operador dejase de aplicar fuerza sobre la carga. Este comportamiento se debe a que la interfaz de guantes de datos y el manipulador están dinámicamente desacoplados.

El segundo tipo de pruebas aplicadas a la interfaz fueron de tipo dinámico, éstas involucraron el uso de las lecturas de fuerza obtenidas mediante la interfaz de guantes datos para el control de impedancia del manipulador de 6 GDL. Bajo este escenario, las lecturas de fuerza provenientes del sensor JR3 no pudieron utilizarse como referencia para comparar, ya que las fuerzas de inercia afectan las lecturas del JR3. Análogamente a los resultados obtenidos de las pruebas estáticas, los resultados de la prueba dinámica demostraron la factibilidad de uso de la interfaz de guantes de datos para operar bajo el esquema *hands-on-payload* al proveer de perfiles de fuerza suaves al algoritmo de control de impedancia, permitiendo así, movimientos coordinados en el manipulador robótico.

7.3.3 Uso interdisciplinario de la interfaz basada en guantes de datos

La interfaz basada en guantes de datos ha demostrado ser una herramienta adecuada para estimar la intención de movimiento de los humanos durante tareas de agarre y manipulación de objetos. Adicionalmente las pruebas presentadas en esta memoria de tesis demostraron la factibilidad de la interfaz para ser usada en un control de impedancia sobre un manipulador de 6 GDL. Ante todo, debe aclararse que las lecturas de fuerza arrojadas por la interfaz pueden usarse para controlar cualquier clase de manipulador robótico. En tal sentido, la única información requerida del manipulador es la concerniente a su cinemática, sin embargo no es necesario tener conocimiento sobre el modelo dinámico del robot. Esta particularidad, ofrecida por la interfaz de guantes de datos, es de gran utilidad para su fácil integración a cualquier robot.

La interfaz basada en guantes de datos encuentra también múltiples posibilidades dentro del campo de rehabilitación. Esto es así porque la información recopilada por la interfaz, posición de los dedos y la fuerza que éstos aplican, resulta de gran utilidad

para registrar progresos en procesos post-operatorios o sencillamente para evaluar el progreso después de sufrir alguna enfermedad en las manos.

Dentro del campo de investigaciones deportivas, la interfaz basada en guantes de datos puede usarse para recopilar información relativa a las fuerzas de agarre de instrumentos de deporte, tales como: palos de golf, raquetas de tenis o bolas. El registro de datos de fuerza en ambientes poco estructurados es posible mediante la interfaz debido a que ésta es portable y alimentada mediante baterías. Análogamente, el registro de datos de fuerza es de gran importancia en múltiples líneas de investigación que tienen como centro de estudio la mano humana y requieren de mediciones confiables y que ejerzan poca o ninguna interferencia con la actividad que se intenta monitorear. Nótese que esta afirmación es consistente con las hechas previamente al resumir los resultados de la investigación sobre el sensor FlexiForce A201-100.

7.4 Posibles trabajos futuros relacionados con la interfaz basada en guantes de datos

Existen múltiples aproximaciones para futuros desarrollos relacionados con la interfaz de guantes de datos, a continuación se describen algunos de ellos:

7.4.1 Experimentación con diferentes configuraciones digitales

Las pruebas presentadas en esta memoria de tesis fueron realizadas usando los agarres *Surrounding Mild Flexion (SMF)* y *Parallel Mild Flexion (PMF)*. Estos agarres fueron los más adecuados para la carga voluminosa que colgaba del elemento final del manipulador. Con el fin de realizar una verificación exhaustiva de la interfaz, es necesario cambiar la carga actual por una menos voluminosa y posteriormente probar la interfaz con otros tipos de agarre. Sin embargo, y considerando que los sensores de fuerza se distribuyeron de forma óptima de acuerdo a los agarres *SMF* y *PMF*, puede resultar necesario añadir más sensores o cambiar su distribución actual.

En aquellos casos que se usasen tipos de agarres de precisión o de tipo intermedio [83] los cuales ameritan movimientos de abducción en los dedos de la mano, pudiera ser necesario hacer uso de un guante de datos más realista. Esto requeriría de al menos 21 GDL de medición en la mano humana para alcanzar niveles de realismo aceptables. Debe recordarse que el guante de datos X-IST, usado en esta investigación, posee un total de 15 GDL y que la medición de abducción de los dedos no es posible.

7.4.2 Realizar movimiento del Robot en un espacio de tareas de 6 D

Las fuerzas recolectadas por el guante de datos se hicieron sobre la base de un espacio de tarea 3 D **(F_x-F_y-F_z)**. Consecuentemente, el movimiento del robot se realizó en un espacio de tareas de igual dimensión **(x-y-z)**. Con el fin de permitir el movimiento del robot en un espacio de tareas de 6 D, las fuerzas medidas por el guante deben ser convertidas a pares. Esto requiere de una convención para poder realizar la conversión. No obstante, el marco de referencia para la conversión puede tomar múltiples formas o aproximaciones.

Una de las posibles aproximaciones es la de emplear un segundo guante de datos en la mano izquierda. Esto permitiría estimar los pares aplicados en la base de dos vectores de fuerza aplicados sobre una carga en el espacio. El punto de pivote para el cálculo de los momentos de fuerza pudiera estar ubicado justo en el medio de las dos fuerzas, esto es, justo en el medio de las dos manos. Un análisis detallado de esta posible solución se presenta en el Apéndice B de esta memoria de tesis.

7.4.3 Implementar mediciones capacitivas sobre los sensores de fuerza

Con los resultados plasmados en esta memoria de tesis se demostró que las estimaciones de fuerza en sensores piezoresistivos basadas en lecturas combinadas de capacitancia y conductancia arrojan un mayor nivel de exactitud que aquellas basadas únicamente en lecturas de conductancia. Por tanto, resulta lógico que en aras de mejorar el desempeño de la interfaz, se incorporen lecturas de capacitancia a la interfaz para poder así realizar una mejor estimación de la fuerza aplicada.

Sin embargo, tomando en cuenta que ambas líneas de investigación fueron llevadas en paralelo a lo largo del tiempo, la mayoría de los avances y mejoras realizados sobre el sensor FlexiForce se realizaron justo después de que la interfaz de guantes de datos fue diseñada y construida. Esto trajo como consecuencia que buena parte de dichas mejoras no pudieran ser incorporadas a esta versión de la interfaz basada en guantes de datos.

Summary in English

Abstract

This thesis presents a dataglove-based interface for the impedance control of robotic manipulators. The interface comprises a commercial dataglove for measuring fingers' position, an Inertial Measurement Unit (IMU) for tracking hand motion and 11 piezoresistive sensors to measure the applied hand forces. The interface was thoroughly tested on a 6-DOF manipulator with a load cell installed near the robot's end effector. The accuracy of the dataglove interface was assessed through a static test in which the load cell measurements were used as reference on a time-basis. The final test comprised the implementation of an impedance control algorithm in the aforesaid manipulator, in which the interface force readings were used as input for controlling robot motion.

A second line of research is addressed on this thesis regarding the modeling of the piezoresistive sensor FlexiForce A201-100. The sensor, used in the assembling of the dataglove interface, was thoroughly characterized under DC and AC sourcing for multiple applied forces and different puck areas. Three new properties that enhance sensor's capabilities and sensor's response were found. First, it was studied the conductance nonlinearity for DC input voltages under **1 V** and a method to estimate sensor's sensitivity was presented. Second, a piezocapacitive response was found in the sensor which demonstrated its usefulness towards the reduction of the force estimation error, and third; a combined estimation of the applied force and the exertion area was presented through the combined conductance-capacitance estimation.

Chapter 1

1. Introduction: Understanding the basis of haptic perception and object manipulation

The identification and manipulation of objects through tactile exploration is a daily life activity for humans. Turning a door knob is a common, yet not simple, task that involves the combination of multiple sources of information from the visual, tactile and motion domains. This ability, almost exclusive of humans, relies mostly on the visual and somatosensory receptors that together with the central nervous system generate a suitable trajectory for the hand and fingers. Two separate tasks, hand approach to the knob and knob turning, are the subjects to be introduced in this chapter towards the understanding and further emulation of human skills in bioinspired robots.

1.1 The importance of force measurements in Hand-Centered Studies

The Human hand is a complex 27 degrees-of-freedom (DOF) member [108]. It provides humans with a huge variety of grasp types that may be classified in 4 major categories: power grip, intermediate grip, precision grip and grips with no thumb involvement [83]. Human-hand dexterity is especially remarkable, among the rest of species, due to the ability to fully oppose the thumb to rest of the fingers [21]. Analogously, primates such as chimpanzees and orangutans are able to partially oppose their thumbs which allow them to use a variety of sophisticated tools [114]; the restriction of partially opposition implies that pulp-to-pulp contact is not possible between the primates' thumb and the rest of fingers, even though, primates' dexterity is highly remarkable among animals. They are capable of constructing elaborate sleeping nests each night from branches and foliage. These handling abilities are far from being reached by robotic hands, thereby a great effort has been placed to track and understand the primates and humans prehension in an attempt to emulate their abilities.

There are two basic properties that a cybernetic hand must have: an adequate sensory and actuator system accordingly designed for the task to perform, and the ability to gather and analyze the sensory data in order to perform the proper finger and hand motion commands.

A bioinspired sensory system should be available in cybernetic hands if the required dexterity is similar to that of a real hand. This is a major challenge in nowadays research because sensors tend to be bulky, expensive and unable to measure certain properties of the grasped objects such as sharpness, rigidness and temperature. Likewise, the hand muscles exhibit power densities that the leading-edge servomotors are still unable to provide [16], this yields underactuated robotic hands (in an attempt to save space) or off-the-robot location of actuators. In any case, finger motion of cybernetic hands is awkward compared to those of a real hand; even for the *shadow hand* [161], the most realistic realization of a robotic hand ever made with a total of 24 DOF.

The development of adaptive and flexible algorithms for controlling cybernetic hands is also an active research in robotics. Hiden-Markov Models and neural network

techniques are often used to obtain a human-like behavior in robotic hands [1]. The ability to deal with unstructured environments and with constantly changing objects is the key factor to overcome in the development of control algorithms. However, there is still a long road ahead to emulate human skills when manipulating objects of different sizes and weights in a time shared basis. The lack of dexterity not only lies in the existing algorithms intended to control hand motion; the sensory system also plays an important role in this task, because as previously stated, the sensory system of robotic hands is not yet capable of measuring certain properties of the grasped objects, and thus, the control algorithm generates grasp commands based on incomplete-object information.

1.2 Emulating haptic perception in robotic applications: A challenging task for the leading-edge technology of force sensors

The process of recognizing objects through tactile exploration is known as *haptic perception*, which is an ability that the proprioceptors and kinesthesic senses provide to the humans. Proprioceptors and kinesthesis senses are also responsible for a wide variety of human skills such as: sense of equilibrium, ability to determine where a particular body part is located in the space and the ability to determine if a body part has moved. People can rapidly and accurately identify three-dimensional objects by touch; this outstanding human ability combines two processes: *proprioceptive perception* (hand and finger position) and *somatosensory perception of patterns* (texture, edge and curvature of the grasped object). Human skin plays a key role in the latter process because mechanoreceptors and nociceptors lie in the skin; these receptors are responsible for pressure and pain measurement respectively.

A human-like robotic skin should be able to measure, at least, the same object properties than a real hand can actually do. Carrozza and Lamy have presented partial solutions for this task employing strain gages and piezoresistive sensors respectively [16, 100]. These solutions are addressed as partial because current technology is only capable of measuring force and contact. However, these solutions combined with an adequate control algorithm can improve the interaction between the cybernetic hands and the grasped objects in terms of new skills, such as: slippage detection, precision grasp and object liftoff [16].

Likewise, human-like robotic skins can help to ensure safety in a shared human-robot environment by detecting unwanted collision during comanipulation tasks [100]. Safety is of great importance in the domain of Collaborative Robots (Cobots) [98]. In such scenarios, an operator and a robot are working in the same space and physically interacting. Comanipulation is often used to mix the advantages of human workers, such as:

- Outstanding sensory system
- Ability to learn complex tasks and
- Adaptability to changing environments

with the benefits of robots, such as:

- Precision and strength in motion, without getting tired after hours of continuous work and
- Highly Repeatable trajectories, this is of great importance when performing repetitive tasks.

Above advantages must be combined in a framework that ensures comfort and safety for the operator. Then, it becomes natural that force and motion are the variables to monitor and control in a shared human-robot environment. This statement yields the *impedance control of robots*; which has been an active research trend for many years.

Joint encoders, force/torque sensors and accelerometers have been widely used in impedance control applications to provide force/position feedback. A thorough review of impedance control of manipulators shows that force sensors have been usually mounted on the robot end effector, whereas position/speed sensors are integrated in the robot joints. However, this sensory set-up does not warrant user safety, because as previously stated, unwanted collision during comanipulation tasks may still occur. It must be remarked that impedance control is only effective around the robot end effector, but not around the whole robot´s structure, and thus, an unwanted collision between the operator and the robot´s body may go unnoticed and robot motion unaffected.

Human-like robotic skins are a promising approach in the direction of ensuring safety in shared human-robot environments, since they can detect unwanted collision during comanipulation tasks. However, it has not been yet implemented a control layout where the only source of force feedback is provided by such a robotic skin, just as a mute volunteer guides a blind person to walk across the street by holding the blind-person's arm. Under this scenario, the person responds to the force commands from the volunteer in a compliant way, relying solely on her arm mechanoreceptors, just like a robot should respond to the operator intention in case of motion guidance.

Sudden Collisions between the mute volunteer and the blind person are likely to happen during the guidance process. Nevertheless, these collisions do not represent serious harm for any of them; due to the sophisticated proprioceptive system and the intelligence available in both subjects. Hence, it is a logical approach of current research to focus on providing robots with the aforementioned two capabilities (sophisticated proprioceptive system and intelligence); this fact is the main motive for the realization of this thesis.

1.3 Statement of Purpose

This thesis addresses two issues emerging from the interaction of human and robots in cooperative environments. Consequently, two goals are presented as alternatives for overcoming such restrictions.

The first issue is the lack of a detailed model for most of the available skin sensors. This condition is one of the key aspects for the underperformance of such devices and the consequent underused in robotic applications. Skin sensors are mostly of piezoresistive type, which means that incremental forces yield proportional changes in conductance.

The first goal of the current research is to improve the performance of the piezoresistive sensors by modeling sensors' response under DC and AC sourcing. Sensor characterization is merely empirical, and is presented in terms of conductance and capacitance. The force sensor chosen for the current research is the *A201-100 FlexiForce* manufactured by Tekscan Inc, with a nominal range of **440 N** and a sensing area of **71 mm^2** (similar to the size of a 1 cent Euro coin).

The second issue is the employment of piezoresistive sensors in an impedance control application involving a robotic manipulator and an operator. This is a major concern in a shared workspace application if the robot reaction is likely to emulate that of a human being.

The second goal is to implement an impedance control scheme on a manipulator using piezoresistive sensors as the only source of force feedback to the control loop. The developed application uses impedance control as the underlying basis for controlling robot motion. However, an important difference exists with the robotic-skin approach. Instead of placing the force sensors along the robot´s structure, the operator wears a handheld device with the sensors integrated into the palm-side fabric of a 15-DOF dataglove. An Inertial Measurement Unit (IMU) is integrated to the dorsal-side of the dataglove to measure hand orientation within the workspace.

The proposed dataglove-based interface is capable of measuring individual force contributions through a combination of finger position, force sensors and hand orientation. A resultant force vector is calculated and proper motion is achieved in the manipulator. This vector represents user intention, just as a human-like robotic skin measures the operator applied forces.

1.4 Summary of the Remaining Chapters

Chapter 2 reviews the state of the art in force measurements. A comparison is presented for the different approaches of each technology, with special focus on the noninvasive force measuring techniques. A thorough revision of the A201-100 force sensor is presented with representative examples of industrial and research applications.

In Chapter 3 the capabilities of the A201-100 sensor are exploited by performing a set of empirical tests on the sensor. An electrical model for the A201-100 sensor is obtained by combining test results with curve fitting techniques. A series of benefits are derived from the proposed sensor model: the force estimation error is dwindled when combined capacitance-conductance estimation is done. Also, a method to predict sensor's sensitivity under a specific driving voltage is derived.

The ability to determine the applied-force area is a novel property found in the sensor; it implies that the A201-100 device is not only capable of measuring the applied force, but also capable of estimating the area where the force is being applied.

In Chapter 4 a review of the most relevant implementation of IADs is presented. IAD Operation Modes and IAD Control Algorithms are addressed. Passive and Active implementations of assistive robots are explored and compared from the safety and the flexibility standpoints. The notion of non-colocation of actuators and sensors in

IADs is introduced together with the complication arising from such condition. Some solutions for the instability problems resulting from the non-colocation are discussed.

A thorough description of the developed dataglove interface is presented in Chapter 5. Static and dynamic tests are presented in order to demonstrate the feasibility of the interface to operate in a shared human-robot environment. A 6-DOF manipulator and a 6-DOF force/torque sensor are arranged for performing validation and throughput tests. The 6-DOF force/torque sensor is installed on the manipulator`s wrist.

Additional tests comprising the 6-DOF manipulator and the dataglove interface are introduced on Chapter 6. Handling operations with a dummy load are therein presented. Some conclusions and future work are presented in Chapter 7, with emphasis on the possible applications for the new techniques herein proposed.

Chapter 7

7. Conclusions, contributions and future work

This Chapter summarizes the most remarkable facts and findings presented in this thesis. It is also presented some ideas for future developments and improvements regarding the contributions herein presented. Since this thesis has two differentiated, but highly related focuses; the conclusions and the possible future works are presented separately.

7.1 Conclusions regarding the modeling of the piezoresistive sensor model FlexiForce A201-100

An equivalent electrical model was presented and validated for the FlexiForce sensor model A201-100 with some restrictions. An operational amplifier, in inverting configuration, was used along all the tests herein described according to the recommendations given by the device's manufacturer.

7.1.1 Sensor Modeling and identification of non-linearities

The best match model was a parallel Resistor-Capacitor (RC), but some non-linearities were found in sensor's response that restricted the extensive usage of the proposed equivalent circuit. Specifically, two types of non-linearities were found:

Frequency non-linearity: The RC parallel model is a match for the FlexiForce sensor until a certain frequency, conveniently named as divergent frequency, is reached. For driving signals running over such magnitude, saturation in sensor's output is observed and the output phase shift is clamped to **70º** regardless of frequency increases. Slight changes were observed in the magnitude of the divergence frequency from one device to another, as well as little dependency between the applied force and the divergence frequency; this implies that no matter what the applied force is, the divergence frequency remains unchanged. It can be concluded that in order to ensure sensor operation within its linear region, the driving frequency must be held below **4 KHz**.

Amplitude non-linearity: This was probably the hardest to detect non-linearity in the FlexiForce sensor, since it neither produces saturation, nor exponential growth in the output signal of the amplifier circuit. When dealing with amplitude non-linearity, it must be understood as a non-linearity in sensor's resistance, because sensor's resistance is directly responsible for the output voltage under DC sourcing condition.

The type of amplitude non-linearity is that of a hyperbolic tangent function (**tanh**), i.e., the input and output voltage of the conditioning circuit running the FlexiForce sensor is related by a **tanh** function, so incremental input voltages produce hyperbolic tangent variations in the output signal. Nonetheless, and similarly to the frequency non-linearity, the **tanh** model is not comprehensive, and it is only capable of modeling the sensor's non-linearity when the magnitude of the driving voltage is held below **1 V**. For

sourcing voltages over **1 V**, it has not been yet found a suitable function capable of modeling sensor's resistance.

7.1.2 Linear Region of Operation for the FlexiForce sensor

Once the aforementioned non-linearities were delimited, it was possible to define a linear region of operation for the sensor. This is one of the contributions of the present work that could help others to further research in the understanding of piezoresistive sensors. So, in order to operate the FlexiForce sensor within its linear region, the DC voltage must be held constant meanwhile the force is varied. This statement adds no knowledge to the information already given by the manufacturer. However, by recalling that the amplitude non-linearity can be modeled when the sourcing voltage is held below **1 V**, it was demonstrated that it is possible to predict the changes in sensor's sensitivity produced by changes in the driving voltage using the **tanh** model; this yields an accurate force estimation whether the driving voltage is held constant or not during the force estimation process.

Changing the driving voltage is one of the two possible ways to trim a desired sensor's sensitivity. The second way is to change the value of the feedback resistor in the driving circuit.

For such cases that the input voltage is taken off from the range **(-1 V, 1 V)**, it has not been yet developed a sensor's model capable of correcting the amplitude nonlinearity, and consequently, the only way to perform force measurements is to held the input voltage constant meanwhile the force is varied.

Under the case of AC sourcing, the frequency of the driving signal must be held below **4 KHz** with the aim of operating the sensor within its linear region. The amplitude non-linearity is also present under AC sourcing, and thus, the AC-input amplitude was initially held below **1 V**. Nonetheless, a method to bypass the amplitude non-linearity was presented. The proposed method allows the decoupling between the non-linear conductance and the linear capacitance regardless of the magnitude of the AC input signal. This method is another of the main contributions presented in this thesis.

7.1.3 Piezocapacitive response and reduction in the force estimation error

A piezocapacitive response was found in the FlexiForce sensor A201-100. This is a novel property found on the device, and it is clearly another of the main contributions herein presented. The piezocapacitive property demonstrated to be useful to increase sensor's accuracy by means of performing a two-variable estimation of force. The reduction in the force estimation error is of paramount importance for the extensive usage of FlexiForce sensors in robotics applications which demand accurate and noninvasive force measurements.

Three different models working on the basis of combined conductance-capacitance estimation were presented. The traditional conductance model was also implemented for comparison purposes. The results reported an average reduction of **64%** in the force estimation error when compared with the conductance model proposed by the manufacturer. The method for computing the estimation error was based on the Mean Squared Error.

A decoupling method was used to perform capacitance readings over the sensors. For such purpose, the output signal from the driving circuit is multiplied by a cosine function which is then low-pass filtered to produce a DC signal which is only dependent on sensor's capacitance. This method was above declared as one of the contributions from this thesis. Despite all the aforesaid improvements, there is still a long road ahead for polymer piezoresistive sensors to match the sensitivity of load cells.

7.1.4 Combined estimation of the applied force and the exertion area

It was demonstrated that a combined estimation of the applied force and the exertion area is possible. For such purpose, a characterization involving different puck areas and force sweep was performed; meanwhile, sensor's conductance and capacitance were collected. With the data collected and the previous knowledge of capacitance and conductance variations, it was possible to arrange an equation system which could estimate both: the exertion area of the applied force and the force itself. This development is also claimed as one of the contributions of this thesis.

7.2 Future work regarding the modeling of the piezoresistive sensor model A201-100

Within the field of piezoresistive sensing technology, there are multiple approximations to follow on future researches. Next are addressed only some of the possible lines of research in regard with the contributions herein presented. However, a broader scope of the possible approximations was presented by Liu [107], with special focus on the new polymer materials and its usage on the manufacturing of piezoresistive sensors.

In order to follow the research lines summarized in Section 7.1, it should be first modeled the amplitude non-linearity of the FlexiForce sensor for input amplitudes greater than **1 V**. This is probably the most straightforward task to perform in the short term since the amplitude non-linearity was only studied for input voltages under **1 V**. A comprehensive sensor model without voltage restrictions is necessary for multiple reasons, e.g., to match a desired sensitivity in a multi sensor development or to develop more realistic models that include the temperature drift as input variable.

Modeling amplitude non-linearity for any input voltage would also allow to theoretically demonstrate the feasibility of the measuring scheme presented in Section 3.3.3, which is able to bypass the nonlinear behavior of sensor's conductance. This is important because only a partial demonstration was presented with the restriction of $\mathbf{|V_s| < 1\ V}$.

This thesis has presented plenty of empirical and theoretical data to support the usage of capacitance variation as an effective way to reduce the force estimation error. As above mentioned, a method to read sensor's capacitance through the bypass of conductance non-linearity was also presented. Later efforts can either focus on improving the performance of such devices or in providing additional functionalities to them, e.g., a combined estimation of the applied force and the exertion area. This property was already presented but there are many others available such as: the development of a thermal model to estimate the sensitivity variations produced by temperature changes. It is also possible to further research in the reduction of the force

estimation error through the proposal of new relationships between conductance and capacitance changes.

A combined estimation of the applied force and the exertion area was presented. However, no results were offered regarding the accuracy of such method because not enough experimental data were collected. Further researches could take as start point the framework for performing the combined estimation of force and area; this would include the set of pucks with different puck areas, the testbench and the equation system itself. The combined estimation of force and area is probably the most challenging task within the field of piezoresistive sensing because it demands full knowledge of resistive and capacitive variations as a function of the applied force.

Formulating a unifying model that embraces the exertion area, the applied force and temperature under a wide range of voltages is also a challenging task to perform. The model should be able to predict capacitance and conductance changes for the four mentioned variables. This could make available a wide range of capabilities to the sensor and yield a broader usage on robotic applications. However, it cannot be ascertained that such a model is possible to be formulated because the relationship between temperature, capacitance and conductance has not been yet explored.

Finally, it must be recalled that the modeling and methods presented in Chapter 3 have been developed for the sensor FlexiForce A201-100. However, there are multiple manufacturers of piezoresistive sensors as reported in Chapter 4. A broader study could embrace the application of the techniques learned in Chapter 3 to the Interlink sensor or to any other sensor working on the basis of piezoresistive sensing.

7.3 Conclusions regarding the dataglove interface for the impedance Control of Robotic Manipulators

The dataglove interface demonstrated to be a valid solution for determining the hand applied forces during object manipulation. Multiple applications can be encountered to the interface; this thesis has focused on only of them, the impedance control of a robotic manipulator.

7.3.1 Interface Functioning and Overview

The dataglove interface is a multi-sensor development capable of gathering the hand applied forces during object manipulation through the 11 piezoresistive sensors installed on the palm side. The instantaneous finger position is collected through the X-IST dataglove with a resolution of 15 DOF. Finally, the hand orientation within the task space is provided by an Inertial Measurement Unit, IMU, with magnetic field compensation. The IMU has been conveniently located on the dorsal side of the dataglove for comfort purposes.

The force sensor distribution along the palm side of the dataglove was based on previous hand grip studies and on the size of the robot's load. A match between the load size and the optimum sensor distribution was made with the goal of maximizing the user's comfort while reducing sensor number to a minimum. Given the bulky

characteristics of the load, the Surrounding Mild Flexion (SMF) and the Parallel Mild Flexion (PMF) grips were chosen to exert forces during load manipulation [83].

Through the combination of the information provided by the multiple sensors, it was possible to estimate, in a real-time basis, the hand applied forces meanwhile the operator manipulates the robot's endpoint or the robot's load. The hand applied forces are taken as the user's intention of motion, and thus, they are used to perform an impedance control scheme over the 6-DOF manipulator. Nonetheless, robot motion is only possible under a 3D (**x-y-z**) task space in this version of the interface.

This control scheme is based on the hands-on-payload concept, which states that the control interfaces of Intelligent Assist Devices should be as natural as possible, and likewise, the robot's maneuvers, levers or push button should be replaced by direct contact interfaces. The tests performed during this thesis demonstrated the feasibility of the dataglove interface to operate under the hands-on-payload concept.

It must be remarked that robot motion was done only with information from the dataglove interface and the robot kinematics. No information regarding the dynamic model of the manipulator was required. This is the most remarkable contribution of the dataglove interface, since the formulation of the robot dynamic model can be skipped.

When attempting to control a robotic manipulator under the hands-on-payload scheme, a load cell is usually installed near the robot's end point to collect the user applied forces. However, a robot dynamic model is required to discriminate among the user applied forces and the self-robot forces. The dataglove interface avoids the formulation of the robot dynamic model because the user's forces are directly obtained through the sensors installed on the palm side of the dataglove. Considering the decoupled dynamics that exists between the hand-dataglove system and the robot's structure, the self-robot forces do not affect the force readings acquired from the dataglove interface, and thus, they can be directly fed back to the impedance control loop. This is a clear advantage provided by the dataglove interface.

7.3.2 Resume of the tests performed over the dataglove interface

The force readings acquired from the dataglove interface were compared with the force measurements collected from a JR3 sensor installed near the end point of the 6-DOF manipulator. The JR3 sensor is a multi-axis load cell capable of collecting the forces and torques over all the axes with remarkable accuracy due to its built-in strain gauges. Considering that the JR3 readings were affected by the self-robot forces, two types of tests were performed.

First, a motionless test was performed and the force readings from the dataglove were compared with the JR3 force readings. The comparison was made on a time basis in separate plots for each axis. A separate plot was presented with the error along each axis. Considering that robot motion was disabled, the inertial forces were absent in the force plots from the JR3 sensor, and an objective comparison could be performed. The test results demonstrated the feasibility of the dataglove interface to track the hand applied forces over all the axes, but with certain inaccuracies in the force magnitude and direction.

One of the key advantages demonstrated during the motionless test was the ability of the dataglove interface to filter the hand applied forces from the forces produced by the robot's compliance. To understand this, it must be recalled that after the operator stopped from applying forces over the load, the manipulator kept oscillating for a few seconds due to the robot's compliance. This oscillating behavior was collected by the JR3 sensor, and was represented in the force plots with an oscillation pattern right after lifting the hand from the load. On the opposite side, the force readings collected by the interface exhibited a smooth decay when the hand force faded; this occurred due to the decoupled dynamics between the robot's structure and the hand-dataglove system.

The Second test applied to the dataglove interface was of dynamic type; this test embraced the usage of the real-time force measurements for the impedance control of a 6-DOF manipulator. In this case, the JR3 readings could no longer be considered as reference because the self-robot forces stemming from inertia affected the force measurements. Similar to the results stemmed from the static test, the experimental results demonstrated the feasibility of the interface to operate under the hands-on-payload mode by providing smooth force profiles and consequently adequate robot motion.

7.3.3 Broad usage of the dataglove interface in other research fields

The dataglove interface is an effective way of assessing the human intention during object's grasping and manipulation. The results herein presented demonstrated the feasibility of the interface for the impedance control of a 6-DOF manipulator. However, there are multiple applications that the dataglove interface could encounter. First of all, the force information stemmed from the interface could be used to control any type of manipulator. The only information required from the manipulator is the kinematic model to control the joint trajectories of each axis, but no information from the dynamic model is required. This fact eases the integration of the interface to any type of robotic manipulator.

The dataglove interface also finds possible applications within the field of rehabilitation. The force information gathered from the piezoresistive sensors, together with the finger flexion information is highly valuable when tracking patient's progress after any type of hand disease.

Within the field of sport researches, the dataglove interface could be used to track the hand applied forces together with hand motion during the holding stage of specific instruments of each sport, such as: golf sticks, tennis racquets and balls. Force tracking in unstructured environments is possible with the proposed interface since it is portable and battery sourced. Likewise, force and motion tracking is of paramount importance in multiple research fields which are hand-centered and demand reliable measuring solutions with little or null interference to the user's activity (noninvasive force readings). This statement is on the same trend with the above conclusions regarding the research over the FlexiForce sensor.

7.4 Future work regarding the dataglove interface

There are multiple approaches for future developments related with the dataglove interface, they are next listed:

7.4.1 Different Finger Configurations

The tests presented in this thesis were done using the Surrounding Mild Flexion (SMF) and the Parallel Mild Flexion (PMF) grips. These were the most appropriate grips for the bulky load held by the manipulator. With the aim of exhaustively testing the interface, it is necessary to change the load, for a less bulky one, and then use different grips to interact with it. Under such scenario, it could be necessary to either add more force sensors, or change its distribution over the hand.

If multiple hand grips are to be implemented, or if manipulation with precision grip is required, it would be necessary to use a more realistic dataglove capable of measuring finger abduction over all the fingers. This would require a minimum of 21 DOF to achieve a realism level capable of coping with the precision grips. The X-IST dataglove, employed in this research, is capable of measuring up to 15 DOF but only finger flexion is measured.

7.4.2. Allow full robot motion over a 6-D taskspace.

The forces gathered by the dataglove interface were done on the basis of a 3-D taskspace, (**F_x-F_y-F_z**). Consequently, robot motion was performed in a 3-D taskspace (**x-y-z**). In order to allow full robot motion in a 6-D taskspace, the measured forces must be converted to torques. This requires a conversion convention that may have multiple possibilities.

One of the possible solutions is to employ a second dataglove on the left hand. This would allow torque estimation on the basis of two force vectors applied over a free load in the space. The pivot point for the moment torque calculation could be located in the middle of both forces; that is, in the middle of both hands. An in-depth analysis of this approach is available on the Appendix B of this thesis.

7.4.3 Implement capacitive measurements over the piezoresistive sensors.

This thesis has demonstrated the advantages of combined conductance-capacitance estimation towards the reduction of the force estimation error in piezoresistive devices. The most straightforward way of improving the accuracy of the dataglove interface is, therefore, to implement capacitance readings on the piezoresistive sensors, and then, implement a combined conductance-capacitance estimation of the exerted force.

Considering that both research lines have been performed in parallel, the most remarkable improvements on force sensing were discovered right after the dataglove interface was designed and built. This caused that many of the force sensing improvements could not be implemented on this version of the dataglove interface.